Probing plasmonic nanostructures:
A theoretical study of light-matter interaction in graphene-based and metallic systems

Dissertation

zur Erlangung des akademischen Grades

doctor rerum naturalium

(Dr. rer. nat.)

im Fach Physik

Spezialisierung: Theoretische Physik

eingereicht an der

Mathematisch-Naturwissenschaftlichen Fakultät

der Humboldt-Universität zu Berlin

von

Diplom-Physikerin Julia Franziska Maria Werra

Präsidentin der Humboldt-Universität zu Berlin

Prof. Dr. Sabine Kunst

Dekan der Mathematisch-Naturwissenschaftlichen Fakultät

Prof. Dr. Elmar Kulke

Gutachter/innen: 1. Prof. Dr. Kurt Busch

2. Prof. Dr. N. Asger Mortensen

3. Prof. Dr. Stefan Scheel

Tag der mündlichen Prüfung: 13.10.2016

To my dad

*who has always been, still is, and
always will be my source of
inspiration.*

Introduction

Even before the Nobel prize winning development of Stefan Hell (see Refs. [1–3]) it has been known (see Refs. [4, 5]) that quantum emitters, emitting single photons by the relaxation from a high to a low energy state, are useful for imaging a variety of different objects and processes. These objects and processes of interest stem from a wide range of areas. The use of quantum emitters provides access to a number of observation quantities including, among others, the possibility to image biomedical processes (see, e.g., Ref. [6, 7]). It also allows to obtain information with regards to the characterization of engineered nanostructures such as the optical and electronic properties at the edges of a graphene flake or the exact shape of metallic nanostructures (see, e.g., Ref. [8]). In the case of graphene, research has been conducted by the use of different methods such as scanning electron microscopy or scanning near-field optical microscopy (see Refs. [9, 10]). However, using emitters to probe graphene (as well as other materials) allows access to additional physical properties such as magneto-optical properties (see Ref. [11, 12]) by detecting the modification of the emitters' emission dynamics.

Besides from their usefulness in imaging, quantum emitter have also become important in hybrid light-matter devices whose development has evolved to a goal in itself. Here, the challenge lies in sufficiently enhancing the coupling between the emitter (radiating photons) and the nanophotonic system (matter) such that a controlled interaction occurs (cf. Ref. [13] for a current review). Hybrid systems discussed in the literature, are, among others, single emitters coupling to conducting nanostructures (see Ref. [14]) and cold atom clouds coupling to graphene (see Ref. [15]) or other conducting materials (see Ref. [16]). Especially, hybrid light-matter systems applied in the areas of quantum cryptography and quantum information processing attract attention (see Refs. [17–20]).

Here, one of the important properties of an emitter is the capability to store information (cf., e.g., Ref. [21]). This is needed when moving from all-electronic devices to optical chips which are hopeful candidates for next generation computers (see Refs. [20, 22]). Since optical components bare much smaller Ohmic losses than traditional electronic devices and have much higher switching times, researchers have been trying to develop optical chips for years. Until now there has not been made a final decision on the most suited material system for these chips such that a commercialization is still lacking. Eventually, however, one will not only need to provide a storage medium (such as possibly provided by emitters) but also waveguiding elements that are able to highly confine and guide the light that transports the information between different computational sites. These photonic parts might consist of dielectric waveguides possibly containing plasmonic elements close to which the coupling of emitters to light is enhanced. In conclusion, within the research on emitters its interaction with suited photonic and plasmonic environments is of interest.
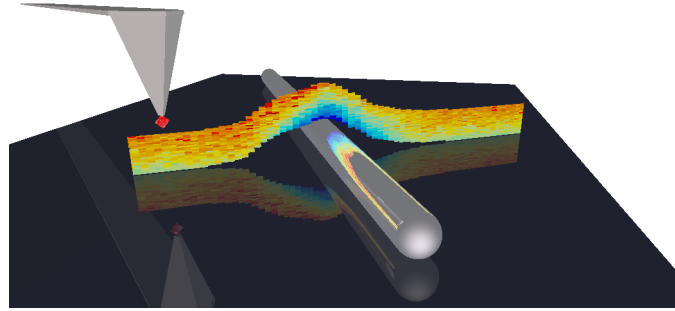
Figure 1: Sketch on three-dimensional scanning probe fluorescence lifetime imaging microscopy. By gluing a nanodiamond containing a single nitrogen-vacancy color center to a cantilever, we are able to not only measure the height profile of plasmonic structures but at the same time the lifetime modifications of a single quantum emitter due to the photonic environment. Figure adapted from Ref. [W2], doi:10.1021/nl500460c.

In this field of light-matter coupling research where, on the one hand, the community uses emitters in order to probe electromagnetic environments with increasing accuracy and, on the other hand, the community tailors the coupling of emitters to their photonic environment in order to develop light-matter devices with enhanced properties, this thesis is located.

In the following, we present studies on different plasmonic systems (matter) coupling to emitters (radiating photons). We especially focus on the probing capabilities of the emitters which promise an increased understanding of fundamental electronic and optical properties. For example, we discuss the lifetime modifications and their implications for emitters placed above graphene which is known to be "a platform for strong light-matter interactions" (cf. Ref. [23]). Although graphene is a system that exhibits with respect to its two-dimensionality a strong coupling and low Ohmic losses, we also focus on the coupling of emitters to well-known plasmonic nanostructures. Here, we concentrate on the theoretical description of expected modifications of the emitters' radiation dynamics when probing these nanostructures to eventually achieve an enhanced light-matter coupling in these systems.

Outline

The thesis is structured as follows: in chapter 1, we introduce the theoretical background (see chapter 1) required within this work. We will begin with a basic discussion of Maxwell's equations and the properties of the electromagnetic fields, continue with the introduction to some elements of quantum mechanics such as the quantum mechanical equations of motion and an introduction to quantum field theory and close with an inspection of elements of response theory where we focus specifically on the response of the electrons in a medium to the electromagnetic field.

In chapter 2, we discuss some elements of the theory of graphene. We start out by considering the tight-binding description and explaining the approximations necessary to

arrive at the Dirac formalism before focusing on the nature of a band gap in graphene. This lays the foundation to introduce the electromagnetic response of graphene within different approximations using quantum-field theoretical descriptions. Together with the review of the general response of the electrons in a medium, this allows for a description of all plasmonic materials within this thesis, both graphene and metals.

In chapter 3, we focus on radiation dynamics of those emitters that will be discussed in the main chapters of the thesis. Here, we distinguish between electric and magnetic dipole transitions and discuss the classical description of an emitter, the influence of the photonic environment leading to a modification of the emitter's lifetime and transition frequency and the experimental realization of these dipoles. With these foundations, we can then study the light-matter interaction in different plasmonic systems.

In chapter 4, we discuss the influence of graphene exhibiting a band gap onto electric and magnetic emitters. Such a band gap is relevant since in experimental setups graphene is often deposited on a substrate such as hexagonal boron nitride and in this case researchers find the opening of a meV band gap in graphene. Additionally, the electromagnetic modes in slab dielectric - graphene - slab dielectric waveguides are discussed in detail.

When moving to nanostructured systems, we require a computational modeling of the nanophotonic systems to describe the radiation dynamics of the emitters accurately. In chapter 5, we present the basics on the numerical method applied in this thesis, the Discontinuous Galerkin Time-Domain method. Furthermore, we report on different numerical tools implemented within the scope of this thesis such as current sheets suited to incorporate graphene into the electromagnetic modeling. Furthermore, the concept of oblique incidence within the Discontinuous Galerkin Time-Domain method is discussed and made use of for a graphene multilayer system.

We furthermore make use of the Discontinuous Galerkin Time-Domain method to probe more involved plasmonic nanostructures in chapter 6. Specifically, we demonstrate the advantages of numerical modeling in order to characterize a three-dimensional scanning-probe fluorescence lifetime imaging microscopy probe that allows for the three-dimensional investigation of the lifetime modifications of a single-photon quantum emitter in such a nanoplasmonic system (see Fig. 1). Additionally, we introduce a self-consistent dipole description within the Discontinuous Galerkin Time-Domain method and display its usefulness by studying the lifetime modification of picosecond emitters (such as found, e.g., in the intersystem crossing in iridium or copper complexes, see Refs. [24, 25]) in the proximity of a gold pentamer leading to involved radiation dynamics. These are relevant since plasmonic structures allow to decrease the lifetime of emitters even further (see Ref. [26]) and thus might allow to detect processes on very short time scales with an appropriate spatial resolution and thus can be applied, e.g., in biological imaging.

In chapter 7, we conclude this work by summing up the outcomes and discussing in an outlook future research questions including past and present work that is closely related to the results presented here.

Contents

Contents

List of Figures

List of Figures

Acronyms

0D zero-dimensional. 25

1D one-dimensional. 10, 25, 106

2D two-dimensional. 7, 25, 26, 85, 106, 130, 176

3D three-dimensional. 25, 37, 38, 56, 106, 112, 114, 116, 130, 133, 137, 138

ADE auxiliary differential equation. 111–113, 116, 117, 132, 189

AFM atomic force microscope. 137–139, 141–143, 145, 146, 165

ARPES angle-resolved photoemission spectroscopy. 62, 165

CP critical point. 115–117

DGTD Discontinuous Galerkin Time-Domain method. 105–107, 111, 114–122, 125, 126, 131, 133, 139, 141, 146–148, 150–152, 154, 155, 166, 167, 191, 192

FDTD Finite Difference Time-Domain method. 105, 106, 114, 117, 119, 120, 123, 126, 131, 147, 148

FLIM scanning-probe fluorescence lifetime imaging microscopy. 133, 137

FV Finite Volume. 116

hBN hexagonal boron nitride. 30, 40, 62, 68, 118–121, 130

HMM hyperbolic metamaterial. 119–121, 130–132

LSRK low storage Runge Kutta. 109, 149–153, 167

NV nitrogen-vacancy. 43, 45, 61, 98, 103, 133–146, 165

ODE ordinary differential equation. 109, 149, 150, 152, 153

PEC perfect electric conducting. 108, 110

PMC perfect magnetic conducting. 108, 110

Acronyms

PML perfectly matched layer. 111, 126

QE quantum emitter. 133, 134, 137, 146

QE-FLIM three-dimensional scanning-probe fluorescence lifetime imaging microscopy performed by a single quantum emitter. 133, 137, 138, 144–146, 165, 166

QED quantum electrodynamics. 29, 47, 175

QFT quantum field theory. xv, 6, 7, 9, 10, 13, 14, 16, 22, 25, 29, 96, 169, 172

QM quantum mechanics. 7–10, 14, 53, 169

Sf scattered-field. 109, 110, 126, 127, 148

SiC silicon carbide. 62

SiV silicon-vacancy. 45, 61

SPE single-particle excitation. 20, 67, 69, 70, 72, 73, 76, 79, 83–85, 92–98, 100–103, 183, 185

TE transverse electric. 38, 39, 64, 66–71, 73–90, 95, 97–100, 118, 120, 121, 129, 173, 174, 176, 181, 186

Tf total-field. 109, 127

TfSf total-field/scattered-field. 109, 110, 119, 124, 126, 127, 139, 148, 150, 152–155

TM transverse magnetic. 38, 39, 64, 66, 69, 71, 75–77, 81–83, 85, 90, 95, 99, 100, 118, 120, 121, 129, 130, 173–176, 182, 183

uPML uniaxial perfectly matched layer. 111, 119, 126, 127

ZPL zero phonon line. 135, 136

Theoretical background

> *"Whatever difficulties we may have in forming a consistent idea of the constitution of the aether, there can be no doubt that the interplanetary and interstellar spaces are not empty, but are occupied by a material substance or body, which is certainly the largest, and probably the most uniform body of which we have any knowledge."* [1]

> James Clerk Maxwell

In this first chapter of the dissertation, we discuss the fundamentals used throughout the thesis. Since the thesis covers the electromagnetic interaction of emitters with plasmonic nanostructures, a description of both the electromagnetic field propagation as well as the surrounding matter is obligatory. For this reason, we split the first chapter into three parts: first we discuss the propagation of the classical electromagnetic fields, then we introduce quantum mechanical notations and last we cover methods to determine the electronic response to an electromagnetic perturbation.

1.1 The electromagnetic field

1.1.1 Maxwell's equations

Maxwell's equations are at the core of every description of the time evolution of electromagnetic fields and thus are the starting point of this work. Since they were introduced in a rather complicated formulation by J. C. Maxwell, they have been reformulated in a number of ways suitable for different problems. In this work, we follow the notation in Ref. [27] for the macroscopic Maxwell's equations

$$\nabla \cdot \mathbf{D}(\mathbf{r}, t) = \rho_{\text{free}}(\mathbf{r}, t) \,, \tag{1.1a}$$

$$\nabla \cdot \mathbf{B}(\mathbf{r}, t) = 0 \,, \tag{1.1b}$$

$$\nabla \times \mathbf{H}(\mathbf{r}, t) - \partial_t \mathbf{D}(\mathbf{r}, t) = \mathbf{j}_{\text{free}}(\mathbf{r}, t) \,, \tag{1.1c}$$

$$\nabla \times \mathbf{E}(\mathbf{r}, t) + \partial_t \mathbf{B}(\mathbf{r}, t) = 0 \,. \tag{1.1d}$$

---

[1] "Ether", Encyclopædia Britannica Ninth Edition

1 Theoretical background

Above, $\rho_{\text{free}}(\mathbf{r}, t)$ and $\mathbf{j}_{\text{free}}(\mathbf{r}, t)$ describe the free charge density and charge current density that are not constituents of a macroscopic object and obey the continuity equation (see Ref. [27])

$$\partial_t \rho_{\text{free}}(\mathbf{r}, t) + \boldsymbol{\nabla} \cdot \mathbf{j}_{\text{free}}(\mathbf{r}, t) = 0 \,. \tag{1.2}$$

To complete this set of equations, we additionally list the constitutive relations that connect the electric field $\mathbf{E}(\mathbf{r}, t)$ with the electric displacement vector $\mathbf{D}(\mathbf{r}, t)$ and the magnetic field $\mathbf{H}(\mathbf{r}, t)$ with the magnetic flux density $\mathbf{B}(\mathbf{r}, t)$, respectively (cf. Ref. [27])

$$\mathbf{D}(\mathbf{r}, t) = \varepsilon_0 \mathbf{E}(\mathbf{r}, t) + \mathbf{P}(\mathbf{r}, t) \,, \tag{1.3a}$$

$$\mathbf{H}(\mathbf{r}, t) = \frac{1}{\mu_0} \mathbf{B}(\mathbf{r}, t) + \mathbf{M}(\mathbf{r}, t) \,, \tag{1.3b}$$

where we introduce the vacuum permittivity ε_0 that connects to the vacuum speed of light via the vacuum permeability μ_0 with

$$c^{-2} = \varepsilon_0 \mu_0 \,. \tag{1.4}$$

In Eq. (1.3a), the macroscopic electric polarization $\mathbf{P}(\mathbf{r}, t)$ is defined as the sum over the dipole moments $\mathbf{p}_i$ of each of the different types of molecules i bound in a material

$$\mathbf{P}(\mathbf{r}, t) = \sum_i N_i \langle \mathbf{p}_i(\mathbf{r}, t) \rangle \,, \tag{1.5}$$

where N_i are the average number of molecules of type i in a small volume around a point $\mathbf{r}$ over which $\mathbf{p}_i$ is averaged. The magnetic polarization $\mathbf{M}(\mathbf{r}, t)$ is given analogously to Eq. (1.5)

$$\mathbf{M}(\mathbf{r}, t) = \sum_i N_i \langle \boldsymbol{\mu}_i(\mathbf{r}, t) \rangle \,, \tag{1.6}$$

summing over the averaged magnetization of all molecules in a small volume around position $\mathbf{r}$. With these definitions, we can derive the microscopic Maxwell's equations (relating the electric and magnetic fields to all microscopic charges, free and bound in the material, $\rho = \rho_{\text{free}} + \rho_{\text{b}}$ and equivalently currents $\mathbf{j} = \mathbf{j}_{\text{free}} + \mathbf{j}_{\text{b}}$, see Ref. [27]). The macroscopic electric and magnetic polarization relate then to the bound charge and current as (see Ref. [27])

$$\rho_{\text{b}} = -\boldsymbol{\nabla} \cdot \mathbf{P}(\mathbf{r}, t) \,, \qquad \text{and} \qquad \mathbf{j}_{\text{b}} = \boldsymbol{\nabla} \times \mathbf{M}(\mathbf{r}, t) + \partial_t \mathbf{P}(\mathbf{r}, t) \,. \tag{1.7}$$

In the case of a spatial homogeneous medium, another way to introduce the material's properties into Maxwell's equations is given by (see Ref. [27])

$$\mathbf{D}(\mathbf{r}, t) = \int_{\mathcal{V}} \mathrm{d}^3 r' \int_{-\infty}^{\infty} \mathrm{d}t' \underline{\varepsilon}(\mathbf{r}', t') \cdot \mathbf{E}(\mathbf{r} - \mathbf{r}', t - t') \,, \tag{1.8a}$$

$$\mathbf{B}(\mathbf{r}, t) = \int_{\mathcal{V}} \mathrm{d}^3 r' \int_{-\infty}^{\infty} \mathrm{d}t' \underline{\mu}(\mathbf{r}', t') \cdot \mathbf{H}(\mathbf{r} - \mathbf{r}', t - t') \,, \tag{1.8b}$$

where the spatial integration is performed over the mode volume $\mathcal{V}$ in which the electromagnetic radiation is contained.

The temporal and spatial dependent dielectric and magnetic tensors $\underline{\varepsilon}(\mathbf{r}, t) \equiv \varepsilon_0 \underline{\varepsilon}_r(\mathbf{r}, t)$ and $\underline{\mu}(\mathbf{r}, t) \equiv \mu_0 \underline{\mu}_r(\mathbf{r}, t)$, respectively, describe the macroscopic material's "response"[2] to an electromagnetic field. Here, we split the dielectric and magnetic tensors into the vacuum permittivity and permeability (see Eq. (1.4)) and the material dependent contribution. As discussed above, the electromagnetic fields are then influenced not only by external, free charges $\rho_{\text{free}}(\mathbf{r}, t)$ and charge currents $\mathbf{j}_{\text{free}}(\mathbf{r}, t)$ in Maxwell's equations (1.1) but are also governed strongly by dielectric and metallic structures and its bound charges whose responses to the electromagnetic fields are described in an effective manner via the dielectric and magnetic tensor.

In parallel to the time-domain and spatial description, all quantities introduced above can be converted into frequency ω and wavevector $\mathbf{q}$ domain using the Fourier transform $\mathcal{F}_{(\mathbf{r},t)}[A(\mathbf{r}, t)]$ of a function $A(\mathbf{r}, t)$ and the inverse transform $\mathcal{F}_{(\mathbf{r},t)}[A(\mathbf{r}, t)](\mathbf{q}, \omega)$

$$A(\mathbf{r}, t) = \mathcal{F}_{(\mathbf{q},\omega)}[\mathcal{A}(\mathbf{q}, \omega)](\mathbf{r}, t) \equiv \frac{1}{(2\pi)^4} \int_{-\infty}^{\infty} \mathrm{d}\omega \int_{-\infty}^{\infty} \mathrm{d}^3 q \, \mathcal{A}(\mathbf{q}, \omega) \mathrm{e}^{-\mathrm{i}(\omega \cdot t - \mathbf{q} \cdot \mathbf{r})} \,,$$

$$\Updownarrow$$

$$\mathcal{A}(\mathbf{q}, \omega) = \mathcal{F}_{(\mathbf{r},t)}[A(\mathbf{r}, t)](\mathbf{q}, \omega) \equiv \int_{-\infty}^{\infty} \mathrm{d}t \int_{-\infty}^{\infty} \mathrm{d}^3 r \, A(\mathbf{r}, t) \mathrm{e}^{\mathrm{i}(\omega \cdot t - \mathbf{q} \cdot \mathbf{r})} \,. \tag{1.9}$$

Jointly with the convolution theorem

$$\mathcal{F}_\omega[(f * g)(t)](\omega) \equiv \mathcal{F}_\omega\left[\int_{-\infty}^{\infty} \mathrm{d}\tau \, f(\tau) g(t - \tau)\right] \equiv \mathcal{F}_\omega[f(t)] \, \mathcal{F}_\omega[g(t)] \,, \tag{1.10}$$

Equations (1.1) and (1.3) read

$$\mathbf{q} \cdot \boldsymbol{\mathcal{D}}(\mathbf{q}, \omega) = \rho_{\text{free}}(\mathbf{q}, \omega) \,, \qquad\qquad \mathbf{q} \cdot \boldsymbol{\mathcal{B}}(\mathbf{q}, \omega) = 0 \,, \tag{1.11a}$$

$$\mathbf{q} \times \boldsymbol{\mathcal{H}}(\mathbf{q}, \omega) + \mathrm{i}\omega \boldsymbol{\mathcal{D}}(\mathbf{q}, t) = \mathbf{j}_{\text{free}}(\mathbf{q}, \omega) \,, \qquad \mathbf{q} \times \boldsymbol{\mathcal{E}}(\mathbf{q}, \omega) - \mathrm{i}\omega \boldsymbol{\mathcal{B}}(\mathbf{q}, \omega) = 0 \,, \tag{1.11b}$$

$$\boldsymbol{\mathcal{D}}(\mathbf{q}, \omega) = \underline{\varepsilon}(\mathbf{q}, \omega) \cdot \boldsymbol{\mathcal{E}}(\mathbf{q}, \omega) \,, \qquad\qquad \boldsymbol{\mathcal{B}}(\mathbf{q}, \omega) = \underline{\mu}(\mathbf{q}, \omega) \cdot \boldsymbol{\mathcal{H}}(\mathbf{q}, \omega) \,. \tag{1.11c}$$

In this thesis we limit the discussion to materials for which $\underline{\mu}_r = \mathbb{1}$ in the range of frequencies of interest. Additionally, we assume only isotropic materials (since glasses and metals discussed as material components in this thesis are in first approximation isotropic) such that $\underline{\varepsilon}_r = \varepsilon_r \mathbb{1}$.

The wavevector $\mathbf{q}$ is connected to the wavelength of light λ via $q \equiv |\mathbf{q}| = 2\pi/\lambda$ while wavevector and angular frequency are connected via the material's phase velocity $q = \omega/\tilde{c}$ with the speed of light in a material defined via

$$\tilde{c} = \frac{1}{\sqrt{\varepsilon \mu}} = \frac{c}{\varepsilon_r \mu_r} \,. \tag{1.12}$$

---

[2]See sections 1.3 and 1.3.1 for more details on the correct formulation of the electron's response to an external or internal electromagnetic field.

1 Theoretical background

Last, we can derive the wave equations for the electric and magnetic fields (compare Ref. [28]) for constant dielectric functions $\varepsilon_r(\mathbf{r}, \omega) = \varepsilon_r$ (assuming a local and non-dispersive material[3])

$$\mathbf{q} \times \mathbf{q} \times \boldsymbol{\mathcal{E}}(\mathbf{q}, \omega) - \frac{\omega^2}{c^2} \varepsilon_r \boldsymbol{\mathcal{E}}(\mathbf{q}, \omega) = \mathrm{i}\omega\mu_0 \mathbf{j}_{\mathrm{free}}(\mathbf{q}, \omega), \tag{1.13a}$$

$$\mathbf{q} \times \mathbf{q} \times \boldsymbol{\mathcal{H}}(\mathbf{q}, \omega) - \frac{\omega^2}{c^2} \varepsilon_r \boldsymbol{\mathcal{H}}(\mathbf{q}, \omega) = \mathbf{q} \times \mathbf{j}(\mathbf{q}, \omega). \tag{1.13b}$$

and for $\varepsilon_r \neq 0$, the use of Eqs. (1.1a) and (1.8a) and $\boldsymbol{\nabla} \times \boldsymbol{\nabla} \times \boldsymbol{\mathcal{A}} = \boldsymbol{\nabla}\boldsymbol{\nabla} \cdot \boldsymbol{\mathcal{A}} - \Delta\boldsymbol{\mathcal{A}}$, the wave equations then read

$$\left(\Delta + \frac{\omega^2}{\tilde{c}^2}\right) \boldsymbol{\mathcal{E}}(\mathbf{r}, \omega) = -\mathrm{i}\omega\mu_0 \mathbf{j}_{\mathrm{free}}(\mathbf{r}, \omega) + \frac{\boldsymbol{\nabla}\rho_{\mathrm{free}}(\mathbf{q}, \omega)}{\varepsilon_0\varepsilon_r}, \tag{1.14a}$$

$$\left(\Delta + \frac{\omega^2}{\tilde{c}^2}\right) \boldsymbol{\mathcal{H}}(\mathbf{r}, \omega) = -\boldsymbol{\nabla} \times \mathbf{j}(\mathbf{r}, \omega). \tag{1.14b}$$

Here, we reverse the Fourier transform of the real space component with the notation

$$\mathcal{A}(\mathbf{r}, \omega) \equiv \mathcal{F}_{\mathbf{q}}[\mathcal{A}(\mathbf{q}, \omega)](\mathbf{r}, \omega), \tag{1.15}$$

where $\mathcal{A}(\mathbf{r}, \omega)$ and $\mathcal{A}(\mathbf{q}, \omega)$ exhibit different functional dependencies regardless of the same symbolic notation.

1.1.2 Poynting's theorem

For the description of the nanostructure's electrons' interaction with the electromagnetic fields, energy considerations allow for the calculation of physical quantities, i.e., the losses or later the decay rate of an emitter in proximity of the nanostructure. Considering a single particle of charge q and velocity $\mathbf{v}$, an external electric field $\mathbf{E}$ and magnetic flux density $\mathbf{B}$ perform via the Lorentz force $\mathbf{F}_{\mathrm{Lorentz}}(\mathbf{r}, t) = q\mathbf{E}(\mathbf{r}, t) + q[\mathbf{v} \times \mathbf{B}(\mathbf{r}, t)]$ work of $\partial_t W(\mathbf{r}, t) = \mathbf{v} \cdot \mathbf{F}_{\mathrm{Lorentz}}(\mathbf{r}, t) = q\mathbf{v} \cdot \mathbf{E}$ per time unit on this particle. The magnetic field cannot perform work due to its orthogonal action on the charged particle with respect to the particle's velocity. Considering now a continuous particle current, we arrive for the rate of energy dissipation $\partial_t W(t)$ in a finite volume V per time unit at (cf. Ref. [28])

$$\partial_t W(t) = \int_V \mathrm{d}^3 r \, \mathbf{j}_{\mathrm{free}}(\mathbf{r}, t) \cdot \mathbf{E}(\mathbf{r}, t). \tag{1.16}$$

Rewriting the free current by use of Maxwell's equation (1.1c), we find

$$\int_V \mathrm{d}^3 r \, \mathbf{j}_{\mathrm{free}}(\mathbf{r}, t) \cdot \mathbf{E}(\mathbf{r}, t) = \int \mathrm{d}^3 r \left[\mathbf{E}(\mathbf{r}, t) \cdot (\boldsymbol{\nabla} \times \mathbf{H}(\mathbf{r}, t)) - \mathbf{E}(\mathbf{r}, t) \cdot \partial_t \mathbf{D}(\mathbf{r}, t) \right]. \tag{1.17}$$

---

[3]In general, non-dispersive, being frequency independent, dielectric functions are non causal and thus unphysical. However, especially glasses exhibit a constant dielectric function over a broad frequency window. Whenever one is interested in exclusively this window and considers linear phenomena, a non-dispersive description is appropriate.

With the vector identity

$$\boldsymbol{\nabla} \cdot (\mathbf{E}(\mathbf{r},t) \times \mathbf{H}(\mathbf{r},t)) = \mathbf{H}(\mathbf{r},t) \cdot (\boldsymbol{\nabla} \times \mathbf{E}(\mathbf{r},t)) - \mathbf{E}(\mathbf{r},t) \cdot (\boldsymbol{\nabla} \times \mathbf{H}(\mathbf{r},t)) \,,$$

and electric field's rotation Equation out of Maxwell's equations (1.1d), we arrive at

$$\int_V \mathrm{d}^3 r \, \mathbf{j}_{\mathrm{free}}(\mathbf{r},t) \cdot \mathbf{E}(\mathbf{r},t) = - \int \mathrm{d}^3 r \left[\boldsymbol{\nabla} \cdot (\mathbf{E}(\mathbf{r},t) \times \mathbf{H}(\mathbf{r},t)) \right. \tag{1.18}$$
$$\left. + \mathbf{E}(\mathbf{r},t) \cdot \partial_t \mathbf{D}(\mathbf{r},t) + \mathbf{H}(\mathbf{r},t) \cdot \partial_t \mathbf{B}(\mathbf{r},t) \right] \,.$$

Considering the special case of a linear macroscopic medium without dispersion and internal losses, we can define

$$u(\mathbf{r},t) = \frac{1}{2} \left(\mathbf{E}(\mathbf{r},t) \cdot \mathbf{D}(\mathbf{r},t) + \mathbf{B}(\mathbf{r},t) \cdot \mathbf{D}(\mathbf{r},t) \right) \,, \tag{1.19}$$

and with this we find

$$- \int_V \mathrm{d}^3 r \, \mathbf{j}_{\mathrm{free}}(\mathbf{r},t) \cdot \mathbf{E}(\mathbf{r},t) = \int \mathrm{d}^3 r \left[\boldsymbol{\nabla} \cdot (\mathbf{E}(\mathbf{r},t) \times \mathbf{H}(\mathbf{r},t)) + \partial_t u(\mathbf{r},t) \right] \tag{1.20}$$

$$\Updownarrow$$

$$\partial_t u(\mathbf{r},t) + \boldsymbol{\nabla} \cdot \mathbf{S} = -\mathbf{j}_{\mathrm{free}}(\mathbf{r},t) \cdot \mathbf{E}(\mathbf{r},t) \,, \tag{1.21}$$

where the last reformulation is appropriate considering that we assumed an arbitrary but finite volume V. Above, we introduce the Poynting vector

$$\mathbf{S}(\mathbf{r},t) = \mathbf{E}(\mathbf{r},t) \times \mathbf{H}(\mathbf{r},t) \,, \tag{1.22}$$

which describes the energy flux density. Here, the reader should realize that we define the Poynting vector in real space with real fields $\mathbf{E}(\mathbf{r},t)$ and $\mathbf{H}(\mathbf{r},t)$. Thus $\mathbf{S}(\mathbf{r},t)$ is the instantaneous energy flux density. The common confusion on complex and real valued fields and the way to calculate the Poynting vector correctly stems from the fact that one is often interested in the average energy flux, finding (assuming a plane wave with one frequency ω only)

$$\langle S \rangle_\omega = \frac{1}{T} \int_0^T \mathbf{S}(t) \mathrm{d}t = \frac{1}{T} \int_0^T \mathrm{d}t \left(\mathrm{Re} \left[\boldsymbol{\mathcal{E}} \mathrm{e}^{-\mathrm{i}\omega t} \right] \times \mathrm{Re} \left[\boldsymbol{\mathcal{H}} \mathrm{e}^{-\mathrm{i}\omega t} \right] \right)$$
$$= \frac{1}{2T} \int_0^T \mathrm{d}t \left(\mathrm{Re} \left[\boldsymbol{\mathcal{E}} \times \boldsymbol{\mathcal{H}}^* \right] + \mathrm{Re} \left[\boldsymbol{\mathcal{E}} \times \boldsymbol{\mathcal{H}} \mathrm{e}^{-2\mathrm{i}\omega t} \right] \right) = \frac{1}{2} \mathrm{Re} \left[\boldsymbol{\mathcal{E}} \times \boldsymbol{\mathcal{H}}^* \right] \,. \tag{1.23}$$

In the last step, we neglected the rotating terms since they average out by performing the time integral. Here, it is important to note that although one generally also uses this approach to calculate a frequency dependent Poynting vector, they are only equal in the case of a real plane wave. When using a finite pulse width in theoretical and numerical computations, the Poynting vector is highly nonlinear and therefore in general it is not justified to apply these single-mode considerations to the experiments or numerics realized for broad probe pulses. However, for sufficiently wide pulses in time domain, these approximations still hold.

1 Theoretical background

1.1.3 Electromagnetic potentials

Another possibility to write Maxwell's equations is to introduce a scalar and vector potential instead of the electric and magnetic fields. Especially in quantum field theory (QFT) (see section 1.2.2), this notation is often used (see section 1.2.3) since the potentials allow for Maxwell's equations (see Eq. (1.1)) being formulated in one dense equation (see Eq. (1.31) below).

To fulfill Eq. (1.1b), we can define a vector potential

$$\mathbf{B}(\mathbf{r},t) = \boldsymbol{\nabla} \times \mathbf{A}(\mathbf{r},t) \,, \qquad \text{since} \quad \boldsymbol{\nabla} \cdot \big[\boldsymbol{\nabla} \times \mathbf{A}(\mathbf{r},t) \big] = 0 \,, \tag{1.24}$$

for any vector field. With this definition and Eq. (1.1d), we find

$$\boldsymbol{\nabla} \times \big[\mathbf{E}(\mathbf{r},t) + \partial_t \mathbf{A}(\mathbf{r},t) \big] = 0 \,,$$

that is always fulfilled for

$$\mathbf{E}(\mathbf{r},t) = -\boldsymbol{\nabla}\Phi(\mathbf{r},t) - \partial_t \mathbf{A}(\mathbf{r},t) \,. \tag{1.25}$$

By use of this scalar potential $\Phi(\mathbf{r},t)$ we find the equivalent to Maxwell's equations

$$\Delta\Phi(\mathbf{r},t) + \partial_t \big[\boldsymbol{\nabla} \cdot \mathbf{A}(\mathbf{r},t) \big] = -\frac{\rho_{\text{free}}(\mathbf{r},t)}{\varepsilon_0 \varepsilon_r} \,, \tag{1.26a}$$

$$\Delta\mathbf{A}(\mathbf{r},t) - \frac{\varepsilon_r \mu_r}{c^2} \partial_t^2 \mathbf{A}(\mathbf{r},t) - \boldsymbol{\nabla} \left[\boldsymbol{\nabla} \cdot \mathbf{A}(\mathbf{r},t) + \frac{\varepsilon_r \mu_r}{c^2} \partial_t \Phi(\mathbf{r},t) \right] = -\mu_0 \mu_r \mathbf{j}_{\text{free}}(\mathbf{r},t) \,, \tag{1.26b}$$

where we assumed the surrounding material to be non-dispersive and linear as it is the case for many dielectrics such as glass in the frequency window discussed in this thesis. In general, one has a certain freedom to choose the potentials since the physical quantity, the magnetic flux density $\mathbf{B}$, remains constant even for

$$\mathbf{A}(\mathbf{r},t) \to \mathbf{A}'(\mathbf{r},t) = \mathbf{A}(\mathbf{r},t) + \boldsymbol{\nabla}\Lambda(\mathbf{r},t) \,, \tag{1.27a}$$

$$\Phi(\mathbf{r},t) \to \Phi'(\mathbf{r},t) = \Phi(\mathbf{r},t) - \partial_t \Lambda(\mathbf{r},t) \,. \tag{1.27b}$$

The freedom of the specific choice of the potentials is fixed by the choice of a specific *gauge*, such as, e.g., the Lorenz gauge

$$\boldsymbol{\nabla} \cdot \mathbf{A}(\mathbf{r},t) + \frac{\varepsilon_r \mu_r}{c^2} \partial_t \Phi(\mathbf{r},t) = 0 \,, \tag{1.28}$$

uncouples the equations of motion of both potentials and leading to

$$\Delta\Phi(\mathbf{r},t) - \frac{\varepsilon_r \mu_r}{c^2} \partial_t^2 \Phi(\mathbf{r},t) = -\frac{\rho_{\text{free}}(\mathbf{r},t)}{\varepsilon_0 \varepsilon_r} \,, \tag{1.29a}$$

$$\Delta\mathbf{A}(\mathbf{r},t) - \frac{\varepsilon_r \mu_r}{c^2} \partial_t^2 \mathbf{A}(\mathbf{r},t) = -\mu_0 \mu_r \mathbf{j}_{\text{free}}(\mathbf{r},t) \,. \tag{1.29b}$$

The parallelism of the two equations of motions allows then to rewrite the scalar and vector potential into a covariant four-vector[4] potential (see Ref. [27])

$$A = \{A_\mu\} = (\Phi/\tilde{c}, -\mathbf{A})\,, \tag{1.30}$$

and an equivalent four-vector current $j = \{j_\mu\} = (\tilde{c}\rho, -\mathbf{j})$, Maxwell's equations read

$$\partial^\nu \partial_\nu A_\mu = \mu_0 \mu_r j_\mu\,, \tag{1.31}$$

where we define $\nabla = \{\partial_\mu\} = (\partial_t/\tilde{c}, \boldsymbol{\nabla})$ and use the Einstein convention of summing four-vectors $\partial^\nu \partial_\nu = \sum_{\nu=0}^{3} \partial^\nu \partial_\nu \equiv \partial_t^2/\tilde{c}^2 - \sum_{\nu=1}^{3} \partial_\nu^2$. As in Eq. (1.12), we abbreviate the speed of light in a material as $\tilde{c} = 1/\sqrt{\varepsilon_0\mu_0\varepsilon_r\mu_r}$.

1.2 Elements of quantum mechanics

In the macroscopic Maxwell's equations (see Eqs. (1.11)), the electromagnetic fields are coupled to a dielectric environment described by the dielectric tensor $\underline{\varepsilon}(\mathbf{q}, \omega)$. To derive an appropriate effective model for this macroscopic function from microscopic and quantum mechanics (QM) theories, remains a vivid field in condensed matter research. In the context of graphene plasmonics, the choice of an appropriate dielectric function (or for a two-dimensional medium rather a surface conductivity as discussed in Sec. 2.2.2) is of great importance. Throughout this work, we apply descriptions of different physical realizations of graphene (e.g., graphene with and without band gap, at different temperatures or with and without a finite chemical potential) and compare experimental consequences within these models. They all base on a QFT modeling of the electrons.

In this section, we therefore first introduce the QM notation and then introduce the basic elements of QFT. This is then the basis for the final section of this chapter where we deal with response theory.

1.2.1 Quantum mechanical equations of motion

The time evolution of state $|\psi_S(t)\rangle$ of a QM system in the *Schrödinger representation* is determined by the Schrödinger equation

$$i\hbar\partial_t|\psi_S(t)\rangle = \hat{\mathcal{H}}|\psi_S(t)\rangle\,, \tag{1.32}$$

---

[4]The co- and contravariant vector notation is a notation used especially in the theory of special relativity but is useful in field theories as well. Since the distance squared of a four-coordinate system with the contravariant vector $x = \{x^\mu\} = (t/\tilde{c}, \mathbf{x}) = (x_0, \mathbf{x})$

$$s^2 = x_0^2 - x_1^2 - x_2^2 - x_3^2\,,$$

has to be Lorentz invariant in special relativity, a special *covariant* vector is defined $x = \{x_\mu\} = (t/\tilde{c}, -\mathbf{x}) = (x_0, -\mathbf{x})$ that all physical laws containing Lorentz-scalars, four-vectors and four tensors are Lorentz invariant. The scalar product (also known as Lorentz scalar) can only be Lorentz invariant when it is defined as

$$B \cdot A \equiv B_\alpha A^\alpha = B^0 A^0 - \mathbf{B} \cdot \mathbf{A}\,,$$

with $B_\alpha = g_{\alpha\beta} B^\beta$. Here, we establish the contravariant, metric tensor $\{g_{\mu\nu}\} = \{g^{\mu\nu}\} = \mathrm{diag}(1, -1, -1, -1)$ leading to $B = \{B_\mu\} = (B_0, -\mathbf{B})$.

1 Theoretical background

where $\hat{\mathcal{H}} = \hat{\mathcal{H}}_S$ is the Hamiltonian in Schrödinger representation and $\hbar$ is the Planck constant.

Equivalent to the Schrödinger notation, QM can be expressed in the Heisenberg representation

$$\frac{\mathrm{d}}{\mathrm{d}t}\hat{O}_H(t) = \partial_t \hat{O}_H(t) + \frac{\mathrm{i}}{\hbar}[\hat{\mathcal{H}}_H(t), \hat{O}_H(t)], \tag{1.33}$$

assuming time-dependent operators $\hat{O}_H(t)$ and time-independent states. The two representations are for time-independent Hamiltonians $\hat{\mathcal{H}}_H(t) = \hat{\mathcal{H}}_S = \hat{\mathcal{H}}$ connected via

$$\hat{O}_H(t) = \mathrm{e}^{\mathrm{i}\hat{\mathcal{H}}t}\hat{O}_S \mathrm{e}^{-\mathrm{i}\hat{\mathcal{H}}t},$$

with $\hat{O}_H(-\infty) = \hat{O}_S$ and are thus in a physical sense equivalent since $\langle \psi_S^\dagger(t)|\hat{O}_S|\psi_S(t)\rangle = \langle \psi_H^\dagger(t)|\hat{O}_H(t)|\psi_H\rangle$.

Also for a time-independent Hamiltonian, the solution to Eq. (1.32) is given by the time evolution operator

$$|\psi(t')\rangle = \hat{\mathcal{U}}(t',t)|\psi(t)\rangle, \qquad\qquad \hat{\mathcal{U}}(t',t) \equiv \mathrm{e}^{-\frac{\mathrm{i}}{\hbar}\hat{\mathcal{H}}\cdot(t'-t)}. \tag{1.34}$$

The expectation value of the time evolution operator

$$\mathcal{U}(q',t';q,t) = \langle q'|\hat{\mathcal{U}}(t',t)|q\rangle, \tag{1.35}$$

is known as the propagator. In Eq. (1.35), $|q\rangle$ and $|q'\rangle$ are the initial and final state, respectively, between which the propagator describes the transition probability.

Oftentimes, the Hamiltonian may be written as

$$\hat{\mathcal{H}}(t) = \hat{\mathcal{H}}_0 + \hat{V}(t), \tag{1.36}$$

with an unperturbed, time-independent Hamiltonian $\hat{\mathcal{H}}_0$ for which the solutions are well known and a possibly time-dependent interaction potential $\hat{V}(t)$ that is assumed to vanish $\hat{V}(-\infty) = 0$. Then, it is advantageous to use a third representation, known as the *interaction representation*

$$\hat{O}_I(t) = \mathrm{e}^{\frac{\mathrm{i}}{\hbar}\hat{\mathcal{H}}_0 t}\hat{O}_S \mathrm{e}^{-\frac{\mathrm{i}}{\hbar}\hat{\mathcal{H}}_0 t}, \tag{1.37}$$

$$|\psi_I(t)\rangle = \mathrm{e}^{\frac{\mathrm{i}}{\hbar}\hat{\mathcal{H}}_0 t}\mathcal{T}_t \mathrm{e}^{-\frac{\mathrm{i}}{\hbar}\int_{-\infty}^{t}\mathrm{d}t'\hat{\mathcal{H}}(t')}|\psi_S(-\infty)\rangle. \tag{1.38}$$

The time ordering operator $\mathcal{T}_t$ sorts the time-dependent operators within the exponential operator's series expansion with the smallest time to the rightmost. The general time evolution connecting a state at time t' with a state at time t is then given (compare Ref. [29])

$$|\psi_I(t)\rangle = \mathcal{S}(t,t')|\psi_I(t')\rangle, \tag{1.39}$$

with the S-Matrix

$$\hat{\mathcal{S}}(t,t') = \mathrm{e}^{\frac{\mathrm{i}}{\hbar}\hat{\mathcal{H}}_0(t-t')}\mathcal{T}_t \mathrm{e}^{-\frac{\mathrm{i}}{\hbar}\int_{t'}^{t}\mathrm{d}t''\hat{\mathcal{H}}(t'')}, \tag{1.40}$$
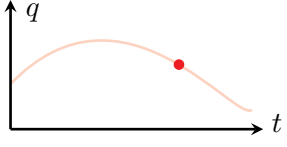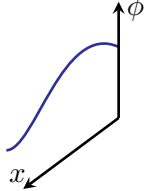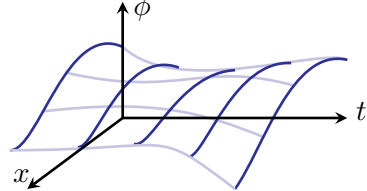
	Degrees of freedom	Path integral
QM		
QFT		

Figure 1.1: The Figure above is adapted with permission from Ref. [30] and shows the differences and similarities between QM and QFT. Due to the difference in degree of freedom, the dimensionality of the path integral changes. In the figure above, the dark red and blue point and lines, respectively, symbolize the QM and QFT quantities at *one* given time, while the shaded lines represent the time evolution of one degree of freedom.

that is also known as the interaction picture time-evolution operator $\hat{\mathcal{U}}_I$ in some literature. The equation of motion for the S-Matrix is given as

$$i\hbar\hat{\mathcal{S}}(t,t') = \hat{V}_I(t)\hat{\mathcal{S}}(t,t')\,, \tag{1.41}$$

leading to the explicit representation

$$\mathcal{S}(t,t') = \mathcal{T}_t\exp\left[-\frac{i}{\hbar}\int_{t'}^{t}dt''\hat{V}(t'')\right]\,. \tag{1.42}$$

In this thesis, we mostly apply the Schrödinger representation. For simplicity, we drop the subscripts and if not otherwise explicitly stated

$$|\psi(t)\rangle \equiv |\psi_S(t)\rangle \qquad \text{and} \qquad \hat{O} \equiv \hat{O}_S\,. \tag{1.43}$$

1.2.2 Elements of quantum field theory

We introduce the basic notion of quantum mechanics in the previous section in order to describe different physical systems in this thesis. On the one hand, this includes emitters (see chapter 3) but on the other hand it is necessary to appropriately describe material models.

For an appropriate material description we focus on the electronic degrees of freedom that are in general multiparticle states. In this case, the time evolution operator and the solution of Eq. (1.34) is not solvable directly due to the dimensionality of the system. In

1 Theoretical background

these cases, it is helpful to make use of Feynman's path integrals (see Refs. [30, 31]). This path integral allows to describe the particles as excited states of a physical field such as, e.g. photons as excitations of the electromagnetic fields. When using fields instead of particles, we need a *QFT* instead of the previously introduced QM description to describe the time evolution of the fields.

The concepts introduced in the following lead beyond others to the QFT description of the electronic response to an external electromagnetic field. The difference between the description of mechanics, e.g., a particle and a field theory can be easily understood by Fig. 1.1. Mechanics starts from one degree of freedom that becomes one-dimensional (1D) by integrating over time t (such as, e.g., a single particle). In field theory, however, a field $\phi(x)$ is already depending on the parameter set x where x is d-dimensional (such as, e.g., the electromagnetic field). This field is then additionally integrated over the time t such that QFT itself maps from a $(d+1)$-dimensional space-time into the field manifold, $(x, t) \rightarrow \phi(x, t)$.

One possible example of such a field is, e.g., an electromagnetic field with different modes (defined, e.g, by parameters as polarizations and wavevector), where a different state can be prepared in each mode, arriving at

$$|\psi\rangle \equiv |\psi_1, \psi_2, \ldots\rangle = |\psi_1\rangle \otimes |\psi_2\rangle \otimes \ldots , \tag{1.44}$$

where the field is described as a product state of the bosonic single-mode states. Since coherent states are the eigenstates of the annihilation operator and additionally the most classical (and therefore the states that are experimentally easiest to prepare), we will use in this thesis (cf. Eq. (A.18))

$$|\psi\rangle \equiv e^{-\sum_i \frac{\psi_i^* \psi_i}{2}} e^{\sum_i \psi_i \hat{a}_i^\dagger} |0\rangle . \tag{1.45}$$

In this case, the over completeness relation reads (cf. Eq. (A.19))

$$\int \prod_i \frac{d\psi_i^* d\psi_i}{\pi} |\psi\rangle\langle\psi| \equiv \int d(\psi^*, \psi)|\psi\rangle\langle\psi| = \mathbb{1}_{\mathcal{F}} , \tag{1.46}$$

with the unit matrix of the Fock states $\mathbb{1}_{\mathcal{F}}$.

Fields in this work are not exclusively bosonic (e.g., electromagnetic fields with the photon as corresponding particle) as discussed above but also fermionic (e.g., electronic fields with the electron as corresponding particle). For both of these entities, we can formulate a QFT in terms of their coherent states (see appendix A and Eq. (1.45)). As described above, these states are d-dimensional and thus a (quantum) field theory is needed for their description (cf. Fig. 1.1).

There are several quantities that may be computed using QFT. One is the partition function

$$\mathcal{Z} = \mathrm{Tr}\left[e^{-\beta\left(\hat{\mathcal{H}} - \mu\hat{N}\right)} \right] = \sum_n \langle n| e^{-\beta\left(\hat{\mathcal{H}} - \mu\hat{N}\right)} |n\rangle . \tag{1.47}$$

This sum over all states in thermal equilibrium is a function from which all thermodynamic quantities can be derived. It is governed by the quantum Gibbs distribution

$$\hat{\rho}_{\mathrm{Gibbs}} = \frac{1}{\mathcal{Z}} e^{-\beta\left(\hat{\mathcal{H}} - \mu\hat{N}\right)} , \tag{1.48}$$

that describes the thermodynamics of a system in contact with a heat bath of temperature T as well as a particle reservoir at chemical potential μ. Then, with $\beta = (k_B T)^{-1}$ and $\hat{N}$ the particle number operator, the temperature T is a measure of entropy exchange due to its contact with the heat bath and the chemical potential μ is a measure of particle exchange due to its contact with the particle reservoir.

In Eq. (1.47), we represent the partition Function in a sum over a complete set of Fock states. In order to rewrite the partition function in terms of coherent states, we insert the unit matrix presented in Eq. (1.46)

$$
\begin{aligned}
\mathcal{Z} &= \int \mathrm{d}(\psi^*, \psi) \sum_n \langle n|\psi\rangle \langle \psi|e^{-\beta\left(\hat{\mathcal{H}} - \mu\hat{N}\right)}|n\rangle \\
&= \int \mathrm{d}(\psi^*, \psi) \sum_n \langle \zeta\psi|e^{-\beta\left(\hat{\mathcal{H}} - \mu\hat{N}\right)}|n\rangle \langle n|\psi\rangle \\
&= \int \mathrm{d}(\psi^*, \psi) \langle \zeta\psi|e^{-\beta\left(\hat{\mathcal{H}} - \mu\hat{N}\right)}|\psi\rangle \,,
\end{aligned}
$$

where we use the completeness relation of Fock states Eq. (A.11). Due to the different nature of fermions and bosons, the factor $\zeta = \pm 1$ for bosonic and fermionic states appears in the equation above when interchanging the order of braket and matrix element (cf. Eq. (A.23)). Splitting the partition function into $N \to \infty$ equivalent temperature slices $\delta = \beta/N$ and inserting a unit matrix Eq. (1.46) at each time step, the partition function reads

$$
\begin{aligned}
\mathcal{Z} &= \lim_{N \to \infty} \int \prod_{n=1}^N \mathrm{d}[(\psi^*)^{(n)}, \psi^{(n)}] \cdot \\
&\quad \cdot e^{-\delta \sum_{n=0}^{N-1} \left\{ \delta^{-1}[(\psi^*)^{(n)} - \psi^*{}^{(n+1)}) \cdot \psi^{(n)} + H[(\psi^*)^{(n+1)}, \psi^{(n)}) - \mu N[(\psi^*)^{(n+1)}, \psi^{(n)}] \right\}} \quad (1.49) \\
&\equiv \int D(\psi^*, \psi) e^{-S[\psi^*, \psi]} \,.
\end{aligned}
$$

Here, we rewrite $D(\psi^*, \psi) = \lim_{N \to \infty} \Pi_{n=1}^N \mathrm{d}\left[(\psi^*)^{(n)}, \psi^{(n)}\right]$ with the states $\psi^{(n)}$ representing the states in each time slice n. The Hamiltonian and particle function read

$$
H(\psi^*, \psi) \equiv \frac{\langle \psi|\hat{\mathcal{H}}(\hat{a}^\dagger, \hat{a})|\psi'\rangle}{\langle \psi|\psi'\rangle} \qquad \text{and} \qquad N(\psi^*, \psi) \equiv \frac{\langle \psi|\hat{N}(\hat{a}^\dagger, \hat{a})|\psi'\rangle}{\langle \psi|\psi'\rangle} \,,
$$

considering the operators $\hat{\mathcal{H}}(\hat{a}^\dagger, \hat{a})$ and $\hat{N}(\hat{a}^\dagger, \hat{a})$ to be *normal ordered*[5]. With this, we find the action

$$
S[\psi^*, \psi] = \int_0^\beta \mathrm{d}\tau \left[\psi^* \partial_\tau \psi + H(\psi^*, \psi) - \mu N(\psi^*, \psi) \right] \,, \qquad (1.50)
$$

---

[5] Normal ordering describes the ordering of the annihilation and creation operators in a general operator in such a way that all the annihilation operators are positioned to the right of the creation operators, e.g., the normal-ordered number operator reads

$$
\hat{n} = \hat{a}^\dagger \hat{a} \,.
$$

1 Theoretical background

where we introduce the inverse temperature derivative $\psi^* \partial_\tau \psi$. On first glance, one does not distinguish between fermions and bosons in Eq. (1.50). However, while $\psi^* \partial_t \psi$ can be understood as an ordinary derivative in the bosonic case, it is not trivial that this is actually true in the fermionic case. Thus, it is simply a notation and describes the expression $\partial_\tau|_{\tau=n\delta} \psi^*(\tau) \equiv \lim_{\delta \to 0} \delta^{-1}[(\psi^*)^{(n)} - (\psi^\dagger)^{(n-1)}]$. Additionally, these coherent states satisfy the boundary conditions $\psi^*(0) = \zeta\psi^*\beta$ and $\psi(0) = \zeta\psi(\beta)$ in the integral in Eq. (1.50).

In Eq. (1.50), the action is represented at finite temperature with the variable τ integrating over inverse temperatures. This temperature dependence can be interpreted as a formulation of the action in terms of imaginary times. Comparing Eq. (1.34) with Eq. (1.47), the upper limit of Eq. (1.50) can be replaced by $\beta \to it/\hbar$. Then, one can rephrase the imaginary time $\tau = it'/\hbar$ and find

$$
\begin{aligned}
S[\psi^*, \psi] &= \frac{i}{\hbar} \int_0^t dt' \left[-i\hbar\psi^* \partial_{t'}\psi + H(\psi^*, \psi) - \mu N(\psi^*, \psi) \right] \\
&\equiv -\frac{i}{\hbar} \int d^n x \mathcal{L}[t'; \psi^*, \psi] \, .
\end{aligned}
\tag{1.51}
$$

In the last reformulation, we define a Lagrangian density $\mathcal{L}$ in parallel to classical field theory and Lagrangian mechanics (see Refs. [32, 33]). For a classical field φ_i the classical action reads

$$
\begin{aligned}
S[\varphi_i] &= \int d^n x \, \mathcal{L}[\varphi_i(x), \partial_{x^\alpha}\varphi_i(x), x^\alpha] \\
&\text{with} \quad L[\varphi_i] = \int d^{n-1} x \, \mathcal{L}[\varphi_i(x), \partial_{s^\alpha}\varphi_i(x), x^\alpha] \, ,
\end{aligned}
\tag{1.52}
$$

where we integrate out all variables of the system but the time. Above, we consider n independent variables $\alpha = 0, \ldots, n-1$ and abbreviate $s = \{x^\alpha\}$ with the time denoted by $t = x^0$. The Lagrangian density $\mathcal{L}$ is obtained with the conjugate momentum of the field

$$
\pi_i = \frac{\partial \mathcal{L}[\varphi_i(x), \partial_{x^\alpha}\varphi_i(x), x^\alpha]}{\partial_{x^\alpha}\varphi_i(x)} \, ,
\tag{1.53}
$$

via a Legendre transformation from the system's Hamiltonian density $\hat{\mathscr{H}}$

$$
\mathcal{L}[\varphi_i(x), \partial_{x^\alpha}\varphi_i(x), x^\alpha] = \sum_{i=1}^n \pi_i \varphi_i(x) - \hat{\mathscr{H}}[\varphi_i(x), \partial_{x^\alpha}\varphi_i(x), x^\alpha] \, .
\tag{1.54}
$$

Above, the Hamiltonian density is related to the Hamiltonian by the integration

$$
\hat{\mathcal{H}} = \int d^{n-1} x \, \hat{\mathscr{H}} \, ,
\tag{1.55}
$$

(see Refs. [32, 33] for further details).

Here, it is advantageous to include all $\hbar$-dependent prefactors into the action as opposed to the classical formulation of the action in Eq. (1.52). When including these prefactors,

it is easier to "hide" them in the specific shape of the action instead of distinguishing between different expressions for the action.

The action Eq. (1.51), is then called *Minkowski action* as opposed to the formulation in imaginary times Eq. (1.50) which is called *Euclidean action*. The reformulation by $\tau = -\mathrm{i}t'/\hbar$ is equivalent to a *Wick rotation* where the terminus "rotation" is motivated by the fact that the integration axis is rotated by 90 degree in the complex plane.

Finally, the expectation value of an operator is then given as the functional average over the action describing the system

$$\langle ... \rangle \equiv \frac{\int D(\psi^*, \psi)\, \mathrm{e}^{-S[\psi^*, \psi]}\,(...)}{\mathcal{Z}}\,, \tag{1.56}$$

where we further define the (free) expectation value of the unperturbed system (with the unperturbed action $S_0 = \int_0^\beta \mathrm{d}\tau \left[\psi^* \partial_\tau \psi + H_0(\psi^*, \psi) - \mu N(\psi^*, \psi) \right]$ and $\hat{\mathcal{H}}_0$ as defined in Eq. (1.36))

$$\langle ... \rangle_0 \equiv \frac{\int D(\psi^*, \psi)\, \mathrm{e}^{-S_0[\psi^*, \psi]}\,(...)}{\int D(\psi^*, \psi)\, \mathrm{e}^{-S_0[\psi^*, \psi]}} \equiv \frac{\int D(\psi^*, \psi)\, \mathrm{e}^{-S_0[\psi^*, \psi]}\,(...)}{\mathcal{Z}_0}\,. \tag{1.57}$$

1.2.3 The action of the electromagnetic field

Since in this work we describe the electromagnetic fields classically, we introduce the *classical* action of the electromagnetic field at the point (cf. Eq. (1.52)). The action of the electromagnetic field is relevant in the context of light-matter interaction especially, when using QFT methods to determine the electron's response to an external field. Following Refs. [27, 30], we introduce the electromagnetic field tensor

$$F(\mathbf{r}, \omega) = \left\{ F_{\mu\nu} \right\} = \begin{pmatrix} 0 & \mathcal{E}_1/\tilde{c} & \mathcal{E}_2/\tilde{c} & \mathcal{E}_3/\tilde{c} \\ -\mathcal{E}_1/\tilde{c} & 0 & -\mathcal{B}_3 & \mathcal{B}_2 \\ -\mathcal{E}_2/\tilde{c} & \mathcal{B}_3 & 0 & -\mathcal{B}_1 \\ -\mathcal{E}_3/\tilde{c} & -\mathcal{B}_2 & \mathcal{B}_1 & 0 \end{pmatrix}\,, \tag{1.58}$$

where we consider a local medium with $\varepsilon_r(\omega) \neq 0$, the speed of light inside a material $\tilde{c}$ (cf. Eq. (1.12)), the electric field $\boldsymbol{\mathcal{E}}(\mathbf{r}, \omega)$ and the magnetic flux density $\boldsymbol{\mathcal{B}}(\mathbf{r}, \omega)$ defined in Eqs. (1.1) and (1.3). The electromagnetic field tensor Eq. (1.58) can also be represented in terms of the four-vector electromagnetic field potential (see section 1.1.3) as

$$F_{\mu\nu} = \partial_\mu \mathcal{A}_\nu - \partial_\nu \mathcal{A}_\mu\,, \tag{1.59}$$

with $\{\partial_\mu\} = (-\mathrm{i}\omega/\tilde{c}, \boldsymbol{\nabla})$ and $\{\mathcal{A}_\mu\} = (\Phi(\mathbf{r}, \omega)/\tilde{c}, -\boldsymbol{\mathcal{A}}(\mathbf{r}, \omega))$.

In order to derive the electromagnetic field's Lagrangian density, we start with a general Lagrangian density (see Eq. (1.52)). Any Lagrangian density that correctly describes a field theory of fields φ_i fulfills the variational principles (see Ref. [32])

$$\frac{\partial \mathcal{L}}{\partial \varphi_\mu} - \partial_\nu \frac{\partial \mathcal{L}}{\partial(\partial_\nu \varphi_\mu)} = 0\,. \tag{1.60}$$

1 Theoretical background

As discussed in Ref. [30], it is possible to find three requirements of the form of the Lagrangian density that are independent of Maxwell's equations. The Lagrangian density has to be (i) invariant under Lorentz transforms, (ii) invariant under Gauge transforms and (iii) as simple as possible. Including a four-vector current $\mathbf{j}_{\text{free}} = \{\mathbf{j}_{\text{free},\mu}\} = (\tilde{c}\rho_{\text{free}}, \mathbf{j}_{\text{free}})$, the simplest Lagrangian density possible

$$\mathcal{L}_{\text{EM}} = \alpha_1 F_{\mu\nu} F^{\mu\nu} + \alpha_2 \mathcal{A}_\mu \mathbf{j}_{\text{free}}^\mu \,. \tag{1.61}$$

Above, we introduce two undetermined prefactors α_1 and α_2 that need to be determined comparing Eq. (1.61) to Maxwell's equations (1.1) and the electromagnetic energy density Eq. (1.19).

The generalized spatial and momentum variables are in the case of the electromagnetic fields A_μ and $\partial_\nu A_\mu$, respectively, such that the variation of the action reads

$$0 = \frac{\partial \mathcal{L}}{\partial A_\mu} - \partial_\nu \frac{\partial \mathcal{L}}{\partial \left(\partial_\nu A_\mu \right)} = \alpha_2 j_{\text{free}}^\mu + 4\alpha_1 \partial_\nu \left(\partial^\mu A^\nu - \partial^\nu A^\mu \right) \,.$$

Applying in parallel to Eq. (1.31) the Lorenz gauge (see Eq. (1.28)]

$$\partial_\nu \mathcal{A}^\nu(\mathbf{r}, \omega) = \frac{-\mathrm{i}\omega}{c^2} \Phi(\mathbf{r}, \omega) + \boldsymbol{\nabla} \cdot \boldsymbol{\mathcal{A}}(\mathbf{r}, \omega) = 0 \,, \tag{1.62}$$

we find that Eq. (1.31) is recovered by $\alpha_1/\alpha_2 = -1/(4\mu_0)$. When we require that the classical Hamiltonian equals the electromagnetic density Eq. (1.19), we find that

$$\mathcal{L} = -\frac{1}{4\mu_0} F_{\mu\nu} F^{\mu\nu} + \mathcal{A}_\mu \mathbf{j}_{\text{free}}^\mu \,, \tag{1.63}$$

fixing the remaining free parameter.

1.3 Elements of response theory

After having discussed the basic elements of QFT, we provide the basis of general response theory[6] following the general discussion in Ref. [30]. In this work, we will use expressions derived from response theory for the description of photonic materials within macroscopic Maxwell's equations. Thus, we dwell in some detail on the basics of this theory that can, in general, not only be used for the description of the electron's response to the electromagnetic fields but for a wide range of applications in a variety of fields in physics.

In general, response theory describes the response of a system to an external, time-dependent and vectorial field $\boldsymbol{\mathcal{F}}(\mathbf{r}, t)$ (also known as generalized force) that, described within Schrödinger representation, couples to one of the vectorial observable of the system, i.e., $\hat{\mathbf{B}}(\mathbf{r})$. The unperturbed system is then approximately described by a time-independent Hamiltonian $\hat{\mathcal{H}}_0$ and the resulting Hamiltonian then reads

$$\hat{\mathcal{H}}_{\mathcal{F}}(t) = \hat{\mathcal{H}}_0 + \boldsymbol{\mathcal{F}}(\mathbf{r}, t) \cdot \hat{\mathbf{B}}(\mathbf{r}) \,. \tag{1.64}$$

---

[6]In general, response theory can be as well be formulated in classical mechanics or QM. However, since we make use of the concept of (linear) response theory mainly in the context of the description of graphene and this will be derived in QFT, we also introduce the response theory in the notation of QFT.

In a series representation, assuming the most general coupling of the external, time-dependent field with the observable, we can write for the expectation value of one component of the observable $B_i(\mathbf{r}, t)$

$$
\begin{aligned}
B_i(\mathbf{r}, t) =& \Big(B_i(\mathbf{r}, t)\Big)_0 + \sum_j \int \mathrm{d}^d r' \int \mathrm{d}t' \, \chi_{ij}^{(1)}(\mathbf{r}, \mathbf{r}'; t, t') \mathcal{F}_j(\mathbf{r}', t') \\
&+ \sum_{j,k} \int \mathrm{d}^d r' \int \mathrm{d}^d r'' \int \mathrm{d}t' \int \mathrm{d}t'' \, \chi_{ijk}^{(2)}(\mathbf{r}, \mathbf{r}', \mathbf{r}''; t, t', t'') \mathcal{F}_j(\mathbf{r}', t') \mathcal{F}_k(\mathbf{r}'', t'') \\
&+ \dots,
\end{aligned}
$$

(1.65)

with the expectation value $(B_i(\mathbf{r}, t))_0 = \langle \hat{B}_i(\mathbf{r}) \rangle_0$ of the free observable, for a d dimensional system and where $\chi^{(i)}$ are called the response functions or generalized susceptibilities. Assuming a weak external field, the second and higher order terms can be considered to be negligible and we arrive at the *linear response theory* where

$$
B_i^{(1)}(\mathbf{r}, t) = \Big(B_i(\mathbf{r}, t)\Big)_0 + \sum_j \int \mathrm{d}^d r' \int \mathrm{d}t' \, \chi_{ij}^{(1)}(\mathbf{r}, \mathbf{r}'; t, t') \mathcal{F}_j(\mathbf{r}', t') \,.
$$

(1.66)

Thus, we define for convenience

$$
\chi_{ij}(\mathbf{r}, \mathbf{r}'; t, t') \equiv \chi_{ij}^{(1)}(\mathbf{r}, \mathbf{r}'; t, t') \,,
$$

as the (linear) generalized susceptibility or linear response function. Without further specification, we can already state the following properties of a susceptibility (cf. Ref. [30], p. 368):

- The external field cannot disturb the observable B_i prior to its action at time t' such that $\chi_{ij}(\mathbf{r}, t; \mathbf{r}', t') = 0$ for $t < t'$.

- For a time-independent, unperturbed Hamiltonian, i.e., the system is translational invariant in time, the linear response function only depends on the difference of time

$$
\chi_{ij}(\mathbf{r}, \mathbf{r}'; t, t') \equiv \chi_{ij}(\mathbf{r}, \mathbf{r}'; t - t') \,.
$$

  This allows for a reformulation of the expectation value

$$
B_i^{(1)}(\mathbf{r}, \omega) = \sum_j \int \mathrm{d}^d r' \chi_{ij}(\mathbf{r}, \mathbf{r}', \omega) \mathcal{F}_j(\mathbf{r}', \omega) \,,
$$

  where one realizes that for a linear response two frequencies do not mix. Thus, only second and higher order susceptibilities lead to a frequency mixing.

- Additionally, for a system homogeneous in space, the response may be written as

$$
\chi_{ij}(\mathbf{r}, \mathbf{r}'; t - t') \equiv \chi_{ij}(\mathbf{r} - \mathbf{r}'; t - t') \,,
$$

  leading to

$$
B_i^{(1)}(\mathbf{q}, \omega) = \sum_j \chi_{ij}(\mathbf{q}, \omega) \mathcal{F}_j(\mathbf{q}, \omega) \,.
$$

  This can be interpreted as the conservation of momentum.

1 Theoretical background

Analogously to Ref. [30], we furthermore assume a single-particle operator[7]

$$\hat{B}_i(\mathbf{r}) = \sum_{a,a'} \hat{c}_a^\dagger B_{i,aa'}(\mathbf{r}) \hat{c}_{a'} \, ,$$

where we consider $\hat{c}_a$ a fermionic or bosonic operator and $B_{i,aa'}(\mathbf{r})$ as an expansion coefficient. Thus, we rewrite the expectation value $B_i(\mathbf{r}, t)$ within QFT at times t as

$$B_i(\mathbf{r}, t) \equiv \langle \hat{B}_i(\mathbf{r}) \rangle = \sum_{a,a'} \langle \psi_a^\dagger(t) B_{i,aa'}(\mathbf{r}) \psi_{a'}(t) \rangle \, , \tag{1.67}$$

and the expectation value defined as in Eq. (1.56). Here, the action of the perturbed system is defined as

$$S[\boldsymbol{\mathcal{F}}(\mathbf{r}, t), \boldsymbol{\mathcal{F}}'(\mathbf{r}', t'), \psi^*, \psi] = S_0[\psi^*, \psi] + \delta S[\boldsymbol{\mathcal{F}}(\mathbf{r}, t), \psi^*, \psi] + \delta S'[\boldsymbol{\mathcal{F}}'(\mathbf{r}', t'), \psi^*, \psi] \, , \tag{1.68}$$

where we artificially introduce (cf. Ref. [30]) a second driving field in order to derive the final expression for the response function. With the definition of the action Eq. (1.51) and the definition of the Hamiltonian Eq. (1.64), we find for the first driving field

$$\delta S[\boldsymbol{\mathcal{F}}(\mathbf{r}, t), \psi^*, \psi] = \frac{\mathrm{i}}{\hbar} \sum_i \int \mathrm{d}t \, \mathcal{F}_i(t) \sum_{a,a'} \psi_a^\dagger(t) B_{i,aa'}(\mathbf{r}) \psi_{a'}(t) \, , \tag{1.69}$$

while $S_0[\psi^*, \psi]$ is the free action caused by the Hamiltonian $\hat{\mathcal{H}}_0$. This equation reads analogously for $\boldsymbol{\mathcal{F}}'$ and $\delta S'[\boldsymbol{\mathcal{F}}'(\mathbf{r}, t), \psi^*, \psi]$. With these definitions and the partition function Eq. (1.47) follows

$$\mathcal{Z}[\boldsymbol{\mathcal{F}}, \boldsymbol{\mathcal{F}}'] \equiv \int D(\psi^*, \psi) \mathrm{e}^{-S[\boldsymbol{\mathcal{F}}(\mathbf{r}, \tau), \boldsymbol{\mathcal{F}}'(\mathbf{r}', \tau'), \psi^*, \psi]} \, , \tag{1.70}$$

which with Eq. (1.69) leads to

$$B_i(\mathbf{r}, t) = \mathrm{i}\hbar \left. \frac{\partial}{\partial \mathcal{F}_i(\mathbf{r}, t)} \right|_{\boldsymbol{\mathcal{F}}=0} \log \left(\mathcal{Z}[\boldsymbol{\mathcal{F}}, \boldsymbol{\mathcal{F}}'] \right) . \tag{1.71}$$

For a weak external field $\mathcal{F}(\mathbf{r}, t)$, we can then expand the functional to first order

$$B_i(\mathbf{r}, t) \approx \left(B_i(\mathbf{r}, t) \right)_1 = \langle \hat{B}_i(\mathbf{r}, t) \rangle_0 + \sum_j \int \mathrm{d}^d r' \int \mathrm{d}t' \left[\left. \frac{\partial}{\partial \mathcal{F}_j'(\mathbf{r}', t')} \right|_{\boldsymbol{\mathcal{F}}'=0} B_j(\mathbf{r}', t') \right] \mathcal{F}_j'(\mathbf{r}', t') \, , \tag{1.72}$$

arriving at (by insertion of Eq. (1.71)]

$$\Delta B_i(\mathbf{r}, t) \equiv B_i(\mathbf{r}, t) - \left(B_i(\mathbf{r}, t) \right)_0$$

$$= \mathrm{i}\hbar \sum_j \int \mathrm{d}^d r' \int \mathrm{d}t' \left[\left. \frac{\partial^2}{\partial \mathcal{F}_i(\mathbf{r}, t) \partial \mathcal{F}_j'(\mathbf{r}', t')} \right|_{\boldsymbol{\mathcal{F}}=\boldsymbol{\mathcal{F}}'=0} \log \left(\mathcal{Z}[\boldsymbol{\mathcal{F}}, \boldsymbol{\mathcal{F}}'] \right) \right] \mathcal{F}_j'(\mathbf{r}', t') \, , \tag{1.73}$$

---

[7]When we derive the reflection coefficients of graphene in section 2.2.1 making use of QFT, we (and the standard literature) limit ourselves to the single-particle picture. This is justified since multi particle interactions have a much smaller cross section (cf. also Ref. [34], p. 115).

By comparing with Eq. (1.65), we find

$$\chi_{ij}(\mathbf{r}, \mathbf{r}', \tau, \tau') = i\hbar \left. \frac{\partial^2}{\partial \mathcal{F}_i(\mathbf{r}, \tau) \partial \mathcal{F}_j'(\mathbf{r}', \tau')} \right|_{\boldsymbol{\mathcal{F}}(\mathbf{r},\tau) = \boldsymbol{\mathcal{F}}'(\mathbf{r}',\tau') = 0} \log \left(\mathcal{Z}[\boldsymbol{\mathcal{F}}, \boldsymbol{\mathcal{F}}'] \right). \qquad (1.74)$$

As a further simplification, we assume that the observable $\langle \hat{B}_i(\mathbf{r}, t) \rangle$ is of such nature that it can only be measured when applying an external field. In other words $\langle \hat{B}_i(\mathbf{r}, t) \rangle_0 = 0$. Rewriting the expectation value for the unperturbed system Eq. (1.57) $(B_i(\mathbf{r}, t))_0 = \mathcal{Z}^{-1} \left. \partial_{\mathcal{F}_i(\mathbf{r},t)} \right|_{\boldsymbol{\mathcal{F}}(\mathbf{r},t)=0} \mathcal{Z}[\boldsymbol{\mathcal{F}}, 0] = 0$, we derive

$$\begin{aligned}
\chi_{ij}(\mathbf{r}, \mathbf{r}'; t, t') =& i\hbar \, \mathcal{Z}^{-1} \left. \frac{\partial^2}{\partial F_i(\mathbf{r}, t) \partial F_j'(\mathbf{r}', t')} \right|_{\boldsymbol{\mathcal{F}}(\mathbf{r},t) = \boldsymbol{\mathcal{F}}'(\mathbf{r}',t') = 0} \mathcal{Z}[\boldsymbol{\mathcal{F}}, \boldsymbol{\mathcal{F}}'] \\
=& -\frac{i}{\hbar} \langle \sum_{aa'} \psi_a^\dagger(\tau) B_{i,aa'}(\mathbf{r}) \psi_a(t) \sum_{bb'} \psi_b^\dagger(\tau') B_{j,bb'}(\mathbf{r}') \psi_b(t') \rangle_0 \qquad (1.75) \\
\equiv& -\frac{i}{\hbar} \langle \hat{B}_i(\mathbf{r}, t) \hat{B}_j'(\mathbf{r}', t') \rangle_0 \, .
\end{aligned}$$

In the second line above, we use the definition of the expectation value Eq. (1.56) explicitly inserting the altered action Eq. (1.68) into the partition function. In the last line we make use of definition Eq. (1.67).

This response function is the *real-time response function* of the observable $B_j(\mathbf{r}, t)$. Due to causality, the physically meaningful response function, however, is the *retarded response function* where the response of an observable to an interaction is only possible at times $t > t'$ and that is given by (see Ref. [30])

$$\chi_{A_i B_j}^{\text{ret}}(\mathbf{r}, \mathbf{r}'; t_1, t_2) = -\frac{i}{\hbar} \Theta(t_1 - t_2) \langle [\hat{A}_i(\mathbf{r}', t_1), \hat{B}_j(\mathbf{r}', t_2)]_\zeta \rangle_0 \, , \qquad (1.76)$$

where by renaming $\hat{B}_i$ by $\hat{A}_i$ we finally stress the point that, in general, $\hat{B}_i$ can be the component of a different operator than $\hat{B}_j$. We denote with $[\cdot, \cdot]_\zeta$ the commutation relation in the bosonic and the anti-commutation relation in the fermionic case (cf. also appendix A.2). The expression Eq. (1.76) can be understood best when considering that any response function enters into the expectation value of an observable quantity via an integral over all times. Thus, Eq. (1.76) corresponds to a time-ordering of the two-operators while not allowing for any response of the observable to future events. More details on this concept can be found in standard textbooks, e.g., in Ref. [30].

1.3.1 Response to the electromagnetic field

The Lagrangian density of the interaction of the electromagnetic field with a medium is given by Eq. (1.63)

$$\mathcal{L} = -\frac{1}{4\mu_0} F_{\mu\nu} F^{\mu\nu} + A_\mu \hat{j}_{\text{free}}^\mu \, ,$$

1 Theoretical background

where we again treat the electrons quantum field theoretically but the electromagnetic field in a classical fashion and again apply Einstein's sum convention as discussed above. The interaction Hamiltonian is thus given as ($\hat{\mathcal{H}} = \int \mathrm{d}^3 r \mathscr{H} = \hat{T} - \hat{V}$)

$$\hat{V}(t) = -\int \mathrm{d}^3 r \, A_\mu(\mathbf{r}, t) \hat{j}^\mu(\mathbf{r}, t) \,, \tag{1.77}$$

where we drop the subscript 'free' for the rest of the section for better readability. The *retarded current-current response function* (see Ref. [35]) is then given as

$$\chi^j_{\alpha\beta}(\mathbf{r}, \mathbf{r}', t - t') = -\frac{\mathrm{i}}{\hbar} \Theta(t - t') \langle [\hat{j}_\alpha(\mathbf{r}, t), \hat{j}_\beta(\mathbf{r}', t')] \rangle_0 \,, \tag{1.78}$$

with the Fourier transformed current-current response function in the case of a spatially homogeneous system $\chi^j_{\alpha\beta}(\mathbf{r}, \mathbf{r}', t - t') \equiv \chi^j_{\alpha\beta}(\mathbf{r} - \mathbf{r}', t - t')$

$$\chi^j_{\alpha\beta}(\mathbf{q}, \omega) = \int \mathrm{d}t \int \mathrm{d}\mathbf{r} \, \chi^j_{\alpha\beta}(\mathbf{r} - \mathbf{r}', t - t') \mathrm{e}^{\mathrm{i}(\omega \cdot (t - t') - \mathbf{q} \cdot (\mathbf{r} - \mathbf{r}'))} \,, \tag{1.79}$$

and

$$\langle \hat{j}^\alpha(\mathbf{q}, \omega) \rangle = (\chi^j)^{\alpha\beta}(\mathbf{q}, \omega) \cdot A_\beta(\mathbf{q}, \omega) \,. \tag{1.80}$$

Due to the considered homogeneity and the isotropy of the system, it is immanent that the longitudinal vector potential ($\mathbf{q} \cdot \mathbf{A}^\mathrm{L}(\mathbf{q}, \omega) = 0$) and the transverse vector potential ($\mathbf{A}^\mathrm{T}(\mathbf{q}, \omega) = \mathbf{A}(\mathbf{q}, \omega) - \mathbf{A}^\mathrm{L}(\mathbf{q}, \omega)$) cannot be coupled by the current and thus the response can be split up in a longitudinal and a transverse part

$$\chi^j_{\alpha\beta}(\mathbf{q}, \omega) = \chi^\mathrm{L}(\mathbf{q}, \omega) \frac{q_\alpha q_\beta}{|\mathbf{q}|^2} + \chi^\mathrm{T}(\mathbf{q}, \omega) \left(\delta_{\alpha\beta} - \frac{q_\alpha q_\beta}{|\mathbf{q}|^2} \right) \,. \tag{1.81}$$

From the current-current density response function, another relevant physical quantities can be derived. By assuming a spatially uniform electromagnetic field ($\boldsymbol{\nabla}\Phi(\mathbf{r}, t) = 0$), the electric field reads $\mathbf{E}(\omega) = \mathrm{i}\omega \mathbf{A}(\omega)$ and thus with

$$\langle \hat{j}^\alpha(0, \omega) \rangle = E_\alpha(\omega) \sigma^{\alpha\beta}(\omega) \,, \tag{1.82}$$

and with Eq. (1.80) the conductivity tensor $\sigma_{\alpha\beta}$ is given by the *Kubo formula* (see Ref. [35], p. 148) as

$$\sigma_{\alpha\beta}(\omega) = \frac{\mathrm{i}}{\omega} \chi^j_{\alpha\beta}(0, \omega) \,. \tag{1.83}$$

The general conductivity $\sigma_{\alpha\beta}(\mathbf{q}, \omega)$ can thus be considered in different limits. The conductivity derived above, $\sigma_{\alpha\beta}(0, \omega)$ is known as the *optical conductivity* because it assumes $\mathbf{q} \approx 0$ which is usually an appropriate approximation for optical excitations. A conductivity with $\sigma_{\alpha\beta}(\mathbf{q}, 0)$ is called *static conductivity* since this determines the current's response to a static electromagnetic field.

The second relevant physical quantity is the *density-density response function* $\chi_{nn}(\mathbf{q}, \omega)$ and with this the dielectric function $\varepsilon(\mathbf{r}, t)$ (see Eq. (1.8a)) for which the same limits

(optical, static) apply. The density-density response function is the response of the electric density in Schrödinger representation $n(\mathbf{r}, t) = \langle \hat{n}(\mathbf{r}) \rangle = \langle \sum_i \delta(\mathbf{r} - \mathbf{r}_i) \rangle$ to the potential of an external charge with potential $V_{\text{ext}}(\mathbf{r}, t) = \int \mathrm{d}^3 r' \frac{4\pi e^2 n_{\text{ext}}(\mathbf{r}', t)}{\varepsilon_0 |\mathbf{r} - \mathbf{r}'|}$ (see Ref. [34, 35])

$$\hat{V}(t) = \int \mathrm{d}^3 r' \, V_{\text{ext}}(\mathbf{r}, t) \hat{\rho}(\mathbf{r}'), \tag{1.84}$$

leading to an induced charge density in a spatially homogeneous physical system

$$\rho_{\text{ind}}(\mathbf{r}, t) = \int \mathrm{d}t' \int \mathrm{d}^3 r' \chi_{nn}(\mathbf{r} - \mathbf{r}', t - t') V_{\text{ext}}(\mathbf{r}', t'), \tag{1.85}$$

with

$$\chi_{nn}(\mathbf{r} - \mathbf{r}', t - t') \equiv \chi_{n(\mathbf{r})n(\mathbf{r}')}(t - t') = -\frac{\mathrm{i}}{\hbar} \Theta(t - t') \langle [\hat{n}(\mathbf{r}), \hat{n}(\mathbf{r}')] \rangle_0. \tag{1.86}$$

Thus, in reciprocal and frequency space, Eq. (1.85) reads

$$\rho_{\text{ind}}(\mathbf{q}, \omega) = \chi_{nn}(\mathbf{q}, \omega) V_{\text{ext}}(\mathbf{q}, \omega). \tag{1.87}$$

Comparing Eq. (1.85) with Maxwell's equations (1.1), the electric polarization (1.7) and the dielectric tensor (1.8a) and using $\rho(\mathbf{r}, t) = en(\mathbf{r}, t)$, one realizes that $V_i(\mathbf{q}, \omega) \propto \rho_i(\mathbf{q}, \omega) \propto \mathbf{q} \cdot \mathbf{E}(\mathbf{q}, \omega)$ and with this we can write

$$\varepsilon_r^{-1}(\mathbf{q}, \omega) = 1 + \frac{v_q}{\varepsilon_0} \chi_{nn}(\mathbf{q}, \omega), \tag{1.88}$$

where we introduce the prefactor of the Fourier transformed Coulomb potential $v_q = e^2/q^2$. Thus, $\varepsilon_r^{-1}(\mathbf{q}, \omega)$ is the true response function of the electron density. The dielectric function itself can be related to a *quasi density-density response function* $\tilde{\chi}_{nn}(\mathbf{r} - \mathbf{r}', \omega)$ giving not the response of the charges in a material to an external charge but rather to the already screened charges

$$\rho_{\text{screened}} = \rho_{\text{ext}} + \rho_{\text{ind}}, \tag{1.89}$$

where the response function is related to the dielectric function via

$$\varepsilon_r(\mathbf{q}, \omega) = 1 - \frac{v_q}{\varepsilon_0} \tilde{\chi}_{nn}(\mathbf{q}, \omega) = \frac{1}{1 - \frac{v_q}{\varepsilon_0} \chi_{nn}(\mathbf{q}, \omega)} \approx 1 + \frac{v_q}{\varepsilon_0} \chi_{nn}(\mathbf{q}, \omega). \tag{1.90}$$

In other words, the dielectric function $\varepsilon_r(\mathbf{q}, \omega)$ is a constructed response function and with this does not measure the response to an external charge but rather to a screened charge and in consequence to an internal charge redistribution (compare also the mentioning of the terminus "response" below Eq. (1.8)). This distinction helps also to understand the difference between the dielectric displacement $\mathbf{D}$ and the electric field $\mathbf{E}$: while the electric field $\mathbf{E}$ is the field induced by all, free and induced, charges, the dielectric displacement $\mathbf{D}$ only takes the effective *external* field into account.

For an easier readability and comparability to the macroscopic Maxwell's equations, we introduce the electromagnetic susceptibility

$$\chi(\mathbf{q}, \omega) \equiv \frac{v_q}{\varepsilon_0} \chi_{nn}(\mathbf{q}, \omega), \tag{1.91}$$

1 Theoretical background

and find for the polarization (see Eq. (1.7))

$$\boldsymbol{P}(\mathbf{q},\omega) = \varepsilon_0 \chi(\mathbf{q},\omega)\boldsymbol{\mathcal{E}}(\mathbf{q},\omega)\,. \tag{1.92}$$

As pointed out in Ref. [35], the density-density response function is connected to the longitudinal component of the current-current response function via

$$\chi_{nn}(\mathbf{q},\omega) = \frac{q^2}{\omega^2}\chi^{\mathrm{L}}(\mathbf{q},\omega)\,. \tag{1.93}$$

When making use of the causal connection between the dielectric displacement vector and the electric field (cf. also Eq. (1.8a)), we can furthermore state the important *Kramers-Kronig relations* that connect the real and imaginary part of the dielectric function (see Ref. [27], p. 386)

$$\mathrm{Re}\left[\varepsilon_r(\mathbf{q},\omega)\right] = 1 + \frac{1}{\pi}\mathcal{P}\int_{-\infty}^{\infty} \frac{\mathrm{Im}\left[\varepsilon_r(\mathbf{q},\omega)\right]}{\omega'-\omega}\mathrm{d}\omega'\,, \tag{1.94a}$$

$$\mathrm{Im}\left[\varepsilon_r(\mathbf{q},\omega)\right] = -\frac{1}{\pi}\mathcal{P}\int_{-\infty}^{\infty} \frac{\mathrm{Re}\left[\varepsilon_r(\mathbf{q},\omega)-1\right]}{\omega'-\omega}\mathrm{d}\omega'\,, \tag{1.94b}$$

where Cauchy's principal value $\mathcal{P}(x)$ is defined as

$$\mathcal{P}\int_a^c \mathrm{d}x\,f(x) \equiv \lim_{\eta\to 0^+}\left[\int_a^{b-\eta}\mathrm{d}x\,f(x) + \int_{b+\eta}^c\mathrm{d}x\,f(x)+\right]\,, \tag{1.95}$$

$$\mathrm{with}\int_a^b \mathrm{d}x\,f(x) = -\int_b^c\mathrm{d}x\,f(x) = \pm\infty\,.$$

The causality, leading to Kramers-Kronig relation, Eq. (1.94), is the reason that any dielectric permittivity unequal from one (vacuum) always exhibits at least at some frequencies an imaginary part and with this losses. Later in this thesis, this very fundamental relationship between the real and imaginary part of the dielectric permittivity facilitates the determination of the functional dependence of the dielectric permittivity (see section 5.5).

The final response functions of, e.g., an electron liquid to a perturbation also includes (depending on the approximations) all possible excitations of a material (see, e.g., Ref. [34]). These include simple scattering processes, excitations of particles (such as electron hole pair creation (*single-particle excitation (SPE)*)) and the excitation of collective modes. It is interesting to note that these collective modes in a response function correspond to poles in the complex plane. For electrons, these collective modes are called *(bulk) plasmons*. Since historically the materials are usually described by the dielectric function $\varepsilon_r(\mathbf{q},\omega)$, but $\varepsilon_r^{-1}(\mathbf{q},\omega)$ is the true response function of the material to a perturbation by an electromagnetic potential, the condition for plasmons reads counter-intuitively as

$$\varepsilon_r(\mathbf{q}_{\mathrm{plasmon}},\omega_{\mathrm{plasmon}}) = 0\,. \tag{1.96}$$

This corresponds to an infinitesimal small, point-like test charge that can already induce such a collective excitation. It is important to note that plasmonic excitations lead to $\mathbf{D}(\mathbf{q}, \omega) = 0$ external field and a purely longitudinal electric field $\mathbf{E}(\mathbf{q}, \omega)$ (cf. Ref. [36]). This can be understood when considering Eq. (1.13a) with $\rho_{\text{free}} = \mathbf{j}_{\text{free}} = 0$ and $\varepsilon_r = 0$ finding for the projection onto the transverse component

$$\mathbf{q} \times \mathbf{q} \times \boldsymbol{\mathcal{E}}(\mathbf{q}, \omega) = [\mathbf{q} \cdot \boldsymbol{\mathcal{E}}(\mathbf{q}, \omega)]\mathbf{q} - |\mathbf{q}|^2 \boldsymbol{\mathcal{E}}(\mathbf{q}, \omega) = 0 \,.$$

Thus, photons propagating in free space ($\varepsilon_r = 1$) and hence are purely transverse with $\mathbf{q} \cdot \boldsymbol{\mathcal{E}}(\mathbf{q}, \omega) = 0$ cannot couple straight forwardly to these oscillating charges. Only when breaking the symmetry as it, e.g., happens at an interface, polaritonic excitations can be excited if the photonic wavevector matches the bulk plasmon's. These excitations are called *surface plasmon polaritons* (SPPs) (see, e.g., Refs. [36–39]). Surface plasmon polaritons are the main source of losses in any plasmonic structure. In metallic nanostructures, these plasmonic modes are also the cause of significant altering of light scattering and absorption and hence are of great importance in these structures. We discuss metallic nanostructures and their collective excitations further in chapter 6.

1.3.2 Electronic and photonic propagators

Additionally to using the response theory to describe the response of any material to an external electromagnetic field, one can relate these response functions to the *particle propagator* that describes the creation and annihilation of excitations in a given system. Oftentimes, a particle propagator is also referred to as the particles *Green's function*. In general, the knowledge of the particle propagator is crucial in order to compute the time evolution and properties of a system containing these particles. For example, in chapter 2, we use graphene's particle propagator to compute the response of graphene to an interaction with the electromagnetic field and obtain reflection and transmission coefficients from this discussion. Since we only give a very short introduction into the basic notation used within the thesis, we refer the reader to the variety of textbooks on the topic of Green's functions and particle propagators, such as Refs. [30, 31].

At finite temperatures, the electronic propagator for an electron in state $\mathbf{p}$ (see Ref. [31]) at real times (cf. Eq. (1.51)) using the Heisenberg representation reads

$$
\begin{aligned}
G^e(\mathbf{p}; t - t') &= -\frac{\mathrm{i}}{\hbar} \langle \mathcal{T}_t \hat{c}_{\mathbf{p},H}(t) \hat{c}^\dagger_{\mathbf{p},H}(t') \rangle \\
&= -\frac{\mathrm{i}}{\hbar} \Theta(t - t') \langle \hat{c}_{\mathbf{p},H}(t) \hat{c}^\dagger_{\mathbf{p},H}(t') \rangle - \frac{\mathrm{i}}{\hbar} \Theta(t' - t) \langle \hat{c}^\dagger_{\mathbf{p},H}(t') \hat{c}_{\mathbf{p},H}(t) \rangle \\
&= G^e_{\text{ret}}(\mathbf{p}; t - t') + G^e_{\text{adv}}(\mathbf{p}; t - t') \,,
\end{aligned}
\tag{1.97}
$$

with the fermionic annihilation operator $\hat{c}_{\mathbf{p}}$ annihilating an electron in state[8] $\mathbf{p}$. The expectation value is defined as before as the thermodynamic average, where the thermodynamic average at zero temperature corresponds to the expectation value of the ground state. Above, the time ordering operator can be reformulated explicitly using the Heaviside function Θ and allowing for the definition of a retarded (forward propagating) and

---

[8]Here, the state can describe anything including the eigenvalue of the position operator $\hat{\mathbf{r}}$ or momentum operator $\hat{\mathbf{p}}$.

1 Theoretical background
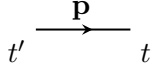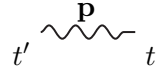
free electronic propagator	$G_0^e(\mathbf{p}; t - t') = -\mathrm{i}\langle \mathcal{T}_t \hat{c}_{\mathbf{p},we}(t)\hat{c}_{\mathbf{p}}^\dagger(t')\rangle$	
free photonic propagator	$G_0^\gamma(\mathbf{p}; t - t') = -\mathrm{i}\langle \mathcal{T}_t \hat{a}_{\mathbf{p},we}(t)\hat{a}_{\mathbf{p}}^\dagger(t')\rangle$	

Table 1.1: In the table above, we present the Feynman diagrams depicting the photonic and electronic propagators in the single-particle limit.

an advanced (backwards propagating) propagator. Especially if the time evolution of the unperturbed ground state is well known it is helpful to rewrite the propagator in the interaction representation:

$$G^e(\mathbf{p}; t - t') = -\frac{\mathrm{i}}{\hbar} \frac{\langle \mathcal{T}_t \hat{c}_{\mathbf{p},I}(t)\hat{c}_{\mathbf{p},I}^\dagger(t')\mathcal{S}(-\infty, \infty)\rangle}{\langle \mathcal{S}(-\infty, \infty)\rangle}\,, \tag{1.98}$$

where we make use of the definition of the S-matrix in Eq. (1.40).

Analogously, we can also define the QFT propagator

$$G^e(\{\mathbf{p}\}; t - t') = -\frac{\mathrm{i}}{\hbar} \frac{\langle \mathcal{T}_t \hat{\psi}_{\{\mathbf{p}\},I}(t)\hat{\psi}_{\{\mathbf{p}\},I}^\dagger(t')\mathcal{S}(-\infty, \infty)\rangle}{\langle \mathcal{S}(-\infty, \infty)\rangle}\,, \tag{1.99}$$

where $\hat{\psi}_{\{\mathbf{p}\}}$ is a fermionic field operator, annihilating a field in state $\{\mathbf{p}\}$. For the non-interacting, free propagator with $\mathcal{S}(-\infty, \infty) = 1$ this reads

$$G_0^e(\{\mathbf{p}\}; t - t') = -\frac{\mathrm{i}}{\hbar}\langle \mathcal{T}_t \hat{\psi}_{\{\mathbf{p}\}}(t)\hat{\psi}_{\{\mathbf{p}\}}^\dagger(t')\rangle\,. \tag{1.100}$$

The propagator above describes the excitation of an electron from the ground state at time t' and the annihilation of this electron at a later time t. In the case of the interacting propagator, Eq. (1.99) the electron can in between the two processes interact with other particles and be scattered. Comparing Eq. (1.97) with Eq. (1.75), one may realize that the propagator agrees with the response function with $\hat{B}_k^{(\prime)}(\mathbf{r}, t) = \hat{\psi}_{\{\mathbf{p}\}}^{(\dagger)}$.

Propagators do not only exist for electrons but for any particle (so also for photons and phonons[9]). The particle propagators can be represented by an intuitive graphical representation developed by Richard Feynman and called the *Feynman diagrams*. In the Feynman diagrammatics, the electronic and photonic propagators are represented according to table 1.1. Here, the physical meaning of the propagators can be understood by realizing that at time t' a particle (photon or electron) is created that is at a later time t destroyed.

Last, the free propagator can be written in terms of its Hamiltonian $\hat{\mathcal{H}}$ where the expectation value in Eq. (1.99) is taken with respect to the eigenstate $\psi_{\{\mathbf{p}\}}$ of the system with $\hat{\mathcal{H}}|\psi_{\{\mathbf{p}\}}\rangle = \epsilon_{\{\mathbf{p}\}}|\psi_{\{\mathbf{p}\}}\rangle$. Therefore, the state is an eigenstate of the Hamiltonian and

---

[9]Phonons are quantized lattice vibrations as they appear, e.g., in solids. They are often considered as a possible energy loss channel but in this thesis not of importance.

the propagator reads (for $\Omega \in \mathbb{R}$)

$$
\begin{aligned}
G_{0,\text{ret}}^e(\{\mathbf{p}\};\Omega) &= -\frac{\mathrm{i}}{\hbar} \int \mathrm{d}t \mathrm{e}^{\mathrm{i}(\frac{\Omega}{\hbar}+\mathrm{i}0^+)t} \langle \hat{\psi}_{\{\mathbf{p}\}}(t) \psi_{\{\mathbf{p}\}}^\dagger(0) \rangle_{\text{ret}} \\
&= -\frac{\mathrm{i}}{\hbar} \int \mathrm{d}t \mathrm{e}^{\mathrm{i}(\frac{\Omega}{\hbar}+\mathrm{i}0^+)t} \langle \hat{\mathcal{U}}(\{\mathbf{p}\},t;\{\mathbf{p}\},0) \rangle \Theta(t) \qquad (1.101) \\
&= -\frac{\mathrm{i}}{\hbar} \int \mathrm{d}t\, \Theta(t) \mathrm{e}^{\frac{\mathrm{i}}{\hbar}(\Omega-\epsilon_{\{\mathbf{p}\}}+\mathrm{i}0^+)t} = \frac{1}{\Omega - \epsilon_{\{\mathbf{p}\}} + \mathrm{i}0^+}\,.
\end{aligned}
$$

Above, we insert the convergence factor 0^+ and the time evolution operator introduced in Eq. (1.34). Additionally, we shift the dependence $t-t'$ to t and use the Fourier transform of the Heaviside step function $\Theta(t)$

$$
\mathcal{F}_t[\Theta(t)](\omega) = \int\limits_{-\infty}^{\infty} \mathrm{d}t \Theta(t) \mathrm{e}^{\mathrm{i}\omega t} = \pi\delta(\omega) + \frac{\mathrm{i}}{\omega}\,. \qquad (1.102)
$$

1.4 Conclusions

Within the first chapter of this thesis, we laid the foundation of discussing the specific electromagnetic responses to plasmonic nanostructures in the research chapters of this thesis. More specifically, we introduced the notation of Maxwell's equations used throughout this work. Additionally, we discussed concepts related to the material's response to an external magnetic field such as response theory, Poynting's theorem to determine losses due to a photonic nanostructure and quantum field theoretical concepts that are necessary for the description of electron liquids. Here, electron liquids are, e.g., the basis of the description of graphene in the next chapter. In order to adequately describe the electron liquid within graphene, we also reviewed the basics of propagators that can be used in the quantum-field theoretical description of the response of graphene to an electromagnetic field within the next chapter. Last, we discussed elements of quantum mechanics that cannot only be used in quantum field theory but as well for the description of quantum emitters in chapter 3.

Elements of the theory of graphene

"We call our world Flatland, not because we call it so, but to make its nature clearer to you, my happy readers, who are privileged to live in Space." [10]

Edwin A. Abbott

In this chapter, we first introduce and motivate the basic tight-binding Hamiltonian for the description of graphene to then make the transition to the QFT description of graphene. From here, we follow the literature to derive the electromagnetic response in terms of the reflection coefficients for several physical conditions under which graphene exists.

2.1 Graphene's Hamiltonian

2.1.1 The tight-binding description of graphene

Graphene is a two-dimensional (2D) allotrope of carbon where the carbon atoms are arranged on a hexagonal lattice (see Fig. 2.1(a)). As such, it is part of the family of carbon allotropes and the basic building block of graphite (stacked graphene layers interacting via van-der-Waals forces, three-dimensional (3D)), carbon nanotubes (a rolled up graphene layer, 1D) and fullerenes (a wrapped up graphene layer in which some pentagons are introduced, zero-dimensional (0D)).

Since graphene is the basic component of these allotropes, a lot of theoretical research has been done on graphene as early as 1947 (see Ref. [41]). In that time, graphite was a material of high scientific interest due to its use in nuclear reactors (see Ref. [42]). However, since the Mermin-Wagner theorem (see Ref. [43]) stated that 2D crystals were not able to exhibit any long range order due to long wavelength fluctuations, graphene was not considered a realistic and existing material for several decades. When in 2004 Novoselov and Geim (see Ref. [44]) first succeeded in isolating *and detecting* single layers of graphene, this prepared the floor to a large field of research. In 2007, researchers were finally able to lift the veil to the question why graphene as a material is stable even at

---

[10]Flatland: A Romance of Many Dimensions (1884)

2 Elements of the theory of graphene
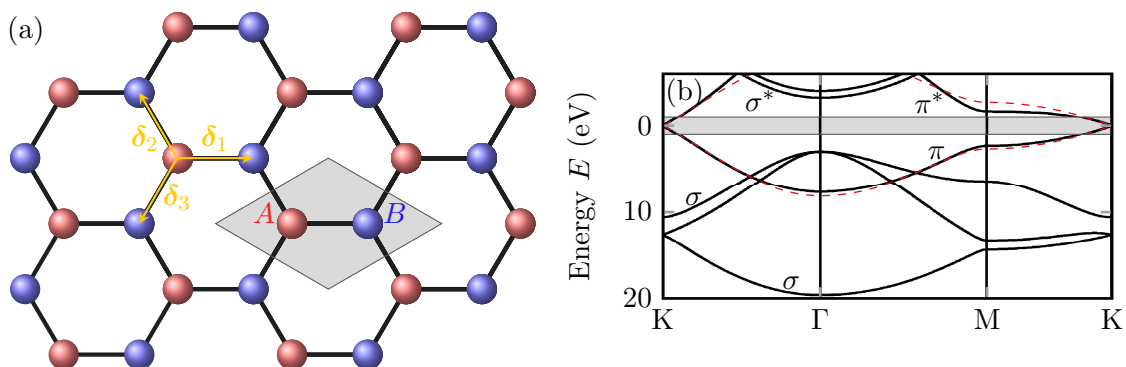
Figure 2.1: The Figure above shows in Panel (a) graphene with its unit cell (gray) consisting of two atoms A and B. The vertical boundary condition is called *zigzag* whereas the horizontal boundary condition is of type *armchair*. The three orange arrows present the vectors $\boldsymbol{\delta}_i$ connecting the atoms A with their three neighboring atoms B. In Panel (b), we present graphene's complete band structure including besides from the π electrons also the σ electrons. The wavevector and energy region approximated by the well-known Dirac cone is marked by the gray area. Panel (b) is adapted from Ref. [40] with permission of the PCCP Owner Societies, doi:10. 1039/C003524F. The red dashed line present the solutions from the tight-binding approximation Eq. (2.4).

room temperature when they found "intrinsic ripples"[11] stabilizing the long-range order in a graphene monolayer against thermal fluctuations (see Refs. [45, 46]).

In graphene, the carbon atoms are covalently σ-bond by its sp^2 hybridized $2s, 2p_x$ and $2p_y$-orbitals while the $2p_z$-orbital of all neighboring atoms are hybridized to create a π orbital. The complete band structure due to the σ-π orbitals is shown in Fig. 2.1(b). In this panel, the gray insets marks the relevant bands for excitations of energies less than $2\,\mathrm{eV}$. These energies comprise not only optical but also magnetic transitions and thus include all the cases discussed in this thesis. In the panel, it is well visible that the σ bands are sufficiently far off in energy that they may be deemed unimportant for the correct description of the band structure of graphene. Additionally, it is notable that the only region of interest is the region around the K-point (also known as Dirac point, see more later) where both π bands are degenerate and can – in first approximation – be described by a linear dispersion relation, the famous *Dirac cone*.

This discussion justifies the treatment of graphene in a tight-binding approximation as done already by Wallace (see Ref. [41]) since the $2p_z$ orbitals of each atom are approximately orthogonal to the plane of the carbon atoms and have only a weak overlap to the neighboring p_z orbitals. As for any hexagonal lattice, the unit cell contains two atoms (cf. gray shaded area in Fig. 2.1(a)) with the creation (annihilation) operators $\hat{a}_{\mathbf{n},\sigma}^{(\dagger)}$ on

---

[11]In fact, graphene monolayers are stabilized via a coupling of bending and stretching phononic modes by deforming the originally 2D crystal into all three dimensions (see Ref. [45]). Then, graphene becomes thermally stable exhibiting local strain variations of up to 1% (see Ref. [45]). The deformations are sufficiently small to still consider graphene a crystal exhibiting a long-range order.

sites A and $\hat{b}^{(\dagger)}_{\mathbf{n}+\boldsymbol{\delta}_i,\sigma}$ on sites B. The vectors $\mathbf{n}$ point to site A of each unit cell while the the vectors $\boldsymbol{\delta}_i$ represent the vectors connecting a carbon atom at site A to its three neighboring carbon atoms at sites B [see the orange arrows in Fig. 2.1(a)). Lastly, $\sigma = \{\uparrow,\downarrow\}$ denotes the two possible spin orientations. The undisturbed graphene tight-binding[12] Hamiltonian then reads (according to Ref. [48])

$$\hat{\mathcal{H}}_0 = -t \sum_{\mathbf{n},\boldsymbol{\delta}_i,\sigma} \left[\hat{a}^\dagger_{\mathbf{n},\sigma} \hat{b}_{\mathbf{n}+\boldsymbol{\delta}_i,\sigma} + \text{C.C.} \right] . \tag{2.1}$$

In the equation above, C.C. denotes the complex conjugate and $t = 2.7\,\text{eV}$ the nearest neighbor hopping parameter (see Ref. [42, 47]) that can in general be computed by calculating the overlap integral between the electronic wavefunctions of two neighboring p-Orbitals. In momentum space, the Hamiltonian then reads

$$\hat{\mathcal{H}}_0 = \sum_\sigma \int_{\text{BZ}} \frac{\mathrm{d}^2 k}{(2\pi)^2} \Upsilon^\dagger_\sigma(k) \begin{pmatrix} 0 & \eta(k) \\ \eta^*(k) & 0 \end{pmatrix} \Upsilon_\sigma(k) , \tag{2.2}$$

with the in-plane wavevector $k = |\mathbf{k}| = |(k_x, k_y)^T|$ where the graphene layer is positioned at $z = z_0$, $\eta(k) = -t \sum_{\boldsymbol{\delta}_i} \mathrm{e}^{\mathrm{i}\mathbf{k}\cdot\boldsymbol{\delta}_i}$ and $\Upsilon_\sigma(k) = [\hat{a}_\sigma(k), \hat{b}_\sigma(k)]^T$.

The energy eigenvalues can be calculated by using the explicit expressions

$$\boldsymbol{\delta}_1 = a(1,0)^T , \qquad \boldsymbol{\delta}_2 = \frac{a}{2}(-1,\sqrt{3})^T \quad \text{and} \quad \boldsymbol{\delta}_3 = \frac{a}{2}(-1,-\sqrt{3})^T , \tag{2.3}$$

with the inter-carbon distance $a = 1.42\,\text{Å}$.

The eigenvalues of the Hamiltonian matrix can then be obtained by

$$\det\left[\begin{pmatrix} 0 & \eta(k) \\ \eta^*(k) & 0 \end{pmatrix} - \epsilon(k)\mathbb{1} \right] = 0 ,$$

leading to

$$\epsilon(k) \equiv \pm|\eta(k)| = \pm t\sqrt{1 + 4\cos^2 \frac{\sqrt{3}k_y a}{2} + 4\cos \frac{3k_x a}{2} \cos \frac{\sqrt{3}k_y a}{2}} . \tag{2.4}$$

The formula above is equal to the results presented in 1947 by Wallace [41] though derived in analogy to Refs. [42, 48].

Here, one sees directly that the exact expression of the following discussed $\mathbf{K}$ points – the points in the band structure at which the two energy bands are degenerate – depends on the definition of the Cartesian coordinate system. The eigenenergies present a hexagonal symmetry with degenerate bands at the six K-points $\pm\frac{2\pi}{3a}\left(1,\frac{1}{\sqrt{3}}\right)^T$, $\pm\frac{2\pi}{3a}\left(-1,\frac{1}{\sqrt{3}}\right)^T$,

---

[12]The tight-binding Hamiltonian presented here only considers next neighbor wavefunction overlaps. Further coupling such as second-nearest neighbor coupling can also be considered and is found to be of order $t' \approx 0.1\,\text{eV}$ (see Ref. [47]). However, this coupling only leads to a fixed offset in the eigenenergies while maintaining the gapless band structure presented in Fig. 2.1 (cf. Ref. [48]). Thus, in this thesis we will not discuss any hopping parameters beyond nearest-neighbor. For further general details see, e.g., Ref. [42].

2 Elements of the theory of graphene

and $\pm \frac{2\pi}{\sqrt{3}a} \left(0, \frac{2}{3}\right)^T$. Due to the two atoms in the unit cell, two of those K-points cannot be mapped onto each other, such as, e.g., $\mathbf{K}_\pm = \pm \frac{2\pi}{\sqrt{3}a} \left(0, \frac{2}{3}\right)^T$. Expanding Eq. (2.4) around these $\mathbf{K}_\pm$ point leads in first order to

$$\epsilon(k) = \pm \hbar v_{\mathrm{F}}\, k\,, \qquad \text{with} \qquad v_{\mathrm{F}} = \frac{\sqrt{3}ta}{2\hbar} \approx \frac{c}{300}\,, \tag{2.5}$$

where the absolute value of the in-plane wavevector is as before given by $k = |\mathbf{k}| = \sqrt{k_x^2 + k_y^2}$.

We compare the result of Eq. (2.4) to a complete band structure in Fig. 2.1(b) choosing the points $\mathbf{\Gamma} = (0,0)^T$, $\mathbf{M} = \frac{2\pi}{3a}(1,0)^T$ and $\mathbf{K} = \frac{2\pi}{3a}(1, \frac{1}{\sqrt{3}})^T$. As one can see, in the energy region of interest (gray region) the electronic dispersion relation is well described within the tight-binding approximation. For larger excitation energies, one would have to take additional terms into account to, e.g., describe the asymmetry between the π and the π^* band appropriately.

2.1.2 The Dirac formalism

As it is discussed in Ref. [48], the Dirac (also known as spinor) representation can be derived by using the approximation derived in Eq. (2.5) when expanding the Hamiltonian in Eq. (2.2) up to first order around the two $\mathbf{K}_\pm$ points. The $\mathbf{K}$ points are consequently referred to as Dirac points. To connect the two representations and explain in section 2.1.3 the possible opening of a band gap in graphene in certain cases, we will follow along the lines of Ref. [48] and repeat the arguments of the authors. Further reference of this will not be mentioned in this section.

With $\epsilon(\mathbf{K}_\pm) = 0$ and the use of Eq. (2.5) for small disturbances by the wavevector $\mathbf{q} = (q_x, q_y)^T$ around the Dirac point, the complex off-diagonal elements of the Hamiltonian matrix can be expanded as

$$\eta(\mathbf{K}_\pm + \mathbf{q}) = -t \sum_{\boldsymbol{\delta}_i} \mathrm{e}^{\mathrm{i}(\mathbf{K}_\pm + \mathbf{q})\cdot \boldsymbol{\delta}_i} \approx \pm \hbar v_{\mathrm{F}}(q_x \mp \mathrm{i}q_y)\,,$$

which leads for the Hamiltonian to (in order to later facilitate the recognizability of the typical Dirac equation $x \to 1$ and $y \to 2$)

$$\begin{aligned}
\hat{\mathcal{H}}_0 = \hbar v_{\mathrm{F}} \sum_\sigma \int_{\mathrm{DC}} \frac{\mathrm{d}^2 q}{(2\pi)^2} &\left[\Upsilon_\sigma^\dagger(\mathbf{K}_+ + \mathbf{q}) \left(\hat{\sigma}_1 q_1 + \hat{\sigma}_2 q_2\right) \Upsilon_\sigma(\mathbf{K}_+ + \mathbf{q}) \right. \\
&\left. + \Upsilon_\sigma^\dagger(\mathbf{K}_- + \mathbf{q}) \left(-\hat{\sigma}_1 q_1 + \hat{\sigma}_2 q_2\right) \Upsilon_\sigma(\mathbf{K}_- + \mathbf{q}) \right].
\end{aligned} \tag{2.6}$$

Above, we introduced the Pauli matrices

$$\hat{\sigma}_1 \equiv \hat{\sigma}_{\mathrm{x}} = \begin{pmatrix} 0 & 1 \\ 1 & 0 \end{pmatrix}, \qquad \hat{\sigma}_2 \equiv \hat{\sigma}_{\mathrm{y}} = \begin{pmatrix} 0 & -\mathrm{i} \\ \mathrm{i} & 0 \end{pmatrix} \qquad \text{and} \quad \hat{\sigma}_3 \equiv \hat{\sigma}_{\mathrm{z}} = \begin{pmatrix} 1 & 0 \\ 0 & -1 \end{pmatrix}, \tag{2.7}$$

and limit the integration to wavevectors in the Dirac cone with cut-off $|\mathbf{q}| < W/(\hbar v_{\mathrm{F}})$. We define the energy cutoff $W = \hbar v_{\mathrm{F}} \sqrt{\frac{\Omega_B}{2\pi}}$ by use of the Brillouin zone area $\Omega_B = (2\pi)^2/A_{\mathrm{hexagon}}$.

To finally rewrite Eq. (2.2) as a Dirac Hamiltonian, we introduce the matrices

$$\boldsymbol{\alpha} = (\alpha^1, \alpha^2, \alpha^3)^T = \hat{\bar{\sigma}}_3 \otimes (\hat{\sigma}_1, \hat{\sigma}_2, \hat{\sigma}_3)^T \quad \text{and} \quad \beta = \hat{\bar{\sigma}}_1 \otimes \mathbb{1}_2 = \begin{pmatrix} 0 & \mathbb{1}_2 \\ \mathbb{1}_2 & 0 \end{pmatrix}, \quad (2.8)$$

where the $\hat{\bar{\sigma}}_i$ are matrices acting in the valley ($\mathbf{K}_\pm$) subspace and each of the α^i then results in

$$\alpha^i = \begin{pmatrix} \hat{\sigma}_i & 0 \\ 0 & -\hat{\sigma}_i \end{pmatrix}.$$

The 4×4 matrices $\alpha^{1,2}$ and β span the Dirac algebra in $(2+1)$ dimensions. These definitions allow then for the definition of the γ matrices

$$\gamma^0 = \beta \quad \text{and} \quad \boldsymbol{\gamma} = \beta\boldsymbol{\alpha}, \qquad \text{with} \quad \{\gamma^\mu, \gamma^\nu\} = 2g^{\mu\nu}\mathbb{1}_4, \quad (2.9)$$

with $g^{\mu\nu} = \text{diag}(1, -1, -1, -1)$, $\{\mu, \nu\} = 0, 1, 2, 3$ and $(\gamma^0)^2 = \mathbb{1}_4$. In QED$_{2+1}$ the γ^3 matrix is not needed for the description of the particles' time evolution. For completeness, the last gamma matrix is given by $\gamma^5 = i\gamma^0\gamma^1\gamma^2\gamma^3$.

The introduction of the α, β and γ matrices finally allows for rewriting Eq. (2.6) in terms of one single spinor

$$\Psi_\sigma(\mathbf{q}) = \begin{pmatrix} \Upsilon_{\mathbf{K}_+,\sigma}(\mathbf{q}) \\ \Upsilon_{\mathbf{K}_-,\sigma}(\mathbf{q}) \end{pmatrix} = \begin{pmatrix} \hat{a}_\sigma(\mathbf{K}_+ + \mathbf{q}) \\ \hat{b}_\sigma(\mathbf{K}_+ + \mathbf{q}) \\ \hat{b}_\sigma(\mathbf{K}_- + \mathbf{q}) \\ \hat{a}_\sigma(\mathbf{K}_- + \mathbf{q}) \end{pmatrix}, \quad (2.10)$$

and introducing[13]

$$\bar{\Psi}_\sigma(\mathbf{q}) \equiv \Psi_\sigma^\dagger(\mathbf{q})\gamma^0, \quad (2.11)$$

we find

$$\hat{\mathcal{H}}_0 = \hbar v_F \sum_\sigma \int_{\text{DC}} \frac{\mathrm{d}^2 q}{(2\pi)^2} \Psi_\sigma^\dagger(\mathbf{q}) \left(\gamma^0\right)^2 \left(\alpha^1 q_1 + \alpha^2 q_2\right) \Psi_\sigma(\mathbf{q})$$

$$= \hbar v_F \sum_\sigma \int_{\text{DC}} \frac{\mathrm{d}^2 q}{(2\pi)^2} \bar{\Psi}_\sigma(\mathbf{q}) \left(\gamma^1 q_1 + \gamma^2 q_2\right) \Psi_\sigma(\mathbf{q}). \quad (2.12)$$

The action for of the $(2+1)$-Hamiltonian (see Eq. (1.51)) consequently reads

$$S_{\text{graphene}} = -\frac{i}{\hbar} \int \mathrm{d}^3 x \mathcal{L}_{\text{graphene}}(t)$$

$$= -\frac{i}{\hbar} \int \mathrm{d}^3 x \bar{\Psi} \left[\gamma^0 \left(i\hbar\partial_t + \mu\right) + \hbar v_F \left(i\partial_1 \gamma^1 + i\partial_2 \gamma^2\right)\right] \Psi, \quad (2.13)$$

where we used the reformulation of the four-vector wavevector operator (see also Eq. (1.32))

$$\{\hat{q}_\mu\} = \left(\frac{\hat{\mathcal{H}}}{c\hbar}, -\hat{\mathbf{q}}\right)^T = i\left(\frac{\partial_t}{c}, \boldsymbol{\nabla}\right)^T = i\{\partial_\mu\}, \quad (2.14)$$

and Eq. (1.51) for the QFT expression of the action.

---

[13]The recast from the complex wavefunction $\Psi^\dagger$ to $\bar{\Psi}$ is necessary since only the scalar $\bar{\Psi}\Psi$ is a Lorentz scalar and thus invariant under Lorentz transform.

2 Elements of the theory of graphene

2.1.3 The opening of a band gap in graphene

The pure tight-binding Hamiltonian leads to a degeneracy of the two energy bands at the Dirac point $\mathbf{K}_{\pm}$. This in turn leads – as presented above – to the Dirac equation describing the motion of massless fermions. In general, the degeneracy is lifted by breaking the symmetries in graphene and with this effectively assigning a mass to the fermions. Besides from magnetic catalysis[14], long-range Coulomb interaction (see Ref. [49]), multilayer graphene (see Ref. [50, 51]), included impurities in the graphene sample (see Ref. [52]) and many others, the placement of graphene on a material with an offset in lattice spacing (e.g., placing graphene on hexagonal boron nitride (hBN) as shown in ab initio calculations in Refs. [53, 54]) leads to the opening of such a gap.

As an example, we will consider this last case where due to the offset in lattice constant the spatial inversion symmetry $\mathcal{P}$ is broken. This inversion we define with respect to the center of the unit cell (cf. Fig. 2.1(a)). We then find in real and reciprocal space

$$\hat{a}_{\mathbf{n},\sigma} \to \mathcal{P}\hat{a}_{\mathbf{n},\sigma}\mathcal{P}^{-1} = \hat{b}_{-\mathbf{n},\sigma} \qquad \text{and} \qquad \hat{b}_{\mathbf{n},\sigma} \to \mathcal{P}\hat{b}_{\mathbf{n},\sigma}\mathcal{P}^{-1} = \hat{a}_{-\mathbf{n},\sigma}$$
$$\Updownarrow$$
$$\hat{a}_{\sigma}(\mathbf{k}) \to \mathcal{P}\hat{a}_{\sigma}(\mathbf{k})\mathcal{P}^{-1} = \hat{b}_{\sigma}(-\mathbf{k}) \qquad \text{and} \qquad \hat{b}_{\sigma}(\mathbf{k}) \to \mathcal{P}\hat{b}_{\sigma}(\mathbf{k})\mathcal{P}^{-1} = \hat{a}_{\sigma}(-\mathbf{k}) \qquad (2.15)$$
$$\Updownarrow$$
$$\Upsilon_{\sigma}(\mathbf{k}) \to \mathcal{P}\Upsilon_{\sigma}(\mathbf{k})\mathcal{P}^{-1} = \hat{\sigma}_1\Upsilon_{\sigma}(-\mathbf{k}) \,.$$

Assuming two different particle densities on sublattice A and B due to the lattice mismatch between graphene and substrate, we can write a new Hamiltonian

$$\hat{\mathcal{H}}_1 = \sum_{\sigma} \int_{\text{BC}} \frac{\mathrm{d}^2 k}{(2\pi)^2} \left[m_a \hat{a}_{\sigma}^{\dagger}(\mathbf{k})\hat{a}_{\sigma}(\mathbf{k}) + m_b \hat{b}_{\sigma}^{\dagger}(\mathbf{k})\hat{b}_{\sigma}^{\dagger}(\mathbf{k}) \right]$$

$$= \sum_{\sigma} \int_{\text{BC}} \frac{\mathrm{d}^2 k}{(2\pi)^2} \left[m_+ \left(\hat{a}_{\sigma}^{\dagger}(\mathbf{k})\hat{a}_{\sigma}(\mathbf{k}) + \hat{b}_{\sigma}^{\dagger}(\mathbf{k})\hat{b}_{\sigma}^{\dagger}(\mathbf{k}) \right) + m_- \left(\hat{a}_{\sigma}^{\dagger}(\mathbf{k})\hat{a}_{\sigma}(\mathbf{k}) - \hat{b}_{\sigma}^{\dagger}(\mathbf{k})\hat{b}_{\sigma}^{\dagger}(\mathbf{k}) \right) \right]$$

$$= \sum_{\sigma} \int_{\text{BC}} \frac{\mathrm{d}^2 k}{(2\pi)^2} \Upsilon_{\sigma}^{\dagger}(\mathbf{k}) \left[m_+ \hat{\sigma}_0 + m_- \hat{\sigma}_3 \right] \Upsilon_{\sigma}(\mathbf{k}) \,, \qquad (2.16)$$

where we introduce $m_{\pm} = (m_a \pm m_b)/2$ and the unit matrix $\hat{\sigma}_0 = \mathbb{1}_2$. Under transformation, we find then

$$\hat{\mathcal{H}}_1 \to \mathcal{P}\hat{\mathcal{H}}_1\mathcal{P} = \sum_{\sigma} \int_{\text{BC}} \frac{\mathrm{d}^2 k}{(2\pi)^2} \Upsilon_{\sigma}^{\dagger}(\mathbf{k}) \left[m_+ \hat{\sigma}_0 - m_- \hat{\sigma}_3 \right] \Upsilon_{\sigma}(\mathbf{k}) \,. \qquad (2.17)$$

It is obvious that the Hamiltonian $\hat{\mathcal{H}}_1$ is not symmetric under spatial inversion. Here, m_+ can be included into an effective chemical potential μ from Eq. (2.12), while m_-, the difference in carrier density on both sublattices, is responsible for the symmetry breaking. Analogously, the symmetry breaking from the other band gap creation mechanisms listed at the beginning of this section can be derived.

---

[14]Magnetic catalysis is the effect of electron-hole pairing in a magnetic field.

A symmetry breaking in one of the original Hamiltonian's symmetries usually also leads to the breaking of other symmetries. In the case of the specific symmetry breaking from a difference in particle densities on the two sublattices, one can show that the new Hamiltonian $\hat{\mathcal{H}}_1$ is also not invariant under time reversal. Additionally, for the undisturbed Hamiltonian $\hat{\mathcal{H}}_0$ two additional symmetry conditions hold

$$\hat{\sigma}_3 \hat{\mathcal{H}}_0(\mathbf{k}) \hat{\sigma}_3 = -\hat{\mathcal{H}}_0(\mathbf{k}) \qquad \text{and} \qquad \hat{\sigma}_2 \hat{\mathcal{H}}^*(\mathbf{k}) \hat{\sigma}_2 = -\hat{\mathcal{H}}_0(\mathbf{k}) \,, \tag{2.18}$$

These two conditions are responsible for the symmetry of the energies around the $\mathbf{K}_\pm$ points where a state $|\psi\rangle$ with eigenenergy ϵ leads to states $\hat{\sigma}_3|\psi\rangle$ and $\hat{\sigma}_2|\psi\rangle^*$ of eigenenergy $-\epsilon$.

However, even in the case of $m_- \neq 0$ the energy spectrum is still symmetric around the Dirac points which one can see when considering the matrix in Eq. (2.2)

$$\det\left[\begin{pmatrix} m_- - \epsilon(\mathbf{k}) & \eta(\mathbf{k}) \\ \eta^*(\mathbf{k}) & -m_- - \epsilon(\mathbf{k}) \end{pmatrix} \right] = 0 \,,$$

leading to

$$\epsilon(\mathbf{k}) = \pm\sqrt{|\eta(\mathbf{k})|^2 + m_-^2} \quad \rightarrow \quad \epsilon(\mathbf{K}_\pm + \mathbf{q}) \approx \pm\sqrt{\hbar^2 v_{\mathrm{F}}^2 q^2 + m_-^2} \,. \tag{2.19}$$

The last approximation is the approximation of the band structure in the proximity of the Dirac point. This symmetry can be explained when realizing that even though the first of the two symmetry conditions Eq. (2.18) is broken by the $m_- \Upsilon_\sigma^\dagger \hat{\sigma}_3 \Upsilon_\sigma$ term, the second (and more general) condition of Eq. (2.18) is still fulfilled. The symmetry around the Dirac point is thus stable even under strong transformations such as inversion symmetry breaking. The gap in graphene itself, however, is topologically protected (cf. Ref. [48], p. 11), where the topological invariant is $N(\mathbf{K}_\pm) = \pm 1$ without a gap and $N = 0$ for a band structure including a gap.

2.2 The electromagnetic response of graphene

The reflection coefficients of graphene are the main ingredient of the description of graphene within this thesis since – as we will later show – they are the quantities that determine the response of a graphene monolayer to an electric or magnetic dipole as well as other electromagnetic excitations.

For the coupling of the electromagnetic field to graphene's action Eq. (2.13), we use the *principle of minimal coupling*

$$\hat{q}_\mu \rightarrow \hat{q}_\mu - \frac{e}{\hbar} A_\mu(\mathbf{r}, t) \,, \tag{2.20}$$

with the definition of the four-vector wavevector operator Eq. (2.14) and the definition of the four-vector electromagnetic potential Eq. (1.30). The principal of minimal coupling above, replaces the kinetic momentum with the canonical momentum (see Ref. [55] for

2 Elements of the theory of graphene

more details). For the resulting action, we therefore find (cf. Ref. [56] and Eq. (1.63)) with $q_\mu = \mathrm{i}\partial_\mu$ (see Eq. (2.14))

$$
\begin{aligned}
S &= S_{\mathrm{EM}} + S_{\mathrm{graphene}}^{\mathrm{min.\,coupl.}} \\
&= \frac{\mathrm{i}}{4\hbar\mu_0} \int \mathrm{d}^4 x F_{\mu\nu} F^{\mu\nu} - \frac{\mathrm{i}}{\hbar} \int \mathrm{d}^3 x \bar{\Psi} \slashed{D} \Psi \,,
\end{aligned}
\tag{2.21}
$$

with

$$
\slashed{D} = \left(\mathrm{i}\hbar\partial_t + \mu - eA_0\right)\gamma^0 + \hbar v_{\mathrm{F}} \left[\left(\mathrm{i}\partial_1 - \frac{e}{\hbar}A_1\right)\gamma^1 + \left(\mathrm{i}\partial_2 - \frac{e}{\hbar}A_2\right)\gamma^2 \right] - m \,,
\tag{2.22}
$$

where the gap m is defined as

$$
m \equiv m_- \gamma^3 \,,
\tag{2.23}
$$

for a band gap created by, e.g., a substrate (cf. Eq. (2.16)).

2.2.1 Reflection coefficients in a 2+1 Dirac model

With the total action given by Eq. (2.21), we can determine the reflection coefficients in the $2+1$ Dirac model for the electromagnetic field impinging out-of-plane onto the graphene monolayer (cf. Fig. 2.3). In parallel to the derivation in Refs. [56, 57], we will present the expressions for the reflection coefficients, including a general gap m, chemical potential μ and temperature T where Ref. [57] presents expressions for real frequencies at finite temperature.

The reflection coefficients of graphene are directly connected to the polarization tensor of graphene. Since we focus on the effect of the electromagnetic fields, we can trace out the fermionic degrees of freedom in the partition function (see Eq. (1.49)) that determines the system's physical quantities, i.e., free energy, charge current. With the action derived in Eq. (2.21), the partition function reads

$$
\mathcal{Z} = \int D(A, \bar{\Psi}, \Psi) \mathrm{e}^{-S[\bar{\Psi}, \Psi, A]} \equiv \int D(A) \mathrm{e}^{-\frac{\mathrm{i}}{4\hbar\mu_0} F_{\mu\nu} F^{\mu\nu} - S_{\mathrm{eff}}(A)} \,,
\tag{2.24}
$$

introducing the effective action[15] (see Ref. [56, 59])

$$
\mathrm{e}^{-S_{\mathrm{eff}}(A)} = \int D(\bar{\Psi}, \Psi) \mathrm{e}^{\frac{\mathrm{i}}{\hbar}\slashed{D}} = \det\left(\slashed{D}\right) \,.
\tag{2.25}
$$

In the last step, we use the definition of a formal Gaussian integral[16]. With the identity (see Ref. [60])

$$
\log\left[\det\left(A\right)\right] = \mathrm{Tr}\left[\log(A)\right] \,,
$$

---

[15]The calculation of the effective action is of interest since it corresponds to the action stemming from the interaction part of the Hamiltonian. In other words, the effective action usually contains the interplay between different parts of a system such as of electrons and photons. The terminus was first introduced by Julian Schwinger in 1951 for a constant electric field interacting with electrons (see Ref. [58]).

[16]The n-dimensional complex Gaussian integral is given as

$$
\int \prod_{i=1}^{n} \mathrm{d}z_i \mathrm{d}z_i^\dagger \mathrm{e}^{-z_j^\dagger M_{jk} z_k} = (2\pi)^n \left[\det\left(M_s\right)\right]^{-1} \,,
$$

that holds for any square non-singular matrix A, we find that the effective action can be computed via

$$\log\left(\slashed{D}\right) = \log\left[(i\hbar\partial_t + \mu)\gamma^0 + \hbar v_{\mathrm{F}}(i\partial_1\gamma^1 + i\partial_2\gamma^2)\right]$$

$$+ \log\left[1 - ev_{\mathrm{F}}A_\mu\gamma^\mu \frac{1}{(i\hbar\partial_t + \mu)\gamma^0 + \hbar v_{\mathrm{F}}(i\partial_1\gamma^1 + i\partial_2\gamma^2)}\right]$$

$$= \log\left[(i\hbar\partial_t + \mu)\gamma^0 + \hbar v_{\mathrm{F}}(i\partial_1\gamma^1 + i\partial_2\gamma^2)\right] \quad (2.26)$$

$$+ \sum_{k=1}^{\infty} \frac{(-ev_{\mathrm{F}})^k}{k}\left[A_\mu\gamma^\mu \frac{1}{(i\hbar\partial_t + \mu)\gamma^0 + \hbar v_{\mathrm{F}}(i\partial_1\gamma^1 + i\partial_2\gamma^2)}\right]^k .$$
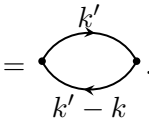
Above, we find that the interaction of the quasi particles[17] in graphene is described by the propagator [see Ref. [56] and Eq. (1.101)]

$$G_{0,\mathrm{ret}}^{gQP}(x) = \frac{1}{(i\hbar\partial_t + \mu)\gamma^0 + \hbar v_{\mathrm{F}}(i\partial_1\gamma^1 + i\partial_2\gamma^2) + i0^+}$$

$$\Updownarrow \quad (2.27)$$

$$G_{0,\mathrm{ret}}^{gQP}(k) = \frac{(k_0 + \mu)\gamma^0 - v_{\mathrm{F}}(\gamma^1 k_1 + \gamma^2 k_2)}{[k_0 + \mu + i0^+\mathrm{sgn}(k_0)]^2 - v_{\mathrm{F}}^2\mathbf{k}^2 - m^2 + i0^+} ,$$

with the $(2+1)$-wavevector $k = (k_0, \mathbf{k})$. The first term in Eq. (2.26) corresponds to the contribution due to the bare quasi particle propagation and can be neglected. Regarding the sum in Eq. (2.26), literature finds that only even numbers of photon fields contribute (see Ref. [61]) and in *quadratic approximation* (second order) this leads to

$$S_{\mathrm{eff}}(A) = \frac{i}{\hbar}\int\frac{\mathrm{d}^3 k}{(2\pi)^3}\int\frac{\mathrm{d}^3 k'}{(2\pi)^3}\frac{e^2 v_{\mathrm{F}}^2}{2}\,\mathrm{Tr}\left[A_\mu(k)\gamma^\mu G_{0,\mathrm{ret}}^{gQP}(k')A_\nu(k)\gamma^\nu G_{0,\mathrm{ret}}^{gQP}(k'-k)\right]$$

$$\equiv \frac{1}{2}\int\frac{\mathrm{d}^3 k}{(2\pi)^3}A_\mu(k)\Pi^{\mu\nu}(k)A_\nu(k) . \quad (2.28)$$

In the last reformulation of the effective action, we introduce the polarization tensor (see Ref. [29, 56, 62–64])

$$\Pi^{\mu\nu}(k) = i\frac{e^2 v_{\mathrm{F}}^2}{\hbar}\int\frac{\mathrm{d}^3 k'}{(2\pi)^3}\,\mathrm{Tr}\left[\gamma^\mu G_{0,\mathrm{ret}}^{gQP}(k')\gamma^\nu G_{0,\mathrm{ret}}^{gQP}(k'-k)\right]$$

$$= \qquad . \quad (2.29)$$

with the symmetrized matrix $M_s = (M + M^\dagger)/2$. For complex *Grassman variables*, as it is the case when integrating out fermionic degrees of freedom as done in Eq. (2.25), the complex Gaussian integral is defined as

$$\int\prod_{i=1}^{n}\mathrm{d}z_i\mathrm{d}z_i^\dagger\mathrm{e}^{-z_j^\dagger M_{jk}z_k} = \det\left(M_a\right),$$

with the anti symmetric matrix $M_a = (M - M^\dagger)/2$. Since $\slashed{D}$ is itself antisymmetric, Eq. (2.25) follows.

[17]Here, we refer to the particles in graphene as quasi particles since due to the expansion of the Dirac cone we do not describe the interaction with electrons any longer but rather obtain an effective quasi particle Hamiltonian in which only electrons close to the Dirac point contribute (cf. Ref. [35], pp. 462). This way, the solid can be described as if it contained of weakly interacting particles in free space allowing to only take first order interaction terms into account.

2 Elements of the theory of graphene

The Feynman diagram can be understood as the creation and annihilation of a quasi particle - anti quasi particle pair with momenta k' and $k - k'$, respectively. With the current operator (see Ref. [64])

$$\hat{j}^{\,i}(\mathbf{r}, t) = -ev_{\mathrm{F}}\bar{\Psi}(\mathbf{r}, t)\gamma^i\Psi(\mathbf{r}, t)\,, \tag{2.30}$$

and the definition of the retarded Green's function Eqs. (1.99) and (1.97), we arrive at the relation (cf. Eqs. (1.78) and (1.92))

$$\Pi_{\mu\nu}(k) = \chi_{\mu\nu}^j(k) = \chi_{\mu\nu}^j(\mathbf{k}, \omega)\,. \tag{2.31}$$

The polarization tensor is the equivalent to the retarded current-current response function which is related to the macroscopic polarization (see Eqs. (1.92) and (1.93)). The terminus polarization tensor can therefore be motivated by the expression for the expectation value of the current operator

$$\langle\hat{\mathbf{j}}(\mathbf{q}, \omega)\rangle = \underline{\underline{\Pi}}(\mathbf{q}, \omega) \cdot \mathbf{A}(\mathbf{q}, \omega)\,, \tag{2.32}$$

where the coupling of the electromagnetic field to the quasiparticles in graphene and the resulting charge current is determined by the polarizability of the prior.

As is shown in Ref. [65], for a medium of $(2 + 1)$-vector velocity $u = (1, 0, 0)$ in its rest frame the polarization tensor is fully described by the tensor structure

$$\Pi^{\mu\nu}(k) = \frac{1}{\tilde{v}_{\mathrm{F}}^2}\tilde{\eta}_i^\mu\left[\left(g^{ij} - \frac{k^i k^j}{k^2}\right)\mathcal{A}(k) + \left(\frac{k^i k^j}{k^2} - \frac{k^i u^j + u^i k^j}{ku} + \frac{u^i u^j}{(ku)^2}k^2\right)\mathcal{B}(k)\right]\tilde{\eta}_j^\nu\,. \tag{2.33}$$

Above, we take into account the quasi relativistic nature of the excitation in graphene (cf. Ref. [56]). This we do via the definition of $\tilde{\eta} = \underline{\mathrm{diag}}(1, \tilde{v}_{\mathrm{F}}, \tilde{v}_{\mathrm{F}})$ introducing the normed Fermi speed $\tilde{v}_{\mathrm{F}} \equiv v_{\mathrm{F}}/c.$. Throughout the rest of the thesis, we denote all quantities normed to the speed of light c by

$$\tilde{a} \equiv \frac{a}{c}\,. \tag{2.34}$$

With $k_0 = \tilde{\omega}$, $q_z^2 \equiv -\kappa^2 = \tilde{\omega}^2 - |\mathbf{k}|^2$ and

$$y^2 = \tilde{\omega}^2 - \tilde{v}_{\mathrm{F}}^2|\mathbf{k}|^2\,, \tag{2.35}$$

the two functions $\mathcal{A}$ and $\mathcal{B}$ reads

$$\mathcal{A}(k) = -\frac{\kappa^2}{\mathbf{k}^2}\Pi_{00} + \Pi_{\mathrm{tr}} \qquad \text{and} \qquad \mathcal{B}(k) = \frac{1}{\tilde{v}_{\mathrm{F}}^2\mathbf{k}^2}\left(\frac{-\kappa^2 + y^2}{\mathbf{k}^2}\Pi_{00} + \Pi_{\mathrm{tr}}\right)\,. \tag{2.36}$$

Here, the choice of Π_{00} and Π_{tr} is arbitrary and for convenience they are chosen as $\Pi_{\mathrm{tr}} = \Pi_\mu^\mu$ ($\mu = \{1, 2\}$) and Π_{00} (cf. Ref. [56]). The diagonal components $\Pi_1^1 = \Pi_2^2$ due to symmetry reasons.

The reflection coefficients read, when considering the appropriate boundary conditions (see Ref. [56] and Appendix B.2),

$$r_g^{\text{TE}} = -\frac{k^2 \Pi_{\text{tr}} - \kappa^2 \Pi_{00}}{k^2 \Pi_{\text{tr}} - \kappa^2 \Pi_{00} + 2k^2 \kappa} \,, \tag{2.37}$$

$$r_g^{\text{TM}} = \frac{\kappa \Pi_{00}}{\kappa \Pi_{00} + 2k^2} \,, \tag{2.38}$$

and $t_g^{\text{TM}} = 1 - r_g^{\text{TM}}$ while $t_g^{\text{TE}} = 1 + r_g^{\text{TE}}$ (see Ref. [66, 67]). Above, $q_z = \mathrm{i}\kappa$.

Polarization tensor for graphene with finite band gap and $\mu = 0$ at $T = 0\,\text{K}$

The expressions for the polarization tensors Π_{00} and Π_{tr} have been calculated for a variety of cases in a number of references. Thus, we only state the outcomes here that base on the above introduced notations and theory.

For the case of a finite band gap, zero chemical potential and zero temperature as it is realized in the case of undoped but strained graphene, the literature (see Ref. [68] for a first calculation with $\tilde{v}_{\text{F}} = 1$ and Refs. [64, 69–73]) finds the general expression for the shape of the polarization tensor components at zero temperature (see Ref. [69] for the explicit notation)

$$\Pi_{00} = -\alpha \frac{k^2}{y^2} \Phi(y) \,, \tag{2.39}$$

$$\Pi_{\text{tr}} = \alpha \frac{2\tilde{\omega}^2 - (\tilde{v}_{\text{F}}^2 + 1)k^2}{y^2} \Phi(y) \,, \tag{2.40}$$

where

$$\alpha = \frac{e^2}{4\pi\varepsilon_0\hbar c} \approx 137^{-1} \,, \tag{2.41}$$

is the fine structure constant that governs the electromagnetic interaction strength with graphene's quasi particles. When applying the definition of y in Eq. (2.35), the function $\Phi(y)$ reads as

$$\Phi(y) = 8\mathrm{i}\,y \int\limits_0^1 \mathrm{d}x \frac{x(1-x)}{\sqrt{x(1-x) - \frac{\Delta^2}{y^2}}} = 2\Big[\Delta - \Big(1 + \frac{\Delta^2}{y^2}\Big) y \operatorname{atanh}(\frac{y}{\Delta})\Big] \,, \tag{2.42}$$

where we introduced the gap energy $\Delta = 2m/(\hbar c)$ with graphene's quasi particle dispersion relation $\epsilon(\mathbf{k}) = \pm\sqrt{\hbar^2 v_{\text{F}}^2 \mathbf{k}^2 + m^2}$, opening a band gap of $2m$ (cf. Eq. (2.4)). For the rest of the thesis we will handle all energies (and thus also the band gap) in units of the wavevector $\mathbf{k}$. This leads eventually to the reflection coefficients

$$r_g^{\text{TE}} = \frac{-\alpha\Phi(y)}{2\kappa + \alpha\Phi(\omega, k)} \,, \tag{2.43}$$

$$r_g^{\text{TM}} = \frac{\alpha\kappa\Phi(y)}{\alpha\kappa\Phi(\omega, k) - 2y^2} \,. \tag{2.44}$$
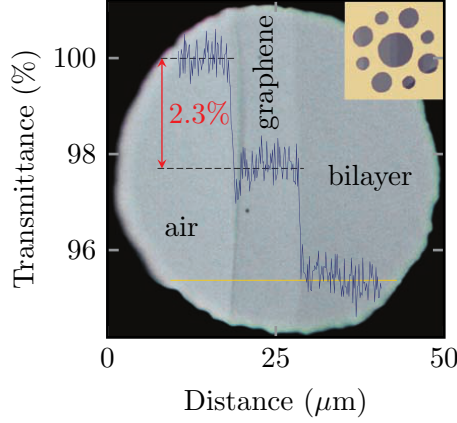
Figure 2.2: The Figure above, shows the experimentally measured data presented in Ref. [75]. It shows a photograph of a $50\,\mu$m aperture where the center is covered with monolayer graphene and the right part of the aperture with bilayer graphene. The authors of Ref. [75] superimpose the spatially resolved transmission measurements. Here the $\pi\alpha$ absorption for each additional graphene layer is well visible (cf. Eq. (2.50) for the reflection coefficients in the optical regime). Figure from R. Nair *et al.*, "Fine structure constant defines visual transparency of graphene", Science **320,** 1308 (2008), doi:10.1126/science.1156965. Adapted with permission from AAAS.

Polarization tensor for graphene without band gap and $\mu = 0$ at $T = 0\,\mathrm{K}$

In the case of zero band gap and zero chemical potential, the quasi particle propagators in general diverge. However, by applying the limit $\Delta \to 0$ as late as in the integral of Eq. (2.42) one arrives at

$$\Phi(y) = \mathrm{i}\pi y\,, \tag{2.45}$$

and with Eqs. (2.39) and (2.40), we find

$$\Pi_{00} = \alpha\pi\frac{k^2}{\mathrm{i}\,y}\,, \tag{2.46}$$

$$\Pi_{\mathrm{tr}} = -\alpha\pi\frac{2\tilde{\omega}^2 - (\tilde{v}_{\mathrm{F}}^2 + 1)k^2}{\mathrm{i}y}\,. \tag{2.47}$$

This results in the reflection coefficients

$$r_g^{\mathrm{TE}} = -\alpha\pi\frac{y}{\alpha\pi y - 2\mathrm{i}\kappa}\,, \tag{2.48}$$

$$r_g^{\mathrm{TM}} = \alpha\pi\frac{\kappa}{\alpha\pi\kappa + 2\mathrm{i}y}\,, \tag{2.49}$$

which correspond to the expressions found when taking renormalization procedures for the initially diverging quasi particle propagators into account (see Refs. [72, 74] for more details).
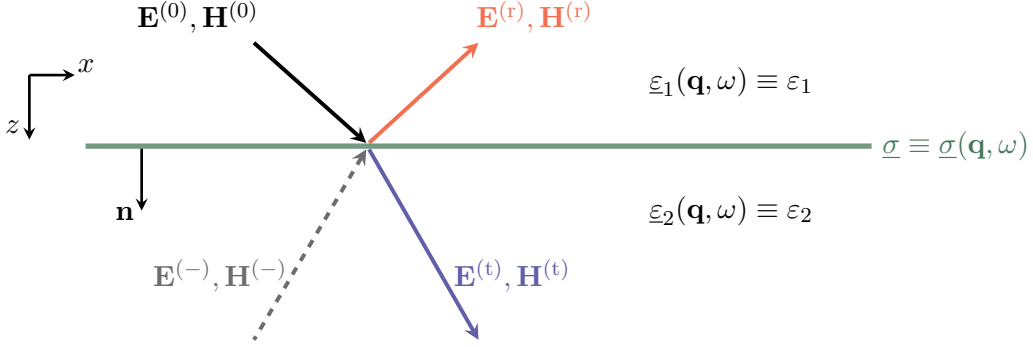
Figure 2.3: The Figure above, shows the electric and magnetic field, $\mathbf{E}$ and $\mathbf{H}$, definitions for incident ($\mathbf{F}^{(0)}$), reflected ($\mathbf{F}^{(\mathrm{r})}$), transmitted ($\mathbf{F}^{(\mathrm{t})}$) and incident from below ($\mathbf{F}^{(-)}$) fields. Here, we describe $\mathbf{F} = \{\mathbf{E}, \mathbf{H}\}$. The material above ($\varepsilon_1$) and below ($\varepsilon_2$: in the Figure $\varepsilon_2 > \varepsilon_1$) the tensorial sheet conductivity ($\underline{\sigma}$) is assumed to be in first approximation isotropic. For simplicity in notation the explicit wavevector and frequency dependence is neglected. The normal on the sheet is denoted by $\mathbf{n}$.

For the optical limit $k \to 0$, Eqs. (2.48) and (2.49) become with $\kappa = \sqrt{k^2 - \tilde{\omega}^2} = -\mathrm{i}\tilde{\omega}$ and $y = \sqrt{\tilde{\omega}^2 - \tilde{v}_{\mathrm{F}}^2 k^2} = \tilde{\omega}$

$$r_g^{\mathrm{TE}} = r_g^{\mathrm{TM}} = \frac{\alpha\pi}{\alpha\pi + 2}, \tag{2.50}$$

corresponding exactly to the theoretically predicted results from early optical conductivity calculations (see Refs. [76, 77]) and the later experimentally measured results where Nair and co-workers measured an absorption of $\pi\alpha = 2.3\%$ for a single graphene layer and $n\pi\alpha$ for n graphene layers stacked on top of each other (see Ref. [75] and Fig. 2.2 taken from within). The connection between optical conductivity and polarization tensor calculation we discuss further in section 2.2.3.

2.2.2 Reflection coefficients of a sheet conductivity

To be able to discuss the difference between polarization tensor and sheet conductivity, we first derive the expressions for the reflection coefficients caused by an arbitrary, frequency and wavevector dependent sheet conductivity (see Fig. 2.3) as it is, e.g., used in Ref. [78]. We split all electromagnetic fields $\mathbf{F} \in \{\mathbf{E}, \mathbf{H}\}$ into the incoming fields incident from above $\mathbf{F}^{(0)}$, the reflected fields $\mathbf{F}^{(\mathrm{r})}$, the incoming fields from below $\mathbf{F}^{(-)}$ and the transmitted fields $\mathbf{F}^{(\mathrm{t})}$ (see Fig. 2.3). The 3D time and space dependent fields are as before denoted by bold letters.

2 Elements of the theory of graphene

In their corresponding Fourier expansion the fields read

$$\mathbf{F}^{(0)}(\mathbf{r},t) = \sum_{\mathbf{q}^{(1)},\omega} \boldsymbol{\mathcal{F}}^{(0)}(\mathbf{q},\omega)\, \mathrm{e}^{\mathrm{i}(q_x^{(1)}x+q_z^{(1)}z)}\, \mathrm{e}^{-\mathrm{i}\omega t}\,,$$

$$\mathbf{F}^{(\mathrm{r})}(\mathbf{r},t) = \sum_{\mathbf{q}^{(1)},\omega} \boldsymbol{\mathcal{F}}^{(\mathrm{r})}(\mathbf{q},\omega)\, \mathrm{e}^{\mathrm{i}(q_x^{(1)}x-q_z^{(1)}z)}\, \mathrm{e}^{-\mathrm{i}\omega t}\,,$$

$$\mathbf{F}^{(-)}(\mathbf{r},t) = \sum_{\mathbf{q}^{(2)},\omega} \boldsymbol{\mathcal{F}}^{(-)}(\mathbf{q},\omega)\, \mathrm{e}^{\mathrm{i}(q_x^{(2)}x-q_z^{(2)}z)}\, \mathrm{e}^{-\mathrm{i}\omega t}\,,$$

$$\mathbf{F}^{(\mathrm{t})}(\mathbf{r},t) = \sum_{\mathbf{q}^{(2)},\omega} \boldsymbol{\mathcal{F}}^{(\mathrm{t})}(\mathbf{q},\omega)\, \mathrm{e}^{\mathrm{i}(q_x^{(2)}x+q_z^{(2)}z)}\, \mathrm{e}^{-\mathrm{i}\omega t}\,,$$

(2.51)

where we return to the in electromagnetics common choice of Cartesian variable names, $1 \to x$ and $2 \to y$, while distinguishing between the fields above (1) and below (2) the conductive sheet.

With this, the position is defined as $\mathbf{r} = (x,y,z)^T$ and we sum over 3D wavevectors $\mathbf{q}^{(1,2)} = (q_x^{(1,2)}, q_y^{(1,2)}, q_z^{(1,2)})^T$ where with $q_y^{(1,2)} = 0$ we choose the incident plane as the x-z plane without loss of generality.

The fields above have to fulfill Maxwell's equations (1.1) with $\underline{\mu}_r = 1$, $\underline{\varepsilon}_i = \varepsilon_i \mathbb{1}_3$ (neglecting the explicit wavevector and frequency dependence for sake of notation) and $\rho_{\mathrm{free}} = \mathbf{j}_{\mathrm{free}} = 0$. Additionally, we have to take the boundary conditions for a surface conductivity in the x-y plane at $z = z_0$ into account (see Ref. [27] and Eq. (1.82))

$$\mathbf{n} \cdot \left[\mathbf{D}^{(2)}(\mathbf{r},t) - \mathbf{D}^{(1)}(\mathbf{r},t) \right]_{z=z_0} = 0\,, \tag{2.52a}$$

$$\mathbf{n} \cdot \left[\mathbf{B}^{(2)}(\mathbf{r},t) - \mathbf{B}^{(1)}(\mathbf{r},t) \right]_{z=z_0} = 0\,, \tag{2.52b}$$

$$\mathbf{n} \times \left[\mathbf{E}^{(2)}(\mathbf{r},t) - \mathbf{E}^{(1)}(\mathbf{r},t) \right]_{z=z_0} = 0\,, \tag{2.52c}$$

$$\mathbf{n} \times \left[\mathbf{H}^{(2)}(\mathbf{r},t) - \mathbf{H}^{(1)}(\mathbf{r},t) \right]_{z=z_0} = \mathbf{j}_{\mathrm{tangential}}(\mathbf{r},t) = \int_{\mathcal{A}} \mathrm{d}^2 r' \int_{-\infty}^{\infty} \mathrm{d}t'\, \mathbf{t} \cdot$$
$$\left[\underline{\sigma}(\mathbf{r}',t') \cdot \mathbf{E}(\mathbf{r}-\mathbf{r}',t-t') \Big|_{z-z'=z_0} \right]\,, \tag{2.52d}$$

where $\mathbf{n}$ describes the unit vector normal to the sheet as depicted in Fig. 2.3, $\mathbf{t}$ the vector tangential to the sheet and $\mathrm{d}^2 r$ the integration along the conductive sheet. The fields are defined as $\mathbf{F}_1(\mathbf{r},t) = \mathbf{F}^{(0)}(\mathbf{r},t) + \mathbf{F}^{(\mathrm{r})}(\mathbf{r},t)$ and $\mathbf{F}(\mathbf{r},t) = \mathbf{F}^{(-)}(\mathbf{r},t) + \mathbf{F}^{(\mathrm{t})}(\mathbf{r},t)$.

For an isotropic, diagonal surface conductivity tensor $\underline{\sigma} \equiv \underline{\mathrm{diag}}\,(\sigma,\sigma,0)$, the problem is separable into its Fourier components and two polarizations: transverse electric (TE) and transverse magnetic (TM)

$$\mathrm{TM}: \qquad \mathbf{H}^{(i)} = H_y^{(i)} \qquad \text{and} \qquad \mathbf{E}^{(i)} = (E_x^{(i)}, 0, E_z^{(i)})^T\,, \tag{2.53a}$$

$$\mathrm{TE}: \qquad \mathbf{E}^{(i)} = E_y^{(i)} \qquad \text{and} \qquad \mathbf{H}^{(i)} = (H_x^{(i)}, 0, H_z^{(i)})^T\,. \tag{2.53b}$$

As discussed in 1.3.1, any response function of the electromagnetic field may be split up

in a longitudinal and transverse part (see Eq. (1.81))

$$\sigma_{\mu\nu}(\mathbf{k},\omega) = \frac{q_\mu q_\nu}{k^2}\sigma^{\mathrm{L}}(\mathbf{k},\omega) + \left(\delta_{\mu\nu} - \frac{q_\mu q_\nu}{k^2}\right)\sigma^{\mathrm{T}}(\mathbf{k},\omega)\,, \tag{2.54}$$

with the previously introduced in-plane wavevector $\mathbf{k} = (q_x, q_y)^T$ leading to (for a sheet at $z = z_0$ and $q_y = 0$)

$$\underline{\sigma}(\mathbf{k},\omega) = \underline{\mathrm{diag}}\left(\sigma^{\mathrm{L}}(\mathbf{k},\omega), \sigma^{\mathrm{T}}(\mathbf{k},\omega), 0\right)\,. \tag{2.55}$$

This result can be understood, when realizing that in the specific choice of coordinate system used in this work σ_{yy} couples to E_y which is always transverse to the in-plane wavevector $\mathbf{k} = q_x \mathbf{e}_x$ while σ_{xx} couples to E_x which is parallel to $\mathbf{k}$ and thus acts with respect to the conductive plane a longitudinal field.

From these considerations, we arrive at the following reflection and transmission coefficients (see Appendix B.1 for a detailed derivation).

TE polarization:

$$r^{\mathrm{TE}} = \frac{\mathcal{E}_y^{(\mathrm{r})}}{\mathcal{E}_y^{(0)}} = \frac{q_z^{(1)} - q_z^{(2)} + \mu_0\omega\sigma^{\mathrm{T}}(\mathbf{k},\omega)}{q_z^{(1)} + q_z^{(2)} - \mu_0\omega\sigma^{\mathrm{T}}(\mathbf{k},\omega)}\,, \tag{2.56a}$$

$$t^{\mathrm{TE}} = \frac{\mathcal{E}_y^{(\mathrm{t})}}{\mathcal{E}_y^{(0)}} = \frac{2q_z^{(1)}}{q_z^{(1)} + q_z^{(2)} - \mu_0\omega\sigma^{\mathrm{T}}(\mathbf{k},\omega)}\,. \tag{2.56b}$$

TM polarization:

$$r^{\mathrm{TM}} = \frac{\mathcal{H}_y^{(\mathrm{r})}}{\mathcal{H}_y^{(0)}} = \frac{\varepsilon_2 q_z^{(1)} - \varepsilon_1 q_z^{(2)} + q_z^{(1)} q_z^{(2)} \frac{\sigma^{\mathrm{L}}(\mathbf{k},\omega)}{\omega}}{\varepsilon_2 q_z^{(1)} + \varepsilon_1 q_z^{(2)} + q_z^{(1)} q_z^{(2)} \frac{\sigma^{\mathrm{L}}(\mathbf{k},\omega)}{\omega}}\,, \tag{2.57a}$$

$$t^{\mathrm{TM}} = \frac{\mathcal{H}_y^{(\mathrm{t})}}{\mathcal{H}_y^{(0)}} = \frac{2\varepsilon_2 q_z^{(1)}}{\varepsilon_2 q_z^{(1)} + \varepsilon_1 q_z^{(2)} + q_z^{(1)} q_z^{(2)} \frac{\sigma^{\mathrm{L}}(\mathbf{k},\omega)}{\omega}}\,. \tag{2.57b}$$

2.2.3 The conductivity of graphene

When comparing the expressions for the reflection coefficients of graphene from a general polarization tensor as described in Sec. 2.2.1 with the expressions for the reflection coefficients from a sheet conductivity, we may relate the expressions for the longitudinal and transverse conductivities with the polarization tensors using Eq. (2.41) (see also Refs. [79, 80] for similar discussions):

$$\sigma^{\mathrm{L}}(\mathbf{k},\omega) = \mathrm{i}\varepsilon_0\omega\frac{\Pi_{00}(\mathbf{k},\omega)}{k^2} = \frac{\mathrm{i}e^2}{4\pi\alpha\hbar}\frac{\omega}{c}\frac{\Pi_{00}(\mathbf{k},\omega)}{k^2}\,, \tag{2.58}$$

$$\sigma^{\mathrm{T}}(\mathbf{k},\omega) = -\frac{\mathrm{i}\varepsilon_0 c^2}{\omega}\left(\frac{q_z^2}{k^2}\Pi_{00}(\mathbf{k},\omega) + \Pi_{\mathrm{tr}}(\mathbf{k},\omega)\right)$$

$$= -\frac{\mathrm{i}e^2}{4\pi\alpha\hbar}\frac{c}{\omega}\left(\frac{q_z^2}{k^2}\Pi_{00}(\mathbf{k},\omega) + \Pi_{\mathrm{tr}}(\mathbf{k},\omega)\right)\,. \tag{2.59}$$

2 Elements of the theory of graphene

As presented in section 1.3.1, different limits to the conductivity exist. A relevant one is the optical conductivity, for which $k \to 0$. In consequence, $q_z \approx \tilde{\omega}$ and with

$$\frac{\Pi_{00}(0, \omega)}{k^2} = -\frac{\alpha \Phi(0, \omega)}{\omega^2} \, ,$$
$$\Pi_{\mathrm{tr}}(0, \omega) = 2\alpha \Phi(0, \omega) \, ,$$

the reflection coefficients at zero temperature read

$$r_g^{\mathrm{TE}} = r_g^{\mathrm{TM}} = \frac{\alpha \Phi(0, \omega)}{\alpha \Phi(0, \omega) - 2\mathrm{i}\omega} \, , \tag{2.60}$$

leading to an isotropic conductivity

$$\sigma(\omega) = \sigma^{\mathrm{L}}(0, \omega) = \sigma^{\mathrm{T}}(0, \omega) = -\frac{\mathrm{i}\varepsilon_0 c^2}{2\omega} \lim_{k \to 0} \left[\Pi_{\mathrm{tr}}(\mathbf{k}, \omega) \right] \, . \tag{2.61}$$

2.2.4 The conductivity of graphene at finite temperatures and chemical potential

Up to this point, we have only discussed the case in which graphene exhibits zero chemical potential and is cooled down to the zero temperature. In real life, finite temperature experiments are however much easier conducted. For a finite temperature setup, the band gap only has an influence if it is much larger in energy than the temperature, finding at room temperature ($T = 300\,\mathrm{K}$)

$$2m > k_{\mathrm{B}}T = 25.85\,\mathrm{meV} \, . \tag{2.62}$$

However, when comparing this to standard values found in literature for a possible gap of graphene, this is at the upper limit achievable by, e.g., breaking the sublattice symmetry by a deposition onto hBN. Thus, for finite temperatures, in this work we only consider (effectively) gapless graphene.

In addition, we can consider the influence of the chemical potential μ. Up to this point, we have considered it to be $\mu = 0$ in the explicit expressions for the reflection and transmission coefficients and the conductivities. However, this parameter is experimentally quite easily accessible and can be changed either by external electrostatic gating (see Refs. [44, 81]) or by substituting carbon atoms in the graphene monolayer with electron donors or acceptors (see Ref. [82] for a numerical ab-initio study and Refs. [83, 84] for experiments in which the authors dope graphene with the electron donor nitrogen while in Ref. [85] the authors present results where doping graphene with the electron acceptor boron). While in the first case, the linear Dirac cone remains degenerate at the Dirac point, in the second case, a band gap opens. We will in this work thus focus on the first and more often applied method, the electrostatic gating. We refer to the corresponding change of the Fermi energy as chemical doping (see Ref. [86]) since it leads to a change in the chemical potential μ.

Using the same effective action Eq. (2.13) as for the previously discussed realizations of graphene, literature (see Refs. [67, 87–89]) finds the optical conductivity of graphene

at temperature T with chemical potential μ as

$$\sigma(\omega) = -\frac{\mathrm{i}e^2}{\hbar\pi} \left\{ \frac{1}{\hbar\omega + \mathrm{i}\Gamma} \int_{-\infty}^{\infty} \mathrm{d}\epsilon \left[|\epsilon|\partial_\epsilon f(\epsilon)\right] \right.$$

$$\left. + \int_{0}^{\infty} \mathrm{d}\epsilon \frac{\hbar\omega + \mathrm{i}\Gamma}{\left(\hbar\omega + \mathrm{i}\Gamma\right)^2 - 4\epsilon^2} \left[f(\epsilon) - f(-\epsilon)\right] \right\} . \tag{2.63}$$

Here, the Fermi function (cf. Eq. (A.1))

$$f(\epsilon) = \frac{1}{\exp\frac{\epsilon - \mu}{k_\mathrm{B}T} + 1} ,$$

describes the electron distribution at finite temperatures. Additionally, we introduce an empirical (and temperature-dependent) decay rate Γ to account for intrinsic losses.

For the case of a finite chemical potential, we can distinguish in Eq. (2.63) between two different contributions – the intraband and the interband part of the conductivity. The intraband contribution describes the electron dynamics in which the electrons remain in the same band while the interband contribution describes electron dynamics in which the electrons change from one band to the other by being either excited into the conduction band (and creating an electron-hole pair or corresponding multiple particle excitations) or decays into the valence band. See Fig. 2.4(a) for the distinction between those two processes in doped graphene. In Eq. (2.63), as before the conductivity is calculated in the limit of single-particle processes and thus additional processes, governed, e.g., by Coulomb-Coulomb interaction (cf. Ref. [90–92][18] and Fig. 2.4(b-e)) are not included in Eq. (2.63).

The intraband conductivity (first integral in Eq. (2.63)) can be solved analytically and for $T \neq 0\,\mathrm{K}$ is equal to

$$\sigma_{\mathrm{intra}}(\omega) = \frac{\mathrm{i}e^2}{\hbar\pi} \frac{1}{\hbar\omega + \mathrm{i}\Gamma} \cdot 2k_\mathrm{B}T \ln\left[2\cosh\left(\frac{\mu}{2k_\mathrm{B}T}\right)\right] . \tag{2.64}$$

while the interband conductivity reads

$$\sigma_{\mathrm{inter}}(\omega) = -\frac{\mathrm{i}e^2}{\hbar\pi} \int_{0}^{\infty} \mathrm{d}\epsilon \frac{\hbar\omega + \mathrm{i}\Gamma}{\left(\hbar\omega + \mathrm{i}\Gamma\right)^2 - 4\epsilon^2} \left[f(\epsilon) - f(-\epsilon)\right] . \tag{2.65}$$

The intraband conductivity, Eq. (2.64) is thus effectively comprised out of a Drude term (see section 5.4.1 for further discussions on this model and the effects described by it) multiplied with a temperature dependent contribution. The interband conductivity is not as easily integrated analytically but can be approximated further and then be included into numeric, electromagnetic field solvers (see section 5.5).

---

[18]In Refs. [90, 92], the authors show that the inclusion of such higher-order processes is necessary when describing, e.g., the ultrashort excitation of graphene by a laser light pulse. The non-equilibrium situation leads to a long-time creation of excess charges in the conduction band. This is known as carrier-multiplication (see Fig. 2.4(d)).
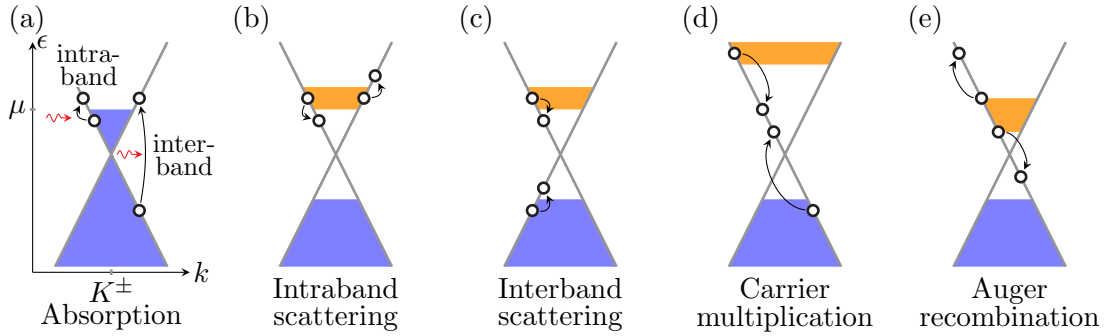
Figure 2.4: Electronic transition processes in graphene. We depict the electron dispersion relation in proximity of the two Dirac points $k = K^{\pm}$. Panel (a) presents an equilibrium electron distribution (blue) with finite chemical potential μ. Via the interaction with the electromagnetic field (red arrow: photon) intra- and interband absorption may occur. When pumping the electrons in graphene with an external laser pulse, a non-equilibrium distribution builds up (blue: electrons in valence band, orange: "hot" electrons in conduction band). Besides from photon absorption and emission processes (analogously to panel (a)), electron- electron scattering processes take place (b)-(e). In panels (b)-(e), each of the two transitions happen by scattering of the two original electrons thus each panel presents one single process (opposite to panel (a) where two different processes are depicted). While inter- and intraband scattering conserve the number of excitations in valence and conduction band, the carrier multiplication and auger recombination allow for a relative change of the numbers of carriers in conduction and valence band (see also Ref. [91] from where this figure is partially adapted by permission from Macmillan Publishers Ltd: Nature Communications, Ref. [91], doi:10.1038/ncomms2987, © 2013). The processes (b)-(e) are not part of this thesis but do have to be included when discussing ultrafast optics in graphene.

2.3 Conclusions

In this chapter, we motivated the quantum-field theoretical description of electrons close to the Dirac point by a discussion of a basic tight-binding theory. With the reflection and transmission coefficients and surface conductivities for the different situations in which graphene monolayers might exist in experiment (with and without band gap, at zero or finite temperature, exhibiting a zero or finite chemical potential), we can study graphene plasmonics in chapters 4 and 5.

Here, it is important to realize also the limitations of our models. For example, in some of the models we will neglect phenomenological damping while in others we will neglect the non-local effects, considering optical properties only. Depending on the specific experimental realization these approximations are appropriate.

Theoretical description of quantum-mechanical and classical emitters

---

"There are two ways of spreading light: to be the candle or the mirror that reflects it." [19]

Edith Wharton

In the first two chapters of this thesis, we concentrated on the material's interaction with electromagnetic radiation. In this chapter, we focus on a source of electromagnetic radiation: the emitter. It is first discussed as general two-level systems, distinguishing between electric and magnetic transitions. This then lays the basis for the treatment of different kind of emitters in the proximity of plasmonic nanostructures later in this thesis, i.e., dipoles, nitrogen-vacancy (NV) centers and atoms.

3.1 The two-level system

The term *emitter* is a rather general expression and describes in this thesis every object that may be described by at least two states where a transition between those states takes place via coupling to some components of the electromagnetic field. Thus, this requires either an electric or a magnetic dipole moment where the electric dipole moment operator $\hat{\mathbf{d}}$ couples to the electric field operator $\hat{\mathbf{E}}(\mathbf{r}, t)$ via the interaction Hamiltonian

$$\hat{\mathcal{H}}_{\text{interaction}} = -\hat{\mathbf{d}} \cdot \hat{\mathbf{E}}(\mathbf{r}_0, t) \,. \tag{3.1}$$

Here, we assume the electric dipole moment distribution to be point-like such that the electric field operator couples to the electric dipole moment only at the center of charge distribution $\mathbf{r}_0$. This assumption is often considered appropriate if the electric field is constant over the extension of the electric dipole distribution, i.e., the wavelength of the electric field is much larger than mentioned spatial extension.

Under the equivalent assumption, the point-like magnetic dipole moment operator $\hat{\boldsymbol{\mu}}$ at position $\mathbf{r}_0$ couples to the magnetic fields by means of the magnetic flux density operator $\hat{\mathbf{B}}(\mathbf{r}, t)$ via the interaction Hamiltonian

$$\hat{\mathcal{H}}_{\text{interaction}} = -\hat{\boldsymbol{\mu}} \cdot \hat{\mathbf{B}}(\mathbf{r}_0, t) \,. \tag{3.2}$$

---

[19] "Vasalius in Zante (1564)", North American Review, p. 625 (1902)

3 Theoretical description of quantum-mechanical and classical emitters
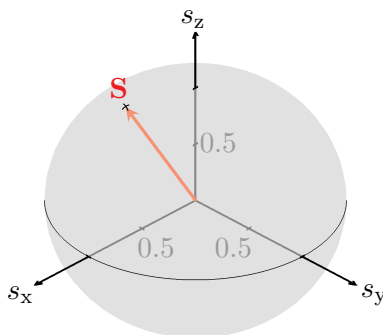
Figure 3.1: The Figure above depicts the Bloch sphere with the expectation value of the Bloch vector $\mathbf{S} = \langle \hat{\mathbf{S}} \rangle$ and $\hat{\mathbf{S}} = (\hat{\sigma}_{\mathrm{x}}, \hat{\sigma}_{\mathrm{y}}, \hat{\sigma}_{\mathrm{z}})^T$. The expectation values of the single operators $\langle \hat{\sigma}_i \rangle = s_i$.

If one considers that two states – although possibly belonging to a more complex energy scheme with a number of additional levels – are decoupled from every other level close by, we can approximate the energy level scheme as a two-level system. This approximation is appropriate in many physical systems such as the Sodium atom (see Ref. [93], p. 33). In such a case, we can introduce a description in terms of the so-called Bloch sphere, where we use operators from the SU(2) symmetry group to describe the transitions in this system. The ground state $|\!\downarrow\rangle$ is depicted as the south pole whereas the totally excited state $|\!\uparrow\rangle$ is depicted at the north pole (cf. Fig. 3.1). The operations on the sphere are described by the set of Pauli matrices defined as (see also Eq. (2.7))

$$\hat{\sigma}_+ = |\!\uparrow\rangle\langle\downarrow\!|, \quad \hat{\sigma}_- = |\!\downarrow\rangle\langle\uparrow\!|, \quad \text{and} \quad \hat{\sigma}_{\mathrm{z}} = |\!\uparrow\rangle\langle\uparrow\!| - |\!\downarrow\rangle\langle\downarrow\!|, \tag{3.3}$$

or as an equivalent complete set of Pauli matrices

$$\hat{\sigma}_{\mathrm{x}} = \hat{\sigma}_+ + \hat{\sigma}_-, \quad \hat{\sigma}_{\mathrm{y}} = \mathrm{i}(\hat{\sigma}_- - \hat{\sigma}_+), \quad \text{and} \quad \hat{\sigma}_{\mathrm{z}} = |\!\uparrow\rangle\langle\uparrow\!| - |\!\downarrow\rangle\langle\downarrow\!|. \tag{3.4}$$

These Pauli matrices obey the commutator relations

$$\begin{aligned} &[\hat{\sigma}_+, \hat{\sigma}_-] = \hat{\sigma}_{\mathrm{z}} \quad \text{and} \quad [\hat{\sigma}_{\mathrm{z}}, \hat{\sigma}_\pm] = \pm 2\hat{\sigma}_\pm, \\ \text{or} \quad &[\hat{\sigma}_{\mathrm{x}}, \hat{\sigma}_{\mathrm{y}}] = 2\mathrm{i}\hat{\sigma}_{\mathrm{z}} \quad \text{and} \quad \text{cyclic permutations}. \end{aligned} \tag{3.5}$$

In order to express the dipole moments in terms of these two-state eigenvectors' system, we have to take the general symmetry properties of both dipole moments into consideration. The definition of the electric (see Ref. [93]) and magnetic (see Ref. [94]) dipole operators is given by

$$\hat{\mathbf{d}} = e\hat{\mathbf{r}}, \tag{3.6a}$$

$$\hat{\boldsymbol{\mu}} = g_F \mu_B \hat{\mathbf{F}}, \tag{3.6b}$$

where $\hat{\mathbf{r}}$ is the position operator, e the electric charge, g_F the nuclear g-factor, μ_B the Bohr magneton and $\hat{\mathbf{F}}$ the total angular momentum of an atom. While the electric dipole moment operator is odd in parity (vector), the magnetic dipole moment operator

is even in parity[20] (pseudovector). Thus, for the case of the electric dipole operator only transitions between states of different parity are allowed while for the case of the magnetic dipole operator only transitions between states of equal parity are allowed.

For the electric dipole operator of an atom in its energy eigenstate, the dipole operator is due to parity and time-reversal symmetry arguments purely off-diagonal (since coupling to the same state obviously couples to two states of same parity) while for the magnetic dipole operator also (possibly small) diagonal matrix entries exist

$$\hat{\mathbf{d}} = \mathbf{d}_{\uparrow\downarrow}\,\hat{\sigma}_+ + \mathbf{d}_{\uparrow\downarrow}^*\,\hat{\sigma}_- \, , \tag{3.7a}$$

$$\hat{\boldsymbol{\mu}} = \boldsymbol{\mu}_{\uparrow\downarrow}\,\hat{\sigma}_+ + \boldsymbol{\mu}_{\uparrow\downarrow}^*\,\hat{\sigma}_- + \frac{\boldsymbol{\mu}_{\uparrow\uparrow} + \boldsymbol{\mu}_{\downarrow\downarrow}}{2}\mathbb{1} + \frac{\boldsymbol{\mu}_{\uparrow\uparrow} - \boldsymbol{\mu}_{\downarrow\downarrow}}{2}\hat{\sigma}_{\mathrm{z}} \, . \tag{3.7b}$$

Here, we use $\mathbf{d}_{\downarrow\uparrow} = \mathbf{d}_{\uparrow\downarrow}^*$ and $\boldsymbol{\mu}_{\downarrow\uparrow} = \boldsymbol{\mu}_{\uparrow\downarrow}^*$, respectively, and $\mathbf{d}_{ij} = \langle i|\hat{\mathbf{d}}|j\rangle$ and $\boldsymbol{\mu}_{ij} = \langle i|\hat{\boldsymbol{\mu}}|j\rangle$ connect the states $|i\rangle$ and $|j\rangle$ with each other. We note that Eq. (3.7a) forbids a permanent electric dipole moment and that this is the topic of on-going research (see Refs. [95, 96]). If any, however, only a very small permanent electric dipole moment exists and a discussion goes well beyond the scope of this thesis.

3.2 The electric dipole

After the general introduction of transitions caused by the electromagnetic fields, in the following we first solely focus on electric dipole transitions. Since these transitions usually take place at optical frequencies and in most cases they couple strongly to the electromagnetic field[21] in nanooptical experiments these transitions are usually the once excited, measured and used.

There are different systems exhibiting electric dipole transitions, e.g., atoms, quantum dots and even small metallic nanoparticles. Very stable and experimentally well controllable objects are the *color-centers* in diamond that in this work we often consider as experimental application. Diamond itself is transparent over a wide range of frequencies and can have a number of defects (cf. Ref. [97]). The two best known of these defects are the nitrogen-vacancy (NV) and the silicon-vacancy (SiV) center. In both cases, one carbon atom is replaced by either a nitrogen or a silicon atom, respectively. Besides these two, more than 100 luminescent defects exist (see Ref. [98]).

When referring to the nitrogen-vacancy (NV) and the silicon-vacancy (SiV) center, in the following, we always consider nanodiamonds including a single defect. These nanodiamonds are even at room temperatures very photostable (almost no blinking or bleaching is reported, see Refs. [99, 100]), can be placed with high precision (see, e.g., Ref. [W2]) and can be purchased commercially. In section 6.1.1, we will discuss the specific properties of the NV center in a nanodiamond in larger detail.

---

[20]Depending on the strength of the magnetic flux density, the total magnetic moment of an atom is different. In weak fields, however, the total angular momentum of the atom is mainly governed by the electron's orbital angular momentum $\hat{\mathbf{L}} = \hat{\mathbf{r}} \times \hat{\mathbf{j}}$ and in the ground state the spin $\hat{\mathbf{S}}$. Both of these are pseudovectors and hence even in parity. For details on the specific expression of $\hat{\mathbf{F}}$, see Appendix C.2.

[21]Electric quadrupole transitions and magnetic dipole transitions are on the same order of magnitude and magnitudes smaller than the electric dipole transition. Higher order multipole transitions of both magnetic and electric coupling are even smaller in magnitude.

3 Theoretical description of quantum-mechanical and classical emitters

3.2.1 Radiation pattern of an electric dipole in an isotropic dielectric medium

Any emitter having an electric dipole moment (be it a classical or a quantum emitter) radiates an electromagnetic field as long as it is not in the groundstate. In homogeneous vacuum or in a loss-less, isotropic, non-dispersive material, the propagation of the radiation of an emitter with the expectation value[22] of the dipole moment $\mathbf{p}(\mathbf{r}, t) = \langle \hat{\mathbf{d}} \rangle (\mathbf{r}, t)$ is well-known (see Ref. [27], pp. 471). Since the knowledge of this radiation pattern is important later on in this work, we shortly sketch the derivation here.

Starting from Eq. (1.29), we can formulate the Green's function (see section 1.3.2) for the four-vector potentials in frequency domain reading

$$(\Delta + q^2) \underline{\mathcal{G}}(\mathbf{r}, \mathbf{r}'; \omega) = \mathbb{1} \delta(\mathbf{r} - \mathbf{r}'), \tag{3.8}$$

with the photon's dispersion relation $q = \sqrt{\varepsilon_r \mu_r} \omega / c$. For the Green's function two solutions – an advanced and a retarded – exist. However, out of these two only the retarded solution fulfills the requirement of causality. Undoing the Fourier transform, we obtain

$$\mathcal{G}^{\pm}(|\mathbf{r} - \mathbf{r}'|; t - t') = \frac{\delta(t' - (t \mp \frac{\sqrt{\varepsilon_r \mu_r}}{c}|\mathbf{r} - \mathbf{r}'|))}{4\pi|\mathbf{r} - \mathbf{r}'|}, \tag{3.9}$$

where "+" describes the retarded and "−" the advanced solution. The retarded Green's function can be used to calculate the vector potential

$$\mathbf{A}(\mathbf{r}, t) = \frac{\mu_0 \mu_r}{4\pi} \int d^3 r' \int dt' \frac{\mathbf{j}(\mathbf{r}', t')}{|\mathbf{r} - \mathbf{r}'|} \delta\left(t' - (t - \frac{\sqrt{\varepsilon_r \mu_r}}{c}|\mathbf{r} - \mathbf{r}'|)\right). \tag{3.10}$$

The current distribution $\mathbf{j}(\mathbf{r}, t)$ describes the current stemming from a point-like charge distribution and at position $\mathbf{r}_0$ such that the charge current can be written as

$$\dot{\mathbf{p}}(\mathbf{r}, t) \equiv \mathbf{j}(\mathbf{r}, t) = \mathbf{j}_0 \delta(\mathbf{r} - \mathbf{r}_0) \eta(t), \tag{3.11}$$

with the time-dependence included in $\eta(t)$ (see section 3.2.2 and section 3.2.3 for equations of motion of the polarization). Here, the prefactor $\mathbf{j}_0$ is time and space independent and only contains the dipole's vector orientation.

Inserting the expression into Eq. (3.10) and defining $\tilde{\mathbf{r}} = \frac{\sqrt{\varepsilon_r \mu_r}}{c}(\mathbf{r} - \mathbf{r}_0)$, $\tilde{r} = |\tilde{\mathbf{r}}|$ and $\tilde{t} = t - \tilde{r}$ the magnetic field reads

$$\mathbf{H}(\mathbf{r}, t) = \frac{\varepsilon_r \mu_r}{4\pi c^2} \left(\mathbf{j}_0 \times \tilde{\mathbf{r}}\right) \left[\frac{\eta(\tilde{t})}{\tilde{r}^3} + \frac{\dot{\eta}(\tilde{t})}{\tilde{r}^2}\right]. \tag{3.12}$$

With Maxwell's equation (1.1), the corresponding electric field reads

$$\mathbf{E}(\mathbf{r}, t) = -\frac{\sqrt{\varepsilon_r \varepsilon_0}(\mu_0 \mu_r)^{3/2}}{4\pi} \cdot \left\{ \mathbf{v}_1 \left[\frac{\int_0^{\tilde{t}} \eta(t')dt'}{\tilde{r}^3} + \frac{\eta(t - \tilde{r})}{\tilde{r}^2}\right] + \mathbf{v}_2 \frac{\dot{\eta}(t - \tilde{r})}{\tilde{r}} \right\}. \tag{3.13}$$

Thus the electric and magnetic fields caused by a point-like dipole are given by Eq. (3.13) and Eq. (3.12).

---

[22]Here, I distinguish between the operator $\hat{d}$ and the expectation value of the system that following the *Ehrenfest theorem* (see Ref. [101]) corresponds to the classical value.

3.2.2 Maxwell-Bloch equations

In the previous section, we discuss the radiation pattern stemming from an arbitrary electric dipole that emits electromagnetic fields with a certain time dependence $\eta(t)$. This time dependence is caused by the specific time evolution that governs the emitter.

As mentioned above, in this thesis we only behold dipole transitions that are described by an effective two-level system with the other levels sufficiently far off resonance or forbidden. Whether or not the electromagnetic field couples to a dipole moment (allowed transition) can be determined using the so-called *selection rules*. In Appendix C, we discuss these in some detail.

Assuming an allowed transition, we derive the Maxwell-Bloch equations that describe the time evolution of the atomic operators $\hat{\sigma}_+$ and $\hat{\sigma}_z$. Commonly, such an electric dipole is described in terms of an unperturbed Hamiltonian

$$\hat{\mathcal{H}}_0 = \frac{\hbar\omega_0}{2}\hat{\sigma}_z \ , \tag{3.14}$$

where we choose the energy of the ground state $|\downarrow\rangle$ to be $\epsilon_{|\downarrow\rangle} = -\hbar\omega_0/2$ and $\hbar\omega_0$ describes the transition energy between the two levels. Together with the interaction Hamiltonian (3.1), the complete Hamiltonian reads

$$\hat{\mathcal{H}} = \frac{\hbar\omega_0}{2}\hat{\sigma}_z \ - \left(\mathbf{d}_{\uparrow\downarrow}\hat{\sigma}_+ + \mathbf{d}_{\uparrow\downarrow}^*\hat{\sigma}_-\right)\cdot\hat{\mathbf{E}}(\mathbf{r}_0,t)\,. \tag{3.15}$$

In the Heisenberg picture, the equation of motion for any operator $\hat{O}(t)$ (see Eq. (1.33) with $\partial_t\hat{O}(t) = 0$) reads

$$i\hbar\mathrm{d}_t\hat{O}(t) = [\hat{O},\hat{\mathcal{H}}]\,,$$

which leads with the commutator relations of the Pauli matrices (3.5) to

$$i\hbar\mathrm{d}_t\hat{\sigma}_-(t) = \hbar\omega_0\hat{\sigma}_-(t) + \mathbf{d}_{\uparrow\downarrow}\hat{\mathbf{E}}(\mathbf{r}_0,t)\hat{\sigma}_z \ , \tag{3.16a}$$

$$i\hbar\mathrm{d}_t\hat{\sigma}_z(t) = -\left[\mathbf{d}_{\uparrow\downarrow}\hat{\sigma}_+ - \mathbf{d}_{\uparrow\downarrow}^*\hat{\sigma}_-\right]\hat{\mathbf{E}}(\mathbf{r}_0,t)\,. \tag{3.16b}$$

From here, different approaches are possible. Within the quantum electrodynamics (QED) research (see e.g. the research regarding waveguide QED in Refs. [21, 102, 103]) the electromagnetic field is kept as an operator and the quantized field interacts with the two-level system. However, when we follow the discussion in Refs. [W1, 93] we can assume that if quantum correlations decay on a time scale much shorter than the time scales at which the system evolves, we can factorize the product of the expectation values

$$\langle\hat{\sigma}_i(t)\cdot\hat{\mathbf{E}}(\mathbf{r}_0,t)\rangle \approx \langle\hat{\sigma}_i(t)\rangle\langle\hat{\mathbf{E}}(\mathbf{r}_0,t)\rangle \equiv \mathbf{E}(\mathbf{r}_0,t)s_i(t)\,. \tag{3.17}$$

Above, the index $i\in\{+,-,z\}$ and following the Ehrenfest theorem (see Ref. [101])

$$\langle\hat{\mathbf{E}}(\mathbf{r}_0,t)\rangle = \mathbf{E}(\mathbf{r}_0,t)\,, \tag{3.18}$$

the expectation value of the electric field operator equals the classical field vector. Additional, we introduced the notation $s_i \equiv \langle\hat{\sigma}_i\rangle$ for the expectation value of the Pauli matrices.

This then leads to the so-called *Maxwell-Bloch equations* that read

$$i\hbar d_t s_{\mp} = \pm\hbar\omega_0 s_{\mp} + \Big[\mathbf{d}_{\uparrow\downarrow}\cdot\mathbf{E}(\mathbf{r}_0,t)\Big]^{(*)} s_z\,, \tag{3.19a}$$

$$i\hbar d_t s_z = -\Big[\mathbf{d}_{\uparrow\downarrow}s_+ - \mathbf{d}_{\uparrow\downarrow}^* s_-\Big]\cdot\mathbf{E}(\mathbf{r}_0,t)\,. \tag{3.19b}$$

3.2.3 Classical limit of the Maxwell-Bloch equations

The Maxwell-Bloch equations (3.19) can be written as a driven harmonic oscillator under certain assumptions. First, rewriting Eqs. (3.6a) and (3.7a), we find for the charge displacement vector

$$\hat{\mathbf{r}} = \frac{1}{e}\Big(\mathbf{d}_{\uparrow\downarrow}\hat{\sigma}_+ + \mathbf{d}_{\uparrow\downarrow}^*\hat{\sigma}_-\Big) = \frac{1}{e}\Big(\mathbf{d}_{\mathrm{r}}\hat{\sigma}_{\mathrm{x}} - \mathbf{d}_{\mathrm{i}}\hat{\sigma}_{\mathrm{y}}\Big)\,, \tag{3.20}$$

with the real valued vectors $\mathbf{d}_{\mathrm{r}}$ and $\mathbf{d}_{\mathrm{i}}$. To build up the equations of motion, we use Eqs. (1.33) and (3.16)[23] with the abbreviation $d_t\hat{\mathbf{r}} \equiv \dot{\hat{\mathbf{r}}}$

$$\hbar^2\ddot{\hat{\mathbf{r}}} = \frac{\hbar^2}{e}\Big(\mathbf{d}_{\mathrm{r}}\ddot{\hat{\sigma}}_{\mathrm{x}} - \mathbf{d}_{\mathrm{i}}\ddot{\hat{\sigma}}_{\mathrm{y}}\Big)$$

$$= \frac{\hbar}{e}\Big\{\mathbf{d}_{\mathrm{r}}\Big[-\hbar\omega_0\dot{\hat{\sigma}}_{\mathrm{y}} + 2(\mathbf{d}_{\mathrm{i}}\cdot\hat{\mathbf{E}})\dot{\hat{\sigma}}_{\mathrm{z}}\Big] - \mathbf{d}_{\mathrm{i}}\Big[\hbar\omega_0\dot{\hat{\sigma}}_{\mathrm{x}} + 2(\mathbf{d}_{\mathrm{r}}\cdot\hat{\mathbf{E}})\dot{\hat{\sigma}}_{\mathrm{z}}\Big] + 2\Big[\mathbf{d}_{\mathrm{r}}(\mathbf{d}_{\mathrm{i}}\cdot\dot{\hat{\mathbf{E}}}) - \mathbf{d}_{\mathrm{i}}(\mathbf{d}_{\mathrm{r}}\cdot\dot{\hat{\mathbf{E}}})\Big]\hat{\sigma}_{\mathrm{z}}\Big\}$$

$$= \frac{1}{e}\Big\{-(\hbar\omega_0)^2(\mathbf{d}_{\mathrm{r}}\hat{\sigma}_{\mathrm{x}} - \mathbf{d}_{\mathrm{i}}\hat{\sigma}_{\mathrm{y}}) - 2\hbar\omega_0\hat{\sigma}_{\mathrm{z}}\Big[\mathbf{d}_{\mathrm{r}}(\mathbf{d}_{\mathrm{r}}\cdot\hat{\mathbf{E}}) + \mathbf{d}_{\mathrm{i}}(\mathbf{d}_{\mathrm{i}}\cdot\hat{\mathbf{E}})\Big]$$

$$+ 2\Big[\mathbf{d}_{\mathrm{r}}(\mathbf{d}_{\mathrm{i}}\cdot\dot{\hat{\mathbf{E}}}) - \mathbf{d}_{\mathrm{i}}(\mathbf{d}_{\mathrm{r}}\cdot\dot{\hat{\mathbf{E}}})\Big]\Big[\hbar\hat{\sigma}_{\mathrm{z}} - 2(\mathbf{d}_{\mathrm{r}}\hat{\sigma}_{\mathrm{y}} + \mathbf{d}_{\mathrm{i}}\hat{\sigma}_{\mathrm{x}})\cdot\hat{\mathbf{E}}\Big]\Big\}\,.$$

By reintroducing the displacement vector and taking the expectation value of the equation of motion (using assumption Eq. (3.17)), we find

$$\ddot{\mathbf{r}}(t) + \omega_0^2\mathbf{r}(t) = \frac{-2\omega_0 s_z}{e\hbar}\Big[\mathbf{d}_{\mathrm{r}}(\mathbf{d}_{\mathrm{r}}\cdot\mathbf{E}) + \mathbf{d}_{\mathrm{i}}(\mathbf{d}_{\mathrm{i}}\cdot\mathbf{E})\Big]$$

$$+ \frac{2\Big[\mathbf{d}_{\mathrm{r}}(\mathbf{d}_{\mathrm{i}}\cdot\dot{\mathbf{E}}) - \mathbf{d}_{\mathrm{i}}(\mathbf{d}_{\mathrm{r}}\cdot\dot{\mathbf{E}})\Big]}{e\hbar^2}\Big[\hbar s_z - 2(\mathbf{d}_{\mathrm{r}}s_{\mathrm{y}} + \mathbf{d}_{\mathrm{i}}s_{\mathrm{x}})\cdot\mathbf{E}\Big]\,. \tag{3.22}$$

In order to recover from Eq. (3.22) the classically known driven, harmonic oscillator, the following conditions have to be fulfilled (the first of those already discussed):

1. The decay of the quantum coherence has to be on a time scale much faster than the time scale at which the two level system evolves.

---

[23]Equations (3.16) are formulated in terms of the operators $\hat{\sigma}_{\pm}$ and $\hat{\sigma}_{\mathrm{z}}$. Rewriting the dipole operator in terms of $\hat{\sigma}_i$ as done in Eq. (3.20), we can then formulate equivalent equations of motions for the $\hat{\sigma}_i$ splitting up real and imaginary parts:

$$\hbar d_t\hat{\sigma}_{\mathrm{x}}(t) = -\hbar\omega_0\hat{\sigma}_{\mathrm{y}}(t) + 2\mathbf{d}_{\mathrm{i}}\cdot\hat{\mathbf{E}}(\mathbf{r}_0,t)\hat{\sigma}_{\mathrm{z}}\,, \tag{3.21a}$$

$$\hbar d_t\hat{\sigma}_{\mathrm{y}}(t) = \hbar\omega_0\hat{\sigma}_{\mathrm{x}}(t) + 2\mathbf{d}_{\mathrm{r}}\cdot\hat{\mathbf{E}}(\mathbf{r}_0,t)\hat{\sigma}_{\mathrm{z}}\,, \tag{3.21b}$$

$$\hbar d_t\hat{\sigma}_{\mathrm{z}}(t) = -2\Big[\mathbf{d}_{\mathrm{r}}\hat{\sigma}_{\mathrm{y}} + \mathbf{d}_{\mathrm{i}}\hat{\sigma}_{\mathrm{x}}\Big]\hat{\mathbf{E}}(\mathbf{r}_0,t)\,. \tag{3.21c}$$

2. The excitation of the two-level atom has to be rather small ($s_z \approx -1$) since only in this limit, the transition described by Eq. (3.22) is not governed by saturation effects. They stem from the fact that in the quantum- mechanical limit a fermionic state cannot be occupied twice.

3. In order to be able to describe the two-level atom as a classical dipole whose dipole moment is additionally fixed in orientation, the dipole transition has to be a one coupling to linear polarized light (mathematically the follows from the discussion of the selection rules in appendix C.1: $\Delta m = 0 \rightarrow \mathbf{d}_i = 0$). The spatial rotation of the emitter in Eq. (3.22) is in the case of circularly polarized light coupling induced by the non-vanishing complex phase of the dipole moment.

Fixing the global phase and with the three conditions mentioned above, we then obtain as the dipole unit vector $\mathbf{e}_d = \mathbf{d}_r/|\mathbf{d}_r|$. With the definition of the "mass" of the harmonic oscillator $\frac{\hbar}{2\omega_0|\mathbf{r}_{max}|^2} \equiv m$ (with $\mathbf{r}_{max} = \frac{\mathbf{d}_r}{e}$), we can write in conclusion

$$\ddot{\mathbf{r}}(t) + \omega_0^2 \mathbf{r}(t) = \frac{e^2}{m}(\mathbf{e}_d \cdot \mathbf{E}(\mathbf{r}, t))\mathbf{e}_d \,. \tag{3.23}$$

3.2.4 Decay rate of an electric dipole

Since the spontaneous emission of a photon from an excited atom is a pure quantum effect, we have to consider the total system including the emitter, the electromagnetic fields and the coupling between the two from a quantum mechanical point of view. After having discussed the emitter already in the last section as a quantum mechanical object, in this section we need to make use of a quantized electromagnetic field and for this reason introduce the explicit shape of the electric field operator $\hat{\mathbf{E}}$ (see Eq. (3.1)). In second quantization (cf., e.g., Ref. [93]) and in the Heisenberg picture, it reads

$$\hat{\mathbf{E}}(\mathbf{r}, t) = \sum_{\mathbf{q}} \frac{1}{\sqrt{2\mathcal{V}\varepsilon_0 \hbar \omega_{\mathbf{q}}}} \Big[\boldsymbol{\mathcal{E}}_{\mathbf{q}}^*(\mathbf{r})\hat{a}_{\mathbf{q}}^\dagger(t) + \boldsymbol{\mathcal{E}}_{\mathbf{q}}(\mathbf{r})\hat{a}_{\mathbf{q}}(t) \Big] \,, \tag{3.24}$$

where we sum over all possible modes $\mathbf{q}$ of the electric field with the electromagnetic mode volume $\mathcal{V}$ (cf. Ref. [104]). With the Hamiltonian of the electromagnetic field $\hat{\mathcal{H}}_{EM} = \sum_{\mathbf{q}} \hbar\omega_{\mathbf{q}}\hat{a}_{\mathbf{q}}^\dagger\hat{a}_{\mathbf{q}}$ (for a derivation see, e.g., Ref. [105]) and the Hamiltonian of the atom Eq. (3.15), the total Hamiltonian reads in rotating-wave approximation (see Ref. [93])

$$\hat{\mathcal{H}} = \frac{\Omega}{2}\hat{\sigma}_z + \sum_{\mathbf{q}} \hbar\omega_{\mathbf{q}}\hat{a}_{\mathbf{q}}^\dagger\hat{a}_{\mathbf{q}} - \sum_{\mathbf{q}} \hbar \Big[g_{\mathbf{q}}^* \hat{a}_{\mathbf{q}}\hat{\sigma}_+ + g_{\mathbf{q}}\hat{a}_{\mathbf{q}}^\dagger\hat{\sigma}_- \Big] \,, \tag{3.25}$$

with the atom-field coupling strength $g_{\mathbf{q}} = \omega_0[\langle\downarrow|\hat{\mathbf{d}}|\uparrow\rangle \cdot \boldsymbol{\mathcal{E}}_{\mathbf{q}}^*]/\sqrt{2\varepsilon_0\hbar\mathcal{V}\omega_{\mathbf{q}}}$.

Assuming an initially excited atom, any state can be expanded as

$$|\psi(t)\rangle = C_0^e(t)e^{-i\omega_0 t}|0,\uparrow\rangle + \sum_{\mathbf{q}} C_{1\mathbf{q}}^g(t)|1_{\mathbf{k}},\downarrow\rangle \,, \qquad \text{with} \qquad |\psi(0)\rangle = |0,\uparrow\rangle \,, \tag{3.26}$$

where in state $|0,\uparrow\rangle$ the two-level system is excited while no photons exist in free space and in state $|1_{\mathbf{k}},\downarrow\rangle$ the two-level system is in its ground state and a single-photon Fock

3 Theoretical description of quantum-mechanical and classical emitters

state in mode $\mathbf{q}$ is excited. With the Schrödinger equation (1.32) the coupled equations of motion for the amplitudes are

$$\dot{C}_{1\mathbf{q}}^g(t) = \mathrm{i}g_{\mathbf{q}}\mathrm{e}^{-\mathrm{i}(\omega_{\mathbf{q}}-\omega_0)t}C_0^e(t)\,,$$

$$\dot{C}_0^e(t) = \mathrm{i}\sum_{\mathbf{q}}g_{\mathbf{q}}^*\mathrm{e}^{-\mathrm{i}(\omega_{\mathbf{q}}-\omega_0)t}C_{1\mathbf{q}}^g(t)\,.$$

For a large volume $V\to\infty$ resulting in $\sum_{\mathbf{q}}\to\mathcal{V}\int\mathrm{d}^3q/(2\pi)^3$, we arrive at (cf. Ref. [28, 104])

$$
\begin{aligned}
\dot{C}_0^e(t) &= -\frac{\omega_0^2|\mathbf{d}|^2}{2\varepsilon_0\hbar(2\pi)^3}\int_0^t\mathrm{d}t'\int\mathrm{d}^3q\frac{\mathrm{e}^{-\mathrm{i}(\omega_{\mathbf{q}}-\omega_0)(t-t')}}{\omega_{\mathbf{q}}}\frac{|\mathbf{d}\cdot\boldsymbol{\mathcal{E}}_{\mathbf{q}}(\mathbf{r})|^2}{|\mathbf{d}|^2}C_0^e(t')\,,\\
&= -\frac{\omega_0^2|\mathbf{d}|^2}{2\varepsilon_0\hbar(2\pi)^3}\int_0^t\mathrm{d}t'\int_0^\infty\mathrm{d}\omega\frac{\mathrm{e}^{-\mathrm{i}(\omega-\omega_0)(t-t')}}{\omega}C_0^e(t')\int\mathrm{d}^3q\frac{|\mathbf{d}\cdot\boldsymbol{\mathcal{E}}_{\mathbf{q}}(\mathbf{r})|^2}{|\mathbf{d}|^2}\delta(\omega-\omega_{\mathbf{q}})\,,\\
&\equiv -\frac{\omega_0^2|\mathbf{d}|^2}{2\varepsilon_0\hbar(2\pi)^3}\int_0^t\mathrm{d}t'\int_0^\infty\mathrm{d}\omega\frac{\mathrm{e}^{-\mathrm{i}(\omega-\omega_0)(t-t')}}{\omega}C_0^e(t')\mathcal{N}_p(\mathbf{e_d},\mathbf{r}_0,\omega)\,,
\end{aligned}
$$

$$(3.27)$$

where as before $\mathbf{d}=\langle\uparrow|\hat{\mathbf{d}}|\downarrow\rangle$ and we consider due to an appropriate choice of the energy groundstate only positive frequency contributions. In the last line the photonic projected local density of states equals

$$\mathcal{N}_p(\mathbf{e_d},\mathbf{r},\omega) = \int\mathrm{d}^3q\,|\mathbf{e}_d\cdot\boldsymbol{\mathcal{E}}_{\mathbf{q}}(\mathbf{r})|^2\delta(\omega-\omega_{\mathbf{q}})\,, \tag{3.28}$$

that describes the photonic mode density at position $\mathbf{r}$ and of polarization $\mathbf{e_d}=\mathbf{d}/|\mathbf{d}|$. By averaging over all possible dipole orientations one can define the photonic local density of states (see Ref. [104])

$$\mathcal{N}_l(\mathbf{r},\omega) = \frac{3}{4\pi}\langle\mathcal{N}_p(\mathbf{e_d},\mathbf{r},\omega)\rangle_\theta = \int\mathrm{d}^3q\,|\boldsymbol{\mathcal{E}}_{\mathbf{q}}(\mathbf{r})|^2\delta(\omega-\omega_{\mathbf{q}})\,, \tag{3.29}$$

while the total photonic density of states is defined as a sum over all available modes

$$\mathcal{N}(\omega) = \int\mathrm{d}^3q\,\delta(\omega-\omega_{\mathbf{q}})\,. \tag{3.30}$$

To obtain the vacuum decay rate γ_0, we apply the *Weisskopf-Wigner approximation* (see Refs. [28, 106]) where two assumptions come into play:

1. Field modes exhibit a large spectral width with respect to the linewidth of the dipole transition,

2. $C_e^0(t)$ changes slowly in time compared to the oscillation at frequency $\omega-\omega_0$, $\forall\omega\not\cong\omega_0$.

Then, the factors $\mathrm{e}^{-\mathrm{i}(\omega-\omega_0)(t-t')}$ are highly oscillatory for all contributions but $t' \approx t$ and thus it averages the integral to zero for all contributions but $\omega \approx \omega_0$:

$$
\begin{aligned}
\dot{C}_0^e(t) &\approx -\frac{\omega_0^2|\mathbf{d}|^2}{2\varepsilon_0\hbar(2\pi)^3}C_0^e(t)\int\limits_0^\infty \mathrm{d}\omega \int\limits_0^\infty \mathrm{d}t' \frac{\mathrm{e}^{-\mathrm{i}(\omega-\omega_0)(t-t')}}{\omega}\mathcal{N}_p(\mathbf{e_d},\mathbf{r}_0,\omega) \\
&= -\frac{\omega_0^2|\mathbf{d}|^2}{2\varepsilon_0\hbar(2\pi)^3}C_0^e(t)\int\limits_0^\infty \mathrm{d}\omega \frac{\mathcal{N}_p(\mathbf{e_d},\mathbf{r},\omega)}{\omega}\left[\pi\delta(\omega-\omega_0)+\mathrm{i}\mathcal{P}\left(\frac{1}{\omega-\omega}\right)\right] \\
&= -\left(\frac{\gamma_\mathbf{d}}{2}+\mathrm{i}\Delta\omega_\mathbf{d}\right)C_0^e(t)\,.
\end{aligned}
\tag{3.31}
$$

Above, we make use of Sokhotsky formula (see Ref. [107])

$$
\lim_{\eta\to 0^+}\frac{1}{x\pm\mathrm{i}\eta}=\mathcal{P}\frac{1}{x}\mp\mathrm{i}\pi\delta(x)\,,
\tag{3.32}
$$

where Cauchy's principal value $\mathcal{P}(x)$ is defined in Eq. (1.95). Additionally, we introduce the causality creating factor η that ensures that the events happening at one time only affect other events at later times. With Eq. (3.31), we then find the decay rate of an emitter with orientation $\mathbf{e_d}$

$$
\gamma_\mathbf{d}=\frac{\omega_0|\mathbf{d}|^2}{8\pi^2\varepsilon_0\hbar}\mathcal{N}_p(\mathbf{e}_d,\mathbf{r},\omega_0)\,,
\tag{3.33}
$$

the averaged decay rate

$$
\gamma=\langle\gamma_\mathbf{d}\rangle=\frac{\omega_0|\mathbf{d}|^2}{6\pi\varepsilon_0\hbar}\mathcal{N}_l(\mathbf{r},\omega)\,,
\tag{3.34}
$$

and the Lamb shift

$$
\Delta\omega_\mathbf{d}=\frac{\omega_0^2|\mathbf{d}|^2}{2\varepsilon_0\hbar(2\pi)^3}\mathcal{P}\int\limits_0^\infty \mathrm{d}\omega\,\frac{\mathcal{N}_p(\mathbf{e_d},\mathbf{r},\omega)}{\omega(\omega-\omega_0)}\,.
\tag{3.35}
$$

Calculating the decay rate from the Green's function

To explicitly calculate the photonic local density of states, we turn back to Eq. (1.14a) and make use of the frequency dependent dyadic Green's function $\underline{\mathcal{G}}(\mathbf{r},\mathbf{r}';\omega)$ to the electric field $\mathbf{E}(\mathbf{r},\omega)$ (see Eq. (3.8)). For a point-like dipole placed in a medium of permittivity ε_r, the Green's tensor then solves the equation

$$
\Delta\underline{\mathcal{G}}(\mathbf{r},\mathbf{r}';\omega)+\varepsilon_r\frac{\omega^2}{c^2}\underline{\mathcal{G}}(\mathbf{r},\mathbf{r}';\omega)=\mathbb{1}\delta(\mathbf{r}-\mathbf{r}')\,,
\tag{3.36}
$$

choosing the Ansatz

$$
\underline{\mathcal{G}}(\mathbf{r},\mathbf{r}';\omega)=\frac{1}{(2\pi)^3}\int \mathrm{d}^3q\, a_\mathbf{q}(\mathbf{r}',\omega)\boldsymbol{\mathcal{E}}_\mathbf{q}(\mathbf{r},\omega_\mathbf{q})\,,
\tag{3.37}
$$

3 Theoretical description of quantum-mechanical and classical emitters

where due to the choice in Eq. (3.24), in a closed space $\mathcal{V}$ the mode amplitudes $\boldsymbol{\mathcal{E}}_{\mathbf{q}}$ are orthogonal to each other in a non-dissipative medium. Inserting the expansion in Eq. (3.36), multiplying both sides of the equation with $\boldsymbol{\mathcal{E}}_{\mathbf{q}}^*$ and using the orthogonality, we find

$$\underline{\mathcal{G}}(\mathbf{r}, \mathbf{r}'; \omega) = \int \mathrm{d}^3 q \, \frac{c^2}{\varepsilon_r} \frac{\boldsymbol{\mathcal{E}}_{\mathbf{q}}^*(\mathbf{r}', \omega_{\mathbf{q}}) \boldsymbol{\mathcal{E}}_{\mathbf{q}}(\mathbf{r}, \omega_{\mathbf{q}})}{\omega_{\mathbf{q}}^2 - \omega^2} \, . \tag{3.38}$$

Using Eq. (3.32) we obtain

$$\lim_{\eta \to 0} \left\{ \mathrm{Im} \left[\int \mathrm{d}^3 q \, \frac{f(\mathbf{r}, \mathbf{r}', \omega_{\mathbf{q}})}{\omega_{\mathbf{q}}^2 - (\omega + \mathrm{i}\eta)^2} \right] \right\} = \int \mathrm{d}^3 q \, \frac{\pi}{2\omega_{\mathbf{q}}} [\delta(\omega - \omega_{\mathbf{q}}) - \delta(\omega + \omega_{\mathbf{q}})] f(\mathbf{r}, \mathbf{r}', \omega_{\mathbf{q}}) \, ,$$

where the factor η is introduced to guarantee causality as it is a necessary physical requirement for a response function, we can rewrite the decay rate Eq. (3.33) as

$$\gamma_{\mathbf{d}} = \frac{2\omega_0^2 |\mathbf{d}|^2}{\varepsilon_0 \hbar c^2} \left\{ \mathbf{e}_{\mathbf{d}} \cdot \mathrm{Im} \left[\underline{\mathcal{G}}(\mathbf{r}, \mathbf{r}; \omega_0) \right] \cdot \mathbf{e}_{\mathbf{d}} \right\} \, . \tag{3.39}$$

With this, we can then calculate the vacuum decay rate (with the vacuum dyadic Green's function $\mathbf{e}_{\mathbf{d}} \cdot \mathrm{Im} \left[\underline{\mathcal{G}}_0(\mathbf{r}, \mathbf{r}; \omega_0) \right] \cdot \mathbf{e}_{\mathbf{d}} = \omega_0 / 6\pi c$, e.g., Ref. [28], p. 241)

$$\gamma_0 = \frac{\omega_0^3 |\mathbf{d}|^2}{3\pi \varepsilon_0 \hbar c^3} \, . \tag{3.40}$$

Additionally, by definition of the dyadic Green's function (assuming all fields are caused by the electric dipole moment and since for a point-like dipole $\mathbf{j}(\mathbf{r}, \omega)$ given by Eq. (3.11)), the classic electromagnetic fields relate to the dyadic Green's function as

$$\begin{aligned}
\mathbf{E}(\mathbf{r}, \omega) &= \langle \hat{\mathbf{E}}(\mathbf{r}, t) \rangle = \omega^2 \mu_0 \underline{\mathcal{G}}(\mathbf{r}, \mathbf{r}_0; \omega) \cdot \mathbf{d} \, , \\
\mathbf{H}(\mathbf{r}, \omega) &= \langle \hat{\mathbf{H}}(\mathbf{r}, t) \rangle = -\mathrm{i}\omega [\boldsymbol{\nabla} \times \underline{\mathcal{G}}(\mathbf{r}, \mathbf{r}_0; \omega)] \cdot \mathbf{d} \, ,
\end{aligned} \tag{3.41}$$

such that the decay rate of a dipole of orientation $\mathbf{e}_d$ and at position $\mathbf{r}_0$ is given by

$$\gamma_{\mathbf{d}} = \frac{2}{\hbar} \mathrm{Im} \left[\mathbf{d}^* \cdot \mathbf{E}(\mathbf{r}_0, \omega_0) \right] = \gamma_0 \left(1 + \frac{6\pi \varepsilon_0 c^3}{|\mathbf{d}|^2 \omega_0^3} \mathrm{Im} \left[\mathbf{d}^* \cdot \mathbf{E}_{\mathrm{scat}}(\mathbf{r}_0, \omega_0) \right] \right) \, . \tag{3.42}$$

The last equality is obtained by splitting the electric field emitted by the dipole into $\mathbf{E}(\mathbf{r}_0, \omega_0) = \mathbf{E}_0(\mathbf{r}_0, \omega_0) + \mathbf{E}_{\mathrm{scat}}(\mathbf{r}_0, \omega_0)$ where the field $\mathbf{E}_0$ corresponds to the field emitted by the dipole in vacuum and via its self-interaction causes the vacuum decay rate γ_0 while the field $\mathbf{E}_{\mathrm{scat}}$ is the field back scattered from the surrounding photonic environment different from vacuum.

Relating the quantum-mechanical and classical decay rate

Following the classical equation (1.16) and assuming the emitter embedded in a harmonic, linear, local and non-dispersive material, the Poynting theorem Eq. (1.21) becomes

$$\begin{aligned}
P(\omega) \equiv \oint_{\mathrm{d}V} \mathrm{d}^2 r \langle \mathbf{S} \rangle \cdot \mathbf{n} &= -\frac{1}{2} \int_V \mathrm{d}^3 r \, \mathrm{Re} \left[\mathbf{j}^*(\mathbf{r}, \omega) \cdot \boldsymbol{\mathcal{E}}(\mathbf{r}, \omega) \right] \\
&= \frac{\omega}{2} \mathrm{Im} \left[\mathbf{p}^*(\mathbf{r}, \omega) \cdot \boldsymbol{\mathcal{E}}(\mathbf{r}, \omega) \right] \, ,
\end{aligned} \tag{3.43}$$

where here, as in section 3.2.1, $\mathbf{p}$ describes the classical dipole moment of a point emitter. Using Eq. (3.41) in the classical limit, we arrive at

$$P(\omega) = \frac{\omega^3 |\mathbf{p}|^2}{2c^2 \varepsilon_0 \varepsilon_r} \left\{ \mathbf{e_d} \cdot \text{Im} \left[\underline{\mathcal{G}}(\mathbf{r}, \mathbf{r}; \omega_0) \right] \cdot \mathbf{e_d} \right\} . \tag{3.44}$$

Comparing Eq. (3.44) to Eq. (3.39), one actually realizes that this corresponds to an equivalence of the decay process. This is due to the fact that the decay of a two-level system can in general be split into a radiative and a non-radiative contribution. In the case of a two-level system, the radiative contribution here describes the energy loss of the system due to far-field emission of the electromagnetic radiation. On the other hand in the case of non-radiative losses of a two-level system, optical modes such as the surface plasmon polaritons discussed in section 1.3.1 and other collective excitations lead to further energy losses. There the energy is eventually dissipated into heat. At this point, it is important to mention that in the case of multilevel systems, additional non-radiative energy transitions within the atom contribute to the total loss rate.

The connection of the radiative decay and the flux radiated into all directions eventually leads to the possibility to obtain a measure on the spontaneous emission by the use of classical computations

$$\frac{P(\omega)}{P_0(\omega)} = \frac{\gamma}{\gamma_0} , \tag{3.45}$$

where $P_0(\omega)$ describes the power radiated from an emitter in vacuum analogously to the decay rate of an emitter in vacuum γ_0. Here, the analogy requires the equivalence of the classical dipole moment and the QM matrix element $\mathbf{p} \approx \mathbf{d}$ which is – as discussed before – only true in the limit of low excitation.

3.2.5 Local field correction

In the case of an emitter embedded in a lossless, infinite dielectric, we have to take into account a local-field correction factor ξ to the dipole decay rate to calculate the spontaneous emission decay rate from the vacuum decay rate γ_0

$$\gamma_{\text{SE}} = \sqrt{\varepsilon_r}\, \xi\, \gamma_0 , \tag{3.46}$$

as discussed in Ref. [108]. This is caused by the fact that in reality the atom is not "only" situated in a continuous dielectric as described within macroscopic electrodynamics (corresponding to a dressing of $\gamma_{\text{SE}} = \sqrt{\varepsilon_r}\, \gamma_0$, cf. Eq. (3.39)) but actually is in vacuum and surrounded by the atoms that the dielectric consists of. In the macroscopic electrodynamic picture, this corresponds to an effective cavity for the emitter. It has actually been a question in research how to describe those cavities finding experimental proof for two different models: the virtual cavity (VC) and the real cavity (RC) local-field correction factor

$$\xi_{\text{VC}} = \left(\frac{\varepsilon_r + 2}{3} \right)^2 , \tag{3.47a}$$

$$\xi_{\text{RC}} = \left(\frac{3\varepsilon_r}{2\varepsilon_r + 1} \right)^2 , \tag{3.47b}$$
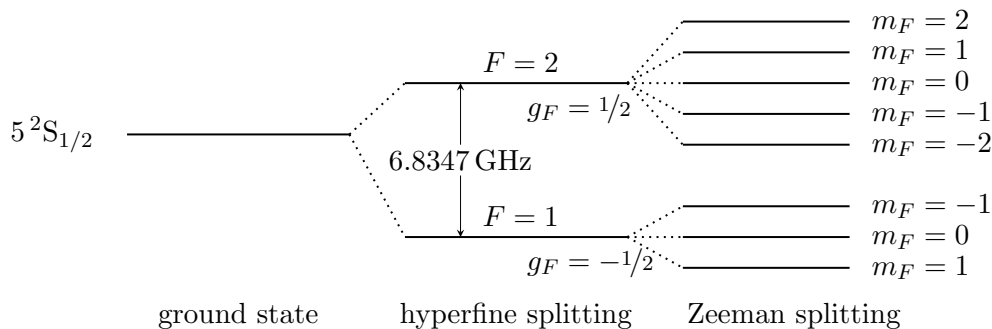
Figure 3.2: Above, we present the level scheme of a $^{87}_{37}Rb$ atom (adapted from Ref. [114]). Rubidium as an alkali metal possesses one electron in the $5\,^2S_{1/2}$ orbital. Its degenerate ground state is split into two distinct states by the coupling of the nucleus momentum to internally created electric and magnetic field. When applying an external magnetic field, the still degenerate states split up into $2F + 1$ states that are eigenstates to the projection of the total momentum operator onto the direction of the external field (*space quantization*). The Zeeman transition is determined by the external magnetic field and reads for all transitions with $\Delta F = 0$ and $\Delta m_F = \pm 1$, $\Delta \varepsilon = 0.7\,\mathrm{MHz/G}$ (adapted from Refs. [114–116]).

derived in Ref. [109] and Ref. [110], respectively. These correction factors have been determined for non-dissipative materials which is also the case considered in this thesis. For the case of dissipative materials, see Refs. [108, 111]. In Ref. [112], the authors develop a microscopic theory unifying both local-field factors as limiting cases and find as a practical rule that ξ_{VC} is the appropriate local-field correction when an emitter acts as an interstitial ion. This is the case, e.g., when the emitter is of the same species as the atom or molecule it replaces. However, in the case in which the emitter expels the dielectric material and thus creates a true real cavity (also known as substitution) the real cavity description is appropriate.

These rules were finally validated by the authors of Ref. [113] who show that some experiments contradicting the practical rules from Ref. [112] were actually misinterpreted. Thus, whenever choosing a local-field correction factor, one has to take into account the specific material the emitter is embedded in and whether or not a real cavity is created by the emitter. In this work we will only use the local-field correction factor ξ not specifying the specific expression. This is appropriate since for non-dispersive materials the local-field correction is a simple and frequency independent prefactor scaling the decay rate for all parameters uniformly.

3.3 The magnetic dipole

As discussed in Eq. (3.6b), any atom possessing a total angular momentum $\hat{F}$ with quantum number m_F, exhibits a magnetic dipole moment to which the electromagnetic field can couple via Eq. (3.2). A transition between the states take place if allowed due to symmetry and algebraic arguments (for a detailed discussion of the magnetic *selection rules* see Appendix C.2).

An atom typically used in cold atom experiments (see, e.g., Refs. [117, 118]) is the rubidium allotrope $^{87}_{37}$Rb. The atom's groundstate is degenerate. By taking the coupling between the internal electric and magnetic fields and the nucleus' spin into account, this degeneracy can be partially lifted (see Fig. 3.2). When considering that the nucleus itself exhibits a magnetic moment $\boldsymbol{\mu}_I$ via its spin and the motions of the atom's electrons lead to a magnetic field, the internal interaction Hamiltonian reads (see Ref. [119], p. 663)

$$\hat{\mathcal{H}}_{\mathrm{HFS}} = -\hat{\boldsymbol{\mu}}_I \cdot \hat{\mathbf{B}}_{e^-}(\mathbf{r}_0) = A_J \hat{\mathbf{I}} \cdot \hat{\mathbf{J}} \, , \tag{3.48}$$

where the factor A_J is the hyperfine structure constant. Additionally, smaller contributions to the lifting of the degeneracy arise also from higher order electric and magnetic multipole interactions. Here, the multipole contribution is due to the finite size of the nuclear charge distribution. These couplings lead to the hyperfine splitting (see Fig. 3.2) and are independent of an additional external magnetic flux density.

When additionally applying an external magnetic field which is done when, e.g., trapping the atom in a magnetic trap, the last degeneracy with respect to its *quantization axis* is lifted by the Zeeman interaction. The external magnetic field couples to the total electron angular momentum $\hat{\mathbf{J}}$ and the nucleus' spin $\hat{\mathbf{I}}$ such that the Zeeman interaction Hamiltonian here reads

$$\hat{\mathcal{H}}_{\mathrm{Zeeman}} = -g_J \mu_B \hat{\mathbf{J}} \cdot \mathbf{B}(\mathbf{r}_0, t) - g_I \mu_n \hat{\mathbf{I}} \cdot \mathbf{B}(\mathbf{r}_0, t) \, , \tag{3.49}$$

with the spin g-factor $g_I/|g_F| \ll 1$ and the total angular momentum g-factor that is also known as the Landé factor. The resulting *Zeeman splitting* can be tuned via the strength of the external magnetic field and is also shown in Fig. 3.2.

Depending on the strength of the magnetic flux density $\mathbf{B}$, different set of quantum numbers are considered as good quantum numbers for the description of the physical problem. This is due to the case that sufficiently strong magnetic fields, nuclear spin $\hat{\mathbf{I}}$ and the electron's total angular momentum $\hat{\mathbf{J}}$ decouple. However, for the case of weak magnetic fields, $g_J \mu_B B \ll A_J$, where the approximation holds for $B < 1\,\mathrm{mT}$, the nuclear spin $\hat{\mathbf{I}}$ and the electron's total angular momentum $\hat{\mathbf{J}}$ remain coupled and $|F, m_F\rangle$ are good quantum numbers. In this thesis, we exclusively consider magnetic fields fulfilling this condition.

The strong **I-J** coupling leads to the fact that the total angular momentum $\hat{\mathbf{F}}$ and the projection onto the magnetic field $m_F = m_i + m_j$ describe the system fully. Then, with Eq. (3.2), an external magnetic field only leads to an additional Hamiltonian term

$$\hat{\mathcal{H}}_{\mathrm{interaction}} = -\hat{\boldsymbol{\mu}} \cdot \hat{\mathbf{B}}(\mathbf{r}_0, t) = -g_F \mu_B \hat{\mathbf{F}} \cdot \mathbf{B}(\mathbf{r}_0, t) = -g_F \mu_B m_F |\mathbf{B}(\mathbf{r}_0, t)| \, , \tag{3.50}$$

with the g-factor (see Ref. [119], p. 670)

$$g_F = g_J \frac{F(F+1) + J(J+1) - I(I+1)}{2F(F+1)} - \frac{g_I \mu_n}{\mu_B} \frac{F(F+1) + I(I+1) - J(J+1)}{2F(F+1)} \, ,$$

with the nuclear magneton μ_n with $1836\mu_B = \mu_n$. Thus, the second term is suppressed and depending on the relative orientation of electron and total spin, the nuclear g-factor can be either positive or negative.
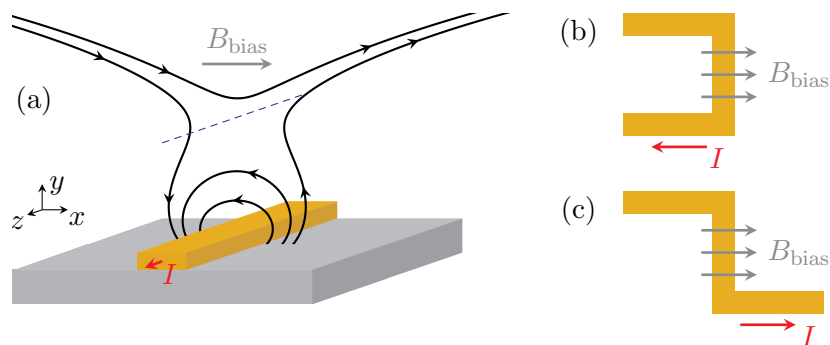
Figure 3.3: The Figure displays three wire traps. In panel (a) the magnetic field lines resulting from an infinite wire overlaid with a bias field **B**$_\text{bias}$. When a current of I flows through the gold wire, a magnetic flux density minimum at the blue dashed line parallel to the wire is created. For finite wire trap realizations (see panel (b,c)) the easiest realizations can be divided into two different kinds. The depiction in panel (b) represents a so-called *U trap* exhibiting a quadrupole potential while the depiction in panel (c) represents a *Z trap* exhibiting a harmonic potential. The potential created by the latter is equivalent to the potential of a *Ioffe trap* consisting of large-scale magnetic coils and commonly used for the trapping of cold atoms in 3D (see Ref. [120]). Depiction adapted with permission from J. Fortágh and C. Zimmermann, "Magnetic microtraps for ultracold atoms", Rev. Mod. Phys. **79,** 235 (2007), doi:10.1103/RevModPhys.79.235. © 2007 by the American Physical Society. The magnetic flux density lines are given by Eq. (3.52).

The Zeeman term additionally leads to the precession of the total angular momentum **F** around the field direction with frequency

$$\omega_\text{L} = \frac{g_F \mu_B}{\hbar} B \, , \tag{3.51}$$

and can thus not lead to a transition between two states with opposite orientation of the magnetic moment.

3.3.1 Trapping of an atom cloud

An atom with a magnetic dipole moment can be trapped via a magnetic trap described by the trapping Hamiltonian Eq. (3.50). Depending on the state an atom (cloud) is prepared in, one can distinguish between *low-field-seeking states* and *high-field-seeking states* where the prior can be trapped at a minimum of the magnetic flux density while the latter can be trapped at a maximum of the magnetic flux density. A minimum in the eigenenergy of the trapping Hamiltonian Eq. (3.50) occurs at the position of a magnetic flux minimum for states with $g_F m_F > 0$, while they occur at a maximum of the magnetic flux density for states with $g_F m_F < 0$.

Since according to the *Earnshaw theorem* (see Ref. [122]) local maxima and minima of the magnetic flux density are forbidden in free space, magnetic traps have to exhibit magnetic flux density minima of the modulus and the atoms are prepared in a low-field-seeking state in order to be trapped. Thus, for the case of rubidium (see Fig. 3.2),

the trapping state with the strongest spatial confinement is the state $|F, m_F\rangle = |2, 2\rangle$ (see Ref. [94]). This is due to the fact that the electron and nuclear spin are oriented parallel to each other for $F = 2$. Two more trapping states are $|F, m_F\rangle = |2, 1\rangle$ and $|F, m_F\rangle = |1, -1\rangle$ since for $F = 1$ in ^{87}Rb, $g_F < 0$ (cf. Ref. [123]). In the very center of the trap, the atom can be prepared in any of these states to not leave magnetic trap.

Magnetic traps can have different forms. One form that is used on atom chips are metallic wires, specifically gold wires. A current I flowing through this (infinite) wire (oriented in z direction) then leads to a magnetic flux density $\mathbf{B}(\mathbf{r}, t)$ (see Ref. [121] and Fig. 3.3(a))

$$\mathbf{B} = B_{\text{bias}}\mathbf{e}_x + \frac{I\mu_0}{2\pi(x^2 + y^2)}\mathbf{e}_z \times \mathbf{r} \, . \tag{3.52}$$

The modulus of the magnetic flux density exhibits a minimum at the line of vanishing field given by

$$x = 0 \qquad \text{and} \qquad y = \frac{\mu_0 I}{2\pi B_{\text{bias}}} \, , \tag{3.53}$$

and displayed as the blue dashed line in Fig. 3.3(a). Alongside with this, in black lines the solutions to Eq. (3.52) are plotted. For a finite length wire, two possible end conditions are presented in panels 3.3(b,c). For further details on the difference in potential between the two configurations see the caption and section 3.3.2.

3.3.2 Loss channels in an atom trap

For an atom in an atom trap different loss channels exist. Some of those are governed by the dielectric and metallic environment others rather by the specific shape of the trap's potential.

Spin flips

In general, losses of atoms occur in a trap when an atom changes its state from a *low-field seeker* to a *high-field seeker*. This happens, when the magnetic moment $\hat{\boldsymbol{\mu}}$ changes sign when undergoing a transition from the state it is originally prepared in $|i\rangle$ into a state $|f\rangle$ with quantum number m_F of opposite sign.

Since all the magnetic trap states ($|1, -1\rangle$, $|2, 1\rangle$ and $|2, 2\rangle$) are not the electronic ground-state of the rubidium atom (cf. Fig. 3.2), flips of the total angular momentum can occur. Since it is appropriate to consider the cold atom in its groundstate (cf. Ref. [124]), $l = 0$, these flips are commonly referred to as *spin flips*. These are highly influenced by the projected local density of states (see in analogy Eq. (3.42)). When an atom is, e.g., trapped in the proximity of a gold wire the decay rate and with this the spin flip rate increases enormously (see Refs. [124, 125]).

In chapter 4, the influence of graphene onto the spin flip rate in dependence of distance from the graphene layer and transition frequency is thus discussed in great detail. There, we discuss that these loss processes can be wanted since they allow for studying the surrounding photonic environment at the transition frequency of the atoms and spatially resolved (see, e.g., Ref. [126]).

3 Theoretical description of quantum-mechanical and classical emitters

Majorana losses

Majorana losses (also known as Majorana spin flips) are losses of the atom from the trap near a zero crossing of the magnetic field lines. For an atom in a slowly changing magnetic field, the magnetic moment of the atom precesses around the magnetic quantization axis with the Larmor frequency (see Eq. (3.51)). However, when the rate of change of the magnetic field is comparable to the Larmor frequency (see Ref. [121]) violating the approximation of an adiabatically changing magnetic field given by

$$\mathrm{d}_t \omega_{\mathrm{L}} \ll \omega_{\mathrm{L}}^2 \,, \tag{3.54}$$

the magnetic moment of the atom cannot adapt to the change to the magnetic quantization adiabatically any longer and a transition into a high-field seeker can occur.

Condition (3.54) is most likely violated close to zero crossings of the magnetic field. Thus, to prevent this effect, in experimental setups those trap realizations are preferred that do not exhibit a zero crossing. For finite wires, this is, e.g., a *Ioffe trap* as shown in Fig. 3.3(c). The *U trap* in Fig. 3.3(b) has a value of zero magnetic flux density at its minimum and is thus experimentally not favorable.

Losses through vibrational states, decoherence and heating

Atoms above a substrate or nanostructure cannot only be lost from their state by coupling to electrons in the material or by influence of the external magnetic field but also by internal and external loss mechanisms. These are, e.g., coupling to internal degrees of freedom, such as vibrational states, by decoherence of the atom and by heating.

Dispersion forces

Another important loss channel for atoms very close to surfaces are dispersion forces. In the very proximity of a surface ($< \lambda/2\pi$, where λ is the atomic transition wavelength) the van-der-Waals potential adds to the trap potential. In this case, an attractive potential $U \propto d^{-n}$ ($n = 3$ for an atom - halfspace system) is created by an unretarded response of the surface to virtual dipole fluctuations of the atom. At larger distances, retardation effects are important leading to an attractive potential $U \propto d^{-(n+1)}$ named the Casimir-Polder interaction (see Refs. [127–129]). In this limit, additional to the quantum and thermal fluctuations of the quantum dipole and the constituents of the substrate, quantum and thermal fluctuations of the electromagnetic field have to be taken into account.

The addition of this attractive force in consequence deforms the trapping potential such that it becomes anharmonic. The closer the atom is trapped to the surface, the shallower the potential well towards the surface becomes until at very small distances the well disappears such that the atom is attracted to the surface. Therefore, the dispersion forces limit the maximal allowed distance between atom and surface and have to be taken into account for a complete description of atoms in a magnetic trap. Although they are not a subject of discussion in this thesis, these effects have been considered for different atom trap setups (see Refs. [124, 130]) and for graphene (see Refs. [56, 66, 69, 79]) by other authors.

3.4 Conclusions

The theoretical description given in this chapter, is a simplified description of natural emitters studied in this work. The description of the different experimental realizations and the influence of the photonic local density of states onto the radiation dynamics of the emitters is at the core of this thesis. In chapter 4, we will discuss the dynamics of both electric and magnetic emitters near graphene monolayer. There, a special focus will be placed on the magnetic emitter due to its presence in atom chips and the small transition energy as compared to electric dipole transitions. This small transition energies allows for the probing of energy ranges and time scales different from the ones of optical transitions.

In chapter 6, we discuss exclusively different electric dipole transitions and focus on the dynamics of these close to plasmonic nanostructures discussing these emitters as possible probes for the plasmonic nanostructures.

Magnetic and electric emitters above graphene

"Equipped with his five senses, man explores the universe around him and calls the adventure science." [24]

Edwin Hubble

In this chapter, we discuss the impact of a graphene monolayer onto the lifetimes of magnetic and electric emitters. For this, we first present a study on the modes in a dielectric-graphene-dielectric slab system (published in and adapted from Ref. [W3]), second we discuss the influence of band gapped graphene on the decay rates of magnetic and electric emitters (published in and adapted from Ref. [W4]) and in the third part of this chapter, we compare the decay rates obtained in the limit of zero band gap to previously published results.

4.1 Introduction

In this chapter, we show how the high degree of control and accuracy available nowadays in quantum systems (such as cold atoms, SiV and NV centers in nanodiamonds) can be used for detailed investigations of graphene's optoelectronic properties (see Refs. [11, 12, 131, 132]). The focus on both electric and magnetic emitters in this chapter, stems from the fact that with the very different transition frequencies, magnetic emitters in the MHz and GHz and electric emitters in the THz regime, a combination of the two allows for the detection of physical effects over a broad range of frequencies. This allows to explore a wide range of physical properties on the nanoscale.

As shown in chapter 3, the determination of the decay rates allows for conclusions on the photonic local density of states and with this on the photonic properties of the environment. Here, we specifically focus on the physical properties of graphene.

Besides from the opportunity to detect optoelectronic properties of graphene, graphene as a material is also of high interest for its application in hybrid "condensed matter - atom" systems such as in atom traps. Atom traps with atoms trapped over a set of wires have been proven to be detectors for spatially varying magnetic flux density fluctuations imaging these with μm resolution (see Ref. [126]). The spatial accuracy is mainly limited

---

[24]E. Hubble, "The Exploration of Space", Harpers Magazine **158,** 732 (1929).

4 Magnetic and electric emitters above graphene

by the atom-probe distance that is determined by (i) the dispersive forces between atom and surface (see section 3.3.2), (ii) thermal fluctuations (see section 3.3.2) and (iii) the spin flip rate due to the modification of the photonic local density of states by the probe and the trap (see section 3.3.2). If this trap is constructed from gold wires, at most distances ($z_0 > 3\,\mu$m at $\omega_0/2\pi = 1.1$ MHz, see Ref. [125]) the third contribution is the only important contribution influencing the lifetimes of the atoms in the trap and does not allow for long-time trapping of the atomic cloud at distances below the metallic skin depth (see Refs. [121, 133]). Thus, new materials are necessary to overcome the current limitations and approach the probe and surface. This then leads to a better spatial resolution and additionally will allow to probe controlled and with high accuracy new physical regimes (i.e., Casimir Polder effects).

In this part of the thesis, we mainly focus on graphene exhibiting a band gap. This is due to two reasons. First, it has been shown in ab-initio studies (see Refs. [53, 54]) and experimental measurements (see Refs. [134]) that the deposition of graphene onto, e.g., hBN or silicon carbide (SiC) substrate can open such a band gap of $2m \approx 5 - 50$ meV and $2m \approx 260$ meV, respectively (compare Fig. 4.1). The underlying theory we present in section 2.1.3 where we show that the band gap is caused by lifting the symmetry between the two sublattices in graphene. In the case of hBN substrate, while the atoms of one sublattice couples to the boron atoms, the other atoms of the other sublattice couple to the nitrogen atoms. Here, it depends highly on the way in which graphene is positioned on the hBN substrate. In the case of a SiC substrate, a band gap was only measured in the case of annealing where the different lattice spacing causes the symmetry break between the two sublattices in graphene (cf. Ref. [135]).

Since the first measurements in 2007 by means of angle-resolved photoemission spectroscopy (ARPES)[25], to the best of our knowledge no additional experimental evidence of this band gap has been reported. However, in 2007 it has been argued that further independent measurements of this band gap are necessary in order to determine that no experimental misinterpretations have occurred (see Ref. [135]). In low temperature experiments and at low frequencies the influence of the band gap on the photonic local density of states is not negligible. Since in experiments, graphene is often deposited on a substrate, such a small band gap might occur and its experimental implications should not straight-forwardly be neglected. Thus, in this part of the thesis we discuss specifically the influence of this band gap on the waveguide modes in section 4.2. The influence of this band gap on the decay rates we then discuss in section 4.3 and compare it to the decay rate modifications of emitters above a graphene monolayer without a band gap in section 4.4.

Additionally to the opening of a band gap by placing graphene on a substrate, breaking of the lattice symmetry due to externally applied strain has been discussed as well (see for the case of graphene nanoribbons Ref. [137]). Here, due to the topological protection of the band gap (cf. section 2.1.3), this strain has to be comparably strong in order to actually open such a band gap. However, besides from an experimental measurement of, e.g., spatially resolved strain fluctuations in graphene by the use of Raman spectroscopy

---

[25]ARPES is a method in which a sample is irradiated with high-energy photons (usually X-rays) and from which the photoemitted electrons are detected. Here, one can obtain information on both energy and momentum of these electrons allowing for the detection of the electronic structure of a solid (see Ref. [136] for a review).
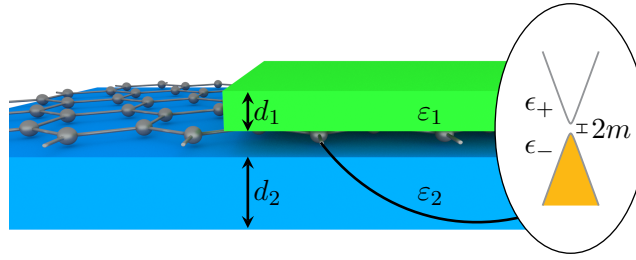
Figure 4.1: The Figure above represents the dielectric-graphene-dielectric slab structure considered in this section. For graphene, we consider a realization with a band gap (see Eq. (2.19)) that can be, e.g., caused by the lattice mismatch between the dielectrics and graphene. In general two different dielectric materials ε_1 and ε_2 of two different thicknesses d_1 and d_2 are considered. Graphene is not chemically doped (see band structure inset). Adapted with permission from Ref. [W3], doi:10.1088/2040-8978/18/3/034001. © IOP Publishing. All rights reserved.

(see Ref. [138]) and theoretical ab initio studies for the induced opening of the corresponding band gap (see Refs. [139–141] and Ref. [142] where the authors additionally discuss the interaction between externally applied strain and resulting nanometer-scale strain variations) no direct measurement of both strain and band gap has been conducted. The active tuning of graphene's band gap as it might be possible, e.g., by actively applying external mechanical strain, would, however, allow to use graphene not only as a material for analog computer chips where the transistor channels consist of graphene[26] (see Refs. [143, 144]) but also as a material for a digital computer chip, where the band gap in graphene allows for the storage of data (see also the investment program by IBM, Ref. [145]). Even if graphene does not turn out to be the optimal suited material with regard to computer chips, mapping out the band gap in graphene (as presented in this work) or other alike materials precisely and spatially resolved by magnetic and electric emitters might allow to lead the community closer to the understanding of the interplay between different external influences and the band gap which is a cornerstone in order to succeed switching graphene's band gap at will.

4.2 Electromagnetic modes in dielectric-graphene-dielectric slab systems

In this section, we now discuss the waveguiding and plasmonic modes present in a dielectric-graphene-dielectric structure (see Fig. 4.1). The knowledge of these modes allows us in the following to calculate the lifetime of an emitter in the direct proximity of graphene and to enhance our understanding of the role of the optical modes involved in the modification of the photonic local density of states.

---

[26]Graphene field effect transistors have been studied since graphene as a material exhibits a few very interesting properties for these transistors: it is much thinner and more heat resistant than common silicon transistors. Additionally, it can operate at much wider frequencies and thus might in the future provide much faster networks.

4 Magnetic and electric emitters above graphene
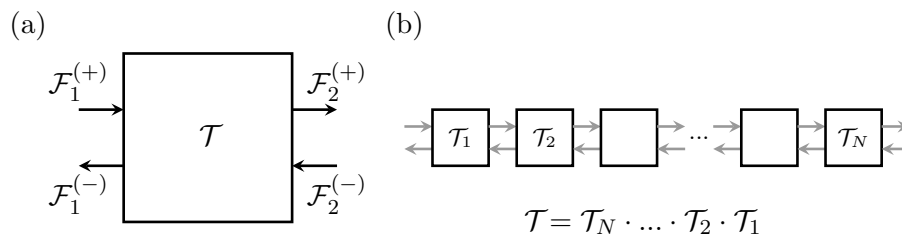
Figure 4.2: The Figure above represent the general setup of the transfer matrix method (adapted with permission from Ref. [158], p. 291, © Wiley-VCH Verlag GmbH & Co. KGaA).

Especially the plasmonic properties of graphene have caused high interest into the use of this material (see Refs. [89, 146]). Besides from lossless plasmonic TM modes in doped graphene (see Refs. [147, 148]), for finite graphene flakes, plasmonic resonances in the visible including quantum and edge effects have been computed (see Refs. [149–154]) and measured (see Ref. [10]). Even more interesting, opposite to common metals graphene exhibits a TE plasmonic mode (see Ref. [155]) to which, e.g., a magnetic emitter would couple. However, as has been discussed in later works, this mode is highly sensitive to a difference in refractive index between the two materials (see Refs. [146, 156]). These discussions and also the computation of dielectric-graphene-dielectric slab waveguide modes (see, e.g., Ref. [78, 157]) has only been conducted in the case of zero band gap. As discussed in the introduction to this chapter, we take into account that the interaction of graphene with the surrounding dielectrics (or other physical mechanisms) opens a band gap, such that the setup has to be reconsidered taking a finite band gap into account. Since we do not consider any external electrostatic gating or chemical doping, we assume a monolayer with chemical potential $\mu = 0\,\mathrm{eV}$ (see inset in Fig. 4.1).

In order to compute the reflection and transmission coefficients for the dielectric-graphene-dielectric setup, we make use of the transfer matrix formalism (see Ref. [158] and Fig. 4.2) that connects incoming ($\mathcal{F}_1^{(+)}$, $\mathcal{F}_2^{(-)}$) and outgoing ($\mathcal{F}_1^{(-)}$, $\mathcal{F}_2^{(+)}$) electric and magnetic fields ($\mathcal{F} = \{\mathcal{E}_i, \mathcal{H}_i\}$ for the Cartesian coordinates $i \in \{x, y, z\}$ with the graphene monolayer orthogonal to the z-axis)

$$\begin{pmatrix} \mathcal{F}_1^{(+)} \\ \mathcal{F}_1^{(-)} \end{pmatrix} = \mathcal{T} \begin{pmatrix} \mathcal{F}_2^{(+)} \\ \mathcal{F}_2^{(-)} \end{pmatrix} = \begin{pmatrix} \mathcal{T}_{11} & \mathcal{T}_{12} \\ \mathcal{T}_{21} & \mathcal{T}_{22} \end{pmatrix} \begin{pmatrix} \mathcal{F}_2^{(+)} \\ \mathcal{F}_2^{(-)} \end{pmatrix}, \tag{4.1}$$

where r_{ij} and t_{ij} are the different reflection and transmission coefficients for forward and backward propagation. For an infinite setup, where no light is introduced into the system from the back plane $\mathcal{F}_2^{(-)} = 0$, we define

$$r = \frac{\mathcal{T}_{21}}{\mathcal{T}_{11}} \qquad \text{and} \qquad t = \frac{1}{\mathcal{T}_{11}}. \tag{4.2}$$

For the specific dielectric-graphene-dielectric slab system, the transfer matrix consists of the transfer matrices of each of the two dielectric slabs $\mathcal{T}_{\mathrm{slab}}$ and the transfer matrix of the monolayer graphene $\mathcal{T}_g$

$$\mathcal{T} = \mathcal{T}_{\mathrm{slab},2} \cdot \mathcal{T}_g \cdot \mathcal{T}_{\mathrm{slab},1}. \tag{4.3}$$

4.2 Electromagnetic modes in dielectric-graphene-dielectric slab systems

Following Ref. [158], the transfer matrix of the slab i of dielectric $\varepsilon_r = \varepsilon_i$ embedded in an infinite dielectric $\varepsilon_r = \varepsilon_0$[27] is given as (please note the changed minus in the propagation matrix with respect to [158] due to the different definition of the Fourier component)

$$\mathcal{T}_{\text{slab},i} = \mathcal{T}_{i0} \cdot \mathcal{T}_{\text{prop.},i} \cdot \mathcal{T}_{0i} \equiv \frac{1}{t_i} \begin{pmatrix} |t_i|^2 - |r_i|^2 & r_i \\ -r_i & 1 \end{pmatrix} , \tag{4.4}$$

where we can define the slab's reflection and transmission matrix, r_i and t_i respectively, taking into account the symmetry of the slab. Here, the transfer matrix for the dielectric-dielectric interface $(i \to j)$ is given as (cf. Ref. [158])

$$\mathcal{T}_{ij} = \frac{1}{t_{ij}} \begin{pmatrix} t_{ij}t_{ji} - r_{ij}r_{ji} & r_{ji} \\ -r_{ij} & 1 \end{pmatrix} , \tag{4.5}$$

and the propagation matrix for a plane wave with wavevector $\mathbf{q} = (\mathbf{k}, q_z)^T$ in the dielectric ε_i is given as

$$\mathcal{T}_{\text{prop.}} = \begin{pmatrix} e^{iq_{z,i}d} & 0 \\ 0 & e^{-iq_{z,i}d} \end{pmatrix} .$$

From these Equations, we obtain the expressions for the reflection and transmission coefficient of the slab

$$
\begin{aligned}
r_i^{\text{TE}} &= \frac{(\kappa_0 - \kappa_i)(\kappa_0 + \kappa_i)\sinh(d\kappa_i)}{2\kappa_0\kappa_i\cosh(d\kappa_i) + (\kappa_0^2 + \kappa_i^2)\sinh(d\kappa_i)} , \\
t_i^{\text{TE}} &= \frac{2\kappa_0\kappa_i}{2\kappa_0\kappa_i\cosh(d\kappa_i) + (\kappa_0^2 + \kappa_i^2)\sinh(d\kappa_i)} , \\
r_i^{\text{TM}} &= \frac{(\varepsilon_i\kappa_0 - \varepsilon_0\kappa_i)(\varepsilon_i\kappa_0 + \varepsilon_0\kappa_i)\sinh(d\kappa_i)}{2\varepsilon_0\varepsilon_i\kappa_0\kappa_i\cosh(d\kappa_i) + (\varepsilon_i^2\kappa_0^2 + \varepsilon_0^2\kappa_i^2)\sinh(d\kappa_i)} , \\
t_i^{\text{TM}} &= \frac{2\varepsilon_0\varepsilon_i\kappa_0\kappa_i}{2\varepsilon_0\varepsilon_i\kappa_0\kappa_i\cosh(d\kappa_i) + (\varepsilon_i^2\kappa_0^2 + \varepsilon_0^2\kappa_i^2)\sinh(d\kappa_i)} .
\end{aligned}
\tag{4.6}
$$

where, as in chapter 2.2.1, $q_{z,i} = i\kappa_i = \sqrt{\varepsilon_i\tilde{\omega}^2 - \mathbf{k}^2}$ and, as introduced above, $q_{z,0} = i\kappa_0 = \sqrt{\tilde{\omega}^2 - \mathbf{k}^2}$. For later discussions, it is important to note that

$$
\begin{aligned}
\left(t_{\text{slab}}^{\text{TE}}\right)^2 - \left(r_{\text{slab}}^{\text{TE}}\right)^2 &= \frac{2\kappa_0\kappa_i\cosh(d\kappa_i) - (\kappa_0^2 + \kappa_i^2)\sinh(d\kappa_i)}{2\kappa_0\kappa_i\cosh(d\kappa_i) + (\kappa_0^2 + \kappa_i^2)\sinh(d\kappa_i)} , \\
\left(t_{\text{slab}}^{\text{TM}}\right)^2 - \left(r_{\text{slab}}^{\text{TM}}\right)^2 &= \frac{2\varepsilon_0\varepsilon_i\kappa_0\kappa_i\cosh(d\kappa_i) - (\varepsilon_i^2\kappa_0^2 + \varepsilon_0^2\kappa_i^2)\sinh(d\kappa_i)}{2\varepsilon_0\varepsilon_i\kappa_0\kappa_i\cosh(d\kappa_i) + (\varepsilon_i^2\kappa_0^2 + \varepsilon_0^2\kappa_i^2)\sinh(d\kappa_i)} ,
\end{aligned}
\tag{4.7}
$$

such that a pole in $r_{\text{slab}}^{\text{TX}}$ ($t_{\text{slab}}^{\text{TX}}$) is of same order as the pole in $\left(t_{\text{slab}}^{\text{TX}}\right)^2 - \left(r_{\text{slab}}^{\text{TX}}\right)^2$ with $X \in \{E, M\}$.

---

[27]Here, we change the notation as compared to chapter 1. In chapter 1, we introduced the dielectric permittivity as $\varepsilon = \varepsilon_0\varepsilon_r$. In this chapter, we do include ε_0 into the speed of light c and instead only use ε_r. Thus, the notation ε_0 refers to the surrounding medium that can in general be any but in all Figures is considered to be vacuum $\varepsilon_0 = 1$.

4 Magnetic and electric emitters above graphene

When inserting Eq. (4.4) for the slabs and Eq. (4.5) for the transfer matrix for graphene where the reflection and transmission coefficients of graphene are given by Eqs. (2.43) and (2.44), this finally leads to the reflection and transmission coefficients of the total system. They read

$$r = r_1 + t_1^2 \frac{r_g + r_2 \left(t_g^2 - r_g^2 \right)}{(r_2 r_g - 1)(r_1 r_g - 1) - r_1 r_2 t_g^2} \,, \tag{4.8a}$$

$$t = -\frac{t_1 t_g t_2}{-1 + r_g \left(r_1 + r_2 \right) + r_1 r_2 \left(t_g^2 - r_g^2 \right)} \,, \tag{4.8b}$$

which correspond to the reflection and transmission coefficients determined in Refs. [66, 159] when taking $\varepsilon_1 = \varepsilon_2$ and $d \to \infty$.

The resonances and modes[28], in response to electromagnetic radiation are determined via the poles of the response functions (see section 1.3.1) where a branch cut corresponds to a many-particle continuum. These poles are equivalent to the poles in the reflection coefficients. In Eq. (4.8a), r_1, r_2 and r_g intrinsically exhibit poles. These poles, however, are no poles of the total reflection coefficient r. One can understand this fact, when considering that $t_g^{\mathrm{TX}} = 1 \pm r_g^{\mathrm{TX}}$ such that $t_g^2 - r_g^2 = 1 \pm 2 r_g$ in the numerator and denominator of Eq. (4.8a). In proximity of the poles of r_g, leading order terms are of order r_g in both the numerator and denominator. Hence, they cancel and r does not exhibit the same resonances as graphene in vacuum. In proximity of the resonances of r_2, denominator and numerator both have terms of leading order one that in return also cancel. Last, for the resonance due to slab '1', we can rewrite Eq. (4.8a)

$$r = \frac{\left(t_1^2 - r_1^2 \right) \left[r_g + r_2 \left(t_g^2 - r_g^2 \right) \right] + r_1 \left(1 - r_2 r_g \right)}{(r_2 r_g - 1)(r_1 r_g - 1) - r_1 r_2 t_g^2} \,,$$

where the pole in $t_1^2 - r_1^2$ is of same order as the pole in r_1 as shown above in Eqs. (4.7) for TE and TM polarization and hence also cancels.

With these considerations, the only resonance that remains is described by the condition

$$\frac{1}{r} = 0 \qquad \Leftrightarrow \qquad (r_1 r_g - 1)(r_2 r_g - 1) = r_1 r_2 t_g^2 \,. \tag{4.9}$$

4.2.1 Graphene embedded in an infinitely extended dielectric

To gain a deeper understanding of the different modes present in a dielectric-graphene-dielectric setup, we start by discussing the case of graphene embedded in an infinite dielectric distinguishing between TE and TM polarization.

---

[28]Oftentimes, modes are considered to be the lossless eigenvalues of a system such that the system can be in the specific state described by the eigenvalue without having to insert additional energy into the system to compensate for losses. When we discuss the existence of modes in this section, we extend the terminus and also discuss lossy modes. These are sometimes instead called resonances or quasi normal modes (see Ref. [160]).

4.2 Electromagnetic modes in dielectric-graphene-dielectric slab systems
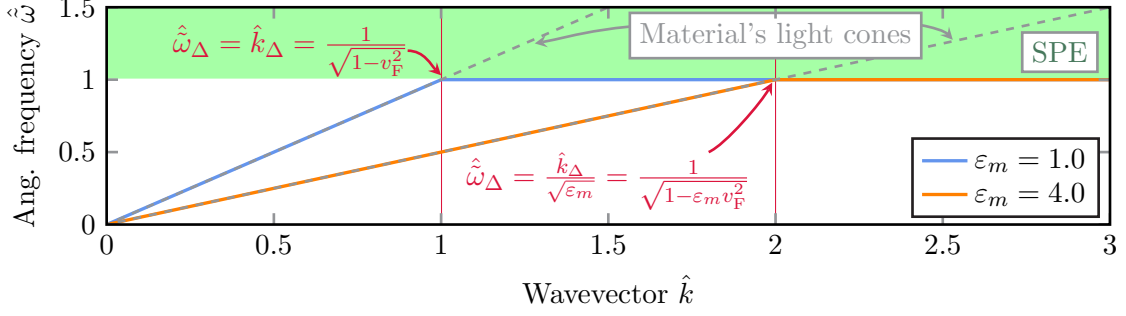
Figure 4.3: TE plasmonic resonances in graphene embedded in an infinite dielectric ε_m where graphene exhibits a band gap of $2m$ (compare section 2.2.1). For wavevectors $\hat{k} < \sqrt{\varepsilon_m/(1 - \varepsilon_m \tilde{v}_F^2)}$ the TE plasmonic resonance shows a dispersion relation very close to the light cone (see Eq. (4.15)), while for wavevectors $\hat{k} > \sqrt{\varepsilon_m/(1 - \varepsilon_m \tilde{v}_F^2)}$ the phase velocity changes drastically and becomes dielectric independent (see Eq. (4.17)]) Due to the smallness of the fine structure constant α the transition between the two regimes appears abrupt. The green region marks the single-particle excitation (SPE) region where a photon of energy $\hbar\omega$ carries sufficient energy to excite an electron-hole pair. Adapted with permission from Ref. [W3], doi:10.1088/2040-8978/18/3/034001. © IOP Publishing. All rights reserved.

TE polarization:

For the case of TE polarization, the reflection coefficient of graphene is given by Eq. (2.43) and Eq. (4.9) accordingly corresponds to

$$\alpha \hat{\Phi}(\hat{y}) + 2\hat{\kappa}_m = 0 \,, \tag{4.10}$$

where we use the definition of $\Phi(y)$ given by Eq. (2.42) and introduce the general notation in dimensionless units

$$\hat{a} = \frac{a}{\Delta} \,, \qquad \text{while} \qquad \check{a} = a \cdot \Delta \,. \tag{4.11}$$

With $\hat{\bar{\omega}}^2 = \hat{y}^2 + \tilde{v}_F^2 \hat{k}^2$ (cf. Eq. (2.35)) and $\hat{\kappa}_m^2 = \hat{k}^2 - \varepsilon_m \hat{\bar{\omega}}^2$, we can rewrite

$$\alpha^2 \hat{\Phi}(\hat{y})^2 = 2(1 - \varepsilon_m \tilde{v}_F^2)\hat{k}^2 - 2\varepsilon_m \hat{y}^2 \,,$$

and with the parametrization $\hat{y} = \tanh(q)$, we find

$$\hat{k}_p[q] = \frac{1}{\sqrt{1 - \varepsilon_m \tilde{v}_F^2}} \sqrt{\varepsilon_m \tanh(q)^2 + \alpha^2 \left(q\frac{\tanh(q)^2 + 1}{\tanh(q)} - 1\right)^2} \,, \tag{4.12a}$$

$$\hat{\bar{\omega}}_p[q] = \frac{1}{\sqrt{1 - \varepsilon_m \tilde{v}_F^2}} \sqrt{\tanh(q)^2 + \alpha^2 \tilde{v}_F^2 \left(q\frac{\tanh(q)^2 + 1}{\tanh(q)} - 1\right)^2} \,. \tag{4.12b}$$

4 Magnetic and electric emitters above graphene

The Equations above present the TE plasmonic resonance in graphene (for further expressions and reformulations of the TE plasmonic mode that come handy in the rest of this chapter, see appendix D.1). In Fig. 4.3, we depict these for two different values of ε_m, one for vacuum ($\varepsilon_m = 1$) and the other one for hBN ($\varepsilon_m \approx 4$). This parametrized solution has been presented for the first time in Ref. [W3] and for the vacuum case corresponds well with the numeric results obtained in Refs. [57, 71]. It will be made use of later in this chapter when determining analytically the TE plasmonic resonance's contributions to the photonic local density of states.

From Fig. 4.3 it is not obvious that the resonance of the reflection coefficient r is indeed for all wavevectors of plasmonic nature. One possible definition a TE plasmon that is commonly applied in literature (and thus leads to the term *TE plasmon*) is that

$$\hat{\kappa}_m^2 > 0 \,, \tag{4.13}$$

being that a plasmonic mode is of evanescent nature. In general, all resonances $\omega(\mathbf{k})$ can be either evanescent ($q_{z,m} \in i\mathbb{R}$, also often termed non-radiative) such that the electromagnetic modes excited on the graphene monolayer fall off exponential perpendicular to the layer or radiative ($q_{z,m} \in \mathbb{R}$) such that the electromagnetic modes excited on the graphene monolayer exhibit a propagative component perpendicular to the layer. In Fig. 4.3, these two regimes are separated by the light cone (gray dashed line) of the material in which graphene is embedded in. Then, the radiative (evanescent) region is above (below) this light cone. In order to determine whether the plasmonic resonance is indeed situated in the evanescent regime, we distinguish between two limiting cases: in the small wavevector regime, we can expand the parametric solution into

$$
\begin{aligned}
\hat{k}_{\mathrm{p}}[q]^2 &\approx \frac{\varepsilon_m q^2 - \left(\varepsilon_m \frac{2}{3} - \frac{2^4}{9}\alpha^2\right) q^4}{1 - \varepsilon_m \tilde{v}_{\mathrm{F}}^2} \,, \\
\hat{\tilde{\omega}}_{\mathrm{p}}[q]^2 &\approx \frac{q^2 - \left(\frac{2}{3} - \frac{2^4}{9}\alpha^2 \tilde{v}_{\mathrm{F}}^2\right) q^4}{1 - \varepsilon_m \tilde{v}_{\mathrm{F}}^2} \,,
\end{aligned}
\tag{4.14}
$$

where we can assign an approximate phase velocity $\hat{\tilde{\omega}}[k] \approx \tilde{\beta}(k)\,k$ with

$$\tilde{\beta}(k) \approx \frac{\sqrt{1 - \frac{16}{9}\alpha^2 \left(\frac{1 - \varepsilon_m \tilde{v}_{\mathrm{F}}^2}{\varepsilon_m}\right)^2 k^2}}{\sqrt{\varepsilon_m}} \quad \Rightarrow \quad \tilde{\beta}(k) \approx \frac{1}{\sqrt{\varepsilon_m}} \quad \text{but} \quad \tilde{\beta}(k) < 1/\sqrt{\varepsilon_m}\,. \tag{4.15}$$

In the large wavevector limit ($q \ll 1$, thus approximating $\tanh(q) \approx 1 - x$ with $x \ll 1$ but nonetheless $x > 0$), we find the approximative expressions

$$
\begin{aligned}
\hat{k}_{\mathrm{p}}[q] &\approx \sqrt{\frac{\varepsilon_m(1 - 2x) + \alpha^2(2q - 1)^2}{1 - \varepsilon_m \tilde{v}_{\mathrm{F}}^2}} \,, \\
\hat{\tilde{\omega}}_{\mathrm{p}}[q] &\approx \sqrt{\frac{1 - 2x + \alpha^2 \tilde{v}_{\mathrm{F}}^2(2q - 1)^2}{1 - \varepsilon_m \tilde{v}_{\mathrm{F}}^2}} \,.
\end{aligned}
\tag{4.16}
$$

4.2 Electromagnetic modes in dielectric-graphene-dielectric slab systems

Inserting Eqs. (4.16) into each other, the TE plasmon dispersion relation for $q \gg 1$ is completely independent of the material ε_m the graphene monolayer is embedded in and reads

$$\tilde{\omega}_{\mathrm{p}}[k] \approx \sqrt{\Delta^2 \left(1 - 2x\right) + \tilde{v}_{\mathrm{F}}^2 k_{\mathrm{p}}^2} < \sqrt{\Delta^2 + \tilde{v}_{\mathrm{F}}^2 k_{\mathrm{p}}^2}\,. \tag{4.17}$$

Equation (4.17) corresponds to the fact that the TE plasmon dispersion is situated outside the single-particle excitation (SPE) region. This is the energy range in which a photon carries a sufficient amount of energy

$$\hat{\tilde{\omega}} > \hat{\tilde{\omega}}_{\mathrm{SPE}}(k) = \sqrt{1 + \tilde{v}_{\mathrm{F}}^2 \hat{k}^2}\,, \tag{4.18}$$

to excite an electron-hole pair in graphene (green region, Fig. 4.3). Hence in this region, the creation of electron-hole pairs present an additional loss channel in graphene, the fact that the TE plasmon resonance is situated outside the SPE region leads to the TE plasmon resonance being not only purely evanescent but also lossless. In the SPE region actually the additional damping due to the electron-hole creation would govern the plasmonic resonance and thus lead to very small lifetimes (cf. Ref. [34]). In this specific case, standard literature does not consider this plasmonic mode as a real collective excitation any longer (see discussion in Ref. [34]).

We can then determine the intersection of Eq. (4.15) and Eq. (4.17) and find for the "kink" marked by red arrows in Fig. 4.3

$$\hat{\tilde{\omega}}_\Delta = \frac{\hat{\tilde{\omega}}_\Delta}{\sqrt{\varepsilon_m}} = \frac{1}{\sqrt{1 - \varepsilon_m \tilde{v}_{\mathrm{F}}^2}}\,. \tag{4.19}$$

The kink that is well visible in Fig. 4.3 is in fact a smooth transition between the low and high wavevector regime. This is well visible in the case of artificially large values of the fine structure constant α (see also Refs. [57, 71] and the red dashed lines in Fig. 4.4 for different values of ε_m and α). In the next subsections, we will thus – in parallel to standard literature – use larger values for α in order to better visualize the distinct features of the structure's modes.

TM polarization:

When we consider the modes in TM polarization, the reflection coefficient of graphene is given in Eq. (2.44) and accordingly Eq. (4.9) leads to

$$-2\varepsilon_m \hat{y}^2 + \alpha \hat{\Phi}(\hat{y})\hat{\kappa}_m = 0\,. \tag{4.20}$$

It can be shown that no solution exists to the equation above since for all $\hat{y}$ both parts of the equation exhibit the same sign (compare derivation in appendix D.2).

Since the TM plasmon only exists at finite doping (see Refs. [146, 147]) but not in the case of zero the chemical potential $\mu = 0$ (independent of the existence of a band gap, see, e.g., for the zero band gap case Ref. [146]), this results in the insight that the TM plasmon is an intraband plasmon. Particularly, it is a collective excitations of the electrons in the conduction band and exists only at finite doping.
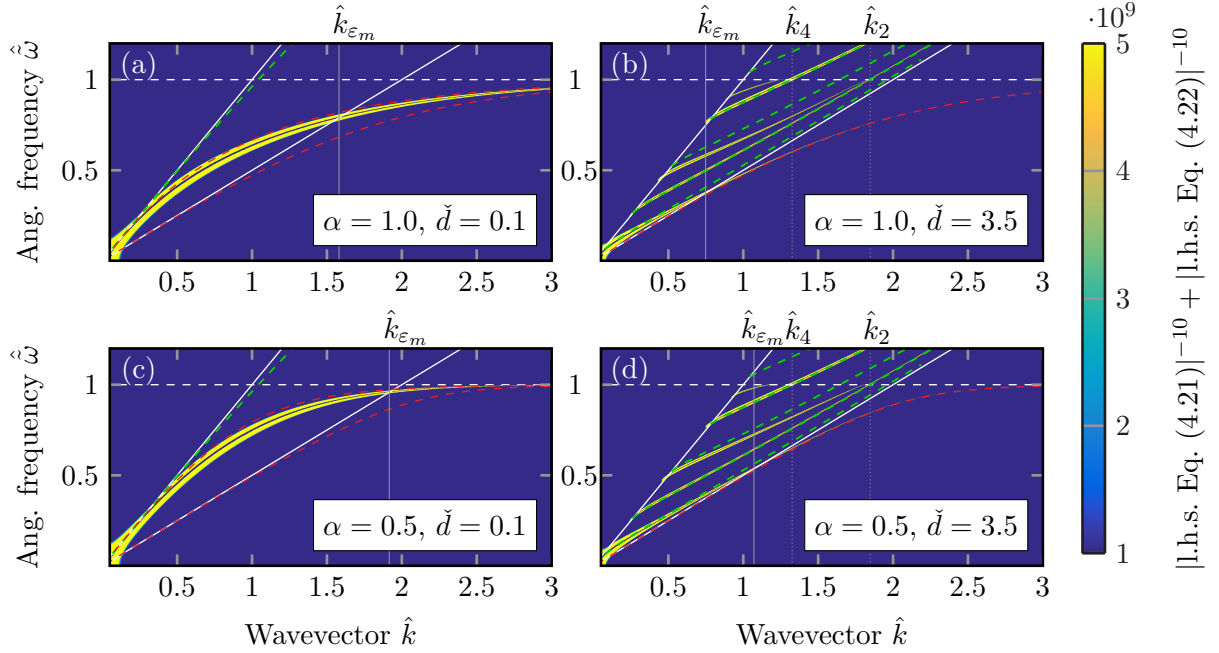
Figure 4.4: Waveguiding and plasmonic modes for TE polarized light propagating through a dielectric-graphene-dielectric slab waveguide. We consider a symmetric setup with $\varepsilon_1 = \varepsilon_2 = \varepsilon_m = 4.0$ and $d_1 = d_2 = d$. The dashed green lines are the waveguide solutions for a dielectric slab waveguide of $d' = 2d$ and the dashed red lines are the solutions of Eq. (4.10) for $\varepsilon_m = 1$ (upper) and $\varepsilon_m = 4.0$ (lower). Panels (a-d) represent results for different slab thicknesses $\check{d} = \Delta \cdot d$ and values of α. The crossover of the zeroth mode to the evanescent (non-radiative) region $\hat{k}_{\varepsilon_m}$ and the crossing of the even modes from the waveguiding to the SPE region $\hat{k}_{2n}$ are depicted in Fig. 4.5(a) and (b), respectively, and given by Eq. (4.27) and Eq. (4.30). Adapted with permission from Ref. [W3], doi:10.1088/2040-8978/18/3/034001. © IOP Publishing. All rights reserved.

4.2.2 Graphene embedded between two identical dielectric slabs of finite thickness

When considering the finite width of the substrate in which graphene is embedded, additional guided modes due to the vacuum-dielectric interface appear. In general, besides from the region of propagating and evanescent modes in both vacuum and dielectric, so-called waveguiding modes – propagating in the dielectric while evanescent in the surrounding vacuum – exist.

4.2 Electromagnetic modes in dielectric-graphene-dielectric slab systems
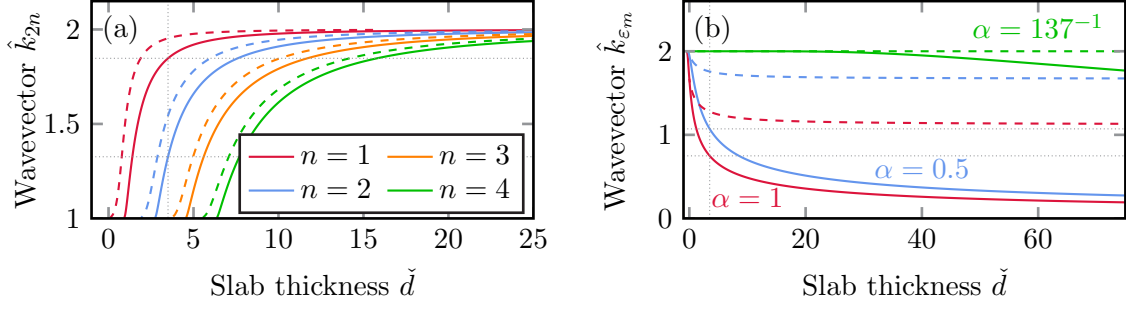
Figure 4.5: Panel (a) shows the thickness dependence of the TE cutoff wavevectors $k_{2n}[d]$ Eq. (4.27) (solid) and of the TM cutoff wavevectors $k_{2n-1}[d]$ Eq. (4.34) (dashed) for $n = 1 \ldots 4$. In panel (b), we display the crossover wavevector $k_{\varepsilon_m}[d]$ Eq. (4.30) where the mode $n = 0$ crosses from the waveguiding region into the evanescent region becoming plasmonic for both graphene embedded between two identical dielectric slabs (solid) and deposited on top of a dielectric slab (dashed). The vertical gray dotted lines in both panels correspond to the wavevector values marked in Fig. 4.4(b,d) with the crossing at $\check{d} = 3.5$ with the horizontal gray dotted line. Adapted with permission from Ref. [W3], doi:10.1088/2040-8978/18/3/034001.

TE polarization:

For the case of the TE polarized light, Eq. (4.9) leads to two different sets of modes. The first set is defined by the solutions to

$$r_m^{\mathrm{TE}} + 1 = 0 \,, \tag{4.21}$$

which corresponds to the mode condition for the odd modes of a dielectric waveguide with ε_m and $d' = 2d$. Thus, the odd modes are not modified by the graphene layer. This is due to the thickness of the monolayer and the symmetry of the waveguide: odd modes of a dielectric slab waveguide have vanishing field value at the center and hence do not couple to graphene's conductivity (compare also Eq. (2.52d)). In Fig. 4.4, we present the solutions to Eq. (4.21) and compare them (yellow part of colorbar) to the undisturbed dielectric waveguide solutions (dashed green lines). In panel (b,d), we show that the first and third modes interfere exactly (note the green dashed lines falling exactly on the yellow odd dielectric-graphene-dielectric waveguide modes).

The second set of modes is given by

$$
\begin{aligned}
\alpha \hat{\Phi}(\hat{y}) &\left[\hat{\kappa}_0 \sinh(\check{d}\hat{\kappa}_m) + \hat{\kappa}_m \cosh(\check{d}\hat{\kappa}_m) \right] \\
&+ 2\hat{\kappa}_m \left[\hat{\kappa}_0 \cosh(\check{d}\hat{\kappa}_m) + \hat{\kappa}_m \sinh(\check{d}\hat{\kappa}_m) \right] = 0 \,,
\end{aligned}
\tag{4.22}
$$

using the notation introduced in Eq. (4.11). The first trivial solution of Eq. (4.22), $\hat{\kappa}_m = 0$, stems from the reformulation of the slab's reflection coefficient and due to (cf. Ref. [161])

$$r_m(\hat{\kappa}_m = 0) \xrightarrow{\mathrm{L'Hospital}} \frac{d\hat{\kappa}_0}{d\hat{\kappa}_0 + 2} \,, \tag{4.23}$$

the singularity is liftable. Equation (4.22) can then be rewritten in the more convenient form

$$\check{d} = \frac{1}{2\hat{\kappa}_m} \ln \left[\frac{(\hat{\kappa}_0 - \hat{\kappa}_m)(\alpha\hat{\Phi}(\hat{y}) - 2\hat{\kappa}_m)}{(\hat{\kappa}_0 + \hat{\kappa}_m)(\alpha\hat{\Phi}(\hat{y}) + 2\hat{\kappa}_m)} \right], \tag{4.24}$$

with the branch cut of the logarithm $\ln(x)$ along the negative real axis.

Solutions to the slabs' thickness have always to be a positive, real numbers which fixes our choice of the logarithm and determines the correct Riemann sheet. Here, we have to distinguish between different regions. First for $\hat{k} < \hat{\tilde{\omega}}$ (waves propagating in the dielectric and vacuum), no undamped waveguide modes exist (remember: $\hat{\kappa}_i = -i\hat{q}_{i,z}$)

$$\check{d} = \frac{1}{-2i\hat{q}_{z,m}} \ln \left[\frac{\left(\hat{q}_{z,0} - \hat{q}_{z,m}\right)\left(\alpha\hat{\Phi}(\hat{y}) + 2i\hat{q}_{z,m}\right)}{\left(\hat{q}_{z,0} + \hat{q}_{z,m}\right)\left(\alpha\hat{\Phi}(\hat{y}) - 2i\hat{q}_{z,m}\right)} \right]. \tag{4.25}$$

In appendix. D.3, we discuss the details of damped modes existing in the propagating region. As known from the case of common dielectric slab waveguides, they start at $\hat{k} = 0$ for finite values of $\hat{\tilde{\omega}}$ and connect to the corresponding undamped waveguide mode at $\hat{\tilde{\omega}} = \hat{k}$. These modes are only very weakly dependent on the graphene monolayer. Instead, they are caused by the dielectric slab waveguide and of the same nature as the damped modes in a regular dielectric slab waveguide. Thus, they are not considered further.

The second region in which no undamped solutions can exist is the SPE region with $\hat{y} > 1$. In this region, damped solutions exist that we discuss in greater detail below. First, we concentrate on the undamped waveguide solutions that appear in this specific waveguide. In the dielectric slabs' waveguiding region where $\hat{\tilde{\omega}} < \hat{k} < \sqrt{\varepsilon_m}\hat{\tilde{\omega}}$, the electromagnetic fields are evanescent in the surrounding vacuum while propagating in the waveguide. Assuming only energies below the SPE threshold (Eq. (4.18)), we can rewrite Eq. (4.24) considering $\hat{\kappa}_m = -i\hat{q}_{z,m} \in i\mathbb{R}$ and $\hat{\kappa}_0 \in \mathbb{R}$

$$\begin{aligned}
\check{d} &= \frac{1}{-2i\hat{q}_{z,m}} \ln \left[\frac{\left(\hat{\kappa}_0 + i\hat{q}_{z,m}\right)\left(\alpha\hat{\Phi}(\hat{y}) + 2i\hat{q}_{z,m}\right)}{\left(\hat{\kappa}_0 - i\hat{q}_{z,m}\right)\left(\alpha\hat{\Phi}(\hat{y}) - 2i\hat{q}_{z,m}\right)} \right] \\
&= \frac{\mathrm{atan}\left(\frac{2\hat{q}_{z,m}}{-\alpha\hat{\Phi}(\hat{y})}\right) - \mathrm{atan}\left(\frac{2\hat{q}_{z,m}}{2\hat{\kappa}_0}\right) + \pi n}{\hat{q}_{z,m}} > 0,
\end{aligned} \tag{4.26}$$

which leads to positive, real-valued slab thicknesses for $n = 1, 2, 3, \ldots$. Each of the values of n correspond to a different, even waveguide mode $2n$. In Fig. 4.4, we display these even modes in addition to the before mentioned undisturbed, odd modes. Here, one notices that the inclusion of the mono-atomic graphene layer has a strong effect on the even waveguide modes introducing a cutoff of the dispersion relation of the lossless modes at the SPE region threshold $\hat{y} = 1$. In terms of the parameter $\hat{q}_{z,m}$ and taking into account
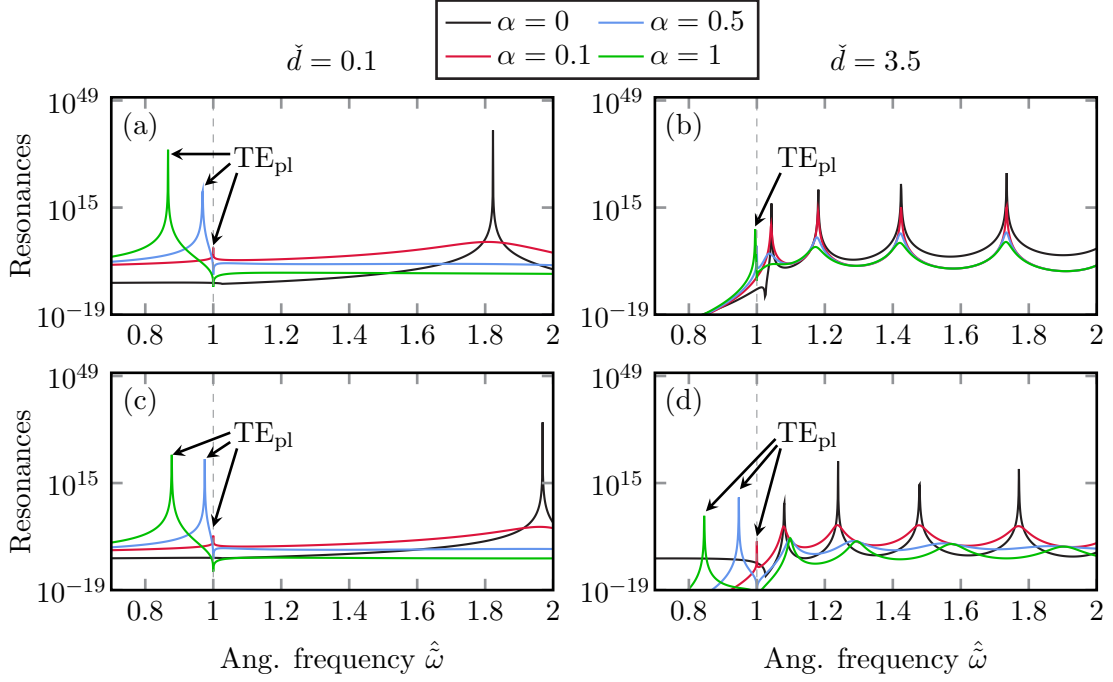
Figure 4.6: Damped modes for $\hat{k} = 2.05$ for two dielectric ($\varepsilon_m = 4.0$) slab thicknesses $\check{d}$ and varying the value of α. Panels (a,b) present the resonances for graphene embedded between two of these dielectric slabs ($|$l.h.s. of Eq. $(4.21)|^{-10} + |$ l.h.s. of Eq. $(4.22)|^{-10}$) while panels (c,d) present the resonances for graphene positioned on top of one of these slabs ($|$l.h.s. of Eq. $(4.40)|^{-10}$). The gray dashed lines present the SPE region threshold Eq. (4.18). In the evanescent region ($\hat{\tilde{\omega}} < \hat{\tilde{\omega}}_{\text{SPE}}$), we mark several distinct resonances, the TE plasmons TE_{pl}. In the SPE region itself, the $\alpha = 0$ represents the mode solutions without graphene, showing very sharp resonances. For increasing values of α the damping becomes larger. Adapted with permission from Ref. [W3], doi:10.1088/2040-8978/18/3/034001. © IOP Publishing. All rights reserved.

$\lim\limits_{\hat{y}\to 1} \hat{\tilde{\Phi}}(\hat{y}) \to -\infty$, the relation $k(d_{2n})$ reads

$$\hat{k}_{2n}[\hat{q}_{z,m}] = \sqrt{\frac{\varepsilon_m - \hat{q}_{z,m}^2}{1 - \varepsilon_m \tilde{v}_{\text{F}}^2}} \ , \tag{4.27a}$$

$$\check{d}[\hat{q}_{z,m}] = \frac{\pi n - \text{atan}\left(\frac{\sqrt{1-\varepsilon_m \tilde{v}_{\text{F}}^2}\,\hat{q}_{z,m}}{\sqrt{(\varepsilon_m - 1) - (1 - \varepsilon_m \tilde{v}_{\text{F}}^2)\hat{q}_{z,m}^2}}\right)}{\hat{q}_{z,m}} \ . \tag{4.27b}$$

At $\hat{y} = 1$, the even modes thus coincide with the condition of the odd mode $2n - 1$ (compare also Fig. 4.4(b,d)). For values $\hat{y} > 1$, the even waveguide modes become lossy. In fact, as soon as graphene's pair-creation threshold is reached, a decay channel is introduced into the optical response of the system. To understand the influence of the

4 Magnetic and electric emitters above graphene

graphene monolayer on the waveguide modes, we assume an effective medium description where we replace the slab-graphene-slab system with an effective dielectric waveguide of dielectric permittivity $\varepsilon_{\text{eff}} = \varepsilon_m + i\varepsilon^{(1)}$ with $\varepsilon_m \in \mathbb{R}$. Then, the perturbation $\varepsilon^{(1)} \ll \varepsilon$ is the complex loss introduced by the monolayer graphene and with this we find (see appendix D.4)

$$\varepsilon^{(1)} \propto \alpha \,, \tag{4.28}$$

which means that the damping itself is also proportional to α (compare Fig. 4.6). Due to the choice for α in Fig. 4.4, these damped modes are not visible in the panels (a-d). For a fixed value $\hat{k} = 2.05$, we display the resonances in Fig. 4.6(a,b) where this dependence is well visible.

Returning to Eq. (4.27), a solution for $n = 0$ is only allowed if $2\hat{\kappa}_0 + \alpha\hat{\Phi}(\hat{y}) > 0$. This condition requires the zeroth mode to be always located below the vacuum TE plasmonic resonance (see Eq. (4.12) and upper red dashed line in Fig. 4.4(a,c)). This leads to the very interesting situation that the zeroth mode has a crossing from the waveguiding region to the evanescent region which is for a pure dielectric waveguide forbidden. The crossing can be found by solving

$$\check{d} = \lim_{\hat{\kappa}_m \to 0} \left\{ \frac{1}{2\hat{\kappa}_m} \ln \left[\frac{\left(\hat{\kappa}_0 - \hat{\kappa}_m\right)\left(\alpha\hat{\Phi}(\hat{y}) - 2\hat{\kappa}_m\right)}{\left(\hat{\kappa}_0 + \hat{\kappa}_m\right)\left(\alpha\hat{\Phi}(\hat{y}) + 2\hat{\kappa}_m\right)} \right] \right\} = -\frac{\alpha\hat{\Phi}(\hat{y}) + 2\hat{\kappa}_0}{\alpha\hat{\kappa}_0\hat{\Phi}(\hat{y})} \,, \tag{4.29}$$

leading to the parametric solution ($\hat{y} = \tanh q$)

$$\hat{k}_{\varepsilon_m}[q] = \sqrt{\frac{\varepsilon_m}{1 - \varepsilon_m\tilde{v}_{\text{F}}^2}} \tanh\left(q\right) \,, \tag{4.30a}$$

$$\check{d}[q] = -\frac{\alpha\hat{\Phi}[\tanh\left(q\right)] + 2\sqrt{\frac{\varepsilon_m - 1}{1 - \varepsilon_m\tilde{v}_{\text{F}}^2}} \tanh\left(q\right)}{\alpha\sqrt{\frac{\varepsilon_m - 1}{1 - \varepsilon_m\tilde{v}_{\text{F}}^2}} \tanh\left(q\right)\hat{\Phi}[\tanh\left(q\right)]} \,, \tag{4.30b}$$

that we show in Fig. 4.5(b). For the large wavevector limit ($\hat{\kappa}_m > 0$), we find from Eq. (4.29) that for real solutions of $\check{d}$ the argument of the logarithm has to be positive. For $\hat{\kappa}_m > 0$, specifically $\hat{\kappa}_0 - \hat{\kappa}_m > 0$, $\hat{\kappa}_i > 0$ and $\alpha\hat{\Phi}(\hat{y}) < 0$ lead to

$$\alpha\hat{\Phi}(\hat{y}) + 2\hat{\kappa}_m < 0 \,,$$

such that for large wavevectors the zeroth mode is always above the TE plasmonic resonance of graphene embedded in an infinite dielectric ε_m (see lower red dashed line in Fig. 4.4(a,c)). On the other hand, for $\hat{k}_0 \to 0$ we can show that due to $\alpha \ll 1$, the condition $\alpha\hat{\Phi}(\hat{y}) + 2\hat{\kappa}_0 = 0$ is the upper limit of the zeroth order TE mode. Additionally, when $\hat{\kappa}_0 \to 0$ while $\hat{\kappa}_0 > 0$, the vacuum TE plasmonic resonance and with it the zeroth order TE slab-graphene-slab mode approach the vacuum light cone from below.

The transition from graphene embedded between the finite dielectric slabs to graphene embedded in an infinite dielectric ($d \to \infty$) can be understood as follows: The larger the thickness of the slab the denser the waveguiding modes in the waveguiding region. This is caused by the fact that the number of modes increases while their dispersion relation

74
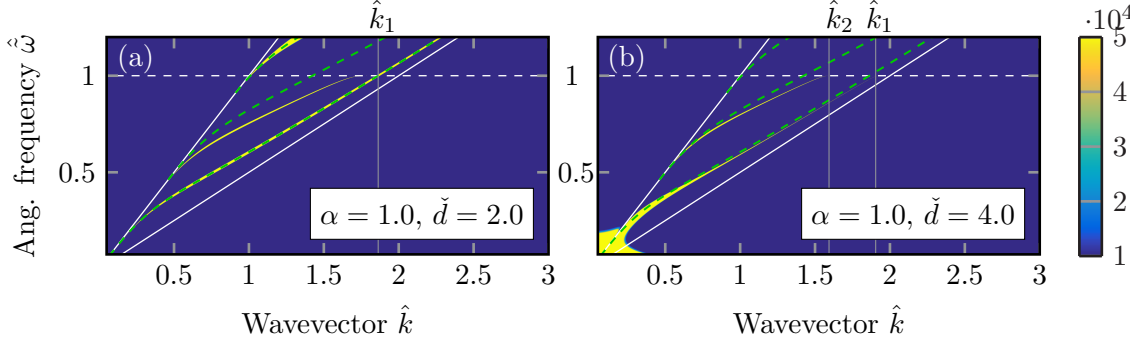
Figure 4.7: TM modes for graphene embedded between two slabs (a) and graphene embedded on one single slab (b) of dielectric ε_m. In panel (a) we depict in the color bar $\sum_{i=31}^{32} |\text{l.h.s. Eq. } (4.i)|^{-10}$ while in panel (b) we depict in the color bar $|\text{l.h.s. Eq. } (4.47)|^{-10}$. The inverse of these equations leads to a value approaching infinite at the position of the modes which are in turn clearly visible (yellow part of colorbar). The gray lines correspond to the wavevector $\hat{k}_{2n+1}$ ($\hat{k}_n$) given by Eq. (4.34) (Eq. (4.50)) for the graphene monolayer embedded between two slabs (on a single slab). The slab thickness dependence of those we display in Fig. 4.5(a) by the dashed lines.

remains confined in the region $\hat{\tilde{\omega}} < \hat{k} < \sqrt{\varepsilon_m}\hat{\tilde{\omega}}$. In this process, the modes tend to the scattering waves of the infinite system (mathematically corresponding to a branch cut in the equations). The singularity with $n = 0$, however, remains isolated and turns into the TE plasmon resonance condition Eq. (4.12).

TM polarization:

Next we discuss the modes of TM electromagnetic fields: with $t_g^{\text{TM}} = 1 - r_g^{\text{TM}}$ once more two sets of modes arise from Eq. (4.9). The first,

$$r_m^{\text{TM}} - 1 = 0\,, \tag{4.31}$$

corresponds to the slab waveguide conditions of the even modes of a slab waveguide of thickness $\check{d}' = 2\check{d}$. This is analogous to the TE case with the only condition that here for TM polarization the even mode exhibit a vanishing electric field value at the position of the graphene layer and thus remain unaffected. The second condition reads

$$
\alpha \hat{\Phi}(\hat{y})\hat{\kappa}_m \left[\hat{\kappa}_m \sinh\left(\check{d}\hat{\kappa}_m\right) + \varepsilon_m \hat{\kappa}_0 \cosh\left(\check{d}\hat{\kappa}_m\right)\right] \\
- 2\varepsilon_m \hat{y}^2 \left[\varepsilon_m \hat{\kappa}_0 \sinh\left(\check{d}\hat{\kappa}_m\right) + \hat{\kappa}_m \cosh\left(\check{d}\hat{\kappa}_m\right)\right] = 0\,,
\tag{4.32}
$$

4 Magnetic and electric emitters above graphene

which then leads in terms of the slab thickness $\check{d}$ to

$$\check{d} = \frac{1}{2\hat{\kappa}_m} \ln \left[\frac{\left(\hat{\kappa}_m - \varepsilon_m \hat{\kappa}_0\right)\left(2\varepsilon_m \hat{y}^2 + \alpha \hat{\Phi}(\hat{y})\hat{\kappa}_m\right)}{\left(\hat{\kappa}_m + \varepsilon_m \hat{\kappa}_0\right)\left(-2\varepsilon_m y^2 + \alpha \hat{\Phi}(\hat{y})\hat{\kappa}_m\right)} \right]. \tag{4.33}$$

As in the case of the TE polarization, we can distinguish between propagating ($\hat{k} < \hat{\tilde{\omega}}$), SPE ($\hat{y} > 1$ and $\hat{k} > \hat{\tilde{\omega}}$), waveguiding ($\hat{\tilde{\omega}} < \hat{k} < \sqrt{\varepsilon_m}\hat{\tilde{\omega}}$ and $\hat{y} < 1$) and evanescent region ($\hat{k} > \sqrt{\varepsilon_m}\hat{\tilde{\omega}}$ and $\hat{y} < 1$). For the first two regions in analogy to TE polarization no or only damped modes exist. In the waveguiding region, undamped odd and even modes exist. The interesting mode, however, is the zeroth order mode that in the case of the TE polarization exhibits a crossover from the waveguiding to the evanescent region. Since for undoped graphene no TM plasmon exists (compare Eq. (4.20)), one would expect the zeroth TM mode to lie completely in the waveguiding region not allowing modes in the evanescent region (since as mentioned above in TM polarization the even modes exhibit zero electric field at the graphene monolayer and are therefore unaffected by the graphene sheet).

However, to exclude the possibility of an additional, evanescent mode appearing, we consider in Eq. (4.33), whether the argument of the logarithm is larger or smaller than one. A mode can only exist if for a pair $(\hat{k}, \hat{\tilde{\omega}})$ a solution with a positive slab thickness exist.

For most parts of the evanescent region, $0 < \hat{y}^2 < 1$ and then $\hat{\Phi}(\hat{y}) < 0$ (see also appendix D.2). With the fact that in the evanescent region both wavevectors $\hat{\kappa}_0 > 0$ and $\hat{\kappa}_m > 0$ leading to $2\varepsilon_m \hat{y}^2 + \alpha \hat{\Phi}(\hat{y})\hat{\kappa}_m < 0$, we find in this first region

$$\left[\frac{\left(\hat{\kappa}_m - \varepsilon_m \hat{\kappa}_0\right)\left(2\varepsilon_m \hat{y}^2 + \alpha \hat{\Phi}(\hat{y})\hat{\kappa}_m\right)}{\left(\hat{\kappa}_m + \varepsilon_m \hat{\kappa}_0\right)\left(-2\varepsilon_m \hat{y}^2 + \alpha \hat{\Phi}(\hat{y})\hat{\kappa}_m\right)} \right] \gtrless 1$$

$$\Updownarrow$$

$$\left(\hat{\kappa}_m - \varepsilon_m \hat{\kappa}_0\right)\left(2\varepsilon_m \hat{y}^2 + \alpha \hat{\Phi}(\hat{y})\hat{\kappa}_m\right) \lessgtr \left(\hat{\kappa}_m + \varepsilon_m \hat{\kappa}_0\right)\left(-2\varepsilon_m \hat{y}^2 + \alpha \hat{\Phi}(\hat{y})\hat{\kappa}_m\right)$$

$$\Updownarrow$$

$$4\varepsilon_m \hat{y}^2 \hat{\kappa}_m \lessgtr 2\varepsilon_m \alpha \hat{\Phi}(\hat{y})\hat{\kappa}_0 \hat{\kappa}_m$$

$$\Updownarrow$$

$$2\hat{y}^2 \lessgtr \alpha \hat{\Phi}(\hat{y})\hat{\kappa}_0,$$

where the last inequality leads to $\check{d} < 0$ since $2\hat{y}^2 > 0$ and $0 > \alpha \hat{\Phi}(\hat{y})\hat{\kappa}_0$ for $\hat{y} < 1$.

For the remaining regions of the evanescent $(\hat{k}, \omega)$-space, $\hat{y}^2 < 0$ and $\hat{\Phi}(\hat{y}) > 0$ while $\hat{\kappa}_0 > 0$ and $\hat{\kappa}_m > 0$ remain (see also appendix D.2). Then in the second to fourth line of the above inequalities, the inequality signs interchange and with $\hat{y}^2 < 0 < \hat{\Phi}(\hat{y})$, again the lower inequality is valid.

Thus in the complete evanescent region, only unphysical solutions with $\check{d} < 0$ exist. This in turn also requires that not a single mode crosses the border to the evanescent

region

$$
\begin{aligned}
\check{d}_{\hat{\kappa}_m=0} &= \lim_{\hat{\kappa}_m\to 0}\left\{\frac{1}{2\hat{\kappa}_m}\ln\left[\frac{\left(\hat{\kappa}_m-\varepsilon_m\hat{\kappa}_0\right)\left(2\varepsilon_m\hat{y}^2+\alpha\hat{\Phi}(\hat{y})\hat{\kappa}_m\right)}{\left(\hat{\kappa}_m+\varepsilon_m\hat{\kappa}_0\right)\left(-2\varepsilon_m\hat{y}^2+\alpha\hat{\Phi}(\hat{y})\hat{\kappa}_m\right)}\right]\right\}\\
&= \frac{1}{2}\lim_{\hat{\kappa}_m\to 0}\left\{\frac{1}{\hat{\kappa}_m-\varepsilon_m\hat{\kappa}_0}-\frac{1}{\hat{\kappa}_m+\varepsilon_m\hat{\kappa}_0}+\frac{\alpha\hat{\Phi}(\hat{y})}{2\varepsilon_m\hat{y}^2-\alpha\hat{\Phi}(\hat{y})\hat{\kappa}_m}+\frac{\alpha\hat{\Phi}(\hat{y})}{2\varepsilon_m\hat{y}^2+\alpha\hat{\Phi}(\hat{y})\hat{\kappa}_m}\right\}\\
&= \frac{1}{\varepsilon_m}\frac{\alpha\hat{\Phi}(\hat{y})\hat{\kappa}_0-\hat{y}^2}{\hat{\kappa}_0\hat{y}^2}<0\,,
\end{aligned}
$$

where the second line is obtained by the use of the rule by L'Hospital (see Ref. [161]). In Fig. 4.7(a), we display the TM modes for a slab of thickness $\check{d}=2.0$, $\varepsilon_m=4$ and $\alpha=1$. Equivalently to Eq. (4.27), we can determine the crossover wavevectors where the originally undamped, odd waveguide modes become damped as

$$
\hat{k}_{2n-1}[\hat{q}_{z,m}]=\sqrt{\frac{\varepsilon_m-\hat{q}_{z,m}^2}{1-\varepsilon_m\tilde{v}_{\mathrm{F}}^2}}\,, \tag{4.34a}
$$

$$
\check{d}[\hat{q}_{z,m}]=\frac{\pi\left(n-\frac{1}{2}\right)-\mathrm{atan}\left(\dfrac{\sqrt{1-\varepsilon_m\tilde{v}_{\mathrm{F}}^2}\hat{q}_{z,m}}{\varepsilon_m\sqrt{\left(\varepsilon_m-1\right)-\left(1-\varepsilon_m\tilde{v}_{\mathrm{F}}^2\right)\hat{q}_{z,m}^2}}\right)}{\hat{q}_{z,m}}\,. \tag{4.34b}
$$

In dashed lines, we present these solutions in Fig. 4.5(a) and mark the specific value of $\hat{k}$ in Fig. 4.7(a) by the dashed, gray line. Again, these values correspond to the value of the undisturbed even mode $2n$ at $\hat{y}=1$.

4.2.3 Graphene on a substrate

One of the driving research questions of this project was motivated by Ref. [156] where the authors found that the TE plasmonic resonance vanishes for even very tiny mismatches between the dielectric permittivity of the two materials above and below the graphene monolayer. Thus, we discuss in the following the modes for graphene on a(n) (in)finite substrate with air surrounding the sample.

TE polarization:

To better understand the TE plasmons when graphene is deposited on a single slab, we first discuss the solution for TE plasmons when the graphene layer is sandwiched between two different dielectric infinite half space and only later focus on the effect of a finite slab thickness. For the case of TE polarization, Eq. (4.9) becomes

$$
\alpha\hat{\Phi}(\hat{y})+\hat{\kappa}_0+\hat{\kappa}_m=0\,. \tag{4.35}
$$
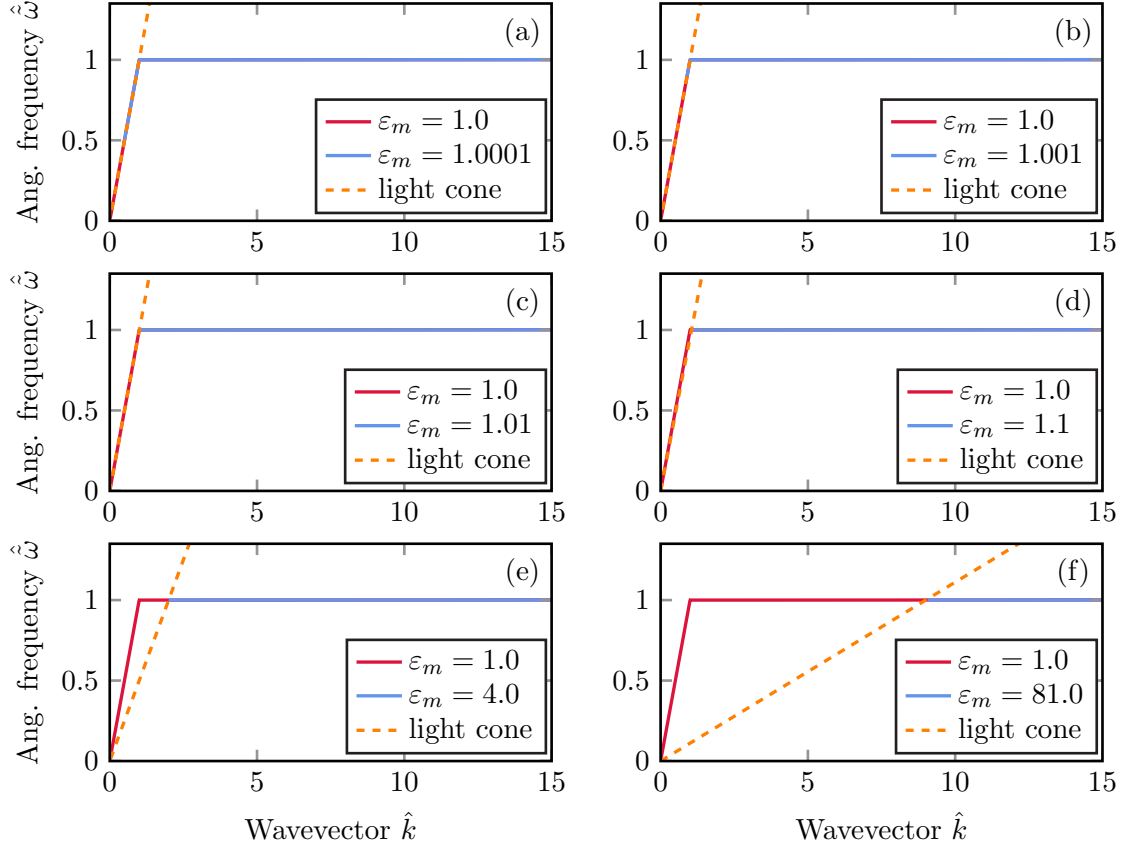
Figure 4.8: TE plasmonic resonances for graphene in vacuum deposited on different infinite dielectric substrates. we compare the solution to the solution for graphene in vacuum (red line) and indicate the substrate's light cone $\hat{\kappa}_m = 0$ by the orange dashed line. Adapted with permission from Ref. [W3], doi:10.1088/2040-8978/18/3/034001. © IOP Publishing. All rights reserved.

After some algebraic reformulations, we find the parametric solution

$$\hat{k}^2[\hat{y}] = \frac{\hat{\tilde{\omega}}[\hat{y}]^2 - \hat{y}^2}{\tilde{v}_{\mathrm{F}}^2} \tag{4.36a}$$

$$\hat{\tilde{\omega}}^2[\hat{y}] = \frac{\frac{4\hat{y}^2 + \alpha^2 \tilde{v}_{\mathrm{F}}^2 \hat{\Phi}(\hat{y})^2}{2 - (\varepsilon_m + 1)\tilde{v}_{\mathrm{F}}^2}}{1 + \sqrt{1 - \left(\frac{\varepsilon_m - 1}{2 - (\varepsilon_m + 1)\tilde{v}_{\mathrm{F}}^2}\right)^2 \frac{4\hat{y}^2 + \alpha^2 \tilde{v}_{\mathrm{F}}^2 \hat{\Phi}(\hat{y})^2}{\alpha^2 \tilde{v}_{\mathrm{F}}^2 \hat{\Phi}(\hat{y})^2}}} \,. \tag{4.36b}$$

Equation (4.36) is accompanied by the additional condition

$$\alpha^2 \hat{\Phi}(\hat{y})^2 \geq \hat{\kappa}_0^2 + \hat{\kappa}_m^2 \,, \tag{4.37}$$

which is lost from Eq. (4.35) when squaring it and stems from the fact that for all $\hat{y} < 1$ $\hat{\Phi}(\hat{y}) < 0$ while in the evanescent region $\hat{\kappa}_i > 0$ and thus Eq. (4.35) always allows for a solution.

4.2 Electromagnetic modes in dielectric-graphene-dielectric slab systems

In Fig. 4.8, we display the solutions to Eq. (4.36) for different values of the lower half space dielectric ε_m. Here, it is obvious that indeed TE plasmons exist even for very large offsets between the dielectric permittivity above the layer of graphene (vacuum) and the substrate (see, e.g., Fig. 4.8(f)). In fact, a TE plasmonic resonance exists for all

$$\varepsilon_m < \tilde{v}_{\mathrm{F}}^{-2} \approx 90.000 \,. \tag{4.38}$$

This is opposite to the case of zero band gap (compare Ref. [156]) and caused by the two very different regimes in the TE plasmonic mode's dispersion relation. Since for large wavevector values the phase velocity is mainly independent of the surrounding material (compare also Eq. (4.16)), in this region ($\hat{k} > \sqrt{\varepsilon_m/(1 - \varepsilon_m \tilde{v}_{\mathrm{F}}^2)}$) a TE plasmonic mode survives. In the case of zero band gap graphene, the TE plasmonic resonance only exhibits a mode structure where the mode is close to the surrounding dielectric's light cone (see also Refs. [57, 71]). Intuitively, the TE plasmonic mode disperses due to the different phase velocities (compare Eq. (4.14)) on both sides of the layer.

Having understood the appearance of a TE plasmonic resonance for a graphene-half space setup, we now turn to the more realistic case of graphene on a finite dielectric slab. This is the case, when in the experiment one studies graphene on a waver or a microscope slide. The mode condition reads as

$$r_m r_g - 1 = 0 \,, \tag{4.39}$$

thus concluding in

$$
\begin{aligned}
-\left(\alpha\hat{\Phi}(\hat{y}) + 2\hat{\kappa}_0\right)\hat{\kappa}_m \cosh\left(\check{d}\hat{\kappa}_m\right) & \\
-\left[\left(\alpha\hat{\Phi}(\hat{y}) + 2\hat{\kappa}_0\right)\hat{\kappa}_0 + \left(\hat{\kappa}_m^2 - \hat{\kappa}_0^2\right)\right]\sinh\left(\check{d}\hat{\kappa}_m\right) &= 0 \,.
\end{aligned}
\tag{4.40}
$$

Due to the asymmetry of the setup, only one set of solutions exist which contains exclusively modes altered by the inclusion of the graphene layer.

As seen in the two-slab setup it is helpful to study the existence of solutions by requiring a real and positive thickness of the substrate

$$\check{d} = \frac{1}{2\hat{\kappa}_m}\ln\left[\frac{\left(\alpha\hat{\Phi}(\hat{y}) + \hat{\kappa}_0 - \hat{\kappa}_m\right)\left(\hat{\kappa}_0 - \hat{\kappa}_m\right)}{\left(\alpha\hat{\Phi}(\hat{y}) + \hat{\kappa}_0 + \hat{\kappa}_m\right)\left(\hat{\kappa}_0 + \hat{\kappa}_m\right)}\right]. \tag{4.41}$$

When comparing Eq. (4.41) with Eq. (4.24), we realize that only small differences exist. This is due to the general similarity of both setups and the discussion for solutions in the propagating and SPE region still holds. The altered waveguiding solutions $n \geq 1$ lead to the exact same cutoff wavevector $\hat{k}_n$ as for the two-slab waveguide Eq. (4.27) with $\hat{k}_n = \hat{k}_{2n}$ where in the SPE region the modes become damped.

As seen in the case of graphene deposited on an infinite half space, the asymmetry in dielectric materials leads to a significant change of the TE plasmonic mode. Thus, we study the solutions to Eq. (4.41), requiring the argument of the logarithm to not only be
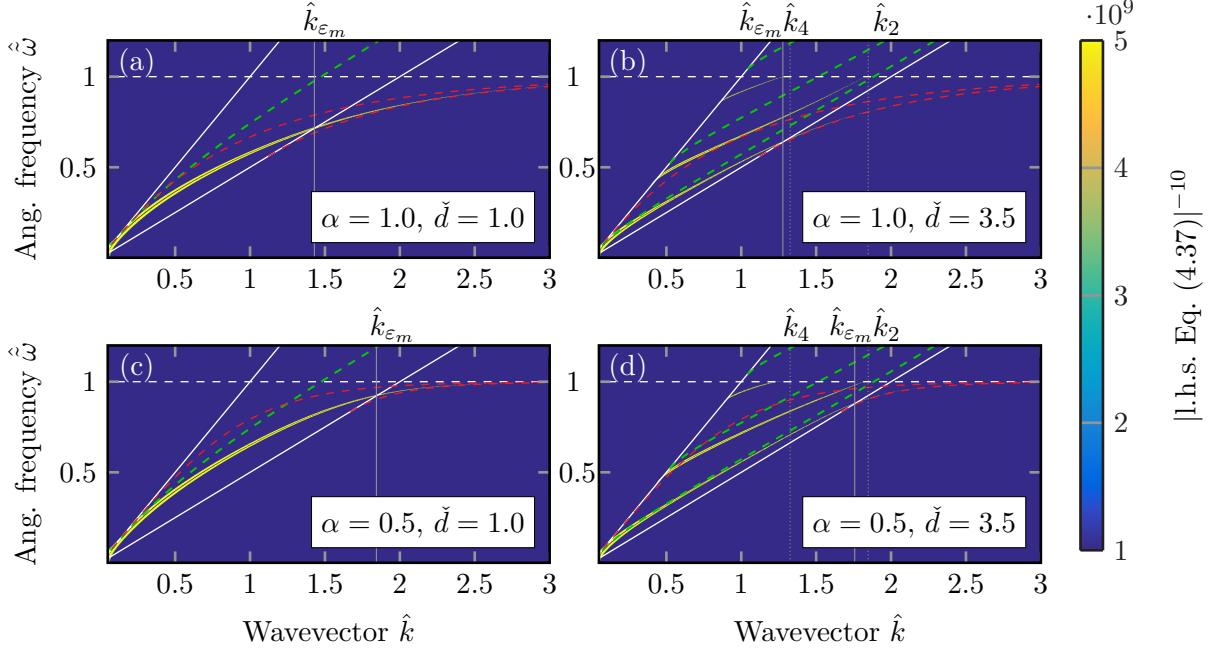
Figure 4.9: TE modes that exist in a waveguide consisting of graphene on top of a single dielectric slab ε_m. As in Fig. 4.4, we vary the value of α. The dashed, red curves present the solution for graphene in vacuum (upper curve) and graphene on top of an infinite dielectric substrate (lower curve), presented in Fig. 4.8. The cutoff values $\hat{k}_{2n}$ correspond to Fig. 4.5(a), solid lines, while the crossover wavevector values for which the zeroth mode's turn into an evanescent mode we present in Fig. 4.5(b), dashed lines. The green dashed lines present the pure dielectric waveguide solutions for a dielectric slab waveguide with $\varepsilon_m = 4.0$ and $\check{d}' = \check{d}$. Adapted with permission from Ref. [W3], doi:10.1088/2040-8978/18/3/034001. © IOP Publishing. All rights reserved.

positive but also

$$\frac{\left(\alpha\hat{\Phi}(\hat{y}) + \hat{\kappa}_0 - \hat{\kappa}_m\right)\left(\hat{\kappa}_0 - \hat{\kappa}_m\right)}{\left(\alpha\hat{\Phi}(\hat{y}) + \hat{\kappa}_0 + \hat{\kappa}_m\right)\left(\hat{\kappa}_0 + \hat{\kappa}_m\right)} > 1$$

$$\left(\alpha\hat{\Phi}(\hat{y}) + \hat{\kappa}_0 - \hat{\kappa}_m\right)\left(\hat{\kappa}_0 - \hat{\kappa}_m\right) \gtrless \left(\alpha\hat{\Phi}(\hat{y}) + \hat{\kappa}_0 + \hat{\kappa}_m\right)\left(\hat{\kappa}_0 + \hat{\kappa}_m\right)$$

$$\alpha\hat{\Phi}(\hat{y}) + 2\hat{\kappa}_0 \lessgtr 0 \, . \tag{4.42}$$

With the fact that in the evanescent region $\hat{\kappa}_0 \pm \hat{\kappa}_m > 0$, the two different cases in the second line above are caused by

$$\alpha\hat{\Phi}(\hat{y}) + \hat{\kappa}_0 \pm \hat{\kappa}_m \gtrless 0 \, ,$$

where we request the minimum condition of a real slab thickness. In Eq. (4.42), $\alpha\hat{\Phi}(\hat{y}) + 2\hat{\kappa}_0 < 0$ leads to a positive thickness when $\alpha\hat{\Phi}(\hat{y}) + \hat{\kappa}_0 \pm \hat{\kappa}_m > 0$. However, simply from

4.2 Electromagnetic modes in dielectric-graphene-dielectric slab systems

$\alpha\hat{\Phi}(\hat{y}) + 2\hat{\kappa}_0 < 0$ follows that

$$\alpha\hat{\Phi}(\hat{y}) + \hat{\kappa}_0 < -\hat{\kappa}_0$$

$$\Updownarrow$$

$$\alpha\hat{\Phi}(\hat{y}) + \hat{\kappa}_0 - \hat{\kappa}_m < -(\hat{\kappa}_0 + \hat{\kappa}_m) < 0 \quad \text{and} \quad \alpha\hat{\Phi}(\hat{y}) + \hat{\kappa}_0 + \hat{\kappa}_m < -(\hat{\kappa}_0 - \hat{\kappa}_m) < 0\,.$$

This is a contradiction and does therefore not lead to a physical solution. The TE plasmon therefore exists for the pairs $(\hat{k}, \hat{\tilde{\omega}})$ for which

$$\alpha\hat{\Phi}(\hat{y}) + 2\hat{\kappa}_0 > 0, \qquad \alpha\hat{\Phi}(\hat{y}) + \hat{\kappa}_0 + \hat{\kappa}_m < 0\,, \tag{4.43}$$

where the last condition automatically leads to $\alpha\hat{\Phi}(\hat{y}) + \hat{\kappa}_0 - \hat{\kappa}_m < 0$. In other words, since $\hat{\kappa}_0$ is monotonically growing and $\hat{\Phi}(\hat{y}) < 0$, the condition $\alpha\Phi + 2\hat{\kappa}_0 > 0$ is always fulfilled in the area below the TE plasmonic resonance for graphene in vacuum.

The condition $\alpha\hat{\Phi}(\hat{y}) + \hat{\kappa}_0 + \hat{\kappa}_m < 0$ is with the same line of argument only fulfilled in the area above the TE plasmonic dispersion relation for graphene on an infinite substrate. Thus, the TE plasmonic resonance for graphene deposited on a finite substrate lies between the TE plasmonic dispersion for graphene in vacuum and graphene on an infinite substrate.

This, we present in Fig. 4.9 where the zeroth waveguide mode lies between the two dashed, red lines representing these two solutions. Additionally, the slab's thickness in the waveguiding region is given by

$$\check{d} = -\frac{\text{atan}\left(\frac{\hat{k}_{z,m}}{\hat{\kappa}_0}\right) + \text{atan}\left(\frac{\hat{k}_{z,m}}{\alpha\hat{\Phi}(\hat{y}) + \hat{\kappa}_0}\right) + n\pi}{\hat{k}_{z,m}}\,, \tag{4.44}$$

for $n = 1, 2, \ldots$ and for $n = 0$ with the additional condition $\alpha\hat{\Phi}(\hat{y}) + 2\hat{\kappa}_0 > 0$ applies (compare also Eq. (4.43) and following discussion) the crossover between waveguiding and evanescent regime is given by

$$\hat{k}_{\varepsilon_m}[q] = \sqrt{\frac{\varepsilon_m}{1 - \varepsilon_m\tilde{v}_{\text{F}}^2}}\tanh q \tag{4.45a}$$

$$\check{d}[q] = -\frac{2 + \frac{\alpha\hat{\Phi}[\tanh(q)]}{\tanh(q)}\sqrt{\frac{1 - \varepsilon_m\tilde{v}_{\text{F}}^2}{\varepsilon_m - 1}}}{\alpha\hat{\Phi}[\tanh(q)] + \sqrt{\frac{\varepsilon_m - 1}{1 - \varepsilon_m\tilde{v}_{\text{F}}^2}}\tanh(q)}\,, \tag{4.45b}$$

and displayed in Fig. 4.5(b) by the dashed lines.

TM polarization:

As before, for the case of graphene deposited on a substrate also TM modes exist. Additionally, also as in the case of a graphene layer on top of a dielectric half space, the TM plasmon condition following from Eq. (4.9)

$$\alpha\hat{\Phi}(\hat{y}) = \hat{y}^2\left(\frac{\varepsilon_m}{\hat{\kappa}_m} + \frac{1}{\hat{\kappa}_0}\right)\,, \tag{4.46}$$

can never be fulfilled. Again (cf. appendix D.2) we can split the evanescent region into two regions with (a) $0 < \hat{y}^2 < 1$ (then $\hat{\Phi}(\hat{y}) < 0$) and (b) $\hat{y}^2 < 0$ (then $\hat{\Phi}(\hat{y}) > 0$). With $\left(\frac{\varepsilon_m}{\hat{\kappa}_m} + \frac{1}{\hat{\kappa}_0} \right) > 0$, this always leads to an opposite sign between the l.h.s and the r.h.s of Eq. (4.46). As discussed in Eq. (D.8), the solution $\hat{y} = 0$ does indeed fulfill Eq. (4.46) but corresponds to a liftable singularity of r_g^{TM} (see Eq. (2.44)).

When considering the TM modes supported by a graphene monolayer on top of a finite dielectric slab given by

$$\alpha\hat{\Phi}(\hat{y})\hat{\kappa}_0\hat{\kappa}_m \left[\varepsilon_m\hat{\kappa}_0 \sinh\left(\check{d}\hat{\kappa}_m \right) + \hat{\kappa}_m \cosh\left(\check{d}\hat{\kappa}_m \right) \right]$$
$$- \hat{y}^2 \left[(\varepsilon_m^2\hat{\kappa}_0^2 + \hat{\kappa}_m^2) \sinh\left(\check{d}\hat{\kappa}_m \right) + 2\varepsilon_m\hat{\kappa}_0\hat{\kappa}_m \cosh\left(\check{d}\hat{\kappa}_m \right) \right] = 0 \,, \tag{4.47}$$

the mode condition in terms of the slab thickness reads

$$\check{d} = \frac{1}{2\hat{\kappa}_m} \ln \left\{ \frac{(\hat{\kappa}_m - \varepsilon_m\hat{\kappa}_0)[(-\alpha\hat{\Phi}(\hat{y})\hat{\kappa}_0 + \hat{y}^2)\hat{\kappa}_m - \varepsilon_m\hat{\kappa}_0\hat{y}^2]}{(\hat{\kappa}_m + \varepsilon_m\hat{\kappa}_0)[(-\alpha\hat{\Phi}(\hat{y})\hat{\kappa}_0 + \hat{y}^2)\hat{\kappa}_m + \varepsilon_m\hat{\kappa}_0\hat{y}^2]} \right\} \,. \tag{4.48}$$

In the evanescent region, with

$$(-\alpha\hat{\Phi}(\hat{y})\hat{\kappa}_0 + \hat{y}^2)\hat{\kappa}_m + \varepsilon_m\hat{\kappa}_0\hat{y}^2 \begin{cases} > 0 \,\text{for}\, \hat{y}^2 > 0 \\ < 0 \,\text{for}\, \hat{y}^2 < 0 \end{cases} \,, \tag{4.49}$$

we start by excluding the existence of a TM mode in the evanescent region for which $\hat{y}^2 > 0$ since that is the valid condition for most of the (k, ω)-parameter space (cf. appendix D.2). With

$$\frac{(\hat{\kappa}_m - \varepsilon_m\hat{\kappa}_0)[(-\alpha\hat{\Phi}(\hat{y})\hat{\kappa}_0 + \hat{y}^2)\hat{\kappa}_m - \varepsilon_m\hat{\kappa}_0\hat{y}^2]}{(\hat{\kappa}_m + \varepsilon_m\hat{\kappa}_0)[(-\alpha\hat{\Phi}(\hat{y})\hat{\kappa}_0 + \hat{y}^2)\hat{\kappa}_m + \varepsilon_m\hat{\kappa}_0\hat{y}^2]} \gtrless 1$$
$$(\hat{\kappa}_m - \varepsilon_m\hat{\kappa}_0)[(-\alpha\hat{\Phi}(\hat{y})\hat{\kappa}_0 + \hat{y}^2)\hat{\kappa}_m - \varepsilon_m\hat{\kappa}_0\hat{y}^2] \gtrless (\hat{\kappa}_m + \varepsilon_m\hat{\kappa}_0) \cdot$$
$$\cdot [(-\alpha\hat{\Phi}(\hat{y})\hat{\kappa}_0 + \hat{y}^2)\hat{\kappa}_m + \varepsilon_m\hat{\kappa}_0\hat{y}^2]$$
$$-\alpha\hat{\Phi}(\hat{y})\hat{\kappa}_0 + 2\hat{y}^2 \lessgtr 0 \,,$$

we find that since $-\alpha\hat{\Phi}(\hat{y})\hat{\kappa}_0 + 2\hat{y}^2 > 0$ no mode exists ($\check{d} < 0$). Also for the (k, ω)-values for which $\hat{y}^2 < 0$, we find that the upper and lower inequality signs in lines two and three switch such that the last inequality reads

$$-\alpha\hat{\Phi}(\hat{y})\hat{\kappa}_0 + 2\hat{y}^2 \gtrless 0 \,,$$

which is in the region with $\hat{y}^2 < 0$ only true for the lower of the two cases. Thus, since $\check{d} < 0$ for all $\hat{y}^2 \in \mathbb{R}$, no TM mode is allowed in the evanescent region.

As in Eq. (4.34a), we can also show that for $\hat{\kappa}_m = 0$ no positive and thus physical slab thickness is allowed. Last, as in the TE polarization case, we can determine the crossing

of the waveguiding modes into the SPE region that correspond to Eq. (4.34)

$$\hat{k}_n[\hat{q}_{z,m}] = \sqrt{\frac{\varepsilon_m - \hat{q}_{z,m}^2}{1 - \varepsilon_m \tilde{v}_{\mathrm{F}}^2}} \,, \tag{4.50a}$$

$$\check{d}[\hat{q}_{z,m}] = \frac{\pi n - \mathrm{atan}\left(\dfrac{\sqrt{1-\varepsilon_m \tilde{v}_{\mathrm{F}}^2}\,\hat{q}_{z,m}}{\varepsilon_m \sqrt{(\varepsilon_m - 1) - \left(1 - \varepsilon_m \tilde{v}_{\mathrm{F}}^2\right)\hat{q}_{z,m}^2}}\right)}{\hat{q}_{z,m}} \,. \tag{4.50b}$$

As for the TE modes, this crossover condition corresponds to the crossover condition for the graphene monolayer embedded between two identical dielectric slabs. Thus, the dashed lines in Fig. 4.5(a) also presents the solutions to Eqs. (4.50). The TM modes for a graphene monolayer deposited on top of a dielectric slab, we display in Fig. 4.7(b). There, we show the exemplary result for $\alpha = 1$ and $\check{d} = 4$ for a non-dispersive dielectric slab with $\varepsilon_m = 4.0$.

4.2.4 Conclusions

In this section (in main parts published in Ref. [W3]), we show that TE plasmonic resonances actually remain when graphene with a band gap in its energy level structure is sandwiched between two dielectrics with a large contrast in refractive index. Additionally, these TE plasmonic resonances even remain in existence when instead of an infinite half space, experimentally more reasonable finite slabs are considered. The influence of the finite slab thickness is especially large for wavevectors at which the TE plasmonic resonance is close to the vacuum's and medium's light cone since in this cases the decay length $\propto \hat{q}_{i,z}^{-1}$ is much larger than for metallic TM plasmons.

Additionally, we show that for TM polarization in undoped graphene indeed no TM plasmonic resonance crossing the slab's light cone can be excited. From the modes appearing in a finite slab waveguide, only the isolated, TE plasmonic mode survives in graphene embedded in an infinite sized medium.

Of special interest is the influence of graphene's SPEs. They lead to a cut-off frequency at which the lossless waveguide modes become damped modes. This is due to the loss mechanisms induced by the electron-hole creation. In conclusion the quantum properties of graphene effect not only the TE plasmonic mode (that in the case of gapless graphene sandwiched between two dielectrics only can be excited for small refractive index offsets) but also the remaining waveguide modes.

The detailed knowledge of the dispersion relation of the modes in dielectric-graphene-dielectric systems, we use in the next section for a discussion of the influence of the photonic local density of states on the lifetimes of electric and magnetic emitters.

4.3 Determining the band gap of graphene using electric and magnetic emitters

As we mention in the introduction to this chapter, some of the exotic properties of graphene, especially the band gap and the influence of external factors on it, are still

4 Magnetic and electric emitters above graphene
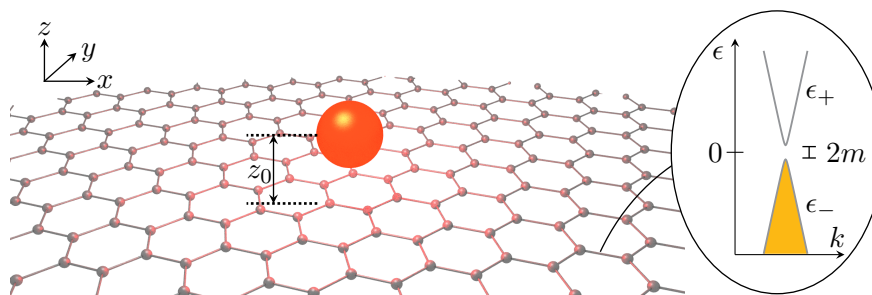
Figure 4.10: Sketch of an emitter above graphene. In this section, we exclusively consider graphene exhibiting a band gap with the electronic dispersion relation $\epsilon_\pm$ given in Eq. (2.19). As in the previous section, the band gap $\Delta = 2m/(\hbar c)$ is normalized. The electronic states are filled up to a chemical potential $\mu = 0$ where the filled band is marked by the yellow area. The emitter is positioned at a distance z_0 from the graphene monolayer at $z = 0$. Adapted with permission from J. F. M. Werra *et al.,* "Determining graphene's induced band gap with magnetic and electric emitters", Phys. Rev. B **93,** 081404(R) (2016), doi:10.1103/PhysRevB.93.081404. © 2016 by the American Physical Society.

subject of discussion in the scientific community. The understanding and mapping of this band gap and other electronic properties are of interest since the special features of graphene's band structure lead to a wide range of unusual phenomena such as the observation of ballistic transport (see Ref. [162]), the quantum Hall effect (see Refs. [163, 164]), and the specifics of its thermal (see Ref. [165]) and electric conductivity (see Refs. [147, 166]). Here, as well as published in Ref. [W4], we thus show how magnetic and electric emitters can be used to determine specifically the exact band gap of a monolayer of graphene with high spectral and spatial precision. Additionally, we can validate the limits of the models applied to the description of graphene within this section by testing the scaling behavior of the lifetime modifications with respect to the emitter's transition frequency and distance variations.

For emitters above an atomic monolayer, small lifetime modifications as compared to plasmonic nanostructures (e.g., a factor 10^{-3} of lifetime reduction for a dipole $1\,\mathrm{nm}$ distant from a $10\,\mathrm{nm}$ silver sphere, cf. Ref. [167]) might be expected. This expectation corresponds to the small optical response of the system as measured by Nair and co-workers (see Ref. [75], Eq. (2.50) and Fig. 2.2, with a transmission of $\approx 98\%$). On the other hand, considering the fact that graphene is a mono-atomic layer it is promising for the light-matter coupling that nonetheless the monolayer has a visible effect on the transmitted light. As discussed in the previous section of this work, the electromagnetic mode density is highly altered when considering graphene with a band gap in between two dielectrics. There, the strongest influence due to the graphene monolayer is caused by the TE plasmonic resonance and the additional loss channel by the SPE region when the electromagnetic fields impinging carry sufficient energy to excite electron-hole pairs. Thus, for a better understanding of the basic mechanisms induced by the graphene monolayer we study in this section explicitly the lifetime modifications due to graphene embedded in an infinite, linear, non-dissipative, non-dispersive, isotropic and local dielectric of di-

4.3 Determining the band gap of graphene using electric and magnetic emitters

electric permittivity ε_m (see Fig. 4.10 for a sketch of the setup). This way, we exclude well-known effects caused by, e.g., the waveguide modes due to the finite thickness of the dielectric substrate (see, e.g., Ref. [124]).

In order to analyze the lifetime modifications in detail, we define the decay rate (cf. Eq. (3.42))

$$\frac{\gamma}{\gamma_0} = 1 + \mathcal{L}\left[\frac{\alpha_\parallel^2}{|\boldsymbol{\alpha}|^2}\Gamma^\parallel + \frac{\alpha_\perp^2}{|\boldsymbol{\alpha}|^2}\Gamma^\perp\right], \tag{4.51}$$

with the decay rate γ_0 of an emitter surrounded exclusively by the dielectric (ε_m), the correction $\mathcal{L}$ due to the local field correction ξ discussed in section 3.2.5 (for $\varepsilon_m = 1$: $\mathcal{L} = 1$) and the matrix elements of the electric (magnetic) dipole moments $\boldsymbol{\alpha} = \mathbf{d}$ ($\boldsymbol{\alpha} = \boldsymbol{\mu}$) where in the case of $\alpha_\perp$ the dipole moment is oriented orthogonal to the graphene monolayer while for $\alpha_\parallel$ it is oriented parallel to the graphene monolayer. The total dipole moment is then given by $|\alpha|^2 = \alpha_\parallel^2 + \alpha_\perp^2$ that lead to $\alpha_\parallel^2 = \alpha_x^2 + \alpha_y^2$ and $\alpha_\perp = \alpha_z$ when we employ the Cartesian coordinate system defined in Fig. 4.10.

Since the magnitude of the dipole moments depends on the emitter used in the specific experimental setup and, additionally, when we only consider lossless, dispersionless, isotropic and local dielectrics the correction $\mathcal{L}$ is dispersionless, we will in the following only discuss Γ^i where $i = \{\parallel, \perp\}$.

The graphene monolayer modifies the photonic local density of states with respect to three different regions (compare also the previous section and Fig. 4.3): the propagating ($\tilde{\omega}_0 \geq k$), the evanescent ($\tilde{\omega} < k$) and the SPE ($\tilde{\omega}_0 > \sqrt{\Delta^2 + \tilde{v}_F^2 k^2}$) regime. Due to the overlap of these three regions, for the contributions to the modifications of the decay rate we add up both SPE and non-SPE region for the propagating electromagnetic modes calling the contribution *radiative* (Γ_r^i) while additionally distinguishing between SPE (Γ_{SPE}^i) and *plasmonic* (Γ_p^i) contribution for the evanescent regimes. Accordingly, we find for $i = \{\parallel, \perp\}$

$$\Gamma^i = \Gamma_r^i + \Gamma_{SPE}^i + \Gamma_p^i. \tag{4.52}$$

4.3.1 Lifetime modifications of a magnetic emitter

Following Ref. [124, 129], the lifetime modifications of a magnetic emitter placed above a 2D infinitely extended, electromagnetic boundary condition is obtained by exchanging with each other the TE and TM reflection coefficients for the altered decay rate of an electric emitter. Such a 2D infinitely extended, electromagnetic boundary condition is oftentimes the interface between two dielectric or metallic half spaces but in our case obviously the graphene monolayer embedded in the infinite dielectric ε_m. With the electric

4 Magnetic and electric emitters above graphene

emitter's decay rate modification (see Ref. [28]), we then arrive at

$$\Gamma^{\parallel}_{\mathrm{magn.}}(\hat{\tilde{\omega}},\check{z}_0) = \frac{3}{4}\frac{1}{\varepsilon_m^{3/2}\hat{\tilde{\omega}}_0^3}\mathrm{Im}\left[\int_{-\mathrm{i}\sqrt{\varepsilon_m}\hat{\tilde{\omega}}}^{\infty}\left[\varepsilon_m\hat{\tilde{\omega}}^2 r^{\mathrm{TM}}+\hat{\kappa}_m^2 r^{\mathrm{TE}}\right]\mathrm{e}^{-2\hat{\kappa}_m\check{z}_0}\mathrm{d}\hat{\kappa}_m\right], \qquad (4.53)$$

$$\Gamma^{\perp}_{\mathrm{magn.}}(\hat{\tilde{\omega}},\check{z}_0) = \frac{3}{2}\frac{1}{\varepsilon_m^{3/2}\hat{\tilde{\omega}}^3}\mathrm{Im}\left[\int_{-\mathrm{i}\sqrt{\varepsilon_m}\hat{\tilde{\omega}}}^{\infty}\left(\varepsilon_m\hat{\tilde{\omega}}^2+\hat{\kappa}_m^2\right)r^{\mathrm{TE}}\mathrm{e}^{-2\hat{\kappa}_m\check{z}_0}\mathrm{d}\hat{\kappa}_m\right], \qquad (4.54)$$

where we use as before normalized quantities (cf. Eqs. (2.34) and (4.11)) with the emitter-graphene distance $\check{z}_0 = \Delta z_0$ (cf. Fig. 4.10). The emitter's transition (angular) frequency is $\hat{\tilde{\omega}} = \hat{\tilde{\omega}}_0$, the dielectric out-of-plane wavevector is $\hat{\kappa}_m^2 = \hat{k}^2 - \varepsilon_m\hat{\tilde{\omega}}^2$ and the reflection coefficients for a graphene monolayer embedded in a dielectric medium follow from Eq. (4.8a) and read as

$$r^{\mathrm{TM}} = \frac{\alpha\hat{\tilde{\Phi}}(\hat{y})\hat{\kappa}_m}{\alpha\hat{\tilde{\Phi}}(\hat{y})\hat{\kappa}_m - \hat{y}^2}, \qquad (4.55)$$

$$r^{\mathrm{TE}} = -\frac{\alpha\hat{\tilde{\Phi}}(\hat{y})}{2\hat{\kappa}_m + \alpha\hat{\tilde{\Phi}}(\hat{y})}. \qquad (4.56)$$

Above, we additionally use the definitions $\hat{y} = \sqrt{\hat{\tilde{\omega}}^2 - \tilde{v}_{\mathrm{F}}^2\hat{k}^2}$ given in Eq. (2.35) and

$$\hat{\tilde{\Phi}}(\hat{y}) = 2\left[1 - \frac{\hat{y}^2+1}{\hat{y}}\mathrm{atanh}(\hat{y})\right],$$

introduced in Eq. (2.42).

Besides from a direct computation of the corresponding integrals (with appropriate integral limits for the three different regions) utilizing the commercial software Mathematica (see Ref. [168], lines in all following Figures), we present in the following the limiting cases for small and large distances and frequencies, respectively. From this we are able to determine the power laws for the distance and frequency dependence of the magnetic decay rates.

TE plasmonic contribution

Starting with the contribution due to the TE plasmonic resonance, we define a function of the denominator of r^{TE} in Eq. (4.56)

$$\Psi(\hat{y}) \equiv \frac{1}{\tilde{v}_{\mathrm{F}}}\sqrt{\frac{\hat{\tilde{\omega}}^2}{\hat{\tilde{\omega}}_\Delta^2} - \hat{y}^2} + \alpha\left[1 - \frac{\hat{y}^2+1}{\hat{y}}\mathrm{atanh}(\hat{y})\right], \qquad (4.57)$$

where we reformulate $\tilde{v}_{\mathrm{F}}\hat{\kappa}_m = \sqrt{\hat{\tilde{\omega}}^2/\hat{\tilde{\omega}}_\Delta^2 - \hat{y}^2}$. In the proximity of the plasmonic mode $\hat{y} \approx \hat{y}_{\mathrm{p}}$ (cf. Eq. (4.12)), we write

$$\Psi(\hat{y}) = \Psi'(\hat{y}_{\mathrm{p}}) \cdot (\hat{y} - \hat{y}_{\mathrm{p}}) + \mathcal{O}[(\hat{y} - \hat{y}_{\mathrm{p}})^2], \qquad (4.58)$$

4.3 Determining the band gap of graphene using electric and magnetic emitters

approximating in the following the denominator to first order in $\hat{y} - \hat{y}_{\mathrm{p}}$ (for a collective resonance, the denominator $\Psi(\hat{y}_{\mathrm{p}}) = 0$) with

$$\Psi'(\hat{y}) = \frac{-\hat{y}}{\tilde{v}_{\mathrm{F}}\sqrt{\hat{\tilde{\omega}}^2/\hat{\tilde{\omega}}_\Delta^2 - \hat{y}^2}} - \alpha\left[\frac{\hat{y}^2 - 1}{\hat{y}^2}\mathrm{atanh}(\hat{y}) + \frac{\hat{y}^2 + 1}{\hat{y}(1 - \hat{y}^2)}\right]. \qquad (4.59)$$

Here, we have to distinguish between the TE plasmonic modes for frequencies below $\hat{\tilde{\omega}} < \hat{\tilde{\omega}}_\Delta$ ($\hat{y} \ll 1$) and above $\hat{\tilde{\omega}} > \hat{\tilde{\omega}}_\Delta$ ($\hat{y} \to 1^-$). Doing so, we can then estimate the derivative of the denominator as

$$\Psi'_{\hat{y}<1}(\hat{y}) \approx \frac{-\hat{y}}{\tilde{v}_{\mathrm{F}}\sqrt{\hat{\tilde{\omega}}^2/\hat{\tilde{\omega}}_\Delta^2 - \hat{y}^2}}, \qquad (4.60)$$

$$\Psi'_{\hat{y}\to1^-}(\hat{y}) \approx \alpha\left[(1 - \hat{y})\ln\left(\frac{1 - \hat{y}}{2}\right) + \frac{1}{1 - \hat{y}} - \frac{1}{2}\right] \approx \frac{\alpha}{1 - \hat{y}}, \qquad (4.61)$$

where we obtain the approximation in the last line by expanding Eq. (4.59) with

$$\frac{\hat{y}^2 - 1}{\hat{y}^2}\mathrm{atanh}(\hat{y}) \overset{\hat{y}\to1^-}{\approx} (1 - \hat{y})\ln\left(\frac{1 - \hat{y}}{2}\right)$$

$$\frac{\hat{y}^2 + 1}{\hat{y}(1 - \hat{y}^2)} \overset{\hat{y}\to1^-}{\approx} \frac{1}{1 - \hat{y}} - \frac{1}{2}.$$

Further on employing Sokhotsky's formula (see Eq. (3.32)), we can express the reflection coefficient as

$$r^{\mathrm{TE}} \approx \frac{\alpha\hat{\Phi}(\hat{y})}{\Psi'(\hat{y}_{\mathrm{p}})\cdot(\hat{y} - \hat{y}_{\mathrm{p}})} = \mathcal{P}\frac{\alpha\hat{\Phi}(\hat{y})}{\Psi'(\hat{y}_{\mathrm{p}})}\frac{1}{\hat{y} - \hat{y}_{\mathrm{p}}} - \mathrm{i}\pi\frac{\alpha\hat{\Phi}(\hat{y})}{\Psi'(\hat{y}_{\mathrm{p}})}\delta(\hat{y} - \hat{y}_{\mathrm{p}}).$$

In conclusion, we insert this expression into the modified lifetime Eqs. (4.53) and (4.54) for which we choose the lower boundary of the integrals to be zero since the TE plasmonic mode is located exclusively in the evanescent region (cf. section 4.2.1). Since we have shown previously that r^{TM} is purely real in this region (see also section 4.2.1), we find with $\hat{y}_{\mathrm{p}} < 1$ (see Eq. (D.3) for the explicit expression for $\hat{y}_{\mathrm{p}}^2$)

$$\Gamma^{\parallel}_{\mathrm{magn.,p}}(\hat{\tilde{\omega}} < \hat{\tilde{\omega}}_\Delta, \check{z}_0) = \frac{3}{4}\int_0^\infty \frac{\hat{\kappa}_m^2}{\varepsilon_m^{3/2}\hat{\tilde{\omega}}_0^3}\mathrm{Im}\left[r^{\mathrm{TE}}\right]\mathrm{e}^{-2\hat{\kappa}_m\check{z}_0}\mathrm{d}\hat{\kappa}_m \approx \frac{16\alpha^3\pi}{9\varepsilon_m^{3/2}}\frac{\hat{\tilde{\omega}}_0^3}{\hat{\tilde{\omega}}_\Delta^3}\mathrm{e}^{-\check{z}_0/\check{\zeta}}, \qquad (4.62a)$$

$$\Gamma^{\perp}_{\mathrm{magn.,p}}(\hat{\tilde{\omega}} < \hat{\tilde{\omega}}_\Delta, \check{z}_0) = \frac{3}{2}\int_0^\infty \frac{\varepsilon_m\hat{\tilde{\omega}}^2 + \hat{\kappa}_m^2}{\varepsilon_m^{3/2}\hat{\tilde{\omega}}^3}\mathrm{Im}\left[r^{\mathrm{TE}}\right]\mathrm{e}^{-2\hat{\kappa}_m\check{z}_0}\mathrm{d}\hat{\kappa}_m$$

$$\approx \frac{2\alpha\pi}{\sqrt{\varepsilon_m}}\frac{\hat{\tilde{\omega}}_0}{\hat{\tilde{\omega}}_\Delta^2}\mathrm{e}^{-\check{z}_0/\check{\zeta}}, \qquad (4.62b)$$

where the characteristic decay length is defined as

$$\check{\zeta} = \frac{3}{8\alpha}\frac{\hat{\tilde{\omega}}_\Delta^2}{\hat{\tilde{\omega}}^2}. \qquad (4.63)$$
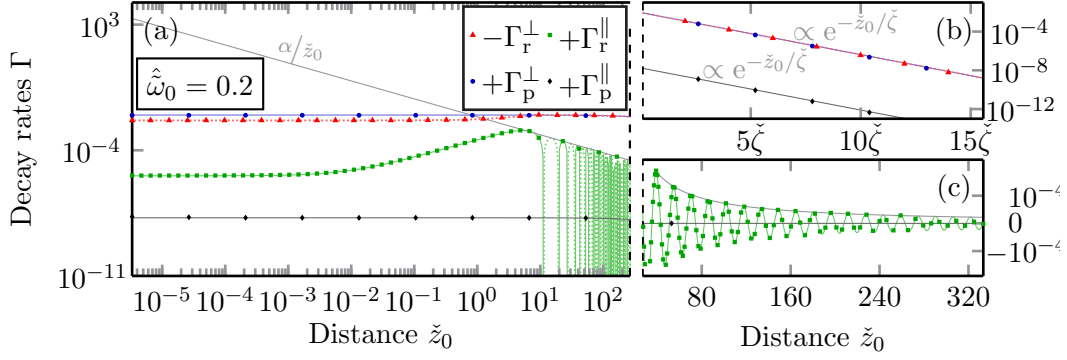
Figure 4.11: Modification of the magnetic emitter's decay rates when varying the emitter-graphene distance. The emitter is dispersed in vacuum ($\varepsilon_m = 1$). In panel (a), we present results for $\hat{\tilde{\omega}}_0 = 0.2$ on a double-logarithmic scale, extending this scale to a semilogarithmic (b) and linear (c) scale to depict the characteristics of the distance dependence for plasmonic as well as perpendicular radiative and parallel radiative, respectively. The analytical values for negative contributions are depicted by dashed lines. Adapted with permission from J. F. M. Werra *et al.*, "Determining graphene's induced band gap with magnetic and electric emitters", Phys. Rev. B **93,** 081404(R) (2016), doi:10.1103/PhysRevB.93.081404. ⓒ 2016 by the American Physical Society.

Due to the magnitude of $\check{\zeta}$, this brings about a very weak exponential distance dependence (cf. blue and black lines in Fig. 4.11(a-c)).

Moving from the small frequency limit to the limit of large transition frequencies (corresponding to $\hat{y} \to 1^-$) where $\hat{y}_{\mathrm{p}}$ is defined in Eq. (D.2), we obtain the following decay rates:

$$\Gamma^{\|}_{\mathrm{magn.,p}}(\hat{\tilde{\omega}} > \hat{\tilde{\omega}}_\Delta, \check{z}_0) \approx \frac{3\pi \left(\frac{\hat{\tilde{\omega}}^2}{\hat{\tilde{\omega}}_\Delta^2} - 1\right) \mathrm{e}^{-(1 + \frac{\sqrt{\hat{\tilde{\omega}}^2 - \hat{\tilde{\omega}}_\Delta^2}}{\alpha \tilde{v}_{\mathrm{F}} \hat{\tilde{\omega}}_\Delta})}}{2\alpha \tilde{v}_{\mathrm{F}}^4 (\sqrt{\varepsilon_m}\hat{\tilde{\omega}})^3} \exp\left(-2\check{z}_0 \frac{\sqrt{\hat{\tilde{\omega}}^2 - \hat{\tilde{\omega}}_\Delta^2}}{\tilde{v}_{\mathrm{F}}\hat{\tilde{\omega}}_\Delta}\right), \quad (4.64a)$$

$$\Gamma^{\perp}_{\mathrm{magn.,p}}(\hat{\tilde{\omega}} > \hat{\tilde{\omega}}_\Delta, \check{z}_0) \approx \frac{3\pi \left(\hat{\tilde{\omega}}^2 - 1\right) \mathrm{e}^{-(1 + \frac{\sqrt{\hat{\tilde{\omega}}^2 - \hat{\tilde{\omega}}_\Delta^2}}{\alpha \tilde{v}_{\mathrm{F}} \hat{\tilde{\omega}}_\Delta})}}{\alpha \tilde{v}_{\mathrm{F}}^4 (\sqrt{\varepsilon_m}\hat{\tilde{\omega}})^3} \exp\left(-2\check{z}_0 \frac{\sqrt{\hat{\tilde{\omega}}^2 - \hat{\tilde{\omega}}_\Delta^2}}{\tilde{v}_{\mathrm{F}}\hat{\tilde{\omega}}_\Delta}\right). \quad (4.64b)$$

When we insert explicit numbers into the expressions above, we obtain values on the order of 1e−100 unless $\hat{\tilde{\omega}} \approx \hat{\tilde{\omega}}_\Delta$ which is due to the small values $\tilde{v}_{\mathrm{F}} \approx 300^{-1}$ and $\alpha = 137^{-1}$.

Thus, for transition frequencies $\hat{\tilde{\omega}}_0 > \hat{\tilde{\omega}}_\Delta$, the modification of the decay rate due to the TE plasmonic mode is much smaller than the alteration due to all other contributions (see below and Figs. 4.12 and 4.13). From a physical point of view, this can be understood when realizing that indeed the TE plasmonic mode deviates largely from the material's light cone $\sqrt{\varepsilon_m}\hat{\tilde{\omega}} = k$. Even though an emitter of transition frequency $\hat{\tilde{\omega}}_0$ emits electromagnetic radiation with a broad range of wavevector values, the emission intensity with these wavevector components that couple to the TE plasmonic mode decreases the further the mode deviates from the material's light cone. In the very proximity of the

kink $\hat{\hat{\omega}}_0 \approx \hat{\hat{\omega}}_\Delta$, the TE plasmonic mode is still in the proximity of the material's light cone and thus not as strongly suppressed.

Radiative contribution

Next we focus on the radiative contributions to the changes in the magnetic emitter's lifetime. Here, we change the integral limits in Eqs. (4.53) and (4.54) to

$$
\begin{aligned}
\Gamma_{\text{magn.,r}}^{\parallel}(\hat{\hat{\omega}}, \check{z}_0) &= \frac{3}{4} \frac{1}{\varepsilon_m^{3/2} \hat{\hat{\omega}}_0^3} \text{Im} \left[\int_{-i\sqrt{\varepsilon_m}\hat{\hat{\omega}}}^{0} \left[\varepsilon_m \hat{\hat{\omega}}^2 r^{\text{TM}} + \hat{\kappa}_m^2 r^{\text{TE}} \right] e^{-2\hat{\kappa}_m \check{z}_0} d\hat{\kappa}_m \right] \\
&= \frac{3}{4} \frac{1}{\varepsilon_m^{3/2} \hat{\hat{\omega}}_0^3} \text{Re} \left[\int_{0}^{\sqrt{\varepsilon_m}\hat{\hat{\omega}}} d\hat{q}_{m,z} (\varepsilon_m \hat{\hat{\omega}}^2 r^{\text{TM}} - \hat{q}_{m,z}^2 r^{\text{TE}}) e^{2i\hat{q}_{m,z}\check{z}_0} \right] , \quad (4.65)
\end{aligned}
$$

$$
\begin{aligned}
\Gamma_{\text{magn.,r}}^{\perp}(\hat{\hat{\omega}}, \check{z}_0) &= \frac{3}{2} \frac{1}{\varepsilon_m^{3/2} \hat{\hat{\omega}}^3} \text{Im} \left[\int_{-i\sqrt{\varepsilon_m}\hat{\hat{\omega}}}^{0} \left(\varepsilon_m \hat{\hat{\omega}}^2 + \hat{\kappa}_m^2 \right) r^{\text{TE}} e^{-2\hat{\kappa}_m \check{z}_0} d\hat{\kappa}_m \right] \\
&= \frac{3}{2} \frac{1}{\varepsilon_m^{3/2} \hat{\hat{\omega}}_0^3} \text{Re} \left[\int_{0}^{\sqrt{\varepsilon_m}\hat{\hat{\omega}}} d\hat{q}_{m,z} (\varepsilon_m \hat{\hat{\omega}}^2 - \hat{q}_{m,z}^2) r^{\text{TE}} e^{2i\hat{q}_{m,z}\check{z}_0} \right] , \quad (4.66)
\end{aligned}
$$

where we in the following distinguish once more between $\hat{\hat{\omega}} \lessgtr 1$ for the approximation of these integrals.

First focusing on transition frequencies with $\hat{\hat{\omega}} \leq 1$, we find $\text{atanh}(\hat{y}) \in \mathbb{R}$ such that $\hat{\Phi}(\hat{y}) \in \mathbb{R}$. We consequently split the reflection coefficients into real and imaginary part

$$
r^{\text{TE}} = \frac{-\alpha^2 \hat{\Phi}^2(\hat{y}) - i\alpha \hat{\Phi}(\hat{y})\hat{q}_{m,z}}{\alpha^2 \hat{\Phi}^2(\hat{y}) + \hat{q}_{m,z}^2} \approx -\frac{4}{3}\alpha\hat{\hat{\omega}}^2 \frac{\frac{4}{3}\alpha\hat{\hat{\omega}}^2 - i\hat{q}_{m,z}}{\left(\frac{4}{3}\alpha\hat{\hat{\omega}}^2\right)^2 + \hat{q}_{m,z}^2} ,
$$

$$
r^{\text{TM}} = \frac{\alpha^2 \hat{\Phi}^2(\hat{y})\hat{q}_z^2 + i\alpha \hat{\Phi}(\hat{y})\hat{q}_{m,z}\hat{y}^2}{\alpha^2 \hat{\Phi}^2(\hat{y})\hat{q}_{m,z}^2 + \hat{y}^4} \approx \frac{4}{3}\alpha \frac{\frac{4}{3}\alpha\hat{q}_{m,z}^2 - i\hat{q}_{m,z}}{\alpha^2 \left(\frac{4}{3}\right)^2 \hat{q}_{m,z}^2 + 1} ,
$$

where we use the approximations $1 - (\hat{y} + \hat{y}^{-1})\text{atanh}(\hat{y}) \approx 4\hat{y}^2/3$ and $\hat{y} \approx \hat{\hat{\omega}}$ for $\hat{y} \ll 1$.

Additionally rewriting $\exp(i2\hat{q}_{m,z}\check{z}_0) = \cos(2\hat{q}_{m,z}\check{z}_0) + i\sin(2\hat{q}_{m,z}\check{z}_0)$, we obtain the

4 Magnetic and electric emitters above graphene

following three integrals (splitting up TE and TM contribution for the parallel orientation)

$$\Gamma_{\mathrm{r}}^{\perp}(\hat{\tilde{\omega}} < \hat{\tilde{\omega}}_{\Delta}, \check{z}_0) \approx -\frac{3d'}{2b^3} \int\limits_0^b \mathrm{d}x \frac{b^2 - x^2}{d'^2 + x^2} \left[x \sin\left(ax\right) + d' \cos\left(ax\right) \right] , \tag{4.67}$$

$$\Gamma_{\mathrm{TE,r}}^{\parallel}(\hat{\tilde{\omega}} < \hat{\tilde{\omega}}_{\Delta}, \check{z}_0) \approx \frac{3d'}{4b^3} \int\limits_0^b \mathrm{d}x \, x^2 \frac{d' \cos\left(ax\right) + x \sin\left(ax\right)}{x^2 + d^2}$$

$$\stackrel{d \ll 1}{\approx} \frac{3d'}{4b^3} \int\limits_0^b \mathrm{d}x \left[d' \cos\left(ax\right) + x \sin\left(ax\right) \right] , \tag{4.68}$$

$$\Gamma_{\mathrm{TM,r}}^{\parallel}(\hat{\tilde{\omega}} < \hat{\tilde{\omega}}_{\Delta}, \check{z}_0) \approx \frac{3d}{4b} \int\limits_0^b \mathrm{d}x \frac{x^2 d \cos\left(ax\right) + x \sin\left(ax\right)}{d^2 x^2 + 1}$$

$$\stackrel{d \ll 1}{\approx} \frac{3d}{4b} \int\limits_0^b \mathrm{d}x \left[x^2 d \cos\left(ax\right) + x \sin\left(ax\right) \right] , \tag{4.69}$$

where for an easier readability we define the four parameters

$$a = 2\check{z}_0 , \qquad b = \sqrt{\varepsilon_m}\hat{\tilde{\omega}} , \qquad d = \frac{4\alpha}{3} , \qquad \text{and} \qquad d' = \frac{4\alpha}{3}\hat{\tilde{\omega}}^2 .$$

and substitute $x = \hat{q}_{m,z}$. By use of Eqs. (4.67), (4.68) and (4.69) and by identifying $\xi = 2\check{z}_0 x$, we finally arrive at

$$\Gamma_{\mathrm{magn.,r}}^{\parallel}(\hat{\tilde{\omega}} < \hat{\tilde{\omega}}_{\Delta}, \check{z}_0) \approx \frac{\alpha(\varepsilon_m + 1)}{2\varepsilon_m \check{z}_0} \left[\frac{4\alpha\hat{\tilde{\omega}}(\varepsilon_m^2 + 3)}{9\sqrt{\varepsilon_m}(\varepsilon_m + 1)} \sin\left(2\sqrt{\varepsilon_m}\hat{\tilde{\omega}}\check{z}_0 \right) \right.$$

$$\left. + \frac{\sin\left(2\sqrt{\varepsilon_m}\hat{\tilde{\omega}}\check{z}_0 \right)}{2\sqrt{\varepsilon_m}\hat{\tilde{\omega}}\check{z}_0} - \cos\left(2\sqrt{\varepsilon_m}\hat{\tilde{\omega}}\check{z}_0 \right) \right] \tag{4.70a}$$

$$\stackrel{\check{z}_0 \ll (\sqrt{\varepsilon_m}\hat{\tilde{\omega}})^{-1}}{\approx} \frac{4\alpha(\varepsilon_m^2 + 3)}{9\varepsilon_m}\hat{\tilde{\omega}}^2, \tag{4.70b}$$

$$\Gamma_{\mathrm{magn.,r}}^{\perp}(\hat{\tilde{\omega}} < \hat{\tilde{\omega}}_{\Delta}, \check{z}_0) \approx -\frac{\hat{\tilde{\omega}}_{\Delta}^2 \check{z}_0}{2\check{\zeta}} \int\limits_0^{2\sqrt{\varepsilon_m}\hat{\tilde{\omega}}\check{z}_0} \mathrm{d}\xi \frac{\left[1 - \left(\frac{\xi}{2\sqrt{\varepsilon_m}\hat{\tilde{\omega}}\check{z}_0} \right)^2 \right] \left[\frac{\xi \sin\left(\xi\right)}{2\sqrt{\varepsilon_m}\hat{\tilde{\omega}}\check{z}_0} + \frac{\hat{\tilde{\omega}}_{\Delta}^2 \cos\left(\xi\right)}{2\sqrt{\varepsilon_m}\hat{\tilde{\omega}}\check{\zeta}} \right]}{\left(\frac{\hat{\tilde{\omega}}_{\Delta}^2 \check{z}_0}{\check{\zeta}} \right)^2 + \xi^2}$$

$$\tag{4.70c}$$

$$\stackrel{\check{z}_0 \ll (\sqrt{\varepsilon_m}\hat{\tilde{\omega}})^{-1}}{\approx} -\frac{\pi\alpha}{\sqrt{\varepsilon_m}}\hat{\tilde{\omega}} \left(1 + \frac{8\sqrt{\varepsilon_m}\hat{\tilde{\omega}}\check{z}_0}{3\pi} \right) . \tag{4.70d}$$

In Fig. 4.11, we display the analytical expressions presented above by the green and red line, respectively. For the parallel radiative modification, the contribution, which is constant at small distances, increases the decay rate and the oscillatory terms begin

to dominate at larger distances. Additionally, Eq. (4.70a) exhibits an envelope function $\alpha/\check{z}_0$ for $\varepsilon_m = 1$ (see gray line in Fig. 4.11(a)). For the perpendicularly to the graphene monolayer oriented magnetic dipole, the radiative modification suppresses the decay rate (cf. Eq. (4.70c)). For larger distances than the one presented in Fig. 4.11, the radiative perpendicular decay rate oscillates as the parallel decay rate.

For the case $\hat{\tilde{\omega}} > 1$ and small distances $2\check{z}_0\hat{\tilde{\omega}} \ll 1$, we can assume the following approximations in the limiting case:

$$
\begin{aligned}
2\check{z}_0\hat{\tilde{\omega}} \ll 1 \qquad &\rightarrow \qquad \mathrm{e}^{2\mathrm{i}\hat{q}_{m,z}\check{z}_0} \approx 1 \,, \\
\tilde{v}_\mathrm{F} \ll 1 \qquad &\rightarrow \qquad \hat{y} \approx \hat{\tilde{\omega}} \qquad \text{and} \\
\hat{y} \approx 1 \qquad &\rightarrow \qquad \frac{\hat{y}^2+1}{\hat{y}}\mathrm{Re}\left[\mathrm{atanh}(\hat{y})\right] \approx -\ln\left(\frac{\hat{\tilde{\omega}}-1}{2}\right) \,.
\end{aligned}
$$

which leads to an orthogonal contribution of

$$
\begin{aligned}
\Gamma^{\perp}_{\mathrm{magn.,r}}(\hat{\tilde{\omega}} > \hat{\tilde{\omega}}_\Delta, \check{z}_0) \approx -&\int\limits_0^{\sqrt{\varepsilon_m}\hat{\tilde{\omega}}} \mathrm{d}\hat{q}_{m,z} \frac{3\alpha\left(\varepsilon_m\hat{\tilde{\omega}}^2 - \hat{q}_{m,z}^2\right)}{2\varepsilon_m^{3/2}\hat{\tilde{\omega}}^3} \\
&\frac{\alpha\left[1+\ln\left(\frac{\hat{\tilde{\omega}}-1}{2}\right)\right]^2 + \frac{\pi}{2}\frac{1+\hat{\tilde{\omega}}^2}{\hat{\tilde{\omega}}}\left(\hat{q}_{m,z} + \frac{\pi}{2}\alpha\frac{1+\hat{\tilde{\omega}}^2}{\hat{\tilde{\omega}}}\right)}{\alpha^2\left[1+\ln\left(\frac{\hat{\tilde{\omega}}-1}{2}\right)\right]^2 + \left[\hat{q}_{m,z} + \alpha\frac{\pi}{2}\frac{\hat{\tilde{\omega}}^2+1}{\hat{\tilde{\omega}}}\right]^2} \\
\approx -&\frac{3\alpha\pi\frac{1+\hat{\tilde{\omega}}^2}{\hat{\tilde{\omega}}}}{4\varepsilon_m^{3/2}\hat{\tilde{\omega}}^3}\int\limits_0^{\sqrt{\varepsilon_m}\hat{\tilde{\omega}}} \mathrm{d}\hat{q}_{m,z}\frac{\varepsilon_m\hat{\tilde{\omega}}^2 - \hat{q}_{m,z}^2}{\hat{q}_{m,z} + \alpha\frac{\pi}{2}\frac{\hat{\tilde{\omega}}^2+1}{\hat{\tilde{\omega}}}} \\
\approx &\frac{3\alpha\pi\frac{1+\hat{\tilde{\omega}}^2}{\hat{\tilde{\omega}}}}{4\varepsilon_m^{1/2}\hat{\tilde{\omega}}^3}\hat{\tilde{\omega}}^2\left(\frac{1}{2} + \ln\left(\alpha\frac{\pi}{2}\right)\right) \approx -\frac{3\alpha\pi}{\sqrt{\varepsilon_m}}\frac{\hat{\tilde{\omega}}^2+1}{\hat{\tilde{\omega}}^2} \rightarrow -\frac{3\alpha\pi}{\sqrt{\varepsilon_m}} \,,
\end{aligned}
$$

(4.71)

and the parallel contributions of

$$
\Gamma^{\|}_{\mathrm{magn.,TE,r}}(\hat{\tilde{\omega}} > \hat{\tilde{\omega}}_\Delta, \check{z}_0) \approx \frac{3}{4\varepsilon_m^{3/2}\hat{\tilde{\omega}}^3} \cdot f(\alpha\left[1+\ln\left(\frac{\hat{\tilde{\omega}}-1}{2}\right)\right], \sqrt{\varepsilon_m}\hat{\tilde{\omega}}, \alpha\frac{\pi}{2}\frac{\hat{\tilde{\omega}}^2+1}{\hat{\tilde{\omega}}}), \quad (4.72)
$$

$$
\Gamma^{\|}_{\mathrm{magn.,TM,r}}(\hat{\tilde{\omega}} > \hat{\tilde{\omega}}_\Delta, \check{z}_0) \approx -\frac{3}{4\varepsilon_m^{1/2}\hat{\tilde{\omega}}} \cdot g(\alpha\left[1+\ln\left(\frac{\hat{\tilde{\omega}}-1}{2}\right)\right], \sqrt{\varepsilon_m}\hat{\tilde{\omega}}, \alpha\frac{\pi}{2}\frac{\hat{\tilde{\omega}}^2+1}{\hat{\tilde{\omega}}}). \quad (4.73)
$$
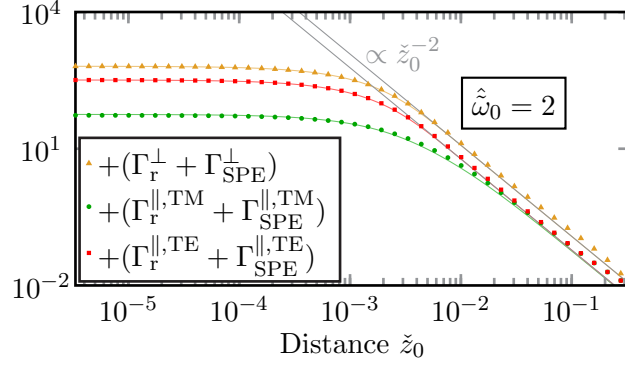
Figure 4.12: Distance dependence of the lifetimes of magnetic emitters for $\hat{\tilde{\omega}}_0 > \hat{\tilde{\omega}}_\Delta$. The analytical approximations (lines) we present in Eqs. (4.81b), (4.82b) and (4.83b), the asymptotic expressions (gray lines) in Eqs. (4.81c) and (4.82c). The discrete marks are numerically computed values. Adapted with permission from J. F. M. Werra *et al.*, "Determining graphene's induced band gap with magnetic and electric emitters", Phys. Rev. B **93,** 081404(R) (2016), doi:10.1103/PhysRevB.93.081404. © 2016 by the American Physical Society.

Once more, we introduce auxiliary functions that in this case read as

$$
f(a,b,d) = \int\limits_0^b \mathrm{d}x\, x^2 \frac{a^2 + d^2 + d\cdot x}{a^2 + (d+x)^2} \approx \int\limits_0^b \mathrm{d}x\, x^2 \frac{d}{(d+x)}
$$

$$
= d\left[\frac{b^2 - 2db}{2} + d\ln\left(1 + \frac{b}{d}\right)\right] \approx \frac{d}{2}b^2\,,
$$

$$
g(a,b,d) = \int\limits_0^b \mathrm{d}x \frac{(d^2 + a^2)x^2 - b^2 d\cdot x}{\left[d\cdot x - b^2\right]^2 + a^2 x^2} \approx \int\limits_0^b \mathrm{d}x \frac{d\cdot x}{d\cdot x - b^2} = b\left[1 + \frac{\ln\left(1 - \frac{d}{b}\right)}{\frac{d}{b}}\right] \approx -\frac{d}{2}\,,
$$

where in the last step we approximate $d/b = \alpha\pi/2 \ll 1$ and $\ln(1-x)/x \approx -(1+x/2)$. Therefore, we find at small distances of the emitter from the graphene monolayer (in parallel to Eq. (4.71)),

$$
\Gamma^{\parallel}_{\mathrm{magn.,TE,r}}(\hat{\tilde{\omega}} > \hat{\tilde{\omega}}_\Delta, \check{z}_0) \approx \Gamma^{\parallel}_{\mathrm{magn.,TM,r}}(\hat{\tilde{\omega}} > \hat{\tilde{\omega}}_\Delta, \check{z}_0) \approx \frac{3\alpha\pi}{16\sqrt{\varepsilon_m}}\frac{\hat{\tilde{\omega}}^2 + 1}{\hat{\tilde{\omega}}^2} \to \frac{3\alpha\pi}{16\sqrt{\varepsilon_m}}\,. \quad (4.74)
$$

For the specific case of large distances, we subsume the radiative contribution into the SPE contribution and discuss the results below. This can be motivated both by the fact that the evanescent SPE contribution is the dominating contribution and that both the propagating and evanescent contribution are driven by SPE effects.

4.3 Determining the band gap of graphene using electric and magnetic emitters

SPE contribution

For the last contribution, the excitation of electron-hole pairs by the emitter's radiation, the decay rate modifications in Eqs. (4.53) and (4.54) can be rewritten as

$$
\Gamma^{\parallel}_{\text{magn.,SPE}}(\hat{\tilde{\omega}}, \check{z}_0) = \frac{3}{4} \frac{1}{\tilde{v}_F^2 \varepsilon_m^{3/2} \hat{\tilde{\omega}}^3} \text{Im} \left[\int\limits_1^{\hat{\tilde{\omega}}/\hat{\tilde{\omega}}_\Delta} \left[\varepsilon_m \tilde{v}_F^2 \hat{\tilde{\omega}}^2 \, r^{\text{TM}} \right. \right.
$$
$$
\left. \left. + \left(\frac{\hat{\tilde{\omega}}^2}{\hat{\tilde{\omega}}_\Delta^2} - \hat{y}^2 \right) r^{\text{TE}} \right] \mathrm{e}^{-\frac{2}{\tilde{v}_F} \sqrt{\frac{\hat{\tilde{\omega}}^2}{\hat{\tilde{\omega}}_\Delta^2} - \hat{y}^2} \check{z}_0} \, \mathrm{d}\hat{y} \right] , \quad (4.75)
$$

$$
\Gamma^{\perp}_{\text{magn.,SPE}}(\hat{\tilde{\omega}}, \check{z}_0) = \frac{3}{2} \frac{1}{\tilde{v}_F^2 \varepsilon_m^{3/2} \hat{\tilde{\omega}}^3} \text{Im} \left[\int\limits_1^{\hat{\tilde{\omega}}/\hat{\tilde{\omega}}_\Delta} (\hat{\tilde{\omega}}^2 - \hat{y}^2) \, r^{\text{TE}} \mathrm{e}^{-\frac{2}{\tilde{v}_F} \sqrt{\frac{\hat{\tilde{\omega}}^2}{\hat{\tilde{\omega}}_\Delta^2} - \hat{y}^2} \check{z}_0} \, \mathrm{d}\hat{y} \right] , \quad (4.76)
$$

where the upper bound

$$
\hat{y} = \sqrt{\hat{\tilde{\omega}}^2 - \tilde{v}_F^2 k^2} = \frac{\hat{\tilde{\omega}}}{\hat{\tilde{\omega}}_\Delta} \qquad \Leftrightarrow \qquad \varepsilon_m \hat{\tilde{\omega}}^2 = k^2 , \qquad (4.77)
$$

corresponds to the material's light cone and the lower bound

$$
\hat{y} = \sqrt{\hat{\tilde{\omega}}^2 - \tilde{v}_F^2 k^2} = 1 \qquad \Leftrightarrow \qquad \tilde{\omega} = \sqrt{\Delta^2 + \tilde{v}_F^2 k^2} , \qquad (4.78)
$$

corresponds to the boundary between SPE region and purely evanescent region. In the SPE region with $\hat{y} > 1$ and the purely real exponential function in Eqs. (4.75) and (4.76), we can rewrite the imaginary parts of the reflection coefficients with $\text{Im}\left[\hat{\Phi}(\hat{y})\right] = -\pi(\hat{y}^2 + 1)/\hat{y}$ for $\hat{y} > 1$,

$$
\text{Im}\left[r^{\text{TE}}\right] = \frac{2\alpha\pi\hat{\kappa}_m \frac{\hat{y}^2+1}{\hat{y}}}{\left(2\hat{\kappa}_m + \alpha\text{Re}\left[\hat{\Phi}(\hat{y})\right]\right)^2 + \left(\alpha\pi\frac{\hat{y}^2+1}{\hat{y}}\right)^2} \approx \alpha\frac{\pi}{2}\frac{\hat{y}^2+1}{\hat{\kappa}_m\hat{y}} , \qquad (4.79\text{a})
$$

$$
\text{Im}\left[r^{\text{TM}}\right] = -\frac{2\frac{\alpha}{\tilde{v}_F}\sqrt{\frac{\hat{\tilde{\omega}}^2}{\hat{\tilde{\omega}}_\Delta^2} - \hat{y}^2}\pi\left(\hat{y}^2+1\right)\hat{y}}{\left(\frac{\alpha}{\tilde{v}_F}\sqrt{\frac{\hat{\tilde{\omega}}^2}{\hat{\tilde{\omega}}_\Delta^2} - \hat{y}^2}\text{Re}\left[\hat{\Phi}(\hat{y})\right] - 2\hat{y}^2\right)^2 + \left(\frac{\alpha}{\tilde{v}_F}\sqrt{\frac{\hat{\tilde{\omega}}^2}{\hat{\tilde{\omega}}_\Delta^2} - \hat{y}^2}\pi\frac{\hat{y}^2+1}{\hat{y}}\right)^2} . \qquad (4.79\text{b})
$$

Here, we notice a significant difference between the expressions for r^{TE} and r^{TM}. Due to the factor $\alpha/\tilde{v}_F$ in the latter, no approximations to the denominator are possible that cast off the dependence on $\text{Re}\left[\Phi(\hat{y})\right]$. For r^{TE}, we can however obtain the last approximation due to $\alpha \ll 1$.

Due to the smallness of the Fermi velocity $\tilde{v}_F$, we can approximate $\hat{\tilde{\omega}}_\Delta \approx 1$ effectively extending the upper limit

$$
\frac{\hat{\tilde{\omega}}}{\hat{\tilde{\omega}}_\Delta} \to \hat{\tilde{\omega}} , \qquad (4.80)
$$

4 Magnetic and electric emitters above graphene

such that the resulting integrals contains both the radiative and the evanescent contributions to the SPE region. In result, we obtain the two contributions

$$\Gamma^{\perp}_{\mathrm{magn.,SPE}}(\hat{\tilde{\omega}} > \hat{\tilde{\omega}}_{\Delta}, \check{z}_0 \gg (2\hat{q}_{m,z})^{-1}) \approx \frac{3}{2\sqrt{\varepsilon_m}^3 \hat{\tilde{\omega}}^2} \frac{\alpha\pi}{2\tilde{v}_{\mathrm{F}}^2} \int\limits_{1/\hat{\tilde{\omega}}}^{1/\hat{\tilde{\omega}}_{\Delta}} \left(\hat{\tilde{\omega}}^2 x^2 + 1\right) \mathrm{e}^{-2\sqrt{1-x^2}\hat{\tilde{\omega}}\frac{\check{z}_0}{\tilde{v}_{\mathrm{F}}}} \mathrm{d}x \,,$$

(4.81a)

$$\approx \frac{-3}{\sqrt{\varepsilon_m}^3 \hat{\tilde{\omega}}^2} \frac{\alpha\pi\hat{\tilde{\omega}}_{\Delta}^2}{4\tilde{v}_{\mathrm{F}}^2} \left(1 + \hat{\tilde{\omega}}^2\right) \int\limits_{\sqrt{1-1/\hat{\tilde{\omega}}^2}}^{0} \chi \mathrm{e}^{-2\chi\hat{\tilde{\omega}}\frac{\check{z}_0}{\tilde{v}_{\mathrm{F}}}} \mathrm{d}\chi$$

$$= -\frac{3\alpha\pi\hat{\tilde{\omega}}_{\Delta}^2}{16\sqrt{\varepsilon_m}^3 \check{z}_0^2} \frac{1+\hat{\tilde{\omega}}^2}{\hat{\tilde{\omega}}^4} \mathrm{e}^{-2\frac{\check{z}_0}{\tilde{v}_{\mathrm{F}}}\sqrt{\hat{\tilde{\omega}}^2-1}} \left(1 + 2\frac{\check{z}_0}{\tilde{v}_{\mathrm{F}}}\sqrt{\hat{\tilde{\omega}}^2-1} - \mathrm{e}^{2\frac{\check{z}_0}{\tilde{v}_{\mathrm{F}}}\sqrt{\hat{\tilde{\omega}}^2-1}}\right) \quad (4.81\mathrm{b})$$

$$\approx \frac{3\alpha\pi\hat{\tilde{\omega}}_{\Delta}^2}{16\sqrt{\varepsilon_m}^3 \check{z}_0^2} \frac{1+\hat{\tilde{\omega}}^2}{\hat{\tilde{\omega}}^4} \propto \check{z}_0^{-2} \,,$$

(4.81c)

$$\Gamma^{\parallel}_{\mathrm{magn.,TE,SPE}}(\hat{\tilde{\omega}} > \hat{\tilde{\omega}}_{\Delta}, \check{z}_0 \gg (2\hat{q}_{m,z})^{-1}) \approx \frac{3}{4\sqrt{\varepsilon_m}^3 \hat{\tilde{\omega}}^2} \frac{\alpha\pi}{2\tilde{v}_{\mathrm{F}}^2} \int\limits_{1/\hat{\tilde{\omega}}}^{1} \left(\hat{\tilde{\omega}}^2 x^2 + 1\right) \mathrm{e}^{-2\sqrt{1-x^2}\hat{\tilde{\omega}}\frac{\check{z}_0}{\tilde{v}_{\mathrm{F}}}} \mathrm{d}x$$

(4.82a)

$$\approx \frac{3}{4\sqrt{\varepsilon_m}^3} \frac{\alpha\pi}{4\tilde{v}_{\mathrm{F}}^2} \frac{\hat{\tilde{\omega}}^2+1}{\hat{\tilde{\omega}}^2} \int\limits_{0}^{\sqrt{1-1/\hat{\tilde{\omega}}^2}} \chi \mathrm{e}^{-2\frac{\check{z}_0\hat{\tilde{\omega}}}{\tilde{v}_{\mathrm{F}}}\chi} \mathrm{d}\chi$$

$$= \frac{3}{64\sqrt{\varepsilon_m}^3} \frac{\alpha\pi}{\check{z}_0^2} \frac{\hat{\tilde{\omega}}^2+1}{\hat{\tilde{\omega}}^4} \mathrm{e}^{-2\frac{\check{z}_0}{\tilde{v}_{\mathrm{F}}}\sqrt{\hat{\tilde{\omega}}^2-1}} \left(-1 - 2\frac{\check{z}_0}{\tilde{v}_{\mathrm{F}}}\sqrt{\hat{\tilde{\omega}}^2-1} + \mathrm{e}^{2\frac{\check{z}_0}{\tilde{v}_{\mathrm{F}}}\sqrt{\hat{\tilde{\omega}}^2-1}}\right) \quad (4.82\mathrm{b})$$

$$\approx \frac{3}{64\sqrt{\varepsilon_m}^3} \frac{\alpha\pi}{\check{z}_0^2} \frac{\hat{\tilde{\omega}}^2+1}{\hat{\tilde{\omega}}^4} \propto \check{z}_0^{-2} \,.$$

(4.82c)

Above, we assume in the second approximation (second lines) of both of the decay rate modifications that for $x = \sqrt{1-\chi^2}$ only the integrand with $\chi \ll 1$ contributes significantly to the integral. We display Eqs. (4.81b) and (4.82b) by the orange and red lines in Fig. 4.12 for the decay rate modification of an emitter embedded in vacuum and above a graphene monolayer. The asymptotic solutions for very large $\check{z}_0$, Eqs. (4.81c) and (4.82c), we illustrate by the two gray lines, showing a clear asymptotic behavior with $\check{z}_0^{-2}$. This distance behavior for the magnetic emitter does not agree with the non-radiative distance behavior for electric emitters. In experiments including electric emitters (see Refs. [169, 170]), a scaling behavior with respect to $\check{z}_0^{-4}$ has been found for intermediate distances between the graphene monolayer and the electric emitter. However, as we see clearly above, this discussion does not hold in the case of magnetic emitters leading for all orientations of a scaling behavior of $\check{z}_0^{-2}$.

However, the results obtained above only hold for medium range distances. For even larger distances, the radiative contributions start to govern the decay rate modifications

4.3 Determining the band gap of graphene using electric and magnetic emitters

due to the long-range nature of radiative electromagnetic modes. This effect is clearly visible for $\check{z}_0 \ll 0.1$. Then, we cannot calculate the correct lifetime modification by assuming $\hat{\tilde{\omega}}_\Delta \approx 1$ but rather have to compute both contributions separately taking care of complex exponential in the case of the radiative contribution. Then, however we cannot obtain a closed-form solution for the evanescent SPE region any longer. On top of this, at, e.g. $\omega = \Delta = 2\pi\,\mathrm{MHz}$ the distance of $\check{z}_0 \ll 0.1$ corresponds to a distance of $z_0 = 5\,\mathrm{m}$ which is not of experimental interest and thus not further discussed in this work.

In the case of the parallel, TM, SPE contribution, we can obtain an analytical solution (under the same limitations as discussed above), by approximating $\mathrm{Re}\left[\hat{\Phi}(\hat{y})\right] \approx \mathrm{Re}\left[\hat{\Phi}(\hat{\tilde{\omega}})\right]$

$$\Gamma^{\parallel}_{\mathrm{magn.,TM,SPE}}(\hat{\tilde{\omega}} > \hat{\tilde{\omega}}_\Delta, \check{z}_0 \gg (2\hat{q}_{m,z})^{-1}) \approx \frac{3}{4\varepsilon_m^{\frac{3}{2}}}\frac{\alpha\pi}{2\tilde{v}_{\mathrm{F}}^2}\int\limits_{1/\hat{\tilde{\omega}}}^{1}\mathrm{d}x\cdot$$

$$\cdot\frac{(\hat{\tilde{\omega}}^2 x^2 + 1)\hat{\tilde{\omega}}^2 x^2 \mathrm{e}^{-2\frac{\check{z}_0\hat{\tilde{\omega}}}{\tilde{v}_{\mathrm{F}}}\sqrt{1-x^2}}}{\left(\alpha\hat{\tilde{\omega}}_0\frac{\sqrt{1-x^2}}{\tilde{v}_{\mathrm{F}}}\mathrm{Re}\left[1 - \frac{\hat{\tilde{\omega}}_0^2 x^2 + 1}{\hat{\tilde{\omega}}_0 x}\mathrm{atanh}(\hat{\tilde{\omega}}_0 x)\right] - \hat{\tilde{\omega}}_0^2 x^2\right)^2 + \left(\hat{\tilde{\omega}}\frac{\alpha\sqrt{1-x^2}}{\tilde{v}_{\mathrm{F}}}\frac{\pi}{2}\frac{\hat{\tilde{\omega}}^2 x^2 + 1}{\hat{\tilde{\omega}} x}\right)^2} \tag{4.83a}$$

$$\approx \frac{3}{4\varepsilon_m^{3/2}}\frac{\alpha\pi\left(\hat{\tilde{\omega}}_0^2 + 1\right)}{2\tilde{v}_{\mathrm{F}}^2}\int\limits_{0}^{\sqrt{1-\frac{1}{b^2}}}\mathrm{d}\chi\frac{\sqrt{1-\chi^2}\chi\mathrm{e}^{-d\cdot\chi}}{(a\chi - b)^2 + e^2\chi^2}$$

$$\approx \frac{3}{4\varepsilon_m^{3/2}}\frac{\alpha\pi\left(\hat{\tilde{\omega}}_0^2 + 1\right)}{2\tilde{v}_{\mathrm{F}}^2}\int\limits_{0}^{\sqrt{1-\frac{1}{b^2}}}\mathrm{d}\chi\frac{\frac{\pi}{4}\chi\mathrm{e}^{-d\cdot\chi}}{(a\chi - b)^2 + e^2\chi^2}\,, \tag{4.83b}$$

where again we assume that for $x = \sqrt{1-\chi^2}$ only the integrand with $\chi \ll 1$ contributes significantly to the integral and using the abbreviations

$$a = \frac{\alpha}{\tilde{v}_{\mathrm{F}}}\mathrm{Re}\left[1 - \frac{\hat{\tilde{\omega}}^2 + 1}{\hat{\tilde{\omega}}}\mathrm{atanh}(\hat{\tilde{\omega}})\right]\,, \quad b = \hat{\tilde{\omega}}, \quad d = 2\frac{\hat{\tilde{\omega}}\check{z}_0}{\tilde{v}_{\mathrm{F}}}, \quad \text{and} \quad e = \frac{\alpha}{\tilde{v}_{\mathrm{F}}}\frac{\pi}{2}\frac{\hat{\tilde{\omega}}^2 + 1}{\hat{\tilde{\omega}}}\,.$$

Furthermore, we obtain the last expression in Eq. (4.83b) by approximating

$$\sqrt{1-\chi^2} \approx \int\limits_{0}^{1}\mathrm{d}\chi\sqrt{1-\chi^2} = \frac{\pi}{4}\,,$$

which is equivalent to taking the mean value over the integral domain. We display Eq. (4.83b) in the green line in Fig. 4.12. As for the orthogonal and TE parallel contribution, also for the TM parallel lifetime modifications these approximations break down for $\check{z}_0 > 0.1$. Again, for a hyperfine splitting of typically $\omega \approx 2\pi\,\mathrm{MHz}$ these distances correspond to a distance of $z_0 > 5\,\mathrm{m}$ and therefore we will once more exclude these distances from our discussion.
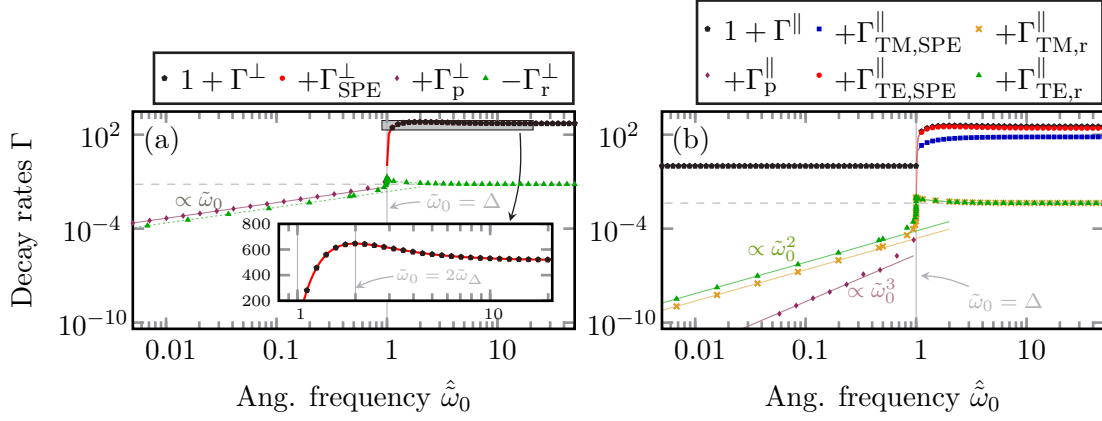
Figure 4.13: Decay rate modification of orthogonal (a) and parallel (b) oriented magnetic dipole moments situated in vacuum ($\varepsilon_m = 1$) at a distance $\check{z}_0 = (3e8)^{-1}$ above the graphene monolayer. Due to the logarithmic scale, we plot the absolute of negative contributions (e.g., $-\Gamma_r^\perp > 0$) where we depict negative analytic approximations by dashed lines. The inset in panel (a) shows the dominating SPE contribution with a maximum at $\hat{\tilde{\omega}}_0 \approx 2\hat{\tilde{\omega}}_\Delta$. Additionally, the condition $\tilde{\omega}_0 = \Delta$ is denoted. Adapted with permission from J. F. M. Werra *et al.,* "Determining graphene's induced band gap with magnetic and electric emitters", Phys. Rev. B **93,** 081404(R) (2016), doi:10.1103/PhysRevB.93.081404. © 2016 by the American Physical Society.

Frequency dependence of lifetime modification

Besides from focusing on the distance dependence, we can also study the frequency dependence of the lifetime modification. Especially in the case of a magnetic emitter where, e.g., the Zeeman of Hyperfine transitions can be tuned via the applied external field, this information bares relevant tests for the physical properties of the environment. In our case, these are, e.g., the validity and limitations of the QFT model applied for the description of the graphene monolayer. In Fig. 4.13, we show the results for a distance $\check{z}_0 = (3e8)^{-1}$.

From Eqs. (4.62), we find that for physical reasonable distances the plasmonic modification of the decay rate has a strongly suppressed distance dependence with $\exp\left(-\check{z}_0/\xi\right) \approx 1$ leading to a linear frequency dependence for the perpendicular lifetime modification (cf. Fig. 4.13(a), purple line) and a cubic frequency dependence for the parallel lifetime modification (cf. Fig. 4.13(b), purple line). For frequencies $\hat{\tilde{\omega}}_0 > \hat{\tilde{\omega}}_\Delta$, as discussed above the plasmonic contribution vanishes.

The radiative modes contribute for both frequencies below and above graphene's gap. From Eqs. (4.70) we see that in the case of frequencies smaller than the band gap, this dependence is linear in the orthogonal case and quadratic in the parallel case with

$$\Gamma_{\mathrm{magn.,TM,r}}^\parallel(\hat{\tilde{\omega}} < \hat{\tilde{\omega}}_\Delta, \check{z}_0) = \frac{\varepsilon_m^2}{3}\Gamma_{\mathrm{magn.,TE,r}}^\parallel(\hat{\tilde{\omega}} < \hat{\tilde{\omega}}_\Delta, \check{z}_0). \tag{4.84}$$

Furthermore, in the case of an emitter with its magnetic dipole moment oriented orthogonal to the graphene monolayer the decay rate is suppressed with respect to the vacuum

4.3 Determining the band gap of graphene using electric and magnetic emitters

decay rate (as compared to the enhancement in the case of parallel orientation). It is also interesting to note that for the perpendicular magnetic dipole moments, the plasmonic contribution relates to the radiative contribution as

$$\Gamma^{\perp}_{\text{magn.,p}} \approx -2\Gamma^{\perp}_{\text{magn.,r}}\,, \tag{4.85}$$

over a very large range of frequencies.

For frequencies larger than graphene's band gap, all the radiative decay rate modifications are almost frequency independent with

$$\Gamma^{\parallel}_{\text{magn.,TM,r}}(\hat{\hat{\omega}} < \hat{\hat{\omega}}_\Delta, \check{z}_0) = \Gamma^{\parallel}_{\text{magn.,TE,r}}(\hat{\hat{\omega}} < \hat{\hat{\omega}}_\Delta, \check{z}_0) = -\frac{\Gamma^{\perp}_{\text{magn.,r}}(\hat{\hat{\omega}} < \hat{\hat{\omega}}_\Delta, \check{z}_0)}{16}\,, \tag{4.86}$$

(compare gray dashed lines in Fig. 4.13).

For relatively small distances $\check{z}_0 \hat{\kappa}_m \ll 1$, we can opposite to Eqs. (4.81b), (4.82b) and (4.83b) obtain analytical closed form solutions even for only the evanescent SPE region. For $\hat{\hat{\omega}}\check{z}_0 < \tilde{v}_{\text{F}}/2$, we can approximate the integrals Eqs. (4.81a) and (4.82a) by evaluating the exponential in the integrands at the integrals' center point

$$x_c = \frac{\hat{\hat{\omega}}_\Delta^{-1} - \hat{\hat{\omega}}^{-1}}{2}\,, \tag{4.87}$$

and then computing the remaining integral. This results in

$$\Gamma^{\parallel}_{\text{magn.,TE,SPE}}(\hat{\hat{\omega}} > \hat{\hat{\omega}}_\Delta, \check{z}_0 \ll \hat{\kappa}_m^{-1}) \approx \frac{\alpha\pi}{8\tilde{v}_{\text{F}}^2\sqrt{\varepsilon_m}^3\hat{\hat{\omega}}_\Delta^3}\left(-\frac{4\hat{\hat{\omega}}_\Delta^3}{\hat{\hat{\omega}}^3} + \frac{3\hat{\hat{\omega}}_\Delta^2}{\hat{\hat{\omega}}^2} + 1\right)\cdot\Xi(\hat{\hat{\omega}})\,, \tag{4.88a}$$

$$\Gamma^{\perp}_{\text{magn.,SPE}}(\hat{\hat{\omega}} > \hat{\hat{\omega}}_\Delta, \check{z}_0 \ll \hat{\kappa}_m^{-1}) \approx 2\Gamma^{\parallel}_{\text{magn.,TE,SPE}}(\hat{\hat{\omega}} > \hat{\hat{\omega}}_\Delta, \check{z}_0 \ll \hat{\kappa}_m^{-1})\,, \tag{4.88b}$$

with $\Xi = \exp[-\sqrt{(4\hat{\hat{\omega}}_\Delta^2 - 1)\hat{\hat{\omega}}^2 + 2\hat{\hat{\omega}}\hat{\hat{\omega}}_\Delta - \hat{\hat{\omega}}_\Delta^2}\frac{\check{z}_0}{\tilde{v}_{\text{F}}\hat{\hat{\omega}}_\Delta}]$. Equation (4.83a) on the other hand can still not be solved analytical due to the fact that $\text{Re}\left[\hat{\Phi}(\hat{y})\right]$ cannot be neglected. The remaining numerical integral of Eq. (4.83a) together with Eqs. (4.88) (further neglecting the exponentials), we present in Fig. 4.13.

The negligence of the exponential in Eqs. (4.88) is appropriate for sufficiently small distances $\check{z}_0 \ll \tilde{v}_{\text{F}}\hat{\hat{\omega}}_\Delta$. Due to the weak distance dependence, this approximation holds for a large range of experimental distances (cf. Fig. 4.14). Then, the SPE contribution is the dominating contribution for frequencies $\hat{\hat{\omega}} > \hat{\hat{\omega}}_\Delta$ (cf. Fig. 4.13) and with this the total decay rate exhibits a maximum (see Fig. 4.13(a), inset) at

$$\Gamma^{\perp}_{\text{magn.,SPE}}(\hat{\hat{\omega}}_{\max} = 2\hat{\hat{\omega}}_\Delta, \check{z}_0) = \frac{\Gamma^{\parallel}_{\text{magn.,TE,SPE}}(\hat{\hat{\omega}}_{\max} = 2\hat{\hat{\omega}}_\Delta, \check{z}_0)}{2} \approx 645\,. \tag{4.89}$$

On the other hand, the decay rate contribution $\Gamma^{\parallel}_{\text{magn.,TM,SPE}}$ is monotonically growing and thus not exhibit such a maximum. Since it is suppressed as compared to the TE contribution, the total parallel decay rate however does exhibit a maximum.
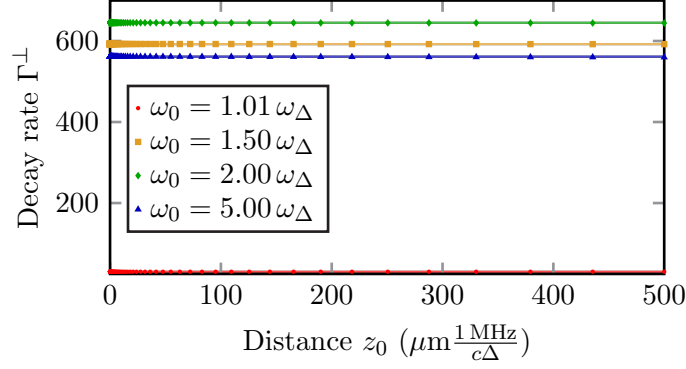
Figure 4.14: Above, we show the validity of the approximation of $\Gamma^{\perp}_{\text{magn.,SPE}}$ where the approximation is valid for various dipole transition frequencies $\hat{\tilde{\omega}}_0$ over a wide range of experimentally accessible

4.3.2 Lifetime modifications of an electric emitter

Analogously to the derivations for magnetic emitters, the decay rate modifications of an electric emitter due to the existence of a graphene monolayer can be obtained. As mentioned at the beginning of section 4.3.1, the decay rate of such an electric emitter can simply be obtained from the interchange of r^{TE} with r^{TM}. This then results in the textbook expression for the decay rate of electric emitters (see Ref. [28])

$$
\frac{\gamma_{\text{el.}}}{\gamma_0}(\hat{\tilde{\omega}}, \check{z}_0) = 1 + \frac{3}{2|\mathbf{d}|^2} \frac{1}{\varepsilon_m^{3/2} \hat{\tilde{\omega}}^3} \left[\frac{d_{\parallel}^2}{2} \text{Im} \left\{ \int\limits_{-\mathrm{i}\sqrt{\varepsilon_m}\hat{\tilde{\omega}}}^{\infty} \left[\varepsilon_m \hat{\tilde{\omega}}^2 r^{\text{TE}} + \hat{\kappa}_m^2 r^{\text{TM}} \right] \mathrm{e}^{-2\hat{\kappa}_m \check{z}_0} \mathrm{d}\hat{\kappa}_m \right\} \right.
$$

$$
\left. + d_{\perp}^2 \text{Im} \left\{ \int\limits_{-\mathrm{i}\sqrt{\varepsilon_m}\hat{\tilde{\omega}}}^{\infty} \left(\varepsilon_m \hat{\tilde{\omega}}^2 + \hat{\kappa}_m^2 \right) r^{\text{TM}} \mathrm{e}^{-2\hat{\kappa}_m \check{z}_0} \mathrm{d}\hat{\kappa}_m \right\} \right] . \quad (4.90)
$$

As for the magnetic case, we will split up the contributions into TE plasmonic, radiative and SPE contribution. With the strongest feature, the possible detection of a band gap in graphene and due to the opportunity to use additionally to the magnetic transition of a given emitter (such as, e.g., an NV center) also the electric transitions at a different frequency, we will exclusively focus on the frequency dependence of the decay rate modifications. The opportunity to make use of electric transitions additionally to the magnetic transitions allows to study a whole new range of energies and thus physical phenomena.

TE plasmonic contribution

As for all of the following contributions, the approximations applied in the magnetic case carry through to the electric case. However, due to the interchange of r^{TE} and r^{TM} only the parallel component couples to the TE polarized modes of the electromagnetic fields

4.3 Determining the band gap of graphene using electric and magnetic emitters
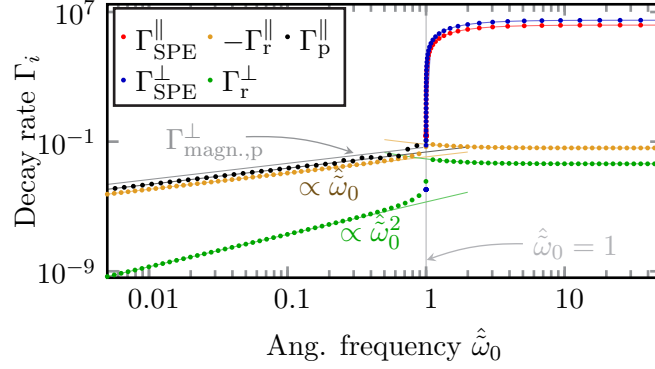

Figure 4.15: Decay rate modification of orthogonal (a) and parallel (b) oriented electric dipole moments situated in vacuum ($\varepsilon_m = 1$) at a distance $\check{z}_0 = (3e8)^{-1}$ above the graphene monolayer. Adapted with permission from J. F. M. Werra *et al.*, "Determining graphene's induced band gap with magnetic and electric emitters", Phys. Rev. B **93,** 081404(R) (2016), doi:10.1103/PhysRevB.93.081404. © 2016 by the American Physical Society.

and with this show a modification due to the TE plasmonic resonance. Thus, with the prior approximations, we arrive at

$$\Gamma_{\text{el.,p}}^{\parallel}(\hat{\tilde{\omega}} < \hat{\tilde{\omega}}_{\Delta}, \check{z}_0) \approx \frac{\pi\alpha}{\sqrt{\varepsilon_m}}\hat{\tilde{\omega}}e^{-\check{z}_0/\zeta} \,, \tag{4.91}$$

where due to the small distance dependence, $\exp(-\check{z}_0/\zeta) \approx 1$. The characteristic decay length $\check{\zeta}$ is given by Eq. (4.63).

We present this asymptotic solution in Fig. 4.15, by the black line. For frequencies $\hat{\tilde{\omega}} > \hat{\tilde{\omega}}_{\Delta}$, as in the magnetic case, the plasmonic contribution is tens of orders of magnitudes smaller than the remaining phenomena. It is worth mentioning that although the influence of r^{TE} is suppressed with a factor c^{-2} in the case of the electric emitter, the plasmonic contribution is only a factor $2\hat{\tilde{\omega}}_{\Delta}^{-2}$ smaller (see gray line in Fig. 4.13).

Radiative contribution

As before, we follow the approximations from the magnetic case and arrive for frequencies $\hat{\tilde{\omega}} < \Delta$ at

$$\Gamma_{\text{el.,r}}^{\perp}(\hat{\tilde{\omega}} < \hat{\tilde{\omega}}_{\Delta}, \check{z}_0) \approx \frac{16}{45}\alpha^2\varepsilon_m\hat{\tilde{\omega}}^2 \,, \tag{4.92}$$

$$\Gamma_{\text{el.,r}}^{\parallel}(\hat{\tilde{\omega}} < \hat{\tilde{\omega}}_{\Delta}, \check{z}_0) = \Gamma_{\text{el.,TE,r}}^{\parallel}(\hat{\tilde{\omega}} < \hat{\tilde{\omega}}_{\Delta}, \check{z}_0) + \Gamma_{\text{el.,TM,r}}^{\parallel}(\hat{\tilde{\omega}} < \hat{\tilde{\omega}}_{\Delta}, \check{z}_0)$$

$$\approx -\alpha\left(\frac{\pi}{2\sqrt{\varepsilon_m}}\hat{\tilde{\omega}} + \alpha\frac{4\varepsilon_m}{15}\hat{\tilde{\omega}}^2\right) \approx -\frac{\alpha\pi}{2\sqrt{\varepsilon_m}}\hat{\tilde{\omega}} \,. \tag{4.93}$$

In the case of a parallel orientation of the electric dipole moment, the TE contribution dominates due to the additional term of the fine structure constant α in the TM contribution.

4 Magnetic and electric emitters above graphene

For frequencies $\hat{\tilde{\omega}} > \Delta$, we find

$$\Gamma_{\text{el.,r}}^{\perp}(\hat{\tilde{\omega}} > \hat{\tilde{\omega}}_\Delta, \check{z}_0) \approx \frac{3}{16}\alpha\sqrt{\varepsilon_m}\pi\frac{\hat{\tilde{\omega}}^2 + 1}{\hat{\tilde{\omega}}^2} , \tag{4.94}$$

$$\Gamma_{\text{el.,r}}^{\parallel}(\hat{\tilde{\omega}} > \hat{\tilde{\omega}}_\Delta, \check{z}_0) = \Gamma_{\text{el.,TE,r}}^{\parallel}(\hat{\tilde{\omega}} > \hat{\tilde{\omega}}_\Delta, \check{z}_0) + \Gamma_{\text{el.,TM,r}}^{\parallel}(\hat{\tilde{\omega}} > \hat{\tilde{\omega}}_\Delta, \check{z}_0)$$

$$\approx -\frac{3}{8\sqrt{\varepsilon_m}}\alpha\pi\frac{\hat{\tilde{\omega}}^2 + 1}{\hat{\tilde{\omega}}^2}\left(\ln\left[\frac{2\sqrt{\varepsilon_m}\hat{\tilde{\omega}}^2}{\alpha\pi(\hat{\tilde{\omega}}^2 + 1)}\right] + \frac{\varepsilon_m}{4}\right) . \tag{4.95}$$

These contributions, Eqs. (4.92), (4.93), (4.94) and (4.95), we display in Fig. 4.15 by the green and orange lines. Here, we once more stress the suppression of the decay rate due to the parallel scattering contribution from both TE and TM modes.

SPE contribution

As in the magnetic case, at frequencies $\hat{\tilde{\omega}} > \Delta$ the largest contribution in Fig. 4.15 is conduced by the excitation of electron-hole pairs (SPE). The determination of analytic closed form solutions is as in the magnetic case not as straight-forward than for the plasmonic and radiative contribution. Thus, we end up with the approximated integrals

$$\Gamma_{\text{el.,SPE}}^{\perp}(\hat{\tilde{\omega}} > \hat{\tilde{\omega}}_\Delta, \check{z}_0) \approx \frac{3}{2\sqrt{\varepsilon_m}^3\hat{\tilde{\omega}}^3}\frac{\alpha\pi}{2\tilde{v}_{\text{F}}^4}$$

$$\int_1^{\hat{\tilde{\omega}}/\hat{\tilde{\omega}}_\Delta} d\hat{y}\frac{\left(\hat{y}^2 + 1\right)\hat{y}^2\left(\hat{\tilde{\omega}}_0^2 - \hat{y}^2\right)}{\left(\alpha\frac{\sqrt{\frac{\hat{\tilde{\omega}}^2}{\check{k}_\Delta^2} - \hat{y}^2}}{\tilde{v}_{\text{F}}}\text{Re}\left[1 - \frac{\hat{y}^2 + 1}{\hat{y}}\text{atanh}(\hat{y})\right] - \hat{y}^2\right)^2 + \left(\alpha\frac{\sqrt{\frac{\hat{\tilde{\omega}}^2}{\hat{\tilde{\omega}}_\Delta^2} - \hat{y}^2}}{\tilde{v}_{\text{F}}}\frac{\pi}{2}\frac{\hat{y}^2 + 1}{\hat{y}}\right)^2} , \tag{4.96}$$

$$\Gamma_{\text{el.,TE,SPE}}^{\parallel}(\hat{\tilde{\omega}} > \hat{\tilde{\omega}}_\Delta, \check{z}_0) \approx \frac{3}{4\sqrt{\varepsilon_m}\hat{\tilde{\omega}}}\frac{\alpha\pi}{2\tilde{v}_{\text{F}}^2}\int_1^{\hat{\tilde{\omega}}/\hat{\tilde{\omega}}_\Delta} d\hat{y}\frac{\hat{y}^2 + 1}{\frac{\hat{\tilde{\omega}}^2}{\hat{\tilde{\omega}}_\Delta^2} - \hat{y}^2 + e^2} \tag{4.97}$$

$$\approx \frac{3\alpha\pi}{8\sqrt{\varepsilon_m}}\hat{\tilde{\omega}}\left[\ln\left(\frac{4}{\alpha\tilde{v}_{\text{F}}\pi}\right) - 1\right] ,$$

$$\Gamma_{\text{el.,TM,SPE}}^{\parallel}(\hat{\tilde{\omega}} > \hat{\tilde{\omega}}_\Delta, \check{z}_0) \approx \frac{3}{4\sqrt{\varepsilon_m}^3\hat{\tilde{\omega}}^3}\frac{\alpha\pi}{2\tilde{v}_{\text{F}}^4}$$

$$\int_1^{\hat{\tilde{\omega}}/\hat{\tilde{\omega}}_\Delta} d\hat{y}\frac{\left(\hat{y}^2 + 1\right)\hat{y}^2\left(\hat{\tilde{\omega}}^2 - \hat{y}^2\right)}{\left(\alpha\frac{\sqrt{\frac{\hat{\tilde{\omega}}^2}{\hat{\tilde{\omega}}_\Delta^2} - \hat{y}^2}}{\tilde{v}_{\text{F}}}\text{Re}\left[1 - \frac{\hat{y}^2 + 1}{\hat{y}}\text{atanh}(\hat{y})\right] - \hat{y}^2\right)^2 + \left(\alpha\frac{\sqrt{\frac{\hat{\tilde{\omega}}^2}{\hat{\tilde{\omega}}_\Delta^2} - \hat{y}^2}}{\tilde{v}_{\text{F}}}\frac{\pi}{2}\frac{\hat{y}^2 + 1}{\hat{y}}\right)^2} , \tag{4.98}$$

that are presented by the lines in Fig. 4.15. The solutions above, we present for small distances $\check{z}_0 \ll \tilde{v}_{\text{F}}/2\hat{\tilde{\omega}}$. Still, we once more could not make use of the small parameters $\tilde{v}_{\text{F}}$ and α due to the fraction of both entering in Eqs. (4.96) and (4.98). However, in the
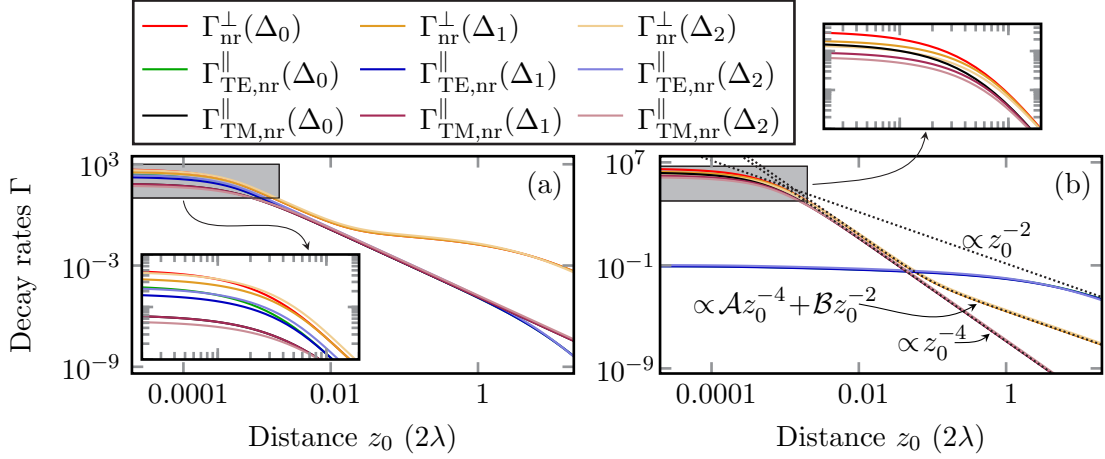
Figure 4.16: Dependence of the non-radiative decay rate modifications for different magnitudes of the band gap ($\Delta_0 = 0$, $\Delta_1 = 10^{-12}\tilde{\omega}_0$ and $\Delta_2 = 0.5\tilde{\omega}_0$ with $\lambda = 2\pi/\tilde{\omega}_0$) of a magnetic (a) and electric (b) emitter. For large distances, only a small difference between Δ_1 and Δ_2 but no difference between Δ_0 and Δ_1 is visible. For small distances, the influence of the band gap is more apparent. For a discussion, see the text. The case $\Delta_0 = 0$ corresponds in panel (b) to the results presented in Ref. [131] with the asymptotic solutions presented within that work displayed by the dashed, black lines (see Eq. (4.100)).

case of Eq. (4.97) where we introduce for better readability the parameter

$$
e = \alpha\tilde{v}_{\mathrm{F}}\frac{\pi}{2}\frac{\hat{\tilde{\omega}}^2 + 1}{\hat{\tilde{\omega}}} \overset{\hat{\tilde{\omega}}\gg\hat{\tilde{\omega}}_\Delta}{\approx} \frac{\pi}{2}\hat{\tilde{\omega}}, \tag{4.99}
$$

where we as for all cases with $\tilde{\omega} > \Delta$ use the approximation $\hat{y} \approx \hat{\tilde{\omega}}$, we are able to obtain for large frequency values $\hat{\tilde{\omega}} \gg \hat{\tilde{\omega}}_\Delta \approx 1$ the last approximations of Eqs. (4.97) and (4.99). Opposite to a magnetic emitter, the SPE contribution does not exhibit a maximum in decay rate but is monotonically increasing. Thus, the only possibility to determine the size of a band gap is by measuring electric transitions slightly above and slightly below the band gap itself. It is not possible to determine the band gap at a multiple of the band gap's frequency by the use of electric emitters.

4.4 Lifetimes of electric and magnetic emitters above undoped graphene without a band gap

Especially when graphene is freely suspended, its band structure does not necessarily need to exhibit a band gap. In this context, the authors of Ref. [131] discuss the lifetime of electric emitters over graphene.

In order to embed the results presented in the previous section into existing literature, we extend the results of the previous sections to $\Delta \to 0$. Here, we can compare the results for the electric emitter straight-forwardly with the existing literature (see Refs. [131, 169, 170]) while for the magnetic emitter we present not so far published results. In parallel to

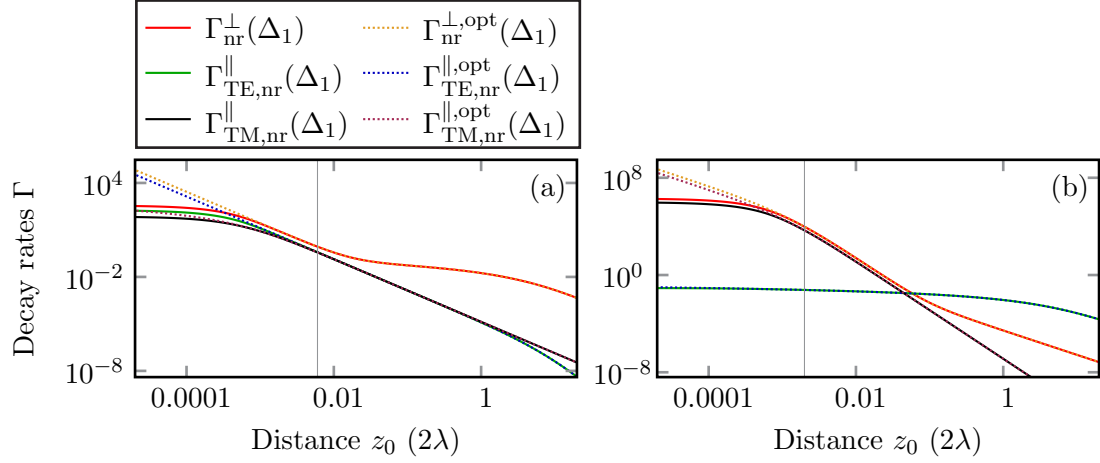# 4 Magnetic and electric emitters above graphene

Figure 4.17: Non-radiative decay rate modifications of a magnetic (a) and electric (b) emitter. The difference between the complete conductivity and the optical conductivity $\sigma_{\text{opt}}(\omega) = \sigma(\mathbf{k} = 0, \omega)$ for a small band gap $\Delta_1 = 10^{-12}\tilde{\omega}$ is displayed. For emitter distances smaller than the gray lines ($z_0 < 0.006 \cdot 2\lambda$ and $z_0 < 0.002 \cdot 2\lambda$ for the magnetic and electric emitter, respectively) the influence of the wavevector dependence and with this of the evanescent region is clearly detectable.

Ref. [131] and due to the magnitude of the SPE contribution as compared to the radiative contribution for $\hat{\tilde{\omega}} \to \infty$, we exclusively focus on the non-radiative contributions (SPE and plasmonic contributions). The limit $\hat{\tilde{\omega}} \to \infty$ is equivalent to the limit $\tilde{\omega} \gg \Delta \to 0$. In this case, one free parameter of the system vanishes and we present the results as distant dependent lifetimes.

As a first step, we use the expressions from the previous section and consider a band gap much smaller than the electric and magnetic transition frequency $\Delta \ll \tilde{\omega}_0$. For three different values ($\Delta_1 = 10^{-12}\tilde{\omega}_0$, $\Delta_2 = 0.5\,\tilde{\omega}_0$ and $\Delta_0 = 0$), we present the results for the magnetic and electric non-radiative contributions in Fig. 4.16(a) and (b), respectively. In the case $\Delta = 0$, we make use of the expressions of the reflection coefficients Eqs. (2.48) and (2.49). Then, for $\Delta = 0$, in the electric case the results correspond exactly to the results presented in Ref. [131]. In Fig. 4.16, we show the large distance behavior that is derived in Ref. [131] and given by

$$\Gamma_{\text{nr}}^{\perp}(z_0 > 1) \approx \frac{3\alpha}{2^6\pi}\frac{\lambda^2}{z_0^2}\left(1 + \frac{3}{8}\frac{\lambda^2}{z_0^2}\right) \equiv \mathcal{A}z_0^{-4} + \mathcal{B}z_0^{-2}\,, \tag{4.100a}$$

$$\Gamma_{\text{TE,nr}}^{\parallel}(z_0 > 1) \approx \frac{3}{2^5\pi^3\alpha}\frac{\lambda^2}{z_0^2}\,, \qquad \Gamma_{\text{TM,nr}}^{\parallel}(z_0 > 1) \approx \frac{9\alpha}{2^10\pi^3}\frac{\lambda^4}{z_0^4}\,, \tag{4.100b}$$

by the gray dashed lines. It is clearly visible that the decay rates are of equal order of magnitudes even at frequencies $\tilde{\omega} = 2\Delta_2$ compared to smaller gaps. However, this difference becomes larger the smaller the distance from the graphene monolayer. This can be understood when assessing the contributions from the SPE region with respect to the distance of these contributions from the material's light cone, both denoted within Fig. 4.3. For the dimensionless units used in this figure, the limit $\Delta \to 0$ does correspond

to the limit $\hat{\tilde{\omega}}_0 \to \infty$. Then, the part of the SPE region becomes larger in which the contributions stem from the evanescent region further away from the material's light cone. The more evanescent a wave, the more confined it is. Thus, the contributions originating from the increased SPE region can only be felt by the emitter at very small distances. Since for a vanishing gap, the SPE region extends over all wavevectors while at a finite but small band gap the SPE region only spans over a finite number of wavevectors, this explains the visible difference in decay rate at very small distances between band gaps of $\Delta_0 = 0$ and $\Delta_1 = 10^{-12}\tilde{\omega}_0$, respectively.

Furthermore, it is important to note that even for the electric emitter the distance scaling of $\check{z}_0^{-4}$ that has been measured experimentally (cf. Ref. [169, 170]) is only valid for intermediate distances between emitter and the graphene monolayer. For large distances independent of the emitter's orientation, a distance dependence of $\check{z}_0^{-2}$ starts to govern the decay rate modifications. These distances, however have not been measured in Ref. [169, 170] but our computations agree well with the theoretically predicted scaling behavior Eq. (4.100) (see Ref. [131]).

In the last part of this chapter, we show the influences of different models of the electromagnetic response and focus on a purely optical response. Hither, we focus on the limits of the applicability of an optical conductivity $\sigma_{\mathrm{opt}}(\omega) = \sigma(\mathbf{k} \to 0, \omega)$ to the description of an experimental setup. In Fig. 4.17(a) and (b), we compare in the limiting case $\Delta_1 = 10^{-12}\tilde{\omega}_0$ the most strongly influenced non-radiative decay rate contribution of parallel and orthogonal oriented magnetic and electric emitters, respectively. Here, we can see that in the magnetic case for $z_0 > 0.006 \cdot 2\lambda$ and for the electric case for $z_0 > 0.002 \cdot 2\lambda$ the decay rates computed from the optical conductivity match the results for the complete description. In other words, at these distances the electromagnetic response of graphene can be approximated as the effects at very small wavevectors with the effects stemming from large wavevectors having decayed away. The largest difference between the magnetic and electric emitter is however the actual transition wavelength λ. Magnetic transitions usually take place at $\omega_0 = 2\pi \, \mathrm{MHz}$ corresponding to $z_0 > 3.6 \, \mathrm{m}$ while electric transitions take place in the optical (e.g., $\lambda = 700 \, \mathrm{nm}$) corresponding to $z_0 > 2.8 \, \mathrm{nm}$. Thus, we can sufficiently describe the decay characteristics of electric emitters at a distance of several nanometers apart from the graphene monolayer when applying the optical conductivity while this approach is for the magnetic emitter only valid at several meters distant. This last requirement is usually not of physical interest and in conclusion we always have to take the complete wavevector dependent conductivity into account when computing the decay rate modification of a magnetic emitter.

4.5 Conclusions

We have shown in the previous sections that atoms, such as Rubidium (see section 3.3), or atom-like emitters, such as quantum dots or an NV center, with their electric and magnetic transitions are suited probes to determine characteristics of a graphene monolayer. By making use of the different transition frequencies and with this temporal scales of both electric and magnetic dipole allowed transitions a wide range of energies can be covered. Here, we have focused mainly on the existence of a band gap that alters the electronic and optical properties of graphene. As discussed in the introduction to this

chapter, by using atom microtraps this high sensitivity of the emitter's decay rate to the band gap can be used to measure even with spatial resolution the band gap of a monolayer at hand. This can then, e.g., compared to spatially resolved strain measurements (see Ref. [138]) such that the question on whether or not mechanical strain is sufficient to open a band gap in graphene might be unambiguously answered. Since here one would expect band gaps in and slightly below the meV, a cooling of the graphene monolayer to mK temperatures is necessary for the determination of the exact band gap.

Additionally, as we show by the study of distance and frequency dependence of the decay rate modifications, the measurement of the decay rate modifications may be also used to validate and determine the limits of the models applied in this work. This understanding would also allow for the engineering of better designs of hybrid graphene - emitter systems, such as atom-chips. Here, due to the relative smallness of all magnetic decay rate modifications as compared, e.g., to gold (see Refs. [28, 124, 171]), graphene monolayers and nanoribbons indeed seem to be appropriate candidates to trap atoms as suspected in Ref. [172].

The Discontinuous Galerkin Time-Domain Method

> *"The good news about computers is that they do what
> you tell them to do. The bad news is that they do what
> you tell them to do."* [29]
>
> Ted Nelson

In this chapter, we present a numerical algorithm – the Discontinuous Galerkin Time-Domain method *that allows us to calculate the propagation of electromagnetic fields in dielectric and plasmonic environments. In section 5.1, we introduce the basic method and explain how electromagnetic fields are inserted into (see section 5.2) and terminated in (see section 5.3) a calculation. In section 5.4 we show how plasmonic nanostructures are modeled within the framework of the Discontinuous Galerkin Time-Domain method (DGTD). In the following section 5.5, we transfer the modeling of metals to the representation of graphene at finite temperatures and given chemical potential within the framework of DGTD. The implementation has been published in Ref. [W7] and is in this chapter adapted from there. Last, in section 5.6 we conclude with another important numerical tool in electromagnetic computations: the implementation of oblique incidence in periodic structures. The application of this technique we show at the example of stacked graphene layers.*

5.1 The Discontinuous Galerkin Time-Domain Method (DGTD)

The Discontinuous Galerkin Time-Domain method (DGTD) is a finite element method and suited to solve partial differential equations. It was applied to the solution of Maxwell's equations by Hesthaven and Warburton (see Ref. [173]) and has since then gained a lot of impact in the community of nanophotonics (see, e.g., Refs. [174–178]). When comparing it to the well-established Finite Difference Time-Domain method (FDTD) that is commonly applied to solve Maxwell's equations (see Ref. [179]), the DGTD exhibits the advantage in its variability of unstructured tessellation due to the well-established choice of a triangular or tetrahedral discretization in two and three dimensions, respectively (cf. Ref. [180]). This allows for a much more accurate modeling of geometric

---

[29]J. Demakis, *"The Ultimate Book of Quotations"* (Lulu Enterprises, Inc., 2012).

5 The Discontinuous Galerkin Time-Domain Method

structures avoiding artificially introduced stair-casing of the structure. Additionally, the DGTD scales more favorably than the FDTD with respect to its spatial convergence.

When utilizing the DGTD to solve Maxwell's equations (for a review see Ref. [180]), the partial differential equations of interest are Maxwell's curl equations in time and 3D space (cf. Eqs. (1.1))

$$\varepsilon_0\varepsilon_r(\mathbf{r})\partial_t\mathbf{E}(\mathbf{r},t) = \quad \boldsymbol{\nabla}\times\mathbf{H}(\mathbf{r},t) - \mathbf{j}(\mathbf{r},t)\,, \tag{5.1a}$$

$$\mu_0\mu_r(\mathbf{r})\partial_t\mathbf{H}(\mathbf{r},t) = -\boldsymbol{\nabla}\times\mathbf{E}(\mathbf{r},t)\,, \tag{5.1b}$$

where $\mathbf{j}(\mathbf{r},t)$ opposite to Eq. (1.1c) may contain both external and material charge currents. Equations (5.1) are then reformulated into a conservation law

$$\underline{\mathcal{D}}(\mathbf{r})\,\partial_t\vec{q}(\mathbf{r},t) + \boldsymbol{\nabla}\cdot\mathbf{F}[\vec{q}(\mathbf{r},t)] = \vec{\mathcal{Q}}(\mathbf{r},t)\,. \tag{5.2}$$

Above, we introduce the material matrix

$$\underline{\mathcal{D}}(\mathbf{r}) = \begin{pmatrix} \varepsilon_0\varepsilon_r(\mathbf{r})\mathbb{1}_3 & 0 \\ 0 & \mu_0\mu_r(\mathbf{r})\mathbb{1}_3 \end{pmatrix}\,, \tag{5.3}$$

the six-dimensional state vector $\vec{q}(\mathbf{r},t) = (\mathbf{E}(\mathbf{r},t),\mathbf{H}(\mathbf{r},t))^T$ and 3D flux $\mathbf{F} = (\vec{F}_x,\vec{F}_y,\vec{F}_z)^T$ consisting of the six-dimensional components

$$\vec{F}_i = \begin{pmatrix} -\mathbf{e}_i\times\mathbf{H}(\mathbf{r},t) \\ \mathbf{e}_i\times\mathbf{E}(\mathbf{r},t) \end{pmatrix}\,, \tag{5.4}$$

and the source terms $\vec{\mathcal{Q}}(\mathbf{r},t) = (-\mathbf{j}(\mathbf{r},t),0)^T$.

As discussed in Refs. [173, 180], the divergence conditions of Maxwell's equations, Eqs. (1.1a) and (1.1b), are conserved within the DGTD and are thus fulfilled for all times when they are fulfilled at the start of the computation $t = t_0$.

By tessellation of the computational domain into individual elements Δ (e.g., in 3D tetrahedrons and in 2D triangles) and when then locally expanding the ith component of the state vector $\vec{q}$ into a set of n Lagrange polynomials $L_i(\mathbf{r})$[30] on each of these elements Δ, we obtain

$$\vec{q}_{i,N}^\Delta(\mathbf{r},t) = \sum_{j=1}^n \vec{q}_{i,j}^\Delta(t)\cdot L_j(\mathbf{r}) \equiv \vec{q}_{i,j}^\Delta(t)\cdot L_j(\mathbf{r})\,, \tag{5.5}$$

---

[30]Since a Lagrange polynomial of order $\mathfrak{p}$ is given by (cf. Ref. [181])

$$L_i(\mathbf{r}) = \sum_{k,l,m=0}^{k+l+m\leq\mathfrak{p}} a_{klm}^{(i)}\,x^k y^l z^m\,,$$

with the expansion coefficients $a_{klm}^{(i)}$, the number of Lagrange polynomials (and with this nodes) on an element for order $\mathfrak{p}$, is for the different dimensionalities of the system given by

$$n = \mathfrak{p}+1 \tag{1D}$$

$$n = \frac{1}{2}(\mathfrak{p}+1)(\mathfrak{p}+2) \tag{2D}$$

$$n = \frac{1}{6}(\mathfrak{p}+1)(\mathfrak{p}+2)(\mathfrak{p}+3) \tag{3D}\,.$$

5.1 The Discontinuous Galerkin Time-Domain Method (DGTD)

with $L_i(\mathbf{r}_j) = \delta_{ij}$ for a given set of spatial discretization (nodal) points $\{\mathbf{r}_j\}$ on each element Δ. With this property of the Lagrange polynomials, we find that the field value at each discretization point $\mathbf{r}_k$ corresponds to the expansion coefficient for the corresponding Lagrange polynomial L_k

$$\vec{q}_N^{\Delta}(\mathbf{r}_k, t) = \vec{q}_k^{\Delta}(t). \tag{5.6}$$

This is the reason why this specific DGTD scheme is also termed a nodal method.

For a better readability, we omit the superscript Δ of the local quantities $\vec{q}_N$. We can then formulate the discretized version of Eq. (5.2) for the discretized state vector $\vec{q}_N(\mathbf{r}, t)$ (see Eq. (5.5))

$$\underline{\mathcal{D}}(\mathbf{r})\partial_t \vec{q}_N(\mathbf{r}, t) + \boldsymbol{\nabla} \cdot \mathbf{F}[\vec{q}_N(\mathbf{r}, t)] - \vec{\mathcal{Q}}(\mathbf{r}, t) = residual \neq 0. \tag{5.7}$$

This non-vanishing equation for the discretized states is then projected onto the set of expansion functions. By requiring orthogonality of the residual and these functions, we arrive at

$$\int\limits_{V_\Delta} \left\{ \underline{\mathcal{D}}(\mathbf{r})\partial_t \vec{q}_N(\mathbf{r}, t) + \boldsymbol{\nabla} \cdot \mathbf{F}[\vec{q}_N(\mathbf{r}, t)] - \vec{\mathcal{Q}}(\mathbf{r}, t) \right\} \cdot L_i(\mathbf{r}) \, \mathrm{d}^3 r \equiv 0, \tag{5.8}$$

where V_Δ is the volume of one element. Equation (5.8) thus describes the purely local propagation of the state vector. As presented in Ref. [173, 182], we can add a coupling between the two elements that additionally enforces the physical boundary conditions. This is done via the *numerical flux* whose introduction we can motivate by first integrating Eq. (5.8) by parts

$$\int\limits_{V_\Delta} \left[\underline{\mathcal{D}}(\mathbf{r})\partial_t \vec{q}_N(\mathbf{r}, t) - \vec{\mathcal{Q}}(\mathbf{r}, t) \right] \cdot L_i(\mathbf{r}) \, \mathrm{d}^3 r$$
$$= - \int\limits_{\partial V_\Delta} \left\{ \hat{\mathbf{n}} \cdot \mathbf{F}[\vec{q}_N(\mathbf{r}, t)] \right\} \cdot L_i(\mathbf{r}) \, \mathrm{d}^2 r, \tag{5.9}$$

with the integration $\mathrm{d}^2 r$ over the faces ∂V_Δ of the element and the normal vector $\hat{\mathbf{n}}$ on those faces. We next replace the physical flux by the numerical flux

$$\mathbf{F}[\vec{q}_N(\mathbf{r}, t)] \rightarrow \mathbf{F}^*[\vec{q}_N(\mathbf{r}, t)], \tag{5.10}$$

and then undo the integration by parts applied in Eq. (5.9)

$$\int\limits_{V_\Delta} \left\{ \underline{\mathcal{D}}(\mathbf{r})\partial_t \vec{q}_N(\mathbf{r}, t) + \boldsymbol{\nabla} \cdot \mathbf{F}[\vec{q}_N(\mathbf{r}, t)] - \vec{\mathcal{Q}}(\mathbf{r}, t) \right\} \cdot L_i(\mathbf{r}) \, \mathrm{d}^3 r$$
$$= \int\limits_{\partial V_\Delta} \left\{ \hat{\mathbf{n}} \cdot \left[\mathbf{F}[\vec{q}_N(\mathbf{r}, t)] - \mathbf{F}^*[\vec{q}_N(\mathbf{r}, t)] \right] \right\} \cdot L_i(\mathbf{r}) \, \mathrm{d}^2 r. \tag{5.11}$$

To complete the numerical scheme, we need an explicit expression for the numerical flux is still missing. Its form is – not surprisingly due to the artificial introduction of it – not

5 The Discontinuous Galerkin Time-Domain Method

Boundary condition	$\mathbf{E}^+$	$\mathbf{H}^+$
perfect electric conducting	$-\mathbf{E}^-$	$\mathbf{H}^-$
perfect magnetic conducting	$\mathbf{E}^-$	$-\mathbf{H}^-$
Silver-Müller	$-\mathbf{E}^-$	$-\mathbf{H}^-$

Table 5.1: Altered face boundary conditions Eq. (5.15) that allow for the termination of the computational domain. For a detailed discussion, see Ref. [181, 183].

unique but as shown in Ref. [173] the so-called upwind flux leads to a numerically stable, consistent and convergent scheme for the choice of Lagrange polynomials as expansion function:

$$\hat{\mathbf{n}} \cdot \left[\mathbf{F}[\vec{q}_N(\mathbf{r},t)] - \mathbf{F}^*[\vec{q}_N(\mathbf{r},t)] \right]$$

$$= \begin{pmatrix} \frac{1}{\bar{Z}} \left\{ \alpha \left[\Delta\mathbf{E} - \hat{\mathbf{n}} \left(\hat{\mathbf{n}} \cdot \Delta\mathbf{E} \right) \right] + Z^+ \hat{\mathbf{n}} \times \Delta\mathbf{H} \right\} \\ \frac{1}{\bar{Y}} \left\{ \alpha \left[\Delta\mathbf{H} - \hat{\mathbf{n}} \left(\hat{\mathbf{n}} \cdot \Delta\mathbf{H} \right) \right] - Y^+ \hat{\mathbf{n}} \times \Delta\mathbf{E} \right\} \end{pmatrix} . \tag{5.12}$$

In the expression above, we define the impedance Z and admittance Y as

$$Z^\pm = \sqrt{\frac{\mu_0 \mu_r^\pm}{\varepsilon_0 \varepsilon_r^\pm}}, \qquad \text{and} \qquad Y^\pm = \sqrt{\frac{\varepsilon_0 \varepsilon_r^\pm}{\mu_0 \mu_r^\pm}}, \tag{5.13}$$

with the local element referred to by the index '$-$' and the neighboring element referred to by '$+$' and the averaged values

$$\bar{Z} = Z^+ + Z^- \qquad \text{and} \qquad \bar{Y} = Y^+ + Y^- . \tag{5.14}$$

The boundary conditions are introduced via $\Delta\mathbf{E}(\mathbf{r},t)$ and $\Delta\mathbf{H}(\mathbf{r},t)$. For a source-free face connecting two elements, each of these elements either metallic or dielectric, these conditions read

$$\Delta\mathbf{E} = \mathbf{E}^+ - \mathbf{E}^- \qquad \text{and} \qquad \Delta\mathbf{H} = \mathbf{H}^+ - \mathbf{H}^- . \tag{5.15}$$

At this point, we can now additionally include any physically required boundary condition into Eq. (5.15). These can be, e.g., boundary conditions to terminate the computational domain, such as Silver-Müller boundary condition, perfect electric conducting (PEC) boundary conditions or perfect magnetic conducting (PMC) boundary conditions. In these three cases, the neighboring element do not exist and with this $\mathbf{E}^+$ and $\mathbf{H}^+$ have to be a priori defined. In the case of Silver-Müller boundary conditions, spherical waves are perfectly absorbed when impinging on a priori designed spherical outer boundaries. In the case of PEC boundary conditions the electric fields vanish at the boundary while in the case of PMC boundary conditions the magnetic fields vanish. For the specific values, see table 5.1. Additionally, $Z^+ = Z^-$ and $Y^+ = Y^-$.

Besides from the terminating boundary conditions, additional boundary conditions are required, e.g. to implement current sheets (see section 5.5 and Ref. [W7]) or hydrodynamic material descriptions (see Ref. [184]). Between neighboring elements without additional requirements, condition (5.15) however suffices.

Finally, the spatially discretized Eq. (5.11) is then reformulated as ordinary differential equation (ODE) (see Ref. [180] for details)

$$\dot{\vec{q}}_N^\Delta(t) = f\left[\vec{q}_N^\Delta(t), t\right],\tag{5.16}$$

where we have reintroduced the reference to the local element Δ. The exact shape of the function f has been discussed in detail elsewhere (see Refs. [180, 181]). This ODE can finally be solved using any ODE solver. Throughout this work, we apply a low storage Runge Kutta (LSRK) of order $\pi = 4$ with $s = 14$ stages (cf. Ref. [185]). Its stability region (see Ref. [186]) is for the case of a linear problem optimized to a general eigenvalue spectrum of a nanophotonic computation described by the linear set of equations Eq. (5.16).

5.2 Initializing electromagnetic fields in the DGTD

One possibility to introduce electromagnetic fields in the calculation are sources of electromagnetic radiation. The two best known types of sources are probably the so-called scattered-field (Sf) and the total-field/scattered-field (TfSf) source (see Ref. [179]). In this work, we used the TfSf source description to induce, e.g., the emitter's field (compare Eqs. (3.13) and (3.12)). The general formalism, however, works for the Sf source in the same general manner.

When applying the TfSf source in order to introduce electromagnetic fields into the computation, we split the computational domain into to regions: the total field region and the scattered field region. In the scattered field region, we only compute the scattered fields that are scattered from nanophotonic structures, while in the total field region, we compute the total electric (and accordingly magnetic) fields defined as

$$\mathbf{E}_t(\mathbf{r}, t) = \mathbf{E}_s(\mathbf{r}, t) + \mathbf{E}_i(\mathbf{r}, t).\tag{5.17}$$

Here, the total field (t) is a sum not only of the scattered field (s) but also of the incident field (i). The incident field is an electric and magnetic field to which the solution in an isotropic material (i.e., vacuum) is analytically known on the complete TfSf contour when considering no scatterer within the total-field (Tf) region. The incident field is then added to the numerical flux at all boundaries (faces) between two elements, out of which one belongs to the Sf region and the other element to the Tf region.

The incident field enters into the numerical flux via the jump condition, Eq. (5.15). When a face is situated either between two total or two scattered field elements, Eq. (5.15) can be applied without modification. If, however, the face is touched by one scattering and one total field element (remember that the index '−' labels the fields on the local and the index '+' labels the fields on the neighboring element) we find that Eq. (5.15) becomes (analogously for the magnetic fields):

$$\Delta\mathbf{E}_t(\mathbf{r}, t) = \mathbf{E}_s^+(\mathbf{r}, t) + \mathbf{E}_i(\mathbf{r}, t) - \mathbf{E}_t^-(\mathbf{r}, t),\tag{5.18a}$$

$$\Delta\mathbf{E}_s(\mathbf{r}, t) = \mathbf{E}_t^+(\mathbf{r}, t) - \mathbf{E}_s^-(\mathbf{r}, t) - \mathbf{E}_i(\mathbf{r}, t),\tag{5.18b}$$

where $\Delta\mathbf{E}_t$ is the boundary condition for the fields on the total field's element side of the face and $\Delta\mathbf{E}_s$ the boundary condition for the fields on the scattered field's element side.

The incident field that is known analytically is in our case a dipole's electric and magnetic field distribution (cf. Ref. [27] and Eqs. (3.12) and (3.13) for the explicit expressions) allowing for an arbitrary temporal profile $\eta(t)$ or a plane wave of polarization $\mathbf{E}_0$ and also with arbitrary temporal profile $\eta(t)$ for which the electric field reads

$$\mathbf{E}(\mathbf{r}, t) = \mathbf{E}_0 \eta(t - \mathbf{k} \cdot \mathbf{r}) \,. \tag{5.19}$$

The alternative to a TfSf source is the aforementioned Sf source. Here, we use the same distinction between the total, scattered and incident fields as before, while defining incident regions in which the solution of an incident field is known for all times and regions in which these fields differ. In this case, instead of the total field in some and the scattered field in other regions, only the scattered fields are computed throughout the computational domain. For the incident fields, the equations of motion for the analytically known electromagnetic fields read

$$\partial_t \mathbf{E}_{\mathrm{i}}(\mathbf{r}, t) = \frac{1}{\varepsilon_0 \varepsilon_{\mathrm{backg}}} \boldsymbol{\nabla} \times \mathbf{H}_{\mathrm{i}}(\mathbf{r}, t) \,, \tag{5.20a}$$

$$\partial_t \mathbf{H}_{\mathrm{i}}(\mathbf{r}, t) = -\frac{1}{\mu_0 \mu_{\mathrm{backg}}} \boldsymbol{\nabla} \times \mathbf{E}_{\mathrm{i}}(\mathbf{r}, t) \,, \tag{5.20b}$$

at all times and assuming a constant background material ($\varepsilon_{\mathrm{backg}}$, μ_{backg}). Here we assume that no external charges or currents exist since this usually leads to a not analytically solvable field propagation. However, for appropriate cases, the approach can be generalized.

For, e.g., a scatterer consisting of a non-dispersive, local, isotropic, lossless, linear dielectric different from the background dielectric, the equation of motion for the scattered fields reads

$$\partial_t \mathbf{E}_{\mathrm{s}}(\mathbf{r}, t) = \frac{1}{\varepsilon_r \varepsilon_0} \boldsymbol{\nabla} \times \mathbf{H}_{\mathrm{s}}(\mathbf{r}, t) + \frac{\varepsilon_{\mathrm{backg}} - \varepsilon_r}{\varepsilon_r} \partial_t \mathbf{E}_{\mathrm{i}}(\mathbf{r}, t) \,, \tag{5.21a}$$

$$\partial_t \mathbf{H}_{\mathrm{s}}(\mathbf{r}, t) = -\frac{1}{\mu_r \mu_0} \boldsymbol{\nabla} \times \mathbf{E}_{\mathrm{s}}(\mathbf{r}, t) + \frac{\mu_{\mathrm{backg}} - \mu_r}{\mu_r} \partial_t \mathbf{H}_{\mathrm{i}}(\mathbf{r}, t) \,. \tag{5.21b}$$

Here, the second terms on the right hand side of the above equations are then volumetric source terms. Similar equations can be derived for a large variety of linear and even some nonlinear materials. See Ref. [179] for further details.

5.3 Terminating electromagnetic fields in the DGTD

In section 5.1, we presented different boundary conditions, such as PEC, PMC and most importantly the Silver-Müller boundary conditions, that are usually applied to the outer boundary of the computational domain and constitute constraints to the electromagnetic waves that impinge on this outer boundary.

Without any additional boundary condition, the boundary condition reads $\mathbf{E}^+ = \mathbf{H}^+ = 0$ and the electromagnetic waves are simply reflected. For the case of perfectly spherical waves, Silver-Müller boundary conditions applied to a spherical outer boundary present in theory perfect absorbers in theory since they reflect no fields back into the computational domain. Thus they mimic an infinite computational domain and allow to compute

electromagnetic scattering problems more efficiently by choosing a finite computational domain.

However, in general the scattered electromagnetic fields may be almost spherical waves but are seldom complete spherical waves. For this reason, a method was developed in which the total computational domain is split into the physical domain and an outer artificial layer, the so-called perfectly matched layer (PML) (see Ref. [187]). In the PML fields are attenuated such that , when they are reflected back, they are sufficiently small meaning they barely interfere with the physical relevant computations. Additionally, we usually apply the Silver-Müller boundary conditions at the outer most boundary to damp the fields additionally.

In order to terminate different materials, in literature there are different methods applied such as, e.g., the stretched-coordinate implementation (see Refs. [181, 188]) in order to terminate, i.e., dissipative materials. In this work, we only apply the most commonly used formulation, the so-called uniaxial perfectly matched layers (uPMLs) (see Refs. [179, 188, 189]), that allows only for the termination of non-dissipative and local materials. The basic idea then is to replace the scalar material parameters ε and μ by the material tensors

$$\underline{\varepsilon}' = \underline{\Lambda}\varepsilon \qquad \underline{\mu}' = \underline{\Lambda}\mu\,, \qquad \text{with } \underline{\Lambda} = \begin{pmatrix} \frac{s_y s_z}{s_x} & 0 & 0 \\ 0 & \frac{s_x s_z}{s_y} & 0 \\ 0 & 0 & \frac{s_x s_y}{s_z} \end{pmatrix}\,, \qquad (5.22)$$

where we introduce the PML parameters

$$s_i = 1 - \frac{\sigma_i}{\mathrm{i}\omega}\,. \qquad (5.23)$$

Here, the parameter σ_i leads to a damping of an electromagnetic wave propagating in i direction. The altered material parameters are implemented in the DGTD by the use of appropriate auxiliary differential equations (ADEs) (see section 5.4 for the concept). The method is called uniaxial due to the fact that an electromagnetic wave is damped only in the direction i. Additionally, it is called perfectly matched since the impedance and admittance of the uPML region are matched to the neighboring physical region

$$Y' = Y \qquad\qquad Z' = Z\,.$$

such that an electromagnetic wave impinging onto the interface to the uPML region is in theory not reflected from it. However, when applying the uPML formalism to an actual computation, besides from the back reflection from the outermost boundary at the edge of the computational domain, back reflection at the boundary between physical and uPML region occur. This is due to the finite discretization since the discretized electromagnetic fields never perfectly fulfill Maxwell's equations. In consequence, one always needs to choose an optimum with regard to the computational error and time between the magnitude of the damping (the smaller, the less reflection at the physical-uPML domain) and the thickness of the uPML (the larger, the more electromagnetic field is absorbed and the smaller the damping can be but at the same time the longer the computational time).

For the specific implementation of the uPML into a DGTD method and the appropriate choice of parameters see Refs. [181, 188].

5.4 Materials in the DGTD: Auxiliary Differential Equations

After having introduced ways to insert and absorb electromagnetic fields in the computation, we next focus on the modeling of standard materials whose dielectric permittivity cannot simply be described by the non-dispersive permittivity introduced in Eq. (5.3). The materials of highest interest in nanoplasmonic modeling are bulk metals. In this section, we present thus two widely applied models to describe these bulk metals (such as, e.g., gold and silver). However, these methods can also be generalized to the description of other materials such as graphene (see section 5.5), dielectrics doped with dyes (using the Maxwell-Bloch equations presented in Eq. (3.19)) or even more advanced material descriptions for the bulk metals, i.e. the hydrodynamic model (see Ref. [184, 190]). The later two are not further discussed in this work.

Opposite to frequency domain methods, the dielectric tensors cannot be included by their discrete and experimentally determined frequency dependent values into a time domain method. This is due to the fact that they have to be transformed into time domain before being introduced into the time domain algorithm. This is done via so called ADEs (see Ref. [179]).

5.4.1 The Drude model

As mentioned above, there exist two widely applied models for the description of bulk metals. The first of these models is the *Drude model* in which a constant, positive ionic background (consisting of the immobile nuclei and the electrons occupying the lower orbitals) and the freely moving valence electrons are assumed. This corresponds to a jellium model (see Ref. [191]). Thus, this model describes the electronic properties of electrons remaining in one band of the material, the so-called intraband absorption, well (see also Fig. 2.4(a) for a very general sketch of the intraband absorption in graphene).

In frequency domain, the 3D optical conductivity $\sigma(\omega)$ with (cf. Eq. (1.82))

$$\mathbf{j}_{\mathrm{Drude}}(\mathbf{r}, \omega) = \sigma_{\mathrm{Drude}}(\omega)\mathbf{E}(\mathbf{r}, \omega), \tag{5.24}$$

that can both describe bulk and surface effects, reads (see Ref. [181])

$$\sigma_{\mathrm{Drude}}(\omega) = \frac{\omega_{\mathrm{Drude}}^2}{\gamma_{\mathrm{Drude}} - \mathrm{i}\omega}. \tag{5.25}$$

Above, $\omega_{\mathrm{Drude}} = \sqrt{e\, n/m_e}$ corresponds to the bulk plasmon frequency with the density of electrons n, where each of the electrons has a mass m_e and a charge $-e$, while γ_{Drude} is a phenomenological collision frequency between the valence electrons.

Inserting Eq. (5.25) into Eq. (5.24) and Fourier transforming the resulting equation into time domain by use of $-\mathrm{i}\omega\mathcal{A}(\omega) \to \partial_t A(t)$ (cf. Eq. (1.9)), leads to the ADE for the Drude model

$$\partial_t\mathbf{j}_{\mathrm{Drude}}(\mathbf{r}, t) = \omega_{\mathrm{Drude}}^2\mathbf{E}(\mathbf{r}, t) - \gamma_{\mathrm{Drude}}\mathbf{j}_{\mathrm{Drude}}(\mathbf{r}, t). \tag{5.26}$$

5.4.2 The Lorentz model

The second important macroscopic description for the metallic properties is the *Lorentz model*. In this model, the electron is described by a driven, harmonic oscillator. This can

be mapped to an interband transition with the electron being excited to another band of the solid. Thus, Lorentz model terms are applied when describing the response to electromagnetic fields in the energy range of such interband transitions.

The conductivity in this case reads (see Ref. [181])

$$\sigma_{\text{Lorentz}}(\omega) = -i\omega \frac{\Delta\varepsilon_{\text{Lorentz}}\omega_{\text{Lorentz}}^2}{\omega_{\text{Lorentz}}^2 - i\gamma_{\text{Lorentz}}\omega - \omega^2}. \tag{5.27}$$

Here, each electron oscillates at an eigenfrequency ω_{Lorentz} and is damped by the damping parameter γ_{Lorentz}. Additionally, an oscillator strength $\Delta\varepsilon_{\text{Lorentz}}$ is introduced that quantifies the coupling of the electrons to the electromagnetic field driving the oscillator (and with this the interband transition).

The conductivity, Eq. (5.27), cannot be as straight-forwardly translated into a time domain method as the Drude conductivity due to two facts: first, it is second order in time (ω^2 in the denominator) and, second, it contains a derivative of the electric field ($-i\omega$ in the numerator). The second derivative in time can be avoided by reformulating Eq. (5.27) in terms of an auxiliary current $\mathbf{q}_{\text{Lorentz}}$ and with some algebraic reformulation (see Refs. [179, 181]), we obtain

$$-i\omega\mathbf{j}_{\text{Lorentz}}(\mathbf{r}, \omega) = \Delta\varepsilon_{\text{Lorentz}}\omega_{\text{Lorentz}}^2\mathbf{E}(\mathbf{r}, \omega)$$

$$\underbrace{-\frac{\gamma_{\text{Lorentz}}\Delta\varepsilon_{\text{Lorentz}}\omega_{\text{Lorentz}}^2\mathbf{E}(\mathbf{r}, \omega) + \omega_{\text{Lorentz}}^2\mathbf{j}_{\text{Lorentz}}(\mathbf{r}, \omega)}{\gamma_{\text{Lorentz}} - i\omega}}_{\equiv\mathbf{q}_{\text{Lorentz}}(\mathbf{r},\omega)}. \tag{5.28}$$

When we then Fourier transform the set of equations above into time domain, we obtain with $\mathbf{j}_{\text{Lorentz}}(\mathbf{r}, \omega) = \sigma_{\text{Lorentz}}(\omega)\mathbf{E}(\mathbf{r}, \omega)$ the complete set of ADEs

$$\partial_t\mathbf{j}_{\text{Lorentz}}(\mathbf{r}, t) = \Delta\varepsilon_{\text{Lorentz}}\omega_{\text{Lorentz}}^2\mathbf{E}(\mathbf{r}, t) + \mathbf{q}_{\text{Lorentz}}(\mathbf{r}, t)$$
$$\partial_t\mathbf{q}_{\text{Lorentz}}(\mathbf{r}, t) = -\omega_{\text{Lorentz}}^2\mathbf{j}_{\text{Lorentz}}(\mathbf{r}, t) - \gamma_{\text{Lorentz}}\Delta\varepsilon_{\text{Lorentz}}\omega_{\text{Lorentz}}^2\mathbf{E}(\mathbf{r}, t) \tag{5.29}$$
$$- \gamma_{\text{Lorentz}}\mathbf{q}(\mathbf{r}, t).$$

5.4.3 The dielectric function of a general bulk material

For the case of bulk material, we can derive the expression for the optical dielectric function $\varepsilon(\omega)$ via the Kubo-formula Eq. (1.83) ($\chi(\omega) = -i\omega\sigma(\omega)$) and find

$$\varepsilon(\omega) = \varepsilon_\infty + \sum_{i=1}^{N_{\text{Drude}}} \chi_{\text{Drude},i}(\omega) + \sum_{i=1}^{N_{\text{Lorentz}}} \chi_{\text{Lorentz},i}(\omega). \tag{5.30}$$

The constant background permittivity ε_∞ can be taken care of in Maxwell's equations themselves while the other $N_{\text{Drude}} + N_{\text{Lorentz}}$ terms are both in frequency and time domain additive and lead to an additional $N_{\text{Drude}} + 2N_{\text{Lorentz}}$ ADEs that are solved alongside with the actual Maxwell equations on each element that contains the material. In other words, the degree of freedom vector $\vec{q}_N(\mathbf{r}, t)$ as well as $f(\vec{q}_N(\mathbf{r}, t))$ from Eq. (5.16) are extended by the currents and auxiliary currents from Eqs. (5.26) and (5.29).
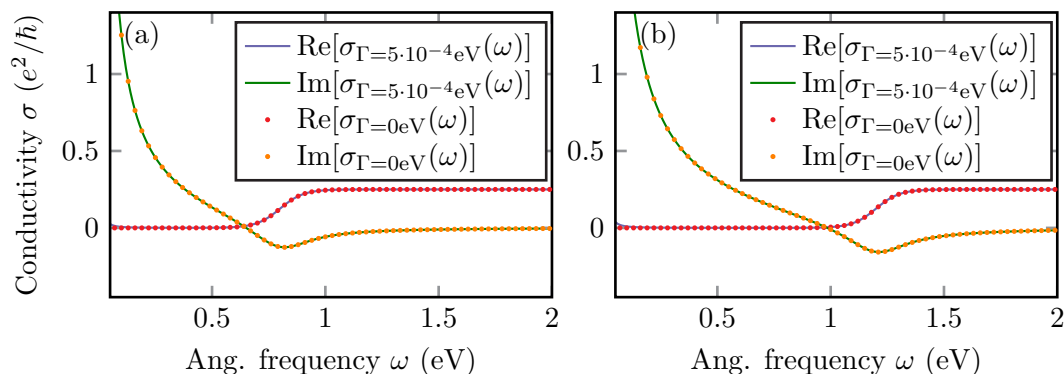
Figure 5.1: Frequency-dependence of the conductivity of graphene for different values of the phenomenological decay rates Γ. Panels (a) and (b) correspond to graphene at doping levels of $\mu = 0.4\,\text{eV}$ and $\mu = 0.6\,\text{eV}$, respectively. Graphene is at room temperature $T = 300\,\text{K}$. The change of the doping level, moves the plasmonic properties of graphene closer to the visible frequency range. All parameters are defined in Eq. (2.63) and similar values have been used in the literature [88, 89, 192]. Adapted from J. F. M. Werra *et al.,* "Current sheets in the Discontinuous Galerkin Time-Domain method: an application to graphene", Proc. SPIE Optics+Optoelectronics **95020,** 95020E (2015).

They couple to Maxwell's equations via the external current at each point in space $\mathbf{r}$ and time t (cf. Eq. (5.1a))

$$
\partial_t \mathbf{E}(\mathbf{r}, t) = \varepsilon_\infty^{-1}(\mathbf{r}) \left[\boldsymbol{\nabla} \times \mathbf{H}(\mathbf{r}, t) - \mathbf{j}_{\text{free}}(\mathbf{r}, t) \right.
$$
$$
\left. - \sum_{i=1}^{N_{\text{Drude}}} \mathbf{j}_{\text{Drude}}(\mathbf{r}, t) - \sum_{i=1}^{N_{\text{Drude}}} \mathbf{j}_{\text{Lorentz}}(\mathbf{r}, t) - \ldots \right] , \tag{5.31}
$$

where we allow for any other material current to be added to the equation above.

5.5 Graphene in the DGTD

Since we usually use the DGTD to model optical effects, we will describe graphene using the optical conductivity (cf. Eq. (2.63))

$$
\sigma(\omega) = \lim_{\mathbf{q} \to 0} \left[\sigma(\mathbf{q}, \omega) \right] , \tag{5.32}
$$

with the previously defined angular frequency ω and the 3D wavevector $\mathbf{q}$. Additionally, we will include temperature dependent and chemical doping effects and thus apply the quantum-field theoretical expressions Eqs. (2.64) and (2.65). Previously, this same material model has been implemented into a FDTD algorithm (see Ref. [192]) and into frequency domain algorithms (see Ref. [193]). In the following we present this approach
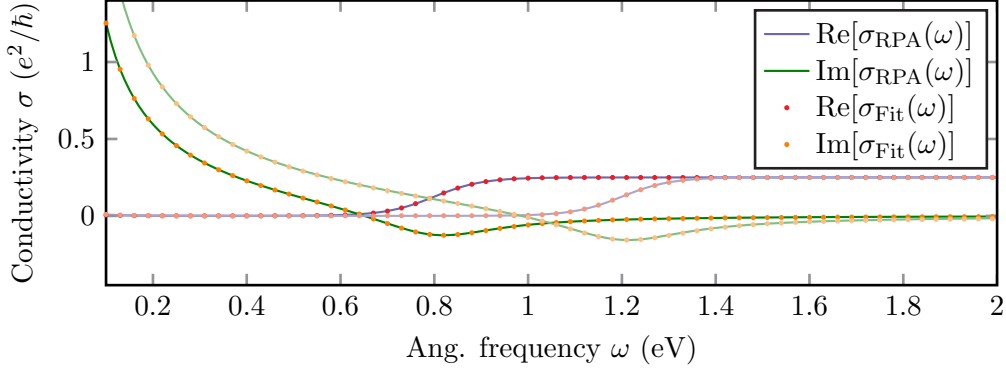
Figure 5.2: Fitted (dots) and RPA (solid lines) data for the full conductivity of graphene, for two different sets of parameters ($\Gamma = 5 \cdot 10^{-4}$ eV and $T = 300$ K). Two different doping levels are used, $\mu = 0.4$ eV and $\mu = 0.6$ eV and are represented by dark and light colors, respectively. Graphene's full conductivity (see Eq. (1.82)) contains both intra- and interband contributions where the intraband contributions are given by an exact Drude term (see Eq. (2.64)) and the interband contributions are fitted with a two-term critical point (CP) model. Adapted from J. F. M. Werra *et al.*, "Current sheets in the Discontinuous Galerkin Time-Domain method: an application to graphene", Proc. SPIE Optics+Optoelectronics **95020,** 95020E (2015).

and a validation of it for the case of the DGTD method. This section is adapted from Ref. [W7].

As discussed in section 2.2.4, the conductivity of doped graphene at finite temperatures can be described by a simple Drude pole and an additional interband term Eq. (2.65). At optical frequencies and low doping levels, the Drude contribution dominates the electromagnetic response. However, at high doping levels or at THz frequencies the interband conductivity governs the properties of graphene. Additionally, for sufficiently high temperatures, the damping Γ can be ignored (see the small differences between the optical conductivity for different values of Γ in Fig. 5.1), i.e., we can consider the limit $\Gamma \to 0$.

Analogously to the work of Prokopeva et al. (see Ref. [192]), we can simplify the interband conductivity's expression Eq. (2.65)

$$\sigma_{\text{inter}}(\omega) = -\mathrm{i}\frac{e^2\omega}{\pi}\mathcal{P}\int\limits_0^\infty \frac{g(E)}{4E^2 - (\hbar\omega)^2}\mathrm{d}E + \frac{e^2}{4\hbar}g\left(\frac{\hbar\omega}{2}\right),$$ (5.33)

where $\mathcal{P}$ denotes the principal value and we have introduced the auxiliary function

$$g(\hbar\omega) = \frac{\sinh\left(\frac{\hbar\omega}{k_{\mathrm{B}}T}\right)}{\cosh\left(\frac{\mu}{k_{\mathrm{B}}T}\right) + \cosh\left(\frac{\hbar\omega}{k_{\mathrm{B}}T}\right)}.$$ (5.34)

Equation (5.33) allows for an analytical expression for the real part. This is very helpful for fitting graphene's interband conductivity using a two-term critical point (CP) models (see Sec. 5.5.1 for the exact expression). Due to the Kramers-Kronig relation (see

Parameters	1st CP	2nd CP
Ω_m (eV)	0.5050	0.7922
Γ_m (eV)	0.6760	0.1700
ϕ_m (°)	-88.5631	-84.3622
A_m ($e^2/\hbar$)	0.1764	0.0456

Parameters	1st CP	2nd CP
Ω_m (eV)	1.1943	0.8751
Γ_m (eV)	0.1807	0.9660
ϕ_m (°)	-88.5762	-84.3661
A_m ($e^2/\hbar$)	0.0230	0.1121

Table 5.2: Parameters of the two-term CP model obtained by fitting the model to the interband conductivity $\mathrm{Re}\left[\sigma_{\mathrm{inter}}(\omega)\right]$ for two doping level, $\mu = 0.4\,\mathrm{eV}$ and $\mu = 0.6\,\mathrm{eV}$ (left and right table), respectively, as described in Fig. 5.2.

Eq. (1.94), this expression can then also be utilized to describe the imaginary part of the interband conductivity (see Ref. [192]).

In Tab. 5.2, we list the fitting parameters of the CP model and present in Fig. 5.2 a comparison between the analytical and the fitted conductivities. For the definition of these CP-parameters and the exact form of the fitting function along with its interconnection to the parameters presented in Tab. 5.2, we refer to appendix E.

5.5.1 Current sheets in the DGTD

The concept of current sheets has first been introduced via boundary conditions by Mohammadian *et al.* into the so-called Finite Volume (FV) methods (cf. Ref. [194]).

Due to the similarities between FV and DGTD methods, this concept can be straight-forwardly adapted to the DGTD method. The boundary condition given in Eq. (5.15) has in this specific case to include the physical boundary condition (cf. Eqs. (2.52))

$$\hat{\mathbf{n}} \times \Delta\mathbf{E}(\mathbf{r}, t) = 0 \qquad \text{and} \qquad \hat{\mathbf{n}} \times \Delta\mathbf{H}(\mathbf{r}, t) = \mathbf{j}_{\mathrm{surf}}\,, \tag{5.35}$$

with $\mathbf{j}_{\mathrm{surf}}$ the local surface current. In frequency domain this reads (cf. Eq. (1.82))

$$\mathbf{j}_{\mathrm{surf}}(\omega) = \sigma(\omega)\left[\hat{\mathbf{n}} \times \mathbf{E}^{\pm}(\mathbf{r}, \omega)\right]\,. \tag{5.36}$$

Opposite to the case of the electromagnetic response of a 3D, bulk material (cf. Eq. (5.31)), the conductivity of a current sheet does not alter the volumetric Maxwell's equations but rather the boundary conditions Eq. (5.15). Then, between two elements there is a current sheet flowing according to

$$\Delta\mathbf{H}(\mathbf{r}, t)' = \Delta\mathbf{H}(\mathbf{r}, t) - \mathbf{j}_{\mathrm{surf}}(\mathbf{r}, t). \tag{5.37}$$

Here, we use that the tangential components of the electric field are continuous across the interface which leads to a continuous surface current $\mathbf{j}_{\mathrm{surf}}$.

In the case of a current sheet, we employ – as is the case for any dispersive material model – ADEs (see Ref. [179] and section 5.4) that here describe the time-evolution of the current density. In the case of graphene, we show in the following (see also Ref. [192]) it is most effectively described by combining a single Drude model (intraband term) with two CP-models into the surface current via (cf. Eqs. (5.30) and (5.31))

$$\mathbf{j}_{\mathrm{surf}}(\mathbf{r}, t) = \sum_{i=1}^{N_{\mathrm{Drude}}=1} \mathbf{j}_{\mathrm{Drude},i}(\mathbf{r}, t) + \sum_{i=1}^{N_{\mathrm{CP}}=2} \mathbf{j}_{\mathrm{CP},i}(\mathbf{r}, t)\,. \tag{5.38}$$

Similarly to the Drude (Eq. (5.25)) and the Lorentz (Eq. (5.27)) conductivities, the conductivity of the CP model reads as (see Ref. [W7, 195, 196])

$$
\begin{aligned}
\sigma_{\mathrm{CP}}(\omega) &= -\mathrm{i}\omega A_m \Omega_m \left(\frac{\mathrm{e}^{\mathrm{i}\phi_m}}{\Omega_m - (\omega + \mathrm{i}\Gamma_m)} + \frac{\mathrm{e}^{-\mathrm{i}\phi_m}}{\Omega_m + (\omega + \mathrm{i}\Gamma_m)} \right) \\
&= -2\mathrm{i}\omega A_m \Omega_m \frac{\cos{(\phi_m)}\Omega_m - \sin{(\phi_m)}\Gamma_m - \mathrm{i}\omega(-\sin{(\phi_m)})}{\Omega_m^2 + \Gamma_m^2 - \mathrm{i}\omega(2\Gamma_m - \mathrm{i}\omega)} \, .
\end{aligned}
\tag{5.39}
$$

Here, the implementation into the DGTD requires a slight reformulation that originates from the fact that within the DGTD method the electromagnetic field is collocated while within the FDTD the electromagnetic field is represented on a staggered Yee-grid. Such reformulations are known for the Drude- and the Lorentz-model (compare sections 5.4.1, 5.4.2 and Refs. [180, 185]).

To find a set of ADEs suited for the DGTD method as in the case of the Lorentz conductivity Eq. (5.29) we have to provide a formulation that only depends on the electric field $\mathbf{E}(\mathbf{r}, t)$ and does not contain its temporal derivative. This can be achieved by introducing two auxiliary currents

$$
\mathbf{p}_{\mathrm{CP}}(\mathbf{r}, \omega) = \mathbf{j}_{\mathrm{CP}}(\mathbf{r}, \omega) + 2A_m \Omega_m \sin{(\phi_m)}\mathbf{E}(\mathbf{r}, \omega) \, ,
\tag{5.40}
$$

$$
\begin{aligned}
\mathbf{q}_{\mathrm{CP}}(\mathbf{r}, \omega) = &-\frac{\left(\Omega_m^2 + \Gamma_m^2\right)}{2\Gamma_m - \mathrm{i}\omega}\mathbf{p}(\mathbf{r}, \omega) \\
&- \frac{2A_m \Omega_m \left[2\Gamma_m \Omega_m \cos{(\phi_m)} + \left(\Gamma_m^2 - \Omega_m^2\right)\sin{(\phi_m)}\right]}{2\Gamma_m - \mathrm{i}\omega}\mathbf{E}(\mathbf{r}, \omega) \, .
\end{aligned}
\tag{5.41}
$$

Inserting these expressions into the current equation $\mathbf{j}_{\mathrm{CP}}(\mathbf{r}, \omega) = \sigma_{\mathrm{CP}}(\omega)\mathbf{E}(\mathbf{r}, \omega)$ and transforming to the time domain, we obtain the ADEs of the CP model

$$
\partial_t \mathbf{p}_{\mathrm{CP}}(\mathbf{r}, t) = \mathbf{q}_{\mathrm{CP}}(\mathbf{r}, t) + 2A_m \Omega_m \left[\cos{(\phi_m)}\Omega_m + \sin{(\phi_m)}\Gamma_m\right]\mathbf{E}(\mathbf{r}, t) \, ,
\tag{5.42}
$$

$$
\begin{aligned}
\partial_t \mathbf{q}_{\mathrm{CP}}(\mathbf{r}, t) = &-2\Gamma_m \mathbf{q}_{\mathrm{CP}}(\mathbf{r}, t) - \left(\Omega_m^2 + \Gamma_m^2\right)\mathbf{p}_{\mathrm{CP}}(\mathbf{r}, t) \\
&- 2A_m \Omega_m \left[2\Gamma_m \Omega_m \cos{(\phi_m)} + \left(\Gamma_m^2 - \Omega_m^2\right)\sin{(\phi_m)}\right]\mathbf{E}(\mathbf{r}, t) \, .
\end{aligned}
\tag{5.43}
$$

Then, the boundary condition for the magnetic field is calculated using the time-dependent expression for the surface current $\mathbf{j}_{\mathrm{CP}}(\mathbf{r}, t)$ obtained from Eq. (5.40)

$$
\mathbf{j}_{\mathrm{CP}}(\mathbf{r}, t) = \mathbf{p}_{\mathrm{CP}}(\mathbf{r}, t) - 2A_m \Omega_m \sin{(\phi_m)}\mathbf{E}(\mathbf{r}, t) \, .
\tag{5.44}
$$

5.5.2 Validation

In this section, we validate our results by comparing DGTD computations in two spatial dimensions with analytic transfer-matrix calculations (see Eq. (4.1) and Fig. 4.2).

In Fig. 5.3 (left column), we depict the frequency-dependence of reflectance from and transmittance through a single layer of graphene suspended in vacuum. In this case, the

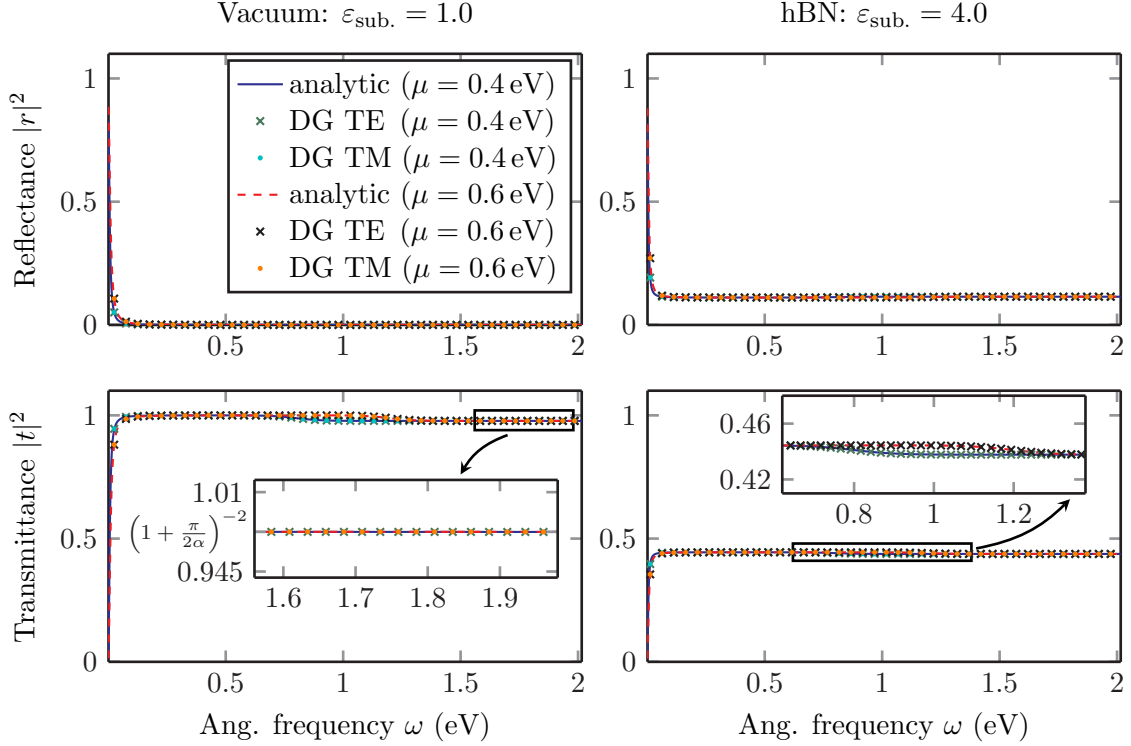## 5 The Discontinuous Galerkin Time-Domain Method

Figure 5.3: Comparison of the frequency-dependence of reflectance from and transmittance through a freely suspended (left column) and on hBN deposited (right column) graphene sheet under normal incidence for DGTD computations (symbols) and analytical calculations (solid and dashed lines) for different doping levels μ (0.4 eV and 0.6 eV) and polarizations (TE and TM). For the hBN substrate we assume $\varepsilon = 4.0$. The inset in the lower right panel shows the influence of different doping values on the transmittance. The legend displayed in the upper left graph applies to all graphs. Adapted from J. F. M. Werra *et al.*, "Current sheets in the Discontinuous Galerkin Time-Domain method: an application to graphene", Proc. SPIE Optics+Optoelectronics **95020,** 95020E (2015).

intraband conductivity of graphene completely dominates for short (optical) wavelengths, leading to a transmittance of (cf. Refs. [75, 197] and Eq. (2.50))

$$T = |t|^2 = \frac{1}{\left(1 - \frac{\pi}{2\alpha}\right)^2} \approx \frac{\pi}{\alpha} \approx 97.74\% \,. \tag{5.45}$$

Within the DGTD, the transmittance (and reflectance) can be calculated via the definition of transmittance (and equivalently reflectance R by interchanging t→r) as

$$T = \frac{\Phi^{\mathrm{t}}(\omega)}{\Phi^{\mathrm{i}}(\omega)} \equiv \frac{\langle \int_{\mathcal{V}} \mathrm{d}^3 x \, \partial_t u^{\mathrm{t}}(t) \rangle_t}{\langle \int_{\mathcal{V}} \mathrm{d}^3 x \, \partial_t u^{\mathrm{i}}(t) \rangle_t} \stackrel{\mathrm{Eq.\ (1.21)}}{=} \frac{\int_{\partial\mathcal{V}} \mathrm{d}^2 x \, \langle \mathbf{S}^{\mathrm{t}}(t) \rangle_t \cdot \mathbf{n}}{\int_{\partial\mathcal{V}} \mathrm{d}^2 x \, \langle \mathbf{S}^{\mathrm{i}}(t) \rangle_t \cdot \mathbf{n}} \,, \tag{5.46}$$
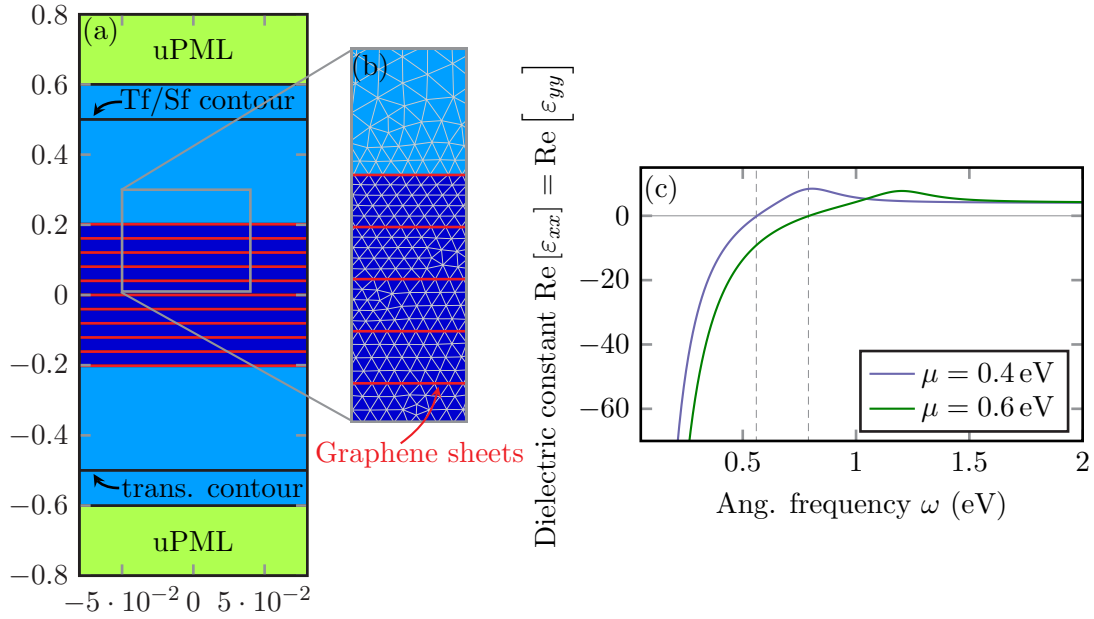
Figure 5.4: Panel (a): Schematic of the setup for a hyperbolic metamaterial (HMM) computation via the DGTD method. There are 11 graphene current sheets (bold red lines with the boundary condition Eq. (5.37)) that are separated by 10 hBN layers (dark blue), each being 50 nm thick. In the vertical direction, the computational domain is terminated by uPMLs and the TfSf contour is marked. In the horizontal direction, periodic boundary conditions are applied. Furthermore, the setup considered is two-dimensional. Panel (b) depicts an inset. Panel (c) shows the frequency-dependence of the real part of transverse effective dielectric constant $\mathrm{Re}[\varepsilon_{xx}(\omega)] = \mathrm{Re}[\varepsilon_{yy}(\omega)]$ for and infinite stack of alternating graphene and hBN layers (thickness 50 nm, dielectric constant $\varepsilon = 4$) for different doping level of graphene (following Ref. [88]). As $\mathrm{Re}[\varepsilon_{zz}] = \varepsilon$, this composite system exhibits the characteristics of a HMM in the frequency range $\omega = 0\,\mathrm{eV}$ to $\omega = 0.56\,\mathrm{eV}$ ($\mu = 0.4\,\mathrm{eV}$) and $\omega = 0.79\,\mathrm{eV}$ ($\mu = 0.6\,\mathrm{eV}$), respectively. Adapted from J. F. M. Werra *et al.,* "Current sheets in the Discontinuous Galerkin Time-Domain method: an application to graphene", Proc. SPIE Optics+Optoelectronics **95020,** 95020E (2015).

where $\Phi^{\mathrm{t(r)}}(\omega)$ is the directed, radiant flux transmitted (reflected) by the periodic structure and $\Phi^{\mathrm{i}}(\omega)$ the directed, radiant radiant flux incident on the periodic structure. Here, we integrate over a volume $\mathcal{V}$ that is surrounded by an in infinity closed surface $\partial\mathcal{V}$ with the normal unit vector $\mathbf{n}$ on the surface. In this section, this integration areas are displayed in Fig. 5.4, where the *TfSf contour* is the integration contour for the reflected and the contour marked by the term *trans. contour* the integration contour for the transmitted, time averaged Poynting flux (cf. Eq. (5.46)).

As demonstrated in the inset of the lower left graph in Fig. 5.3, within the DGTD approach we obtain precisely this value for an infinitesimally thin current sheet and do not have to take into account any artificial thickness of the graphene layer as would be required in FDTD computations [198].

In addition, we test our system for both, TE and TM polarization for the case of graphene on a substrate. Clearly, for normal incidence those two cases coincide analytically but in the DGTD computations different codes (rather different sections of the code) are utilized so that obtaining agreement with the analytical calculations provides a further aspect of validation. As before, we choose hexagonal boron nitride (hBN) as the substrate as this leads to minimal strain effects. In fact, recent ab-initio computations [54] have demonstrated that strain is the main factor for opening an electronic band gap in graphene, an effect which is not contained in our material model. In Fig. 5.3 (right column), we compare the transmittance and reflectance results from analytic calculations with those from DGTD computations and find excellent agreement.

5.5.3 Multilayer systems: hyperbolic metamaterials

Our current sheet approach exhibits significant advantages for a number of situations such as nonlinear material models for graphene and/or complex geometries. For illustration, we focus on the latter and consider stacks that contain multiple layers of graphene that are separated by dielectric spacer layers.

As described above, our approach treats graphene as an infinitely thin current sheet instead of a thin film of somewhat arbitrary (but certainly small) thickness as would be the case for FDTD computations (see Ref. [198]).

From a numerical point of view, perhaps even more important than the somewhat arbitrary thickness is the fact that no matter what the precise value, it will be very, very small compared to other length scales present in nanoplasmonic systems. For instance, typical thicknesses of graphene sheet of 5 Å have to be compared with 700 nm (wavelength of red light) or even 300 μm (wavelength corresponding to the frequency of 1 THz). Corresponding antenna structures are perhaps a factor of 10 (visible frequencies) to 100 (THz frequencies) smaller and may exhibit feature sizes in the range of, say, 10 nm. Because the smallest length scale in the problem generally determines the maximally available time step in explicit time-stepping schemes this suggests that when having to fully resolve the Å length scale as in the FDTD approach, one has to pay double, i.e., one has to deal with many unknowns and acquires very small time steps both of which significantly increase the computational run-times. In contrast, the infinitely thin current sheets of the DGTD approach completely avoid the problem of resolving the Å scale. Rather, the DGTD approach has to resolve the next largest length scale; in our example this would be the typical feature size of a nanoantenna, say, 10nm. From this, obvious gains in efficiency relative to the FDTD approach result.

In the following, we investigate systems with up to 25 graphene layers stacked in the z-direction and separated by hBN layers (thickness 50 nm) for different doping levels and compare the reflectance and transmittance under normal incidence with analytical calculations. Such composite systems are known to exhibit effective hyperbolic dispersion relations as they correspond to effective uniaxial materials and are thus called hyperbolic metamaterial (HMM). For them, the values of the real part of the principal dielectric constants differ in sign (see Ref. [88]).

Such effective hyperbolic dispersion characteristics lead to novel and highly interesting optical phenomena such as enhanced densities of states etc. (see Ref. [199]).

In Fig. 5.5, we depict the results of both, DGTD computations and transfer-matrix
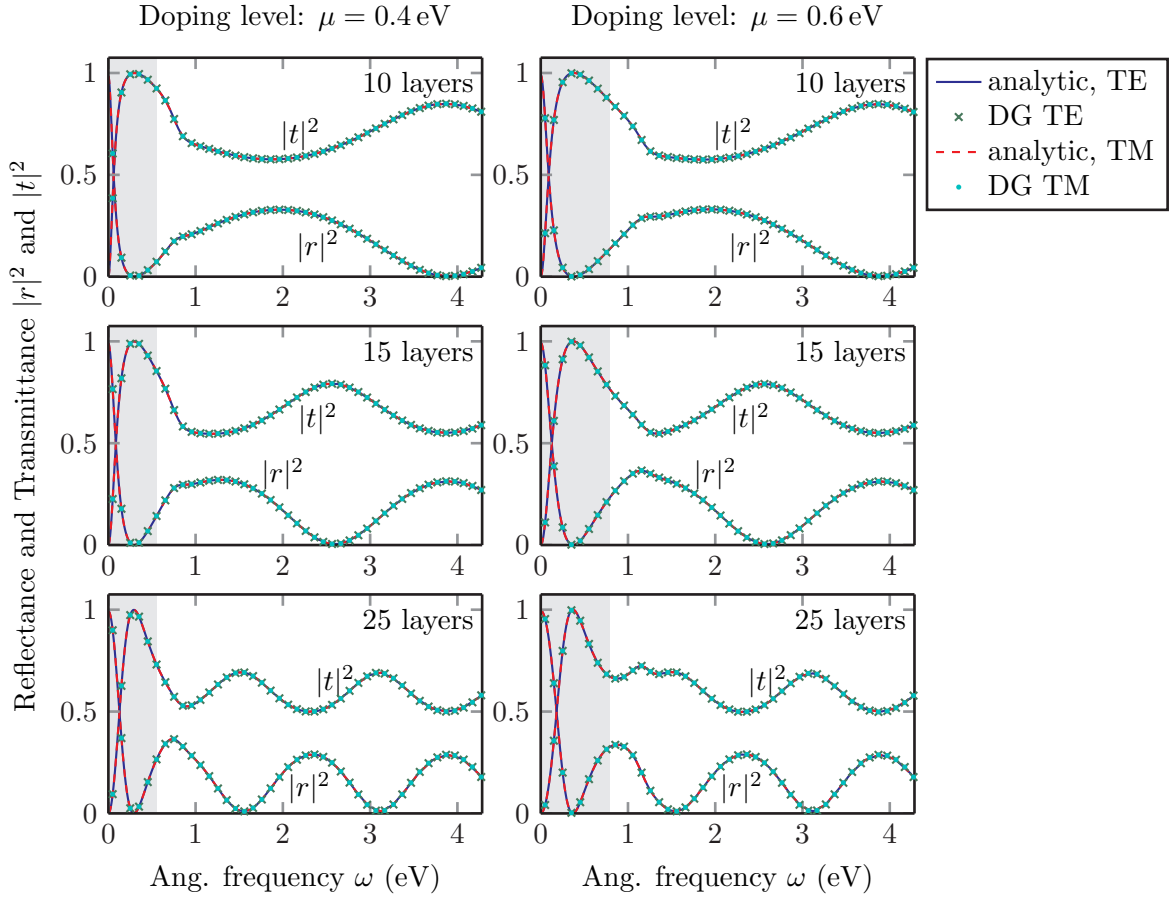
Figure 5.5: Frequency dependence of transmittance and reflectance through 10, 15 and 25 layers hBN of thickness 50 nm, separated by and the whole stack sandwiched between graphene monolayers of different doping level μ (cf. Fig. 5.4 for further details). In the HMM region (gray shaded area), a single peak with near unity transmittance through the stacks is observed. Outside of this region the electromagnetic response is governed by Fabry-Perot oscillations. The DGTD computations (symbols) agree very well with corresponding analytical transfer-matrix calculations for both polarizations, TE and TM. Adapted from J. F. M. Werra *et al.,* "Current sheets in the Discontinuous Galerkin Time-Domain method: an application to graphene", Proc. SPIE Optics+Optoelectronics **95020,** 95020E (2015).

based analytical calculations. In the frequency range of hyperbolic behavior, we observe invariably near-unity transmittance, although a single graphene sheet on a hBN substrate exhibits rather low transmittance values (cf. Fig. 5.3, right column). These peaks are around frequencies $\omega = 0.3$ eV and $\omega = 0.37$ eV for doping levels at $\mu = 0.4$ eV and $\mu = 0.6$ eV, respectively, and exhibit a weak dependence on the number of layers. In contrast to this, outside the HMM frequency range, the systems features ordinary Fabry-Perot oscillations corresponding to the thickness of the entire structure. Finally, we would
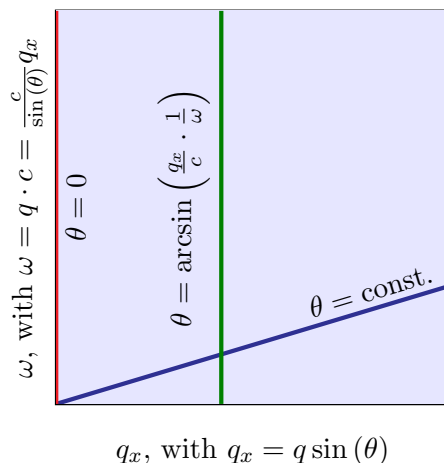
Figure 5.6: The Figure above symbolizes the complete space of the dispersion relation (light blue) that is spanned by the parameters incident angle and frequency. The red line symbolizes the parameters accessed by a time-domain simulation of normal incidence, the blue line the parameter space accessed by a true oblique incident simulation with a fixed incident angle θ and the green line the parameter space accessed by the method introduced in Ref. [200].

like to note, that for these rather complex systems, too, the agreement between DGTD computations and analytical calculations is excellent (relative error $\epsilon_{\text{rel}} < 10^{-7}$).

5.6 Oblique incidence

Up to this point, we have analyzed periodic structures only by impinging with normal incident electromagnetic pulses. However, this only gives access to a very small space of the $(\mathbf{q}, \omega)$ space (cf. Fig. 5.6) and especially for metamaterials that exhibit a very special dispersion relation (see Refs. [88, 199]) but also in the case of periodically structured layered structures (see e.g. Ref. [W5]) a method that allows for varying the incident angle of the electromagnetic excitation is of great interest. In the following, we present a method first introduced in Ref. [200].

5.6.1 General Idea

In general, while normal incidence in periodic structures is straight-forwardly implementable in Time-Domain solvers, oblique incidence is not. This is due to the dispersion relation of light. In general, we define a constant incidence angle θ via

$$q_x = q \cdot \sin\left(\theta\right), \tag{5.47}$$

when the incidence plane is assumed along the (x, y)-direction, the absolute value of the incidence wave vector is given via $q = |\mathbf{q}|$ and the light propagates in z-direction (cf. Fig. 5.8). When the periodic lattice constant in x-direction is given as a, we can connect
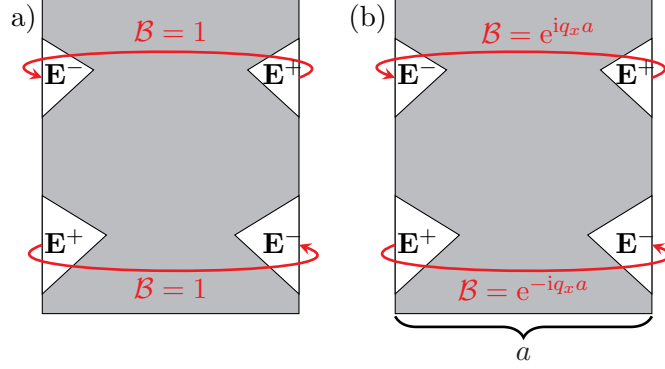
Figure 5.7: When using periodic boundary conditions (a), two periodic elements can be connected by identifying the other element as the neighboring element containing the fields $\mathbf{E}^+$ and $\mathbf{H}^+$ from the numerical flux and Eq. (5.15). When we model oblique incidence, the corresponding periodic elements are in one direction connected via condition (5.53).

the electric and magnetic fields in *frequency domain* via

$$\begin{aligned}
\boldsymbol{\mathcal{E}}(x=0,y,z,\omega) &= \boldsymbol{\mathcal{E}}(x=a,y,z,\omega)\mathrm{e}^{\mathrm{i}q_x a}\,, \\
\boldsymbol{\mathcal{H}}(x=0,y,z,\omega) &= \boldsymbol{\mathcal{H}}(x=a,y,z,\omega)\mathrm{e}^{\mathrm{i}q_x a}\,.
\end{aligned} \tag{5.48}$$

Translating those two equations into time domain yields (for a linear dispersion relation $\omega = k \cdot c$ with the material dependent speed of light c):

$$\begin{aligned}
\mathbf{E}(x=0,y,z,t) &= \mathbf{E}(x=a,y,z,t+a\cdot\frac{\sin(\theta)}{c})\,, \\
\mathbf{H}(x=0,y,z,t) &= \mathbf{H}(x=a,y,z,t+a\cdot\frac{\sin(\theta)}{c})\,.
\end{aligned} \tag{5.49}$$

Equation (5.49) requires the knowledge of the electric and magnetic fields at later points of the simulations. For $q_x = 0$ (normal incidence) this requirement vanishes which makes the case implementable in time-domain Maxwell solvers, however for any other general oblique incidence angle, this is not the case. Several different approaches were therefore developed in the FDTD community to shortcut this problem. One famous approach is the split-field method (cf. Ref. [201]). This approach, however, requires several iterations of the program and is therefore highly inefficient for calculations.

However, truly oblique incidence is only one way to access the complete space spanning over frequency and incidence angle. The sketch in Fig. 5.6 represents this parameter space, where the red line marks the parameter space accessed by a normal incident calculation, the blue line the parameter space accessed by an oblique incidence simulation with a fixed incidence angle and the green line a parameter space accessed by choosing

$$q_x = \text{const.} \tag{5.50}$$

In this case, in linear time-domain simulations the propagation of a pulse with a continuum of incident angles is computed - indeed exactly distributed as the frequency distribution of the implemented pulse. Depending on the research question at hand, this
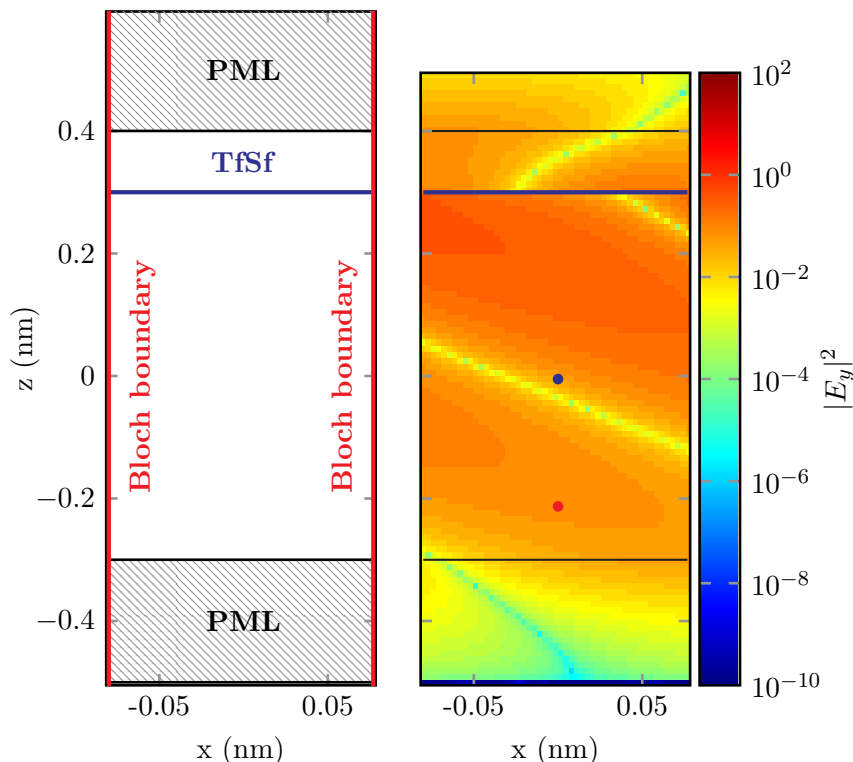
Figure 5.8: Electric field distribution $|E_x(t_1 = 5.4779c/\text{nm})|^2$. The mesh setup is depicted on the left of the picture, where in z-direction the domain is terminated by Silver-Müller boundaries on the top and on the bottom. The TfSf contour (blue line) on which not the exact solution to Maxwell's equations is induced into the system but rather the solution for $q_x = 0$. The Bloch periodic boundaries fulfill the condition $q_x = 10/\text{nm}$ (red line in Fig. 5.10). The blue and red dot represent the positions $\mathbf{r}_0$ chosen for the plots in Fig. 5.9.

approach might be as valid as the oblique incident approach, when we are for example more interested in testing a system for the complete parameter space and not just using one of those lines.

Whenever we choose a constant q_x instead of a constant angle θ for the direction of the incident pulse, we actually implement Bloch boundaries[31]. Then, the projected wavenumber q_x is not dependent on the frequency of the plane wave and therefore also not dependent on time. We accordingly write

$$
\begin{aligned}
\mathbf{E}(x=0,y,z,t) &= \mathbf{E}(x=a,y,z,t)\mathrm{e}^{\mathrm{i}q_x a}\,, \\
\mathbf{H}(x=0,y,z,t) &= \mathbf{H}(x=a,y,z,t)\mathrm{e}^{\mathrm{i}q_x a}\,.
\end{aligned}
\tag{5.51}
$$

---

[31] The Bloch theorem states that for a periodic potential $V(\mathbf{r}) = V(\mathbf{r}+\mathbf{R})$ the solutions of Schrödinger's equations have the form $\psi(\mathbf{r}+\mathbf{R}) = \mathrm{e}^{\mathrm{i}\mathbf{k}\cdot\mathbf{r}}\psi(\mathbf{r})$. Although this setup cannot directly be mapped onto our situation (Bloch's theorem is exactly like Eq. (5.49) stated in Fourier domain), the equations look the same and the name is simply used as an abbreviation.
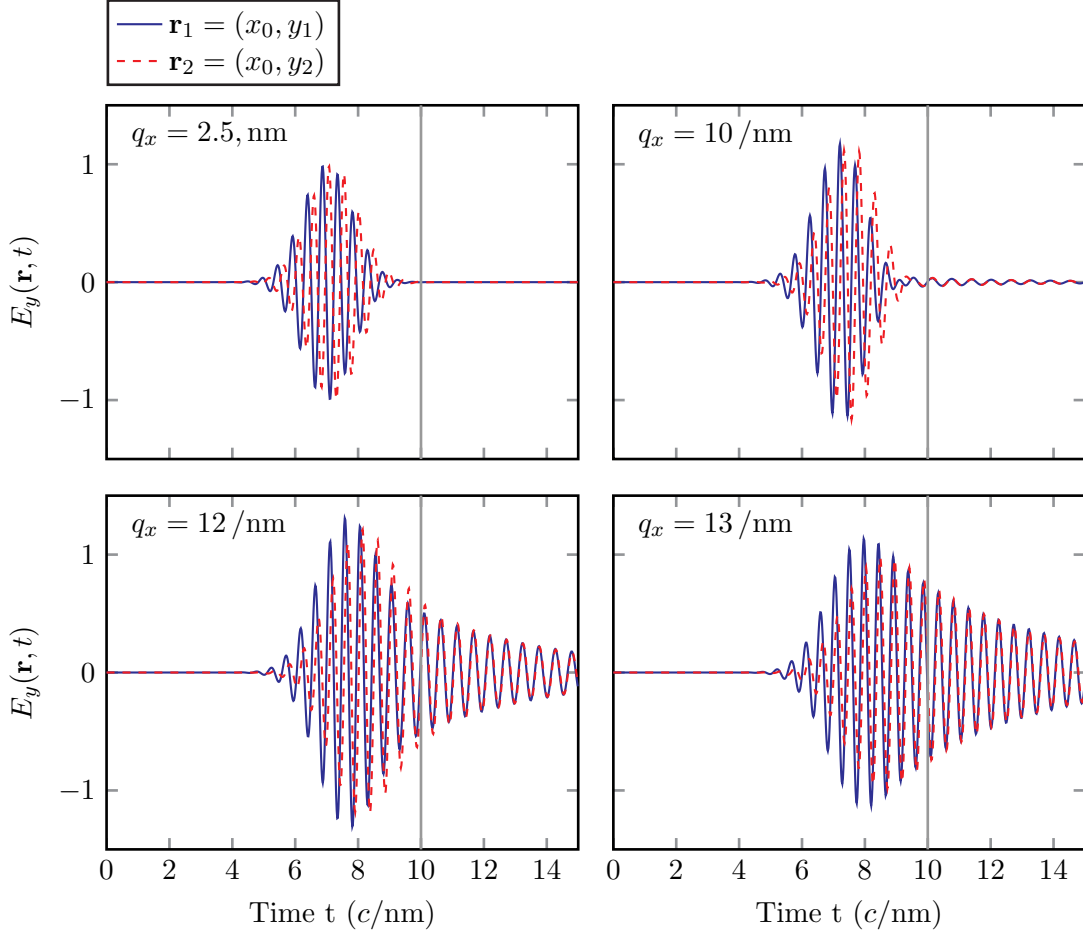
Figure 5.9: In the panels above, we show the fields $E_y(\mathbf{r}_1, t)$ and $E_y(\mathbf{r}_2, t)$ at two horizontally separated points (marked in Fig. 5.8 in blue and red corresponding to the colors of the plots above). For different q_x the long-time horizontal mode has different amplitudes, the higher the closer to the center of the spectrum of the exciting pulse (cf. Fig. 5.10). Gray lines mark the time from which on the fields are dominated by the complete perpendicularly propagating modes are assumed to exist in the systems and which are taken as starting times for the discrete Fourier transform in Fig. 5.10. The time at which the perpendicularly propagating mode is assumed to be dominant is the time at which both electric fields oscillate in phase. Adapted for DGTD data from Ref. [200].

In the following, we will use the term **Bloch factor** $\mathcal{B}$ that is defined as

$$\mathcal{B} = \mathrm{e}^{\mathrm{i}q_x a} \, . \tag{5.52}$$

This can be implemented via Eq. (5.15) where instead of directly connecting the two periodically attached elements (see Fig. 5.7), we alter the boundary condition on one side to

$$\Delta\mathbf{E} = \mathcal{B}^{-1}\mathbf{E}^+ - \mathbf{E}^- \, , \qquad\qquad \Delta\mathbf{H} = \mathcal{B}^{-1}\mathbf{H}^+ - \mathbf{H}^- \, . \tag{5.53}$$
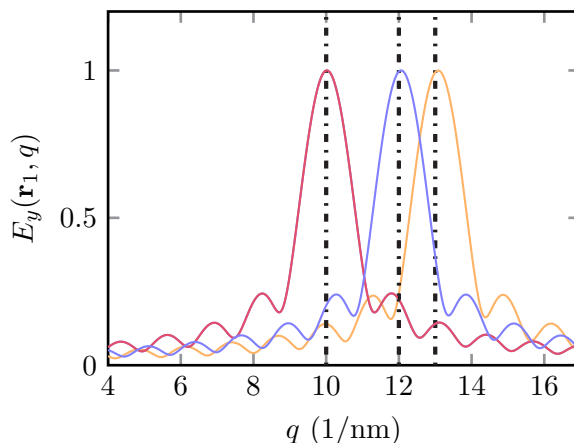
Figure 5.10: Discrete Fourier transform of electric fields from Fig. 5.9 (Fields at $z = 0$ nm, blue curve as marked in Fig. 5.8). For $q_x = 2.5$/nm the remaining electric field is not strong enough to extract the eigenfrequency. The fields from $t_0 = 10$/nm (compare gray lines in Fig. 5.9) are taken into account. Comparing the mode's eigenfrequencies with q_x (dashed lines) gives a very good correspondence.

Another possible implementation of the general idea of quasi-oblique incidence is presented in Ref. [202]. where instead of computing **E** and **H**, the DGTD and with this the numerical flux is reformulated for auxiliary modified fields. We, however, choose the more direct implementation presented similarly for the FDTD case in Ref. [200].

5.6.2 Vacuum tests

With the correct boundary conditions Eq. (5.53), we go ahead and test the implementation with a vacuum setup as a proof of principle. The setup consists of uPMLs on the top and bottom and the electromagnetic field is induced via a TfSf contour (see left panel of Fig. 5.8). The electromagnetic field induced into the computational domain is a pulsed plane wave (cf. Eq. (5.19)). Since we induce at the TfSf contour the incident field for the case of normal incidence instead of the (not known) solution for oblique incidence ($q_x = $ const), parts of the field is scattered into the Sf region. When we later compute physical problems that contain a scatterer, we do thus need to apply some post processing to the electromagnetic fields obtained.

In Fig. 5.10, we plot the spectrum used for all the tests presented here. As a first step, we chose four q_x values, $q_x = \{2.5, 10, 12, 13\}(1/\text{nm})$ to access different weights of the horizontal resonant mode. The setup used for the vacuum simulations is presented in Fig. 5.8. In the right panel, only a part of the physical domain is plotted (the upper PML is cut). In general, one can see the oblique incidence of the plane wave on the left hand side where we display the absolute value of the $\mathbf{E}_y$ component. There, we choose $q_x = 10$/nm corresponding to the red line in Fig. 5.10.

One important fact to mention is that it is of great importance to choose the uPMLs correctly, since the Silver-Müller boundaries only absorb the normal incident plane wave and therefore for an oblique wave the oblique part of the radiation is reflected back into
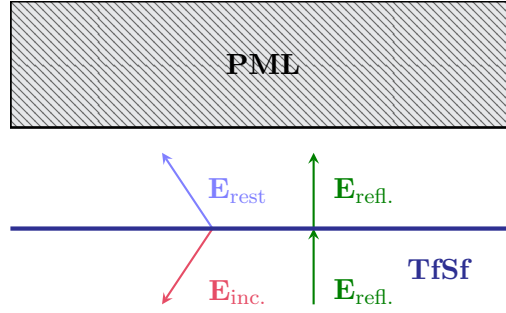
Figure 5.11: The Figure above depicts the problem arising, when we do not add an exact analytical solution of Maxwell's equations to the electric and magnetic field at the TfSf contour. Therefore, a more complicated formula than the usual needs to be used to calculate the reflectance.

the system.

Letting such vacuum simulations evolve in time, one expects the horizontal resonant mode to survive (compare Fig. 5.9). This can also be shown by discrete Fourier transforming the fields starting at a late time t_0 and analyzing the peak eigenfrequency. This corresponds very well with the frequency for which the plane wave propagates parallel to the incident plane (see Fig. 5.10). It is also quite interesting that in Fig. 5.9 one can tell that at two vertically spaced points (see blue and red point in Fig. 5.8) the electric field is excited with a certain retardation. However, when the field has passed and only the horizontal mode survives, the fields oscillate in phase at both vertically distant positions for the remaining time. Besides from the analysis in Fig. 5.10 this is also a proof of the existence of horizontally propagating modes.

5.6.3 The Dielectric Slab

As a second test case, we introduce a scatterer, a dielectric slab, into the computational domain and compute reflection and transmission from this object. As discussed before, due to the fact that the incident electromagnetic field does not fulfill the Bloch boundaries, a part of the incident field is directly scattered into the Sf region (cf. Fig. 5.8).

From Fig. 5.11 it follows that in the short and long computation limit (assuming that all electromagnetic fields leaving the Tf region are completely absorbed by the uPML and Silver-Müller boundary condition) we find for the electric (and analogously magnetic) fields

$$\mathbf{E}(\mathbf{r} = \mathbf{r}_{\mathrm{TfSf}}, t \approx t_0) = \mathbf{E}_{\mathrm{inc.}}(\mathbf{r} = \mathbf{r}_{\mathrm{TfSf}}, t \approx t_0) + \mathbf{E}_{\mathrm{rest}}(\mathbf{r} = \mathbf{r}_{\mathrm{TfSf}}, t \approx t_0),$$
$$\mathbf{E}(\mathbf{r} = \mathbf{r}_{\mathrm{TfSf}}, t \gg t_0) = \mathbf{E}_{\mathrm{refl}}(\mathbf{r} = \mathbf{r}_{\mathrm{TfSf}}, t \gg t_0),$$

where $\mathbf{E}_{\mathrm{inc.}}$ denotes the incident field that propagates into the Tf region, $\mathbf{E}_{\mathrm{rest}}$ denotes the incident field that is scattered into the Sf region and $\mathbf{E}_{\mathrm{refl}}$ the field that is reflected from a periodic scatterer. For all times, we can then write for the outside $\mathbf{E}_{\mathrm{out}}(\mathbf{r}, t)$ and

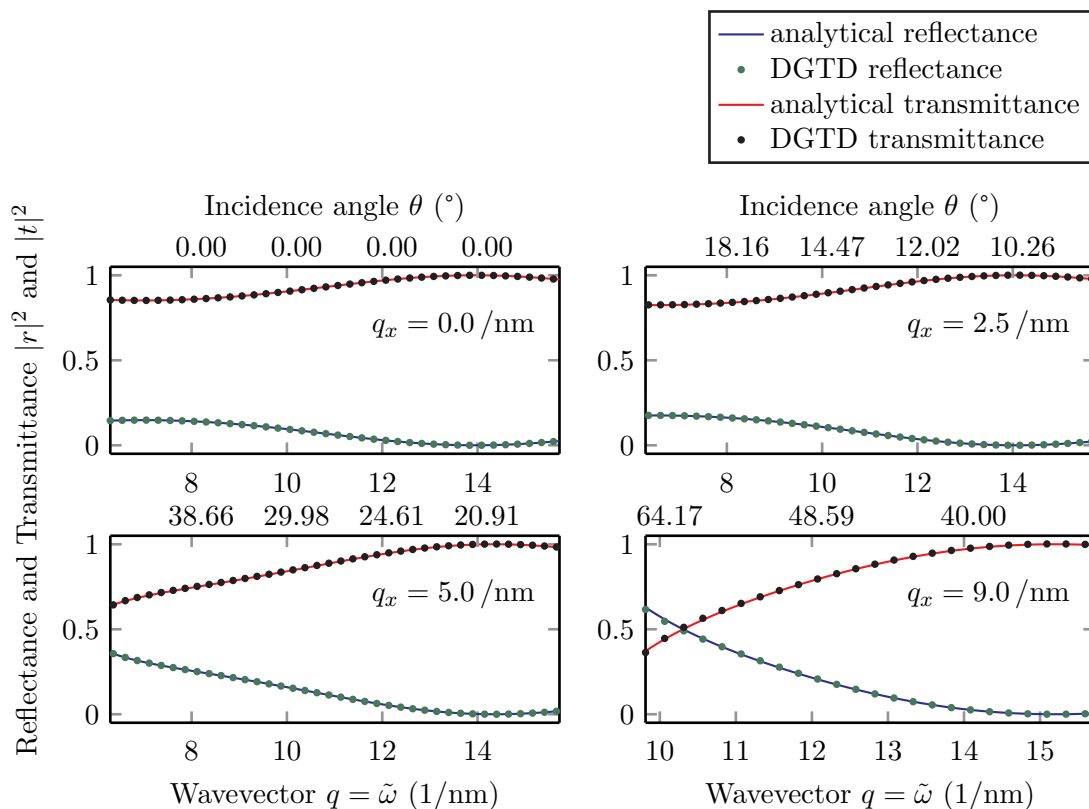# 5 The Discontinuous Galerkin Time-Domain Method

Figure 5.12: The Figure above shows the reflectance and transmittance for three-dimensional TM (magnetic field in incidence plane) computations compared to analytical results obtained by the transmission matrix approach. The calculations were cut for an incidence angle $\theta < 65°$ (or $\tilde{\omega} > 6.5$ /nm for this specific setup) since beyond this the incidence is too flat to obtain results in reasonable computation time using the method applied. The agreement between analytics and numerics, we present in Fig. F.1.

the inside $\mathbf{E}_{\text{in}}(\mathbf{r}, t)$ electric (and analogously magnetic) fields

$$\mathbf{E}_{\text{out}}(\mathbf{r}, t) = \mathbf{E}_{\text{rest}}(\mathbf{r}, t) + \mathbf{E}_{\text{refl.}}(\mathbf{r}, t) \qquad , \qquad (5.54a)$$

$$\mathbf{E}_{\text{in}}(\mathbf{r}, t) = \mathbf{E}_{\text{inc.}} - \mathbf{E}_{\text{refl}} . \qquad (5.54b)$$

Therefore, for the computation of $\mathbf{E}_{\text{refl.}}(\mathbf{r}, t)$ from $\mathbf{E}_{\text{out(in)}}(\mathbf{r}, t)$, information on either E_{rest} or $E_{\text{inc.}}$ is needed, which can be obtained from a vacuum simulation. Then the transmission and reflectance can be obtained from the altered electromagnetic fields

$$\tilde{\boldsymbol{\mathcal{E}}}_{\text{refl}}(\mathbf{r}, \omega) = \boldsymbol{\mathcal{E}}_{\text{out}}(\mathbf{r}, \omega) - \boldsymbol{\mathcal{E}}_{\text{out}}^{\text{vac}}(\mathbf{r}, \omega) \qquad \text{and} \qquad \tilde{\boldsymbol{\mathcal{E}}}_{\text{trans}}(\mathbf{r}, \omega) = \boldsymbol{\mathcal{E}}_{\text{trans}}(\mathbf{r}, \omega) . \qquad (5.55)$$

These and the analogously obtain magnetic fields can then be inserted into Eq. (5.46) to calculate transmittance and reflectance from the scatterer.

Second, we have to consider the fact that the dielectric slab actually touches the Bloch boundary, Whenever a dielectric (or metallic) periodic structure touches the Bloch boundary, we can use the exact same approach as above. This is due to Snell's law and Bloch's
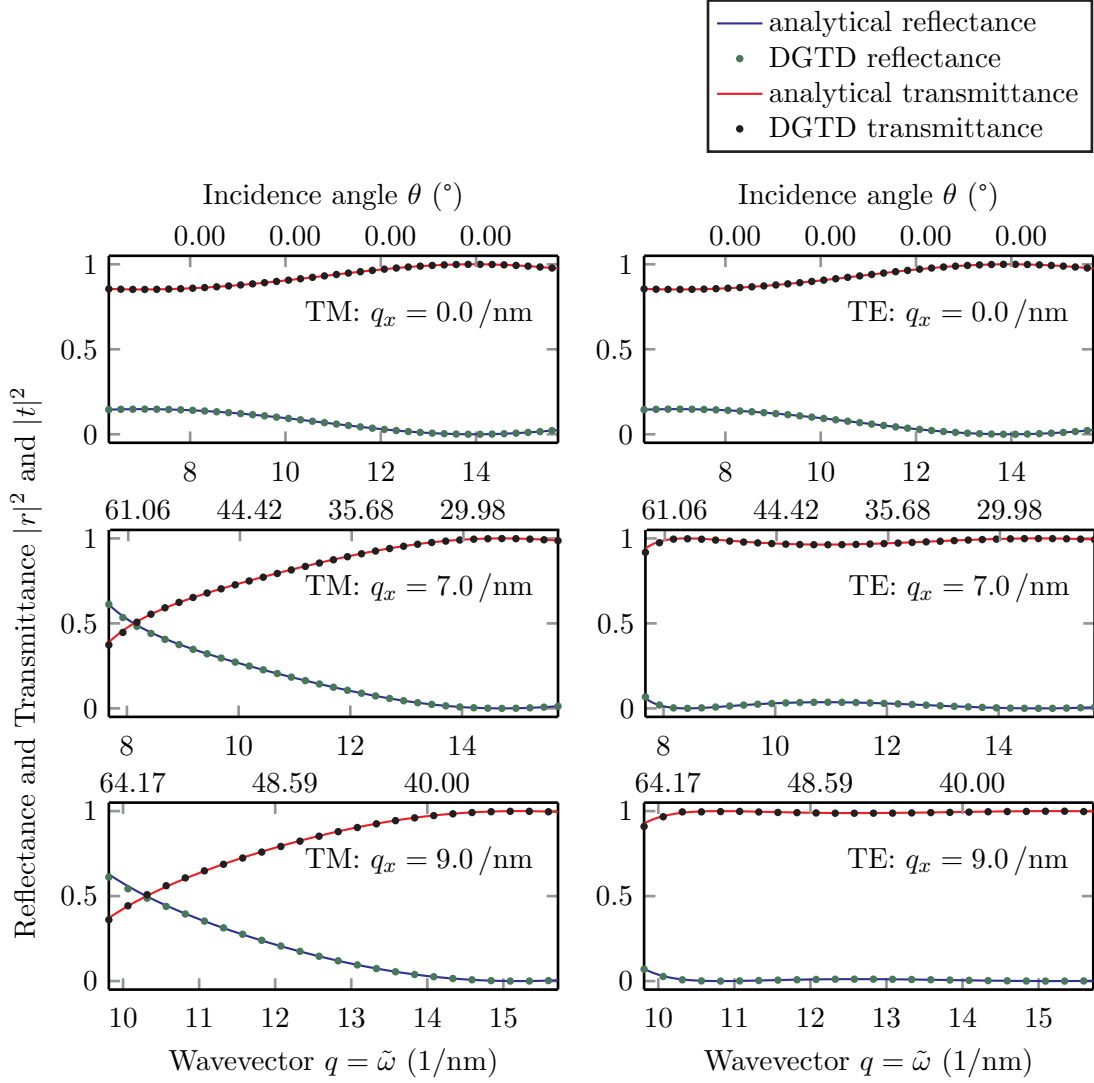
Figure 5.13: The Figure above shows the reflectance and transmittance for two-dimensional TM and TE computations compared to analytical results obtained by the transmission matrix approach. The calculations were cut for an incidence angle $\theta < 65°$ (or $\tilde{\omega} > 6.5$ /nm for this specific setup) since beyond this the incidence is too flat to obtain results in reasonable computation time using the method applied. The agreement between analytics and numerics, we present in Fig. F.2.

theorem leading to

$$n_i \sin(\theta_i) = q_x = \text{const.}, \tag{5.56}$$

and with $q_i = n_i \frac{\omega}{c}$ and $q_x^{(i)} = \sin(\theta_i) q_i = \sin(\theta_i) n_i \frac{\omega}{c}$, we can conclude from Snell's law and energy conservation that

$$q_x^{(i)} = \text{const.} \equiv q_x,$$

for all materials and refractive indices. In other words, the wavenumber parallel to an incident q_x stays constant independent of the refractive index. In conclusion, an interface between two materials touching the Bloch boundary, is no issue if such an interface is orthogonal to the Bloch boundary which is given for most periodic structures. Therefore, choosing the component of the wavevector that is projected orthogonal to the periodicity direction as constant, is still valid when we study periodic structures with material interfaces cutting the Bloch boundary orthogonal.

Using the transfer matrix approach and the Fresnel coefficients for reflection and transmission at one interface, we compare the analytical solution with numeric results. It is important to mention, that those numeric (and analytic) results only hold for $q > q_x$ hence for $\infty > q > q_x$ we vary $0 < \theta < \pi/2$ as incidence angles. Wavevectors smaller then q_x would result in a purely imaginary $q_z = \sqrt{q^2 - q_x^2}$ and therefore to non-propagating modes.

The results of the simulations for 3D are for a slab thickness $d = 0.15\,\text{nm}$ and $\varepsilon = 2.25$, are presented in Fig. 5.12 and for 2D with the same parameters in Fig. 5.13. In both Figures, we vary the constant projected wavenumber q_x. It can be noticed that the numerical values get worse, the closer q_x to the center frequency of the exciting Gaussian pulse and the higher therefore the intensity of the horizontal mode that remains in the system after propagation time. The exact error of the computations is presented in appendix F in Figs. F.1 and F.2.

5.7 Graphene multilayers under oblique incidence

As discussed above, it has been shown in literature (see Ref. [88]) that graphene multilayers stacked between hBN slabs can provide a HMM depending on the chemical potential of the graphene monolayer. Due to the external tunability of the chemical potential by, e.g., electrostatic gating, this is very well suited for optical switching and other applications.

The very specific property that follows from the opposite signs of the anisotropic dielectric tensor (cf. Fig. 5.4(b)) is a hyperbolic isofrequency contour line of the wavevectors. This then leads to an unusual propagation behavior where the propagation direction of the energy flux density (the orientation of the time averaged Poynting vector $\langle \mathbf{S}(\mathbf{r}, t) \rangle_t$ bends into the opposite direction then for a common material).

We present the results in Fig. 5.14 using the example of TM polarization and $q_x = 0.15\,\text{eV}$. In Figs. 5.14(a,b), we compare the analytical results of oblique incidence for reflectance R and transmittance T of a plane wave impinging onto a single graphene monolayer while in Fig. 5.14(c) we present the corresponding results in the case of a multilayer system consisting of 11 layers of graphene with hBN of thickness $50\,\text{nm}$ sandwiched between those (cf. Fig. 5.4(a,b)). The computations presented in Fig. 5.14 have relative errors $\epsilon_{\text{rel}} < 10^{-2}$ in all cases. Here, the error highly depends on the incident frequency with the relative error going down to $\epsilon_{\text{rel}} < 10^{-5}$ at about $\omega = 0.75\,\text{eV}$ stabilizing for higher frequencies with $\epsilon_{\text{rel}} < 10^{-4}$.

Overall the accuracy obtained with the method of oblique incidence as presented in this thesis shows an accuracy worse than normal incidence (cf. Figs. F.1(a) and F.2(a)) however well in the limits of agreement between a theoretical modeling and experimental results usually obtained in nanooptical experiments. This method increases the modeling
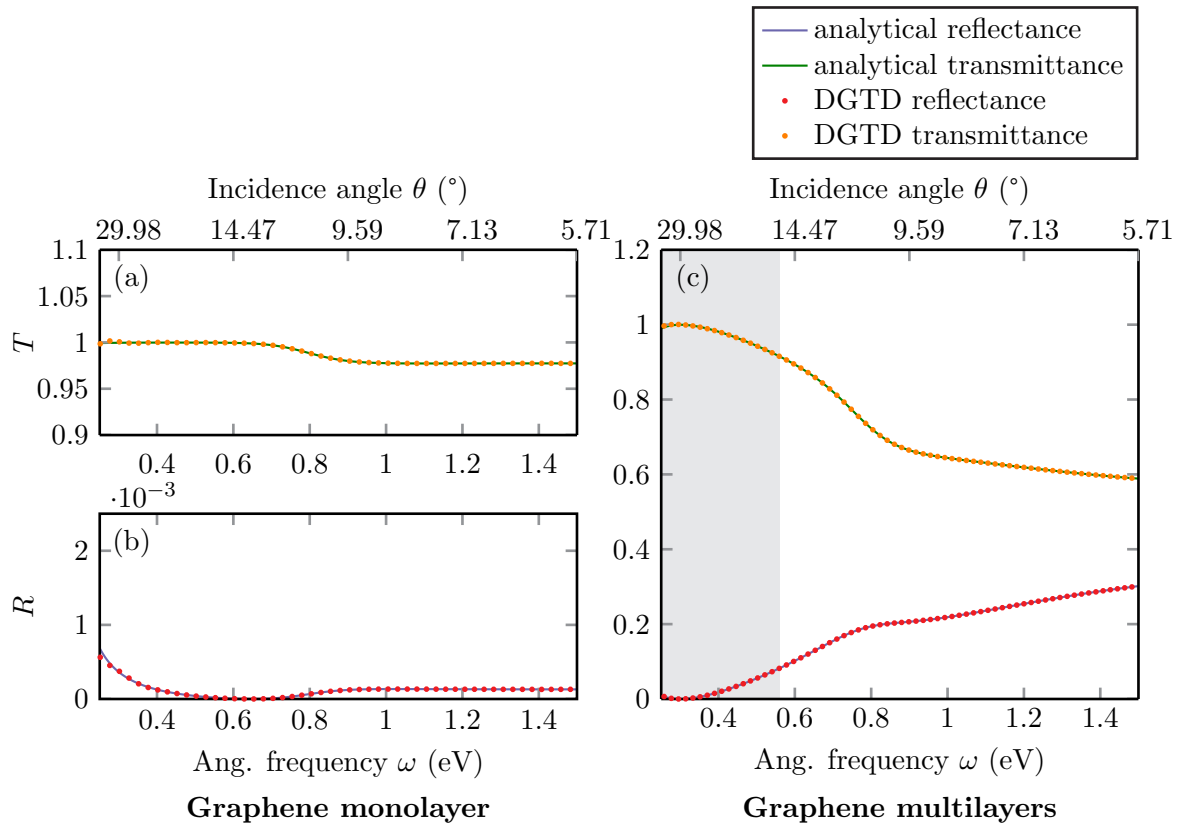
Figure 5.14: TM transmittance and reflectance for graphene mono- and multilayers under oblique incidence ($q_x = 0.15\,\text{eV}$, $\mu = 0.4\,\text{eV}$). The analytical transmittance and reflectance are compared to the transmittance and reflectance obtained from computations using the DGTD. Over wide incidence angles and reaching into the HMM region of the multilayer system (cf. Fig. 5.4(c)), very high agreement between analytical and numerical results is visible (see text).

capabilities within the algorithm of DGTD in order to describe, e.g., typical surface structuring and thin film experiments.

5.8 Conclusions

In this chapter, we discussed the basic algorithm of the DGTD applied in the field of electromagnetics to model electromagnetic field propagation in involved nanostructured systems. Within the scope of this work, we introduced the description of graphene at finite chemical doping and temperatures as a sheet conductivity into the DGTD which was published in Ref. [W7]. At the example of these graphene conductivity sheets and graphene multilayer systems that are known to be HMMs, we furthermore discuss the importance of being able to model oblique incidence even within time domain algorithms and transfer a method of oblique incidence from the FDTD to DGTD. Here, the multilayer

structures exhibit the additional challenge of resulting at certain frequencies in a HMM that can be tuned via the external manipulation of the chemical potential within graphene (cf. Ref. [88]).

The work presented in this chapter, will in the future lay the basis for a variety of applications. The introduction of a sheet conductivity with the appropriate ADEs will allow for further description of other two-dimensional materials as well as for the application to other problems in nanooptics such as modeling the surface roughness of nanostructures utilizing an effective current sheet (see Refs. [203, 204]). Additional, the general setup (combined with the self-consistent dipole model discussed in chapter 6) will allow for including graphene or other materials in need of a quantum-mechanical modeling into an electromagnetic time-domain solver and will in consequence lead to a Maxwell-Schrödinger description. The oblique incidence will in this context allow not only for the testing but also the investigation of many of the above described applications.

CHAPTER 6

Radiation dynamics of emitters close to metallic nanostructures

"Either this is madness or it is Hell."   "It is nei-ther," calmly replied the voice of the Sphere, "it is Knowledge; it is Three Dimensions: open your eye once again and try to look steadily." [32]

Edwin A. Abbott

In this chapter, we study emitter dynamics in the proximity of metallic nanostructures. In section 6.1, we present the changes in the lifetime of an NV center in a nanodiamond in the proximity of a glass substrate and different silver nanowires assuming an emitter under Weisskopf-Wigner approximation (see Eq. (3.31)). We compare the computations to experimental measurements introducing the method of three-dimensional scanning-probe fluorescence lifetime imaging microscopy by use of a single quantum emitter. The section is in large parts published within Ref. [W2]. In the second section of this chapter, we move beyond the Weisskopf-Wigner approximation and introduce a numerical framework for the time dependent description of self-consistent emitters within the Discontinuous Galerkin Time-Domain method. To illustrate the advantages of such a method, we discuss the involved radiation dynamics of several interacting classical dipoles in the direct proximity of a gold pentamer. The results of this section are prepared for submission in Ref. [W6].

6.1 Three-dimensional fluorescence lifetime imaging microscopy performed by a single quantum emitter

In this first section, we present in detail the first results on measurements of a quantitative 3D scanning-probe fluorescence lifetime imaging microscopy (FLIM) by the use of a single quantum emitter (QE) as published in Ref. [W2]. This technique we abbreviate with QE-FLIM.

In the experiments, one makes use of a single QE since it is optimally suited to probe the electromagnetic environment not only due to its intrinsic quantum properties but

---

[32]Flatland: A Romance of Many Dimensions (1884)

also due to the typically small extension of the emitter. Additionally, true QE allow for a reliable excitation as well as an efficient and easy readout.

First scanning quantum probes using optical emitters have been introduced as early as in the year 2000 (cf. Ref. [205]) where the authors placed a p-terphenyl crystal doped with terrylene molecules (of nominal concentration 10^{-7}) at the end of a fiber tip. As described in chapter 3, the detection of lifetime modifications allows directly to conclude on the photonic projected local density of states. Since this is the driver of the light-matter coupling between the photonic environment and an arbitrary emitter, mapping the photonic projected local density of states with a stable and well characterized probe allows for general conclusions on the nanostructure's photonic properties. This knowledge is a necessary ingredient to enhance the functionality of hybrid light-matter quantum technology as pointed out in the introduction of this thesis.

While besides from the already mentioned scanning quantum probes, there exist a wide range of typically employed methods for detecting the photonic density of states of a system, such as coating of the nanostructures with fluorescent dyes (see Ref. [206]), scanning near-field microscopes (see Refs. [207–209]), nano positioning of emitters (see Refs. [210, 211]) and many others. Most of these methods, however, make use of an ensemble of emitters. When averaging over an ensemble of emitters, one in turn also averages over different positions and orientations and cannot obtain the photonic projected local density of states unambiguously. One possible solution for this issue are atoms (see chapter 4), e.g., in atom traps, which however do either not emit radiation at the optical energies of interest (atom trap) or require special experimental conditions such as an ultrahigh vacuum or very low temperatures. On the other hand, nanodiamonds containing NV centers, whose properties we discuss in detail in the following, are ideal QEs for use as a scanning probe since they are extremely photo stable at room temperature and they can be positioned with high accuracy. Nanodiamonds containing only a single vacancy center exist, can be experimentally found and these nanodiamonds are commercially available (compare also section 3.2).

6.1.1 The nitrogen-vacancy center in a nanodiamond

Due to all the characteristics named above, the NV center in nanodiamonds has risen high attraction in the last decade (see Refs. [98, 100, 213]). Besides from its use as an optical quantum probe, it is popular in all kinds of experimental setups, including magnetic resonance experiments (see Ref. [215]) and quantum computation experiments (see Refs. [216, 217]).

However, in this section, we focus on the use as an optical quantum probe and thus the optically allowed electric dipole transitions of the NV center. As discussed in section 3.2, an NV center consists of a vacancy due to the substitution of a carbon atom by a nitrogen atom in the diamond structure and thus creating an effective electron vacancy. In Fig. 6.1(a), we present the resulting crystallographic structure with the carbon atoms presented by gray spheres, the nitrogen atom depicted by the orange atom and the vacancy denoted by V. In the proximity of the vacancy, the electronic orbitals are sketched in blue. The crystallite growth direction is here assumed along the z-axis. The NV center occurs in nature with two different charges, the negatively NV^- and the neutrally charged NV^0 color center (for a review see, e.g., Ref. [100]). Since in nature, the

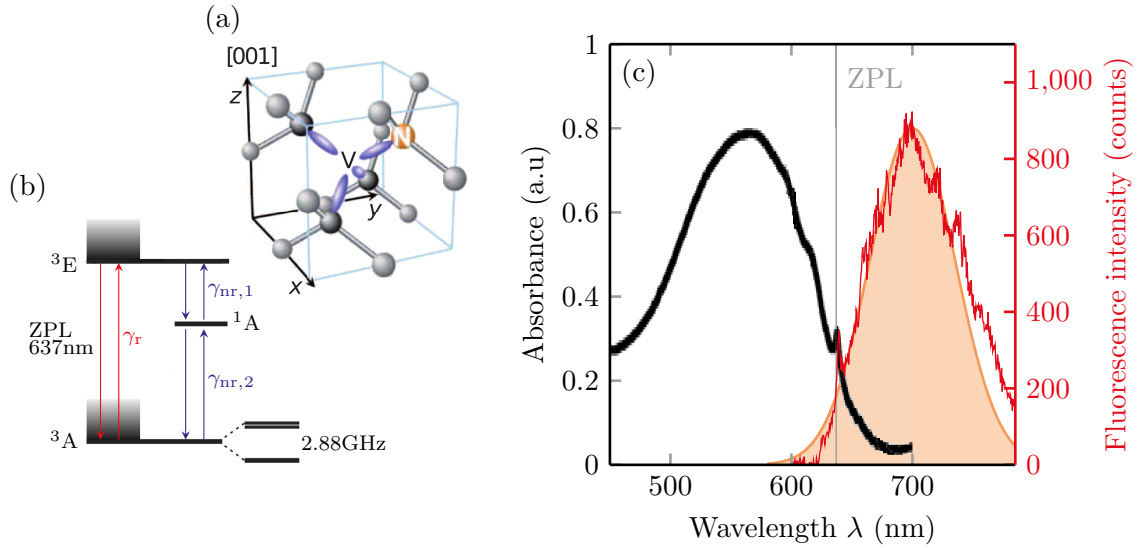## 6.1 Three-dimensional fluorescence lifetime imaging microscopy performed by a single quantum emitter

Figure 6.1: Panel (a) displays the crystallographic structure of an NV center with one electron missing due to the insertion of a nitrogen atom. Panel (b) shows a simplified electronic level structure where an excited NV center can decay either radiatively transition ^{3}A to ^{3}E or non-radiatively via the metastable state ^{1}A. The electronic levels are denoted according to the NV center's C_{3v} symmetry nomenclature. Panel (c) displays the absorbance of an NV center in a bulk crystal (black) and fluorescence of an NV center in a nanodiamond (red) spectrum at room temperature. Here, the zero phonon line (ZPL) and the broadening due to large strain variations and the corresponding Stokes shift (phonon-sideband) are well visible. By the light red area, we denote the simplified fluorescence intensity used as an approximation in this thesis (the emitter spectrum is Gaussian with $\lambda_0 = 700\,\text{nm}$ and $\sigma = 50\,\text{nm}$). Panel (a) is taken from Ref. [212] and reprinted by permission from Macmillan Publishers Ltd: Nature [212],© 2011. Panel (b) is adapted from Refs. [98, 213] and in panel (c), the fluorescence plot is adapted from Ref. [97] with the original data provided as a courtesy by the author and the absorbance plot is adapted from Ref. [214].

first kind occurs far more often, we exclusively focus on the NV$^-$ color center and in the following referring to it for brevity as NV (color) center.

Since the NV center belongs to the C_{3v} group (cf. Ref. [98, 100]), the ground state exhibits a ^{3}A symmetry and the excited state a ^{3}E symmetry (see Fig. 6.1(b)) . Within this group, the excited state contains two degenerate sub states with orthogonal polarization of the optical transition dipole moment. Additionally, both electric dipole transition moments are orthogonal on the crystal axis (cf. Ref. [98] for more details). Thus, the NV center has to be described by two orthogonal electric dipole moments where in vacuum the radiative decay rate γ_r for both degenerate transitions can be considered equal. Additionally, a metastable state ^{1}A exists that couples non-radiatively width decay rates $\gamma_{nr,2}$ and $\gamma_{nr,1}$ to both ground state and excited state, respectively.

The direct transition from the ^{3}A state to the ^{3}E state without any phonon coupling
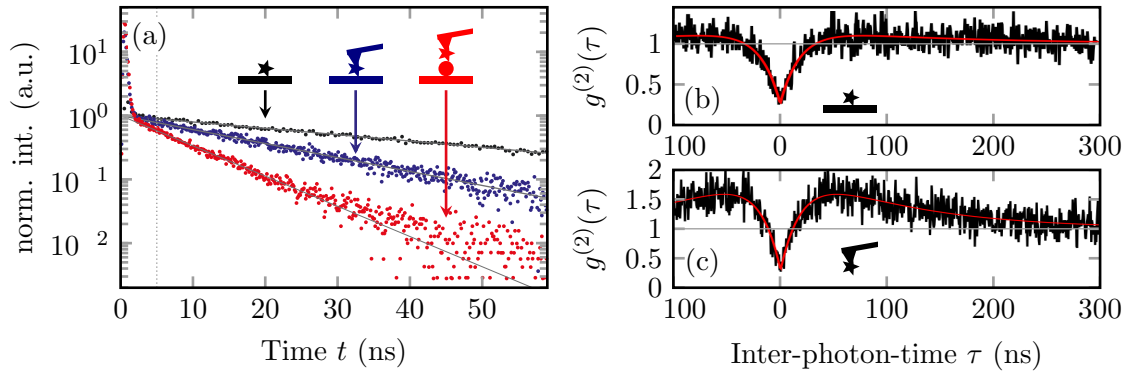
Figure 6.2: Properties of the nitrogen-vacancy (NV) center. Panel (a) displays the number of counts at a time t after the excitation of the NV center in a nanodiamond for three different situations (nanodiamond on a glass substrate, nanodiamond glued to a cantilever tip close to a glass substrate and nanodiamond glued to a cantilever tip close to a silver nanowire laying on a glass substrate. A mono-exponential decay is fitted to the experimentally obtained data (gray line) allowing to determine the lifetime of the quantum emitter. Here, only data $t > 5$ ns is taken into account to neglect excitation effects. Panels (b,c) display the $g^{(2)}$-correlation function for a nanodiamond on a glass substrate and glued to a cantilever tip far away from the substrate. In both cases, with $g^{(2)}(0) < 1/2$ the main photon contribution is indeed caused by a single NV center in the nanodiamond. Thus, we can use the nanodiamond as a single photon source. Figures adapted from Ref. [W2], doi:10.1021/nl500460c.

is in absorbance and fluorescence known as the zero phonon line (ZPL) (see Fig. 6.1(c)). Caused by large strain variations (cf. Ref. [213] and gray faded region in Fig. 6.1(b)), a wide phonon sideband appears that is Stokes-shifted between absorbance and fluorescence. Thus, the broad fluorescence spectrum consists of transitions with a continuum of transition energies each of them approximately decaying at the same rate.

When studying the time-evolution of the excitation of an NV center in a nanodiamond, a corresponding mono-exponential decay can be determined (see Fig. 6.2(a)). This holds under a variety of different conditions (NV center on a substrate, glued to a tip and over a substrate while glued to a tip) exhibiting different decay rates depending on the respective photonic environment (see Fig. 6.2(a)). In consequence, the fluorescence spectrum of an NV center at room temperature can be most simplistic modeled as a Gaussian with $\lambda_0 = 700$ nm and $\sigma = 50$ nm (compare light red area in Fig. 6.1(c)). Here, for simplicity we focus on reproducing the visible part of the spectrum with sufficient accuracy while neglecting the asymmetry of the fluorescence spectrum at higher wavelengths.

Since we are considering NV centers in nanodiamonds, in general, a large number of NV centers can be contained in a single nanodiamond. However, as pointed out in the introduction, the strength of nanodiamonds is the opportunity to determine single-photon emitter, namely nanodiamonds containing a single NV center only.

These nanodiamonds can be experimentally selected by measuring the $g^{(2)}$-correlation

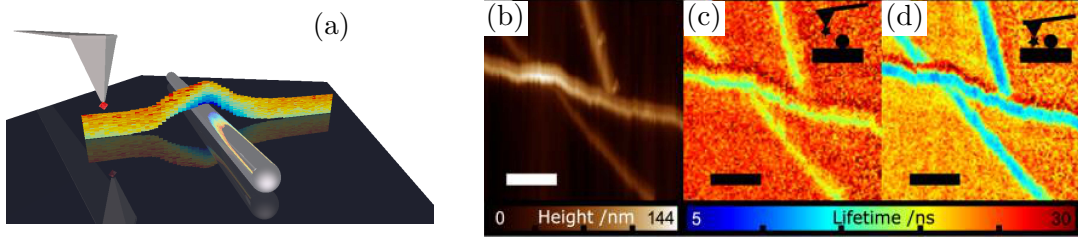## 6.1 Three-dimensional fluorescence lifetime imaging microscopy performed by a single quantum emitter

Figure 6.3: Panel (a): artist's view on the three-dimensional fluorescence lifetime imaging microscopy. The nanodiamond (red) is glued to an atomic force microscope (AFM) made out of silicon and can thus be moved with high accuracy in 3D space scanning, e.g., a silver nanowire. Panels (b-d): experimental results on the three-dimensional scanning-probe fluorescence lifetime imaging microscopy performed by a single quantum emitter (QE-FLIM) for a network of silver wires. Panel (b) shows the height information while panels (c,d) display the fluorescence lifetime measurements for two different distances from the sample. The scale bars in panels (b-d) correspond to 500 nm. Figure adapted from Ref. [W2], doi:10.1021/nl500460c.

function of the nanodiamond. The definition of the $g^{(2)}$-correlation function for a pure photonic state (cf. Ref. [218]) is given by

$$g^{(2)}(\mathbf{r}_1, t_1; \mathbf{r}_2, t_2) = \frac{\langle \hat{\mathbf{E}}^\dagger(\mathbf{r}_1, t_1) \hat{\mathbf{E}}^\dagger(\mathbf{r}_2, t_2) \hat{\mathbf{E}}(\mathbf{r}_1, t_1) \hat{\mathbf{E}}(\mathbf{r}_2, t_2) \rangle}{\langle |\hat{\mathbf{E}}(\mathbf{r}_1, t_1)|^2 \rangle \langle |\hat{\mathbf{E}}(\mathbf{r}_2, t_2)|^2 \rangle} \,. \tag{6.1}$$

Above, $\langle \cdot \rangle$ describes an ensemble average while $g^{(2)}(\tau)$ describes the probability that both a photon is detected at position $\mathbf{r}_1$ and time t_1 and at position $\mathbf{r}_2$ and t_2. In the case of vacancies, photons are emitted into a Fock state (cf. appendix A.1 and specifically Eq. (A.9)). For a Fock state containing n photons, the $g^{(2)}$-correlation function detected at the same position $\mathbf{r} = \mathbf{r}_1 = \mathbf{r}_2$ reads in the limiting cases

$$g^{(2)}(0) = 1 - \frac{1}{n} \qquad\qquad \lim_{\tau \to \infty} g^{(2)}(\tau) = 1 \,. \tag{6.2}$$

Then, when experimentally $g^{(2)}(0) < 1/2$ we can conclude that the main photon contribution is caused by a single emitter. As shown in Fig. 6.2(b), for different situations (NV centers on a plane and glued to a cantilever), indeed for the two nanodiamonds used in the experiments

$$g^{(2)}(0) < \frac{1}{2} \,, \tag{6.3}$$

concluding that these specific nanodiamonds act as single photon sources. Additionally, we find the predicted long inter-photon time behavior $g^{(2)}(\tau) \to 1$.

6.1.2 The experiment

In order perform 3D FLIM by use of a single quantum emitter (QE) as published in Ref. [W2], our experimental collaborators from the group of Oliver Benson at the
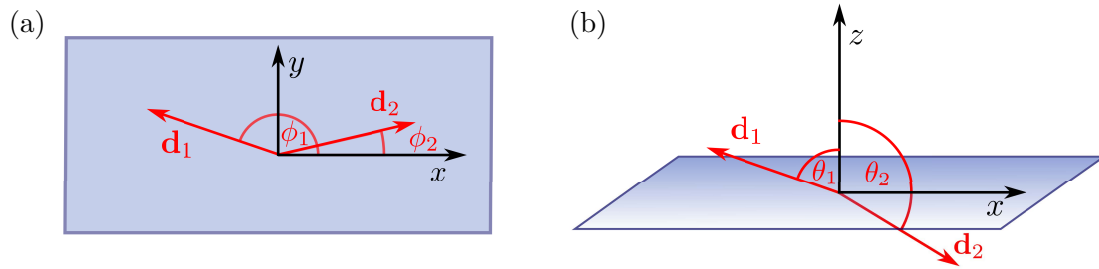
Figure 6.4: Sketch of the orientations of the dipole vectors for the two degenerate optically allowed electric dipole transitions in a nitrogen-vacancy center. These two dipole vectors are due to symmetry reasons orthogonal to each other (see text). In the two panels above, we display the on top view (a) and the side view (b) on the two emitters relative to a reference plane orthogonal to the z axis. The angles ϕ_i and θ_i determine the orientation of the dipole (cf. Eq. (6.12)).

Humboldt-Universität zu Berlin glued a nanodiamond (typically of about 30 nm size) containing a single NV center (see Fig. 6.2(b,c)) to an atomic force microscope (AFM) cantilever tip and thus manage to position the NV center with high precision in 3D space.

As they show in measurements, they preserve the single-photon emitter nature of the NV center even when it is glued to a tip (cf. Fig. 6.2(c)). Additional to the measurement of the position of the NV center, they excite the NV center at each spatial position by a confocal microscope with a picosecond laser at $\lambda_{\text{exc.}} = 531$ nm making use of the Stokes shift of the fluorescence (see Fig. 6.1(c)). Depending on the experimental setup, different repetition rates of the laser are used (10 MHz for the QE-FLIM measurements and 80 MHz for the correlation measurements shown in Fig. 6.2(b,c)). The single photons emitted from the NV center are then measured by spectrally filtering out the laser spectrum and subsequently detecting the photon event time (for exemplary data, see Fig. 6.2(a)). To finally determine NV center's lifetime, a mono-exponential decay is fitted to the data and thus assigned to every position in 3D space.

This QE-FLIM probe can then be used to detect the lifetime modifications to an emitter in an arbitrary photonic environment such as the network of silver nanowires for which we display the measurements in Fig. 6.3(b-d). In panel 6.3(b), we present the height profile of the silver wire's network as measured by the AFM. In panels 6.3(c,d), we display the NV center's lifetime in two different planes each at a constant distance from the glass substrate the silver nanowires are deposited on. Lifetime reductions due to the silver nanowires are well visible while also noticing an increase of the lifetime in panel 6.3(d) right above the horizontal nanowire. Such an increase would usually be attributed to a topography artifact. Due to the method applied, we can however exclude this possibility. Thus, the silver nanowire network does indeed lead to regions of decreased and increased emitter lifetime.

6.1.3 Modeling the nitrogen-vacancy center

In order to model the nitrogen-vacancy center, we make use of two different methods. First, we compute analytical results for emitters above a glass half space to compare to the corresponding measurements and, second, we compute the lifetime modification in more complicated plasmonic systems within the DGTD (see chapter 5) inducing the electromagnetic fields radiated from the emitter via a TfSf contour (see section 5.2 and Eqs. (3.12) and (3.13)). In both cases, we first have to determine the appropriate model of the NV center and the influence of the additional parts of the probe such as the AFM cantilever tip and the nanodiamond itself.

As discussed in chapter 3, the decay rate of an emitter within the Weisskopf-Wigner approximation is proportional to the photonic projected local density of states (cf. Eqs. (3.31) and (3.33)). In the case of a single NV center, we have to take into account that the vacancy center exhibits two degenerate, orthogonal dipole transitions. Then, the decay rate cannot simply be calculated from the field scattered back from the excitation of the electromagnetic environment by one single electric dipole (cf. Eq. (3.42)), but we have to reconsider the equations of motion for the electric dipole moments and the corresponding coupling between the two of them. Assuming a classical equation of motion (cf. Eq. (3.23)), we obtain for the two degenerate transitions

$$\partial_t^2 \mathbf{d}_1(t) + \omega_1^2 \mathbf{d}_1(t) = \frac{e^2}{m}(\mathbf{E}_1(t) + \mathbf{E}_2(t)),\tag{6.4a}$$

$$\partial_t^2 \mathbf{d}_2(t) + \omega_2^2 \mathbf{d}_2(t) = \frac{e^2}{m}(\mathbf{E}_1(t) + \mathbf{E}_2(t)).\tag{6.4b}$$

Next, we make use of the relation between the electric fields and the dyadic Green's function (see Eq. (3.41)), introduce the abbreviation $\mathbf{e}_{\mathbf{d}_i} \cdot \underline{\mathcal{G}}(\mathbf{r}_0, \mathbf{r}_0; \omega) \cdot \mathbf{e}_{\mathbf{d}_j} \equiv \mathcal{G}_{ij}(\omega)$, and choose without loss of generality the Cartesian coordinate system in such a way that $\mathbf{e}_{\mathbf{d}_1} = \mathbf{e}_x$ and $\mathbf{e}_{\mathbf{d}_2} = \mathbf{e}_y$ where $\mathbf{d}_i = d_i \mathbf{e}_{\mathbf{d}_i}$. In order to obtain the eigenfrequencies of the two coupled Equations (6.4), we have to solve the eigenvalue problem stemming from Eqs. (6.4) in frequency domain (cf. Eq. (1.9))

$$\begin{pmatrix} -\omega^2 + \omega_1^2 - \omega^2\frac{e^2\mu_0\mu_r}{m}\mathcal{G}_{xx}(\omega) & \omega^2\frac{e^2\mu_0\mu_r}{m}\mathcal{G}_{xy}(\omega) \\ \omega^2\frac{e^2\mu_0\mu_r}{m}\mathcal{G}_{yx}(\omega) & -\omega^2 + \omega_2^2 - \omega^2\frac{e^2\mu_0\mu_r}{m}\mathcal{G}_{yy}(\omega) \end{pmatrix} \cdot \begin{pmatrix} d_1(\omega) \\ d_2(\omega) \end{pmatrix} = \epsilon_\pm \begin{pmatrix} d_1(\omega) \\ d_2(\omega) \end{pmatrix}.\tag{6.5}$$

In the case of a degenerate transition $\omega_1 = \omega_2 = \omega_0$, the above equation leads to dressed states as eigenstates

$$d_+ = \cos\left(\frac{\theta}{2}\right)d_1 + \sin\left(\frac{\theta}{2}\right)e^{-i\varphi}d_2,$$

$$d_- = -\sin\left(\frac{\theta}{2}\right)e^{i\varphi}d_1 + \cos\left(\frac{\theta}{2}\right)d_2,\tag{6.6}$$

where $e^{i\varphi} = \mathcal{G}_{xy}/|\mathcal{G}_{xy}|$ and

$$\tan(\theta) = \frac{2|\mathcal{G}_{xy}|}{\mathcal{G}_{yy} - \mathcal{G}_{xx}}.\tag{6.7}$$

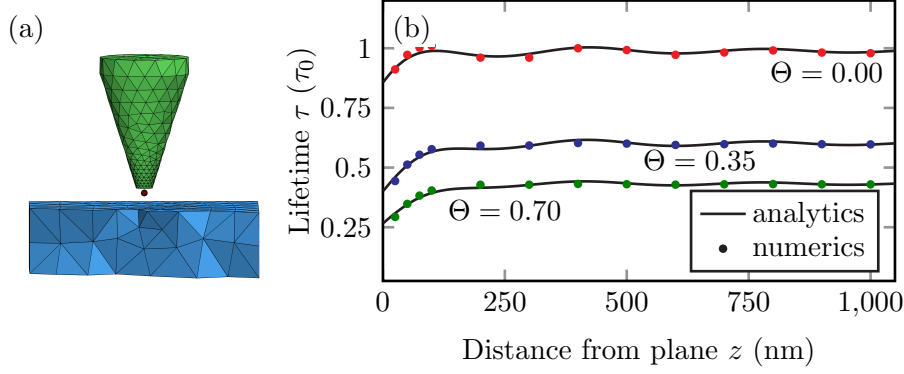# 6 Radiation dynamics of emitters close to metallic nanostructures

Figure 6.5: Panel (a): geometry used in the three-dimensional numerical simulations. The probe consists of two dipoles which are placed in the center of a truncated conical tip made of silicon. The distance of this probe to a dielectric interface is varied. Panel (b): results of the numerical simulations and the analytical solution for two dipoles in front of an interface, corrected for an effective quantum efficiency (see text). Adapted from Ref. [W2], doi:10.1021/nl500460c.

For these states, the corresponding eigenvalues read

$$\epsilon_\pm = \omega_0^2 - \omega^2 - \frac{e^2 \mu_0 \mu_r}{2m} \omega^2 \left[(\mathcal{G}_{xx} + \mathcal{G}_{yy}) \pm \sqrt{(\mathcal{G}_{xx} - \mathcal{G}_{yy})^2 + 4|\mathcal{G}_{xy}|^2} \right] , \qquad (6.8)$$

where for a non isotropic environment, $\mathcal{G}_{xx}$ is not necessarily equal to $\mathcal{G}_{yy}$ and the off–diagonal elements can be non zero as well. For a single dipole with dipole moment $\mathbf{d}$, we would map

$$(\mathcal{G}_{xx} + \mathcal{G}_{yy}) \pm \sqrt{(\mathcal{G}_{xx} - \mathcal{G}_{yy})^2 + 4|\mathcal{G}_{xy}|^2} \equiv 2 \left[\mathbf{e_d} \cdot \underline{\mathcal{G}}(\mathbf{r}_0, \mathbf{r}_0; \omega_0) \cdot \mathbf{e_d} \right] .$$

When we now, however, take into account that at room temperature the two degenerate dipole-allowed transitions are incoherently coupled, we can approximate $\mathcal{G}_{xy} \approx 0$. Additionally including the orthogonality of the two dipole moments we find that the two transitions decouple and the total radiative decay rate reads

$$\gamma_\mathrm{r} = \gamma_1 + \gamma_2 . \qquad (6.9)$$

In order to determine the complete decay rate of the NV center, we also have to consider the non-radiative processes (cf. Fig. 6.1(b)). When we assume that these processes are approximatively independent of the electromagnetic environment ($\gamma_\mathrm{nr} \approx \gamma_{\mathrm{nr},0}$), we can write (cf. Eqs. (3.42) and (3.45))

$$\frac{\gamma_i}{\gamma_0} = 1 + QY \cdot \frac{\mathcal{F}}{\omega^3} \sum_{i=1}^{2} \mathrm{Im}[\mathbf{d}_i^* \cdot \mathbf{E}_{\mathrm{s},i}(\mathbf{r}_0)] \equiv \sum_{i=1}^{2} \frac{P_i}{P_{i,0}} , \qquad (6.10)$$

with the quantum yield that describes the percentage of the decay rate that is radiative

$$QY = \frac{\gamma_{\mathrm{r},0}}{\gamma_{\mathrm{r},0} + \gamma_{\mathrm{nr},0}} , \qquad (6.11)$$

140

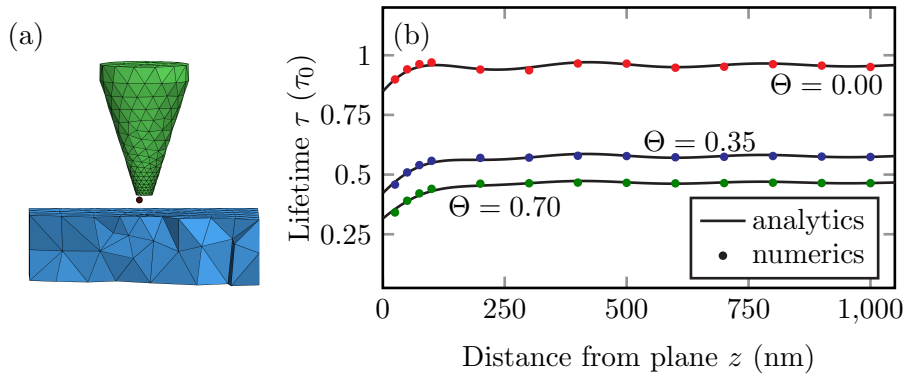## 6.1 Three-dimensional fluorescence lifetime imaging microscopy performed by a single quantum emitter

Figure 6.6: Panel (a): sketch of the geometry used in the three-dimensional numerical simulations. The probe consists of a classical dipole (red) at the tip of a truncated silicon cone. The position of the dipole is displaced from the center of the cantilever by $\Delta y = 30$ nm compared to the centered case displayed in Fig. 6.5. Three orthogonal polarizations of the dipole are probed such that the complete photonic projected local density of states of the two orthogonal dipoles can be back engineered. The distance of this probe to a dielectric interface is varied. Panel (b): shows the results of the numerical simulations for different orientations of the dipole. It can be seen that even for the asymmetrical case, deviations from the adjusted analytical theory are small. Adapted from Ref. [W2], doi:10.1021/nl500460c.

and the frequency independent prefactor $\mathcal{F} = {6\pi\varepsilon_0 c^3}/{|\mathbf{d}|^2}$ assuming $|\mathbf{d}| = |\mathbf{d}_1| = |\mathbf{d}_2|$.

With Eq. (6.10), we obtain an expression for the modeling of the NV center's decay rate. Next, we examine the influence of the additional parts of the probe, such as the cantilever tip and the nanodiamond. This, we accomplish by modeling the complete probe within the DGTD for an NV center with known orientation and comparing the lifetime modifications with the lifetime modifications of an effective NV center that is not contained in a nanodiamond and not mounted to an AFM tip (silicon, $\varepsilon = 14.317$).

We expect the larger influence from the AFM tip and hence start by neglecting the nanodiamond and only modeling the emitter with an AFM tip placed close by. For a better understanding of its influence, we also compare the cases of an NV center glued to the center of a cantilever tip (see Fig. 6.5(a) for a part of the mesh) and an NV center displaced from the center of a cantilever tip by $\Delta y = 30$ nm (see Fig. 6.6(a) for a part of the mesh). We then compute the lifetime modifications when approaching a non-dispersive, lossless, dielectric half space (here: $\varepsilon_{\text{BK7}} = 2.301$) with the emitter. We model the tip of the cantilever as a truncated conical tip with an aperture angle of 17.65°, a radius of the truncated cap of 50 nm and a height of 800 nm.

Using spherical coordinates to describe the dipole vectors' orientation (see Fig. 6.4 for

6 Radiation dynamics of emitters close to metallic nanostructures

	Θ	Θ_{eff}	QY_{eff}	$\mathcal{T}_{\mathbf{d}_1,\mathbf{d}_2}$
	0.00	0.00	0.39	2.54
symmetric	0.35	0.44	0.83	0.73
	0.70	0.66	0.88	0.49
	0.00	0.00	0.33	2.93
asymmetric	0.35	0.53	0.57	1.01
	0.70	0.80	0.62	0.76

Table 6.1: Nonlinear least square root fits (conducted with MATLAB, see Ref. [219]) for symmetrical (see Figure 6.5) and asymmetrical (see Figure 6.6) probes compared to the analytical solution for two dipoles only. Θ describes the chosen orientation of the two perpendicular dipoles attached to the tip, Θ_{eff} the effective orientation of the two dipoles when using only the emitters to model the complete probe. QY_{eff}, the effective quantum yield, absorbs the influences of the tip in the analytic solution. $\mathcal{T}_{\mathbf{d}_1,\mathbf{d}_2}$ is the orientation-dependent conversion factor for the free-space decay rate. Table adapted from Ref. [W2].

a definition)

$$
\mathbf{d}_1 = \begin{pmatrix} \sin(\theta_1)\cos(\phi_1) \\ \sin(\theta_1)\sin(\phi_1) \\ \cos(\theta_1) \end{pmatrix} ,
$$

$$
\mathbf{d}_2 = \begin{pmatrix} \sin(\theta_2)\cos(\phi_2) \\ \sin(\theta_2)\sin(\phi_2) \\ \cos(\theta_2) \end{pmatrix} \equiv \begin{pmatrix} \cos(\alpha)\cos(\theta_1)\cos(\phi_1) - \sin(\alpha)\sin(\phi_1) \\ \cos(\alpha)\cos(\theta_1)\cos(\phi_1) - \sin(\alpha)\cos(\phi_1) \\ -\cos(\alpha)\sin(\theta_1) \end{pmatrix} ,
\tag{6.12}
$$

we find that in the case of two orthogonal emitters (introduction of the relative angle α in the reformulation of $\mathbf{d}_2$, above) in front of an infinitely extended plane the only degree of freedom is given by

$$
\Theta = \cos(\theta_1)^2 + \cos(\theta_2)^2 = \cos(\theta_1)^2 + \cos(\alpha)^2\sin(\theta_1)^2 .
\tag{6.13}
$$

The modification of the decay rate of an NV center glued to a tip above a dielectric half space can be split in the following parts

$$
\gamma_i = \gamma_{\text{nr}} + \gamma_{\text{r,0}} + \gamma_{\text{Tip,System}} ,
\tag{6.14}
$$

where we then assume that the influences of tip and system decouple to

$$
\gamma_{\text{Tip,System}} = \gamma_{\text{Tip}} + \gamma_{\text{System}} .
$$

Then, motivated by the results displayed in Figs. 6.5 and 6.6, we include the effects of the decay rate modification due to the AFM cantilever tip into the non-radiative decay rate $\gamma_{\text{nr,eff}} = \gamma_{\text{nr}} + \gamma_{\text{Tip}}$ and additionally also introduce an effective quantum yield $QY_{\text{eff}} = \frac{\gamma_{\text{r,0}}}{\gamma_{\text{r,0}}+\gamma_{\text{nr,eff}}}$. With these definitions and $\gamma_0 = \gamma_{\text{r,0}} + \gamma_{\text{nr,0}}$, we can recast Eq. (6.10)

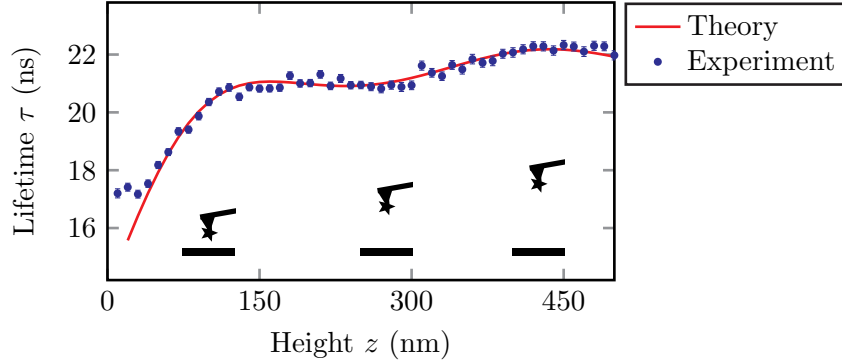## 6.1 Three-dimensional fluorescence lifetime imaging microscopy performed by a single quantum emitter

Figure 6.7: Lifetime modifications of an NV center contained in a nanodiamond which is glued to an AFM cantilever tip when approaching a glass substrate ($\varepsilon_{\mathrm{BK7}} = 2.301$). The red curve is a fit of the analytical solution of the lifetime modification of two dipoles over a non-dispersive and lossless glass half space (cf. Ref. [28]) to the data. For more information, see the corresponding text. Adapted from Ref. [W2], doi:10.1021/nl500460c.

for a single emitter into

$$\frac{\gamma_i}{\gamma_{\mathrm{r},0}} = \frac{1}{QY_{\mathrm{eff},i}} + \mathcal{F}\frac{1}{\omega^3}\mathrm{Im}[\mathbf{d}_i^* \cdot \mathbf{E}_{\mathrm{s},i}(\mathbf{r}_0)] \,. \tag{6.15}$$

For two dipoles, we can then define an effective quantum yield for both dipoles

$$\frac{1}{QY_{\mathrm{eff}}} = \frac{1}{QY_{\mathrm{eff},1}} + \frac{1}{QY_{\mathrm{eff},2}} \,, \tag{6.16}$$

and a joint free-space decay rate

$$\gamma_{0,\mathrm{eff}} = 2 \cdot (\gamma_{\mathrm{r},0} + \gamma_{\mathrm{nr},0}) + \gamma_{\mathrm{Tip},\mathbf{d}_1} + \gamma_{\mathrm{Tip},\mathbf{d}_2} \equiv \mathcal{T}_{\mathbf{d}_1,\mathbf{d}_2}\gamma_{r,0} \,. \tag{6.17}$$

With these definitions and Eq. (6.9), we rewrite the joint decay rate as

$$\frac{\gamma}{\gamma_{0,\mathrm{eff}}} = \frac{1}{\mathcal{T}_{\mathbf{d}_1,\mathbf{d}_2}}\left\{ \frac{1}{QY_{\mathrm{eff}}} + \mathcal{F}\frac{1}{\omega^3}\sum_{i=1}^{2}\mathrm{Im}\left[\mathbf{d}_i^* \cdot \mathbf{E}_{\mathrm{s},i}(\mathbf{r}_0)\right] \right\} \,. \tag{6.18}$$

By use of this definition, we compute for different orientations of the dipole vector the lifetimes and then try to fit analytic results to the numerically obtained values neglecting the cantilever tip. Additionally, we assume as discussed above that the two emitters are incoherently coupled and placed freely hanging in front of a dielectric half space. We obtain the results presented in Fig. 6.5 and 6.6 with the values of the fits given in Tab. 6.1. Analogously to the AFM cantilever tip, we can also include the nanodiamond itself into the effective description of the two emitters.

Thus, for modeling the experimental results, we can minimize the computational overhead by computing the complete Green's tensor for each of the two orthogonal emitters separately. We obtain an effective characterization of the probe then by adding the decay
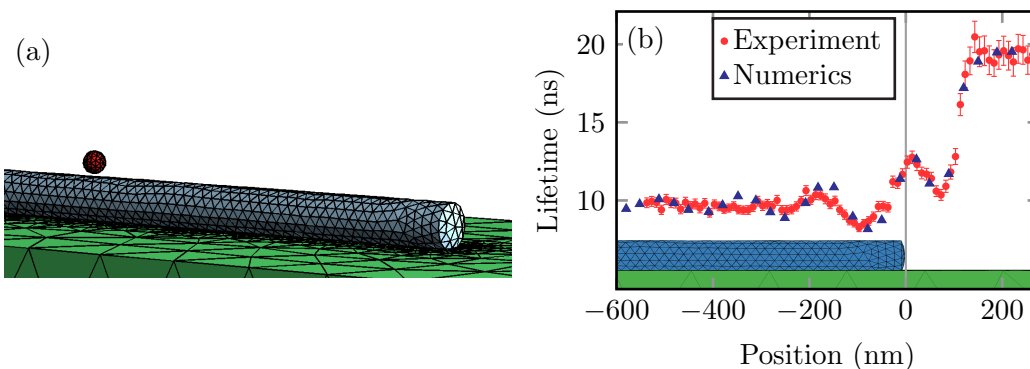
Figure 6.8: Lifetime modifications of an NV center when moving it at a constant distance along a silver nanowire of diameter $d = 50\,\text{nm}$. A section of the mesh used for the computations is shown in panel (a) while same mesh jointly with the experimental and numerical data points is presented in panel (b). For the characterization of the QE-FLIM probe, the theoretically computed dyadic Greens function is fitted to the experimentally measured data set. Here, we determine by use of the complete set of theoretical computation points the two dipole vector's orientation and the position of the NV center in the nanodiamond. Within the degrees of freedom of the fit, we are able to obtain a very high qualitative and quantitative agreement. The lifetime is drastically reduced due to the silver nanowire. On top of that, oscillations of the lifetime due to the excitation of surface plasmon polaritons on the silver nanowire and their back reflection from the end of the wire are well visible. Adapted from Ref. [W2], doi:10.1021/nl500460c.

rate of the two orthogonal emitters and by fitting the orientation of the theoretical values to appropriate experimental data. With an appropriate redefinition of the vacuum's decay rate $\tilde{\gamma}_0$, we find as the typical decay rate expression

$$\frac{\gamma}{\tilde{\gamma}_0} = 1 + QY_{\text{eff}} \frac{\mathcal{F}}{\omega^3} \sum_{i=1}^{2} \text{Im}\left[\mathbf{d}_i^* \cdot \mathbf{E}_{\text{s},i}(\mathbf{r}_0)\right] . \tag{6.19}$$

6.1.4 Results

After having introduced the effective description of the QE-FLIM probe as two effective, orthogonal dipoles described by Eq. (6.19), we validate this approach by analyzing the experimentally measured lifetime modifications when approaching a glass substrate ($\varepsilon_{\text{BK7}} = 2.301$). In Fig. 6.7, we present the results where we consider a Gaussian fluorescence spectrum ($\lambda_0 = 700\,\text{nm}$ and $\sigma = 50\,\text{nm}$) as depicted by the light red area in Fig. 6.1(c). This and the following fits, we perform via a least-squares-root fit by applying the Levenberg-Marquardt method as implemented in MATLAB (see Ref. [219]). In Fig. 6.7, we find as an effective quantum efficiency $QY_{\text{eff}} = 0.703$ and for the dipoles' relative orientation $\Theta_{\text{eff}} = 0.4$. These theoretical values characterize the QE-FLIM probe by determining the NV center's orientation and the effective quantum efficiency of the

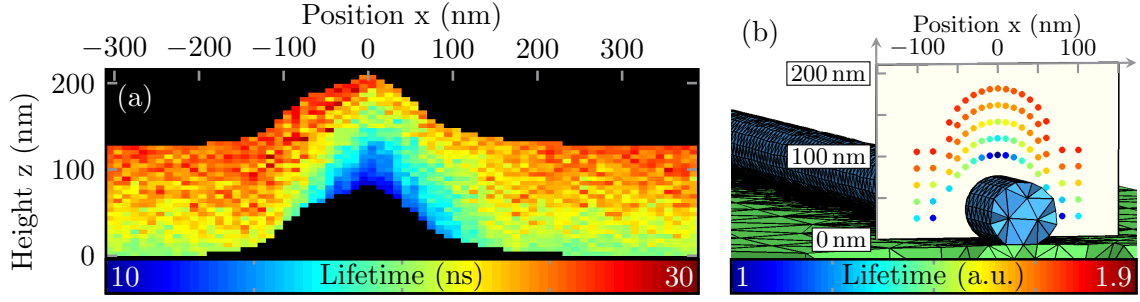## 6.1 Three-dimensional fluorescence lifetime imaging microscopy performed by a single quantum emitter

Figure 6.9: Experimental (a) and theoretical (b) results for the lifetimes of an NV center measured in a plane orthogonal to a silver nanowire (diameter $d = 80\,\text{nm}$, length $l_{\text{wire}} = 4\,\mu\text{m}$ and position $y_{\text{meas.}} \approx 0.618\,l_{\text{wire}}$). Panel (b) contains a section of the mesh applied in the computations. The parameters obtained from Fig. 6.8 are used and lead to a high qualitative agreement. In the experiment, the data is convoluted due to a displacement of the nanodiamond with respect to the center of the AFM cantilever tip. Adapted from Ref. [W2], doi:10.1021/nl500460c.

optical transitions as we discuss above. Furthermore, we can calibrate its position in the nanodiamond and with respect to the center of the AFM cantilever tip.

Additional to moving the nanodiamond closer to the dielectric substrate and detecting the changes in lifetime of the NV center, we also detect the lifetime modifications when studying more involved photonic environments. As an example, we present in Ref. [W2] the lifetime modifications due to a network of silver nanowires. Some of the experimentally obtained results we present in Fig. 6.3(b-d).

For the validation of the experimental results, we compare theory and experiment in the case of different single silver nanowires. Here, we first characterize the probe by fitting the theoretically obtained values to one experimental data set and then compare the theoretical predicted values for another circumstance to the experimentally measured values.

In order to model this photonic environment, we model the material silver by fitting a Drude-Lorentz model to experimental data (see Ref. [220] and Eq. (5.30))

$$\varepsilon = \varepsilon_{\infty} - \frac{\omega_{\text{Drude}}^2}{\omega^2 + i\gamma_{\text{Drude}}\omega} + \frac{\Delta\varepsilon_{\text{Lorentz}}\omega_{\text{Lorentz}}^2}{\omega_{\text{Lorentz}}^2 - i\gamma_{\text{Lorentz}}\omega - \omega^2} , \tag{6.20}$$

and obtaining

	ε_{∞}	ω_{Drude} ($^1/\text{ns}$)	γ_{Drude} ($^1/\text{ns}$)	$\Delta\varepsilon_{\text{Lorentz}}$	ω_{Lorentz} ($^1/\text{ns}$)	γ_{Lorentz} ($^1/\text{ns}$)
Silver	4.6	$1.37 \cdot 10^7$	$1.06 \cdot 10^5$	1.1	$7.44 \cdot 10^6$	$1.83 \cdot 10^7$

With this, we can then characterize the QE-FLIM probe by fitting the results from our numeric computations with respect to its degrees of freedom to the experimental data obtained scanning the fluorescence lifetime parallel to a silver wire . The emitter is positioned at a distance of $27\,\text{nm}$ above the nanowire whose diameter we approximate as $d = 50\,\text{nm}$, whose length is $l_{\text{wire}} = 4\,\mu\text{m}$, which exhibits rounded ends and is flattened

at the bottom by $2\,\mathrm{nm}$ (see Fig. 6.8(a)). This yields $QY_{\mathrm{eff}} = 0.5869$, $\theta_{\mathrm{eff}} = 0.5174\pi$, $\phi_{\mathrm{eff}} = 1.2509\pi$ and $\alpha_{\mathrm{eff}} = 1.19\pi$ for the QE-FLIM probe (compare Eq. (6.12) and Fig. 6.4 for the definition of the parameters).

In Fig. 6.8(b), in both the experimental and the theoretical results oscillations at the end of the silver wire are well visible. These are due to surface plasmon polaritons. The single-photon source couples to these surface plasmon polaritons and excites them. In turn, they propagate along the silver wire and are reflected from there. Depending on the position of the emitter, the back propagating surface plasmon polariton then interferes with the emitter either constructively or destructively and thus increases or decreases the NV center's lifetime, respectively. It is also worth noticing that the damping of these oscillations when receding from the end of the nanowire is much faster than expected due to effects caused by the dipolar plasmon damping and the dephasing due to the broad spectrum of the NV center. This can be explained by the necessity to take into account also the higher order multipole resonances of the silver nanowire to completely describe all decay effects.

With the parameters obtained from the scan of the lifetime modification along the silver nanowire, we compute the lifetime modification vertical through a similar silver wire (we approximate the diameter as $d = 80\,\mathrm{nm}$ with the other parameters of the silver nanowire unchanged) and compare them to the experimental measurements (see Fig. 6.9). In Fig. 6.9(a), we depict the experimental results while in Fig. 6.9(b) we present the theoretical predictions without any additional fitting parameters. Since we compare the theoretical computations to the experimental data obtained at a accidentally chosen point towards the center of a single wire, we position the NV center at the golden ration of the nanowire $y_{\mathrm{meas.}} \approx 0.618\,l_{\mathrm{wire}}$ to avoid high symmetry points. In Fig. 6.9(a), additionally to the height and position information, an additional offset due to the asymmetric mounting of the nanodiamond at the AFM cantilever tip is visible.

Figures 6.3 and 6.9 reveal an additional strength of the QE-FLIM. By this technique, we are able to derive topography corrected lifetime image scans. Here, we present specifically in Fig. 6.3(c,d) two lifetime images at constant distance over the glass substrate (not with respect to the silver nanowires). In Fig. 6.9 on the other hand, we display experimental data obtained in a plane orthogonal to the glass substrate. Therefore, the usage of the AFM cantilever tip and with this the determination of the spatial coordinates allows to avoid artifacts that otherwise oftentimes appear in scanning probe images.

6.1.5 Conclusions

In this section, we presented an experimental method that allows to determine the lifetime modification of a single-photon emitter induced by the photonic environment and with this the photonic projected local density of states. This information is obtained at the same time as the spatial location of the probe. Furthermore, we show how the method highly profits from a characterization of the QE-FLIM probe's properties by numerical methods allowing for an even more advanced and additionally quantitative characterization of a photonic environment. With the help of an in depth analysis of the NV center's optical dipole transitions, we are actually able to describe this QE at room temperature in a purely classical picture and still achieve a high quantitative agreement. Here, especially due to the unstructured tessellation of the computational domain, the DGTD
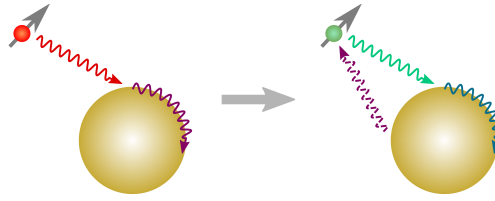
Figure 6.10: Sketch of the interaction of an emitter with the electromagnetic field scattered from a plasmonic nanosphere. The emitter does not only radiate electromagnetic field and thus excites, e.g. plasmons on a gold nano sphere, but it is in return also influenced by the back scattered light and therefore changes its emission pattern. The additional intuition gained from modeling the back action on a (classical) dipole caused by the electromagnetic field scattered from a plasmonic nanostructure nearby is the focus of the work presented in section 6.2.

allows for the necessary accurate description of the plasmonic environment that enables this modeling in the first place.

6.2 Self-consistent dipoles in the proximity of a gold pentamer

As we have shown in section 6.1, plasmonic nanostructures such as a silver nanowire have a strong effect on the lifetime of a (quantum) emitter. Furthermore, when the photonic density of states causes a strong modification of the emitter's lifetime, a significant shift of the emitter's resonance frequency (Lamb shift) is induced (see Eq. (3.35)).

Up to this point and in Eqs. (3.33) and (3.35), we have made use of the Weisskopf-Wigner approximation. However, when we discuss emitters in the proximity of plasmonic nanostructures and these emitters couple strongly to the plasmonic nanostructure (see Refs. [221, 222]) the Weisskopf-Winger approximation is not valid any longer. This fact is also very well known in photonic crystals where due to the photonic band gap the coupling of the emitter to the modes of the electromagnetic field can be significantly increased (see Refs. [223, 224]).

Close to a metallic nanostructure, this Weisskopf-Wigner approximation is especially weak and ultimately breaks down when the lifetime of the emitter is suppressed sufficiently such that it becomes of the order of the surface plasmon polaritons of the structure. Additionally, for high excitation and at strong coupling, the classical emitter description is not any longer appropriate but needs to be replaced by a (nonlinear) quantum-mechanical equation of motion (cf., e.g., Ref. [225] for an implementation of a self-consistent solution of a quantum emitter within the FDTD).

In this section, we present an algorithm of a self-consistent dipole within the numerical framework of the DGTD. As a proof of principle and to display the mere effect of the breakdown of the Weisskopf-Wigner approximation, we concentrate on a classical emitter. In the future, extensive studies on the effects of real quantum emitter will be conducted (see also the work in the Seideman group (see Ref. [225]) for a similar approach within
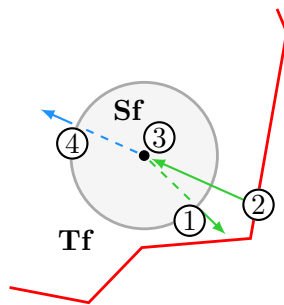
Figure 6.11: Schematics of the implementation of a self-consistent emitter in the DGTD where the position of the emitter is denoted at the black dot. An analytic solution of the electromagnetic fields radiated by the point emitter is added at the total-field/scattered-field (TfSf) contour (1). These fields are then subject to Maxwell's equations: they are evolved in time and back scattered from dielectric and metallic structures (2). At the position of the emitter, the field is recorded and stored (3) and at a corresponding later time added as a source at the TfSf contour (4). The dashed lines represent analytical propagation in time while the solid lines represent numeric propagation in time. Adapted from Ref. [W6].

the FDTD and Ref. [226] for future research planned in the group Theoretical Optics & Photonics at the Humboldt-Universität zu Berlin).

6.2.1 Algorithm of a self-consistent dipole

We begin this section by introducing the implementation of a self-consistent emitter within the DGTD. As discussed in section 5.2, we couple the electromagnetic fields into the calculation via the TfSf and Sf sources (see Ref. [179]). In the following, we exclusively describe the inducement of the electromagnetic radiation via the TfSf contour but the general scheme translates straight-forwardly to the Sf mechanism. However, for large scatterers the TfSf mechanism is much more effective regarding computational run times. This roots in the analytic propagation of the electromagnetic fields to the TfSf contour (respectively the Sf region) and the evaluation of a time interpolation of the recorded electric fields at each point in time and space (on the contour and in the region, respectively). For most scatterers of interest, the number of discretization points in the Sf region is much higher than the number of discretization points on the TfSf contour.

The TfSf source adds incident electric and magnetic fields on the faces of the TfSf contour to the numeric flux as defined in Eq. (5.18)

$$\Delta \mathbf{E}_{\mathrm{t}}(\mathbf{r}, t) = \mathbf{E}_{\mathrm{s}}^{+}(\mathbf{r}, t) + \mathbf{E}_{\mathrm{i}}(\mathbf{r}, t) - \mathbf{E}_{\mathrm{t}}^{-}(\mathbf{r}, t) \,,$$
$$\Delta \mathbf{E}_{\mathrm{s}}(\mathbf{r}, t) = \mathbf{E}_{\mathrm{t}}^{+}(\mathbf{r}, t) - \mathbf{E}_{\mathrm{s}}^{-}(\mathbf{r}, t) - \mathbf{E}_{\mathrm{i}}(\mathbf{r}, t) \,,$$

with the previously specified boundary conditions ΔE_{t} for the fields on the total field's element side of the face and ΔE_{s} for the fields on the scattered field's element side.

The analytically known incident field is in our case a dipole's electric and magnetic field distribution (see Eqs. (3.13) and (3.12)) where $\mathbf{p}(t) = p(t)\,\mathbf{e_p}$ is the emitter's dipole moment with orientation $\mathbf{p}$ and dipole moment amplitude $p(t)$. The time evolution of

6.2 Self-consistent dipoles in the proximity of a gold pentamer

the polarization's amplitude $p(t)$ is hither determined in a self-consistent manner from an equation of motion. This particular equation of motion describes the coupling between emitter and electromagnetic field and is solved alongside with Eq. (5.16) by the low storage Runge Kutta (LSRK) solver. As the specific ODE used in this work, we describe the emitter as a point-like dipole with a fixed dipole orientation positioned at $\mathbf{r}_0$ and couple it with Maxwell's equations via

$$\ddot{p}(t) + \gamma_0 \dot{p}(t) + \omega_0^2 p(t) = A_{\text{pump}}(t) + \frac{e^2}{m} \mathbf{e_p} \cdot \mathbf{E}_{\text{s}}(\mathbf{r}_0, t) \,, \qquad (6.21)$$

where γ_0 and ω_0 characterize the dipole's vacuum decay rate and transition frequency, respectively. Furthermore, we allow for a pump pulse that does not need to be optical and can excite the emitter from the ground to an excited state. The Equation above relates to Eq. (3.22) by assuming a point-like emitter at position $\mathbf{r}_0$ and splitting the electric field at the emitter's position into

$$\mathbf{E}(\mathbf{r}_0, t) = \mathbf{E}_{\text{s}}(\mathbf{r}_0, t) + \mathbf{E}_{\text{RR}}(t) \,, \qquad (6.22)$$

where $\mathbf{E}_{\text{RR}}(t)$ is the radiation reaction describing the field produced by the charged particle itself at the position of the particle $\mathbf{r}_0$ (cf. Ref. [227]) and $\mathbf{E}_{\text{s}}(\mathbf{r}_0, t)$ is the electric field scattered from the photonic structures and evaluated at the dipole's position. In a classical and simplified picture, an accelerated, periodically moving, charged particle radiates electromagnetic energy between the time t_1 and t_2 with $t_2 < t_1$ (see Refs. [27, 227])

$$W_{\text{EM}}(t_2, t_1) = -\frac{2}{3c^3} \int\limits_{t_1}^{t_2} \mathrm{d}t \, \dddot{p}(t) \dot{p}(t) \,, \qquad (6.23)$$

where the change in energy of the charged particle can be ascribed to the radiation reaction such that

$$\mathbf{E}_{\text{RR}}(t) = \frac{2}{3c^3} \dddot{p}(t) \,. \qquad (6.24)$$

This expression is actually the source of a divergence that cannot be straight-forwardly resolved within the limits of a point-like emitter. When describing the emitter as a spatially extended object, however, no divergence occurs. Thus, this divergence is a residual from the point approximation and not of physical origin.

However, within the description of the emitter as a classical, point-like object, the divergence in Eq. (6.24) can be avoided by assuming in a first approximation that the emitter's damping due to the radiation reaction is negligible. Consequently, in vacuum ($\mathbf{E}_{\text{s}}(\mathbf{r}_0, t) = 0$), the emitter then oscillates with $p(t) \propto \exp\left(-\mathrm{i}\omega_0 t\right)$ leading to $\dddot{p}(t) \approx -\omega_0^2 \dot{p}(t)$. This way, we introduce the vacuum decay rate γ_0 in Eq. (6.22) which holds only for sufficiently small vacuum damping $\gamma_0 < 2\omega_0$ (see also Ref. [28]). The charge and mass of the dipole are here connected to the resonance frequency and vacuum decay rate via (see Refs. [T1, 28])

$$\frac{e^2}{m} = 6\pi\varepsilon_0 c^3 \frac{\gamma_0}{\omega_0^2} \,. \qquad (6.25)$$
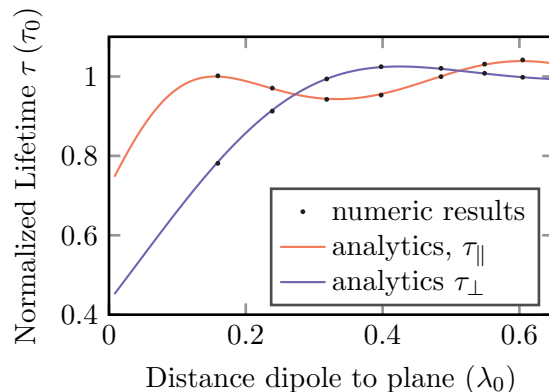
Figure 6.12: Analytical solution (Eq. (6.29)) for a dipole's lifetime enhancement at distance λ_0 to a dielectric half space compared to the lifetime of a self-consistent emitter as implemented in our scheme within the DGTD. The numeric results are obtained expanding the electromagnetic fields on each tetrahedron in fourth order Lagrange polynomials. Adapted from Ref. [W6].

These ODEs (Eq. (6.21) reformulated into two first degree ODEs) are then solved by the LSRK solver, the results at each time step stored and then at time t interpolated at exactly time $t - \tilde{r}$ (for a definition of $\tilde{r}$ see section 3.2.1) and back coupled to the electromagnetic fields by the use of a TfSf contour (see (1) and (4) in Fig. 6.11 and Eqs. (5.18), (3.13) and (3.12)). For a detailed discussion of the solution of the ODE Eq. (6.21) without backscattering using the LSRK solver and the time interpolation applied, see also Ref. [T1].

6.2.2 Convergence studies

In order to check the validity of the implemented method, we calculate the time-dependent polarization of an emitter described by the equation of motion (6.21) placed above a dielectric half space ($z < 0$) using the DGTD and comparing this to the integral description of the problem.

In both cases, the dipole is at the beginning of the computation in its ground state ($p(t_0) = 0$, $\dot{p}(t_0) = 0$) and is excited by the pump pulse which is given by

$$A_{\text{pump}}(t) = \mathcal{A}\, e^{-\frac{(t-t_{\text{pump}})^2}{2\sigma_{\text{pump}}^2}} \sin\left[\omega_{\text{pump}}(t - t_{\text{pump}}) + \phi_{\text{pump}}\right], \qquad (6.26)$$

where t_{pump}, σ_{pump}, ω_{pump} and ϕ_{pump} are freely electable pump pulse parameters. We select the parameter t_{pump} such that at the start time of the numeric computation $t = t_0$ the emitter exhibits no static dipole moment. This is necessary since a static dipole moment implies non-vanishing electric and magnetic fields which need to be initialized in space with their correct analytic expression. In general, this information is not known. The pump pulse's carrier frequency ω_{pump} is in this work chosen equal to the dipole's transition frequency ω_0 assuming a resonant pump pulse. The influence of the choice of the pump pulse's width σ_{pump} is studied below. Last, we introduce an optional phase ϕ_{pump} and set it to $\phi_{\text{pump}} = \pi/2$ in this part of the thesis.
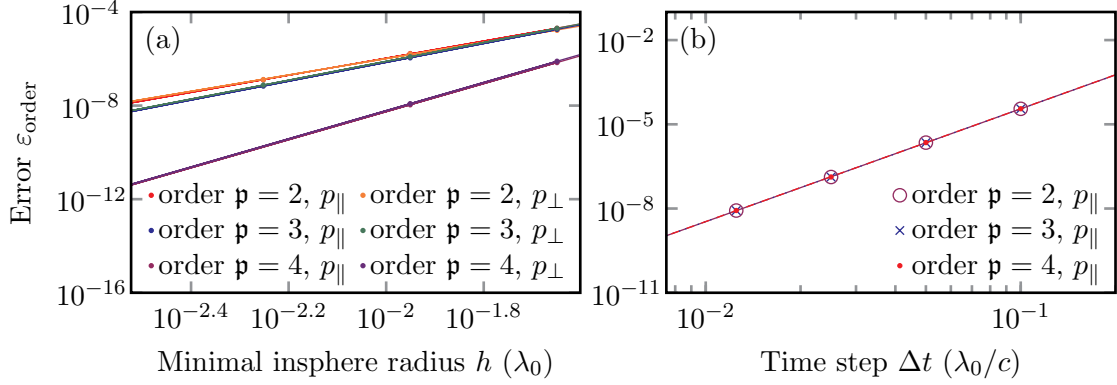
Figure 6.13: Errors for spatial and temporal discretization. The choice of t_N (the time at which the computation ends) is given by the vertical black lines in Fig. 6.14(a) and (b) for the spatial and temporal discretization, respectively. The spatial discretization exhibits a convergence rate $\alpha_{\mathfrak{p}} \geq \mathfrak{p} + 1$ with $\alpha_2 = 3.5$, $\alpha_3 = 4$ and $\alpha_4 = 6$. The temporal discretization exhibits a rate of $\alpha = 4$ independent of the field expansion into polynomial orders and exemplary only shown for one dipole orientation as expected for the global error of a LSRK algorithm of fourth order (see Ref. [186]). Adapted from Ref. [W6].

We find an alternative to the DGTD solution by transforming Eq. (6.21) into frequency domain

$$
p_{\text{int}}(t) = \frac{1}{\sqrt{2\pi}} \int\limits_{-\infty}^{\infty} d\omega \, e^{-i\omega t} \, A_{\text{pump}}(\omega) \cdot \left\{ -\omega^2 - i\gamma_0\omega \left[1 + \right.\right.
$$
$$
\left.\left. \frac{6\pi\varepsilon_0 c^3}{\omega_0^2 \omega} \left(\mathbf{e_p} \cdot \mathbf{E}_{\text{scat}}(\mathbf{r}_0, \omega) \cdot \mathbf{e_p} \right) \right] + \omega_0^2 \right\}^{-1},
$$
(6.27)

where the solution to the scattered field is given by use of the reflection coefficients of a plane (see Ref. [28] and Eq. (4.90))

$$
\mathbf{E}_{\text{scat}}(\mathbf{r}_0, \omega) = \frac{i}{8\pi\varepsilon_0} \int\limits_{0}^{\infty} dk_\rho \frac{k_\rho}{k_{z_1}} \begin{pmatrix} k_1^2 r^{\text{TE}} - k_{z_1}^2 r^{\text{TM}} \\ k_1^2 r^{\text{TE}} - k_{z_1}^2 r^{\text{TM}} \\ 2k_\rho r^{\text{TM}} \end{pmatrix} e^{2ik_{z_1} z_0}.
$$
(6.28)

Above, r^{TE} and r^{TM} are the usual TE and TM reflection coefficients for light propagating from vacuum into an infinite, dielectric half space that we have already made use of in chapter 4.

As presented in Refs. [28, 228], for an emitter decaying with a transition frequency of ω_0, the analytic and experimental distance dependence of the emitter's lifetime is well known and can be approximated by assuming the validity of the Weisskopf-Wigner

approximation with $\omega \approx \omega_0$ (see Eq. (4.90))

$$\frac{\gamma}{\gamma_0} \approx 1 + \frac{3c^3}{4\omega_0^3} \int\limits_0^\infty \mathrm{d}k_\rho \frac{k_\rho}{k_{z_1}} \begin{pmatrix} k_1^2 r^{\mathrm{TE}} - k_{z_1}^2 r^{\mathrm{TM}} \\ k_1^2 r^{\mathrm{TE}} - k_{z_1}^2 r^{\mathrm{TM}} \\ 2k_\rho r^{\mathrm{TM}} \end{pmatrix} \mathrm{e}^{2\mathrm{i}k_{z_1}z_0} \,. \tag{6.29}$$

In Fig. 6.12, we present the numerically obtained altering of the lifetime in comparison to the analytic solution Eq. (6.29). The numeric lifetime is obtained fitting the function

$$p_{\mathrm{fit}}(t) \propto \sin\left(\omega \cdot t + \phi\right) \exp\left[-t/(2\tau)\right], \tag{6.30}$$

to the dipole's polarization starting at times $t > 4\,t_{\mathrm{pump}}$. The nonlinear regression applied leads to errors on the decay rate of $\Delta\gamma < 4 \times 10^{-10}$.

We expect the convergence to be governed by several parameters: (i) the overall spatial discretization of the system , (ii) the time step of the Runge-Kutta scheme, (iii) the spatial discretization of the TfSf contour and (iv) the width of the pump pulse (and with this the slope of the induced fields. For the convergence parameters (i)-(iii), we define the error as

$$\varepsilon(j) = \frac{1}{N} \sum_{i=1}^N \left| p_j(t_i) - p_{\frac{j}{2}}(t_i) \right|, \tag{6.31}$$

where the parameter j describes the spatial discretization of the whole system, the time step of the LSRK scheme or the spatial discretization of the TfSf contour, respectively. Due to the fact that the computations are conducted in time-domain, we only sum up the individual error in each time step up to the time t_N in Eq. (6.31). In Fig. 6.13, we present the results for the error due to discretization (see panel (a)) and time stepping (see panel (b)) where we choose the t_N as marked in Fig. 6.14 that we discuss later in the text. In panel (a), we observe different convergence rates for the different Lagrange polynomial orders $\mathfrak{p}$ into which the fields are expanded. These convergence rates

$$\varepsilon(j) = \mathcal{C}j^\alpha \,, \tag{6.32}$$

with the constant prefactor $\mathcal{C}$ are at least as large as predicted for a pure DGTD algorithm where $\alpha_{\mathfrak{p}} \leq \mathfrak{p} + 1$ (see Refs. [173, 180]). In panel (b), we observe a convergence rate of $\alpha = 4$ which is consistent with the global error for a Runge Kutta method of fourth order (see Ref. [185, 186]).

When studying the robustness of these results when varying t_N, we find two different regimes for the ordinary differential equation (ODE) convergence behavior (see Fig. 6.14). At early times, when the electric field (see Fig. 6.14(c)) governs the ODE, the ODE exhibits a stable convergence rate with respect to discretization. For later times, the polarization and current governs the ODE and thus the spatial discretization for this point source does not matter any longer. Instead, the time discretization is of importance. The black lines in panels (a,b) correspond to the time t_N for which the errors are presented in Fig. 6.13.

Regarding the convergence parameter (iii), the discretization of the TfSf contour, we find a convergence rate of $\alpha \approx 3.6$ for both polarizations at early times (see Fig. 6.15(a)).
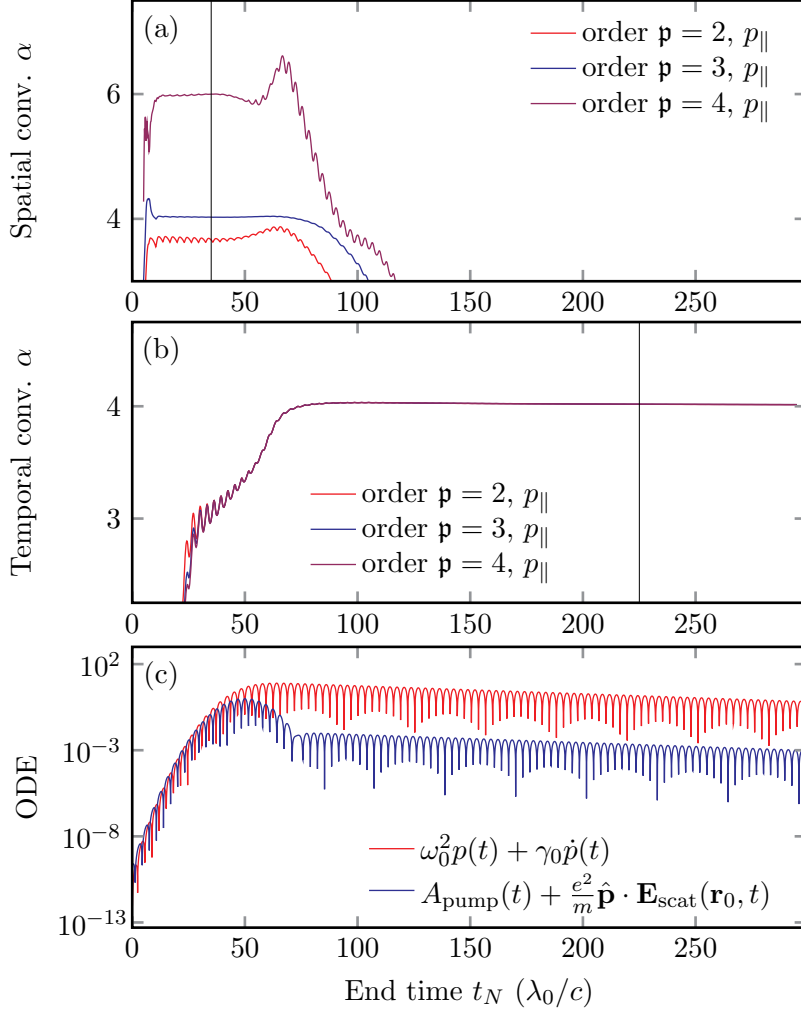
Figure 6.14: Different convergence rates α of the ordinary differential equation (ODE) Eq. (6.21). For early times $t_N < 60\lambda_0/c$, we obtain a fix spatial convergence rate α. This is due to the fact that in Eq. (6.21) the terms proportional to the electric field govern the time evolution (blue curve, panel (c)). For later times, the polarization and current terms govern the ODE. Thus, the convergence rate of the temporal discretization obtains the value $\alpha = 4$ as known for the global error of a LSRK method (see also caption of Fig. 6.13). Adapted from Ref. [W6].

For the last parameter (iv), the width of the pump pulse that effectively changes the steepness of the field induced at the TfSf-contour, the error cannot be determined according to Eq. (6.31) but can only be obtained by comparing to the results from a different computational method. Here, we compute Eq. (5.16) directly and obtain as an error

$$\epsilon = \frac{1}{N} \sum_{i=1}^{N} \left| p_{\text{int}}(t_i) - p_{\text{DGTD}}(t_i) \right| . \tag{6.33}$$

As before, the influence on the error is hugest at small time steps where most of the field
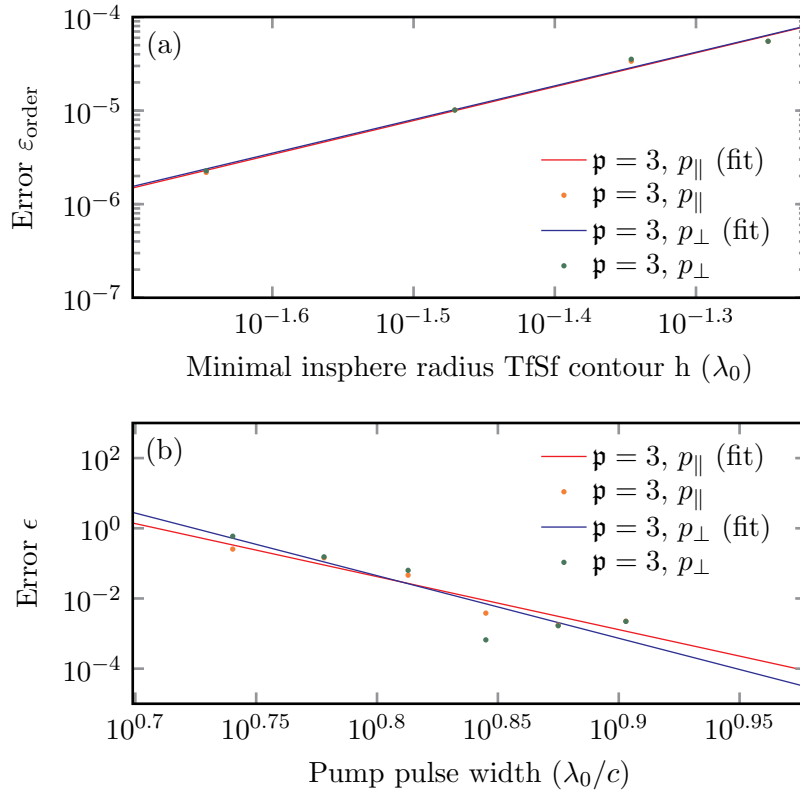
Figure 6.15: Errors for the dependence of the discretization of the TfSf contour (a) and the width of the pump pulse (b). The convergence rate in panel (a) is given as $\alpha_x = 3.6185$ and $\alpha_z = 3.5948$ for a Lagrange polynomial order of $\mathfrak{p} = 3$. In panel (b), we present the DGTD results for different pump pulse width in comparison to the integrated values. We obtain convergence with convergence rates as large as $\alpha > 15$. Adapted from Ref. [W6].

is induced. In Fig. 6.15(b), we find that the convergence rate α for this specific parameter is $\alpha > 15$ for both polarizations.

With these convergence studies in mind, we consider the algorithm introduced in this section stable and working and move on applying this self-consistent modeling of a classical dipole to the case in which we place such an emitter in the proximity of a nanoplasmonic system – specifically a gold pentamer.

6.2.3 The gold pentamer

Before computing the self-consistent emitter dynamics, we start by discussing in this section the general properties of the gold pentamer that we consider in the following. This way, we enhance the understanding of the emitters' radiation dynamics later in this section. We consider a gold pentamer as plasmonic nanostructure since it exhibits a rather broad scattering and absorbance cross section (see Fig. 6.17) covering the visible wavelengths.

6.2 Self-consistent dipoles in the proximity of a gold pentamer

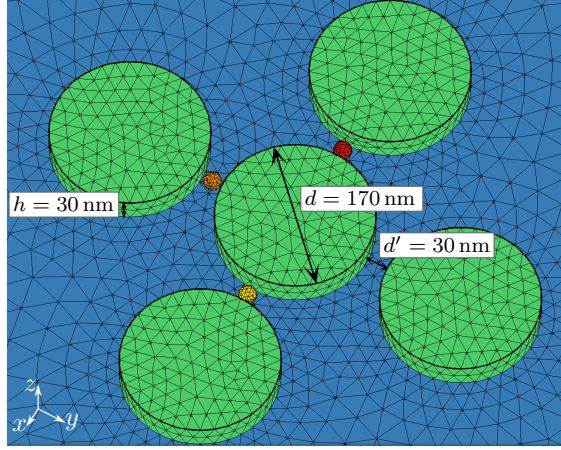**Figure 6.16:** Snippet of the mesh for the emitters in proximity of the pentamer. In green, we present the pentamer structure, in blue a substrate is introduced (BK7) and in red, orange and yellow three different TfSf contours (see Eq. (5.18)) are shown. These TfSf contours are three possible contours to initialize fields radiated from dipoles (positioned at the center of each TfSf domain). We study three different setups: (i) a single emitter (red TfSf contour), (ii) two emitters opposite to each other (red and yellow spheres) with the same polarization and (iii) two emitters at a 90 degree orientation (red and orange sphere) where in (ii) and (iii) the dipole inside the red TfSf is pumped by A_{pump} (see Eq. (6.26)) while the dipoles inside the yellow and orange contour, respectively, are solely responding to the red source dipole.

A snippet of the mesh used for the simulations within the DGTD is shown in Fig. 6.16 with three possible total-field/scattered-field contours (see section 5.2) (red, orange and yellow) in order to introduce the field of the self-consistent dipoles into the computation.

We assume the gold pentamer nanostructure to reside on a dielectric half space (BK7, $\varepsilon_{\text{BK7}} = 2.2836649924$). Each of the pentamer's disks is of diameter $d = 170\,\text{nm}$ and of height $h = 30\,\text{nm}$ and the disks have a distance of $d' = 30\,\text{nm}$ from each other. The gold is modeled using one Drude and one Lorentz pole (cf. Eq. (5.30))

$$
\varepsilon_{\text{Gold}}(\omega) = \varepsilon_{\infty} - \frac{\omega_{\text{Drude}}^2}{\omega(\omega + \mathrm{i}\,\gamma_{\text{Drude}})} \\
+ \frac{\Delta\varepsilon_{\text{Lorentz}}\,\omega_{\text{Lorentz}}^2}{\omega_{\text{Lorentz}}^2 - \mathrm{i}\,\gamma_{\text{Lorentz}}\,\omega - \omega^2}\,.
\tag{6.34}
$$

As parameters we use a fit to experimentally measured values (see Ref. [220]):

$$
\begin{aligned}
\varepsilon_{\infty} &= 6.210576\,, & \Delta\varepsilon_{\text{Lorentz}} &= 1.00\,, \\
\omega_{\text{Drude}} &= 0.04456379\frac{c}{\text{nm}}\,, & \omega_{\text{Lorentz}} &= 0.01341646\frac{c}{\text{nm}}\,, \\
\gamma_{\text{Drude}} &= 0.00034815\frac{c}{\text{nm}}\,, & \gamma_{\text{Lorentz}} &= 0.00193932\frac{c}{\text{nm}}\,.
\end{aligned}
\tag{6.35}
$$

We then calculate the scattering and absorbance spectra (see Fig. 6.17) by exciting the gold pentamer by an electromagnetic pulse with $\mathbf{E} \propto \mathbf{e}_y$ and $\mathbf{q} \propto \mathbf{e}_z$ and compute
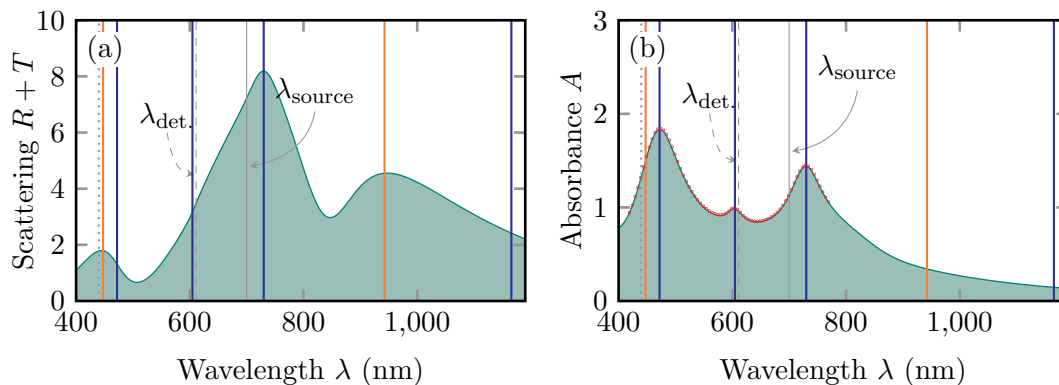
Figure 6.17: Scattering and absorbance of the gold pentamer displayed in Fig. 6.16. In the visible, we can fit (red dots) three Lorentzian (with one additional Lorentzian in the infrared) to the absorbance spectrum where the blue lines correspond to three resonances. For the damping of these resonances, see the text. Due to an overlapping mode structure in the scattering spectrum, we cannot fit Lorentzians to the scattering spectrum in order to determine the eigenfrequencies of the radiative modes. The two remaining maxima in the scattering spectrum that do not show in the absorbance spectrum are simply marked by the orange lines. Additionally, the transition frequencies of the three emitters we consider later are denoted by the dotted, dashed and solid gray lines, respectively. Two of them, at transition wavelength $\lambda_{\mathrm{source}}$ and $\lambda_{\mathrm{det.}}$, we couple in the last part of the section by placing the two at different positions close to the gold pentamer.

the spectra via Eq. (5.46) and the corresponding Equations in Ref. [181]. Due to the symmetry axis of the gold pentamer, we obtain the same results as presented in Fig. 6.17 also for all other excitations with the electric field polarized parallel to the glass substrate (e.g., by choosing $\mathbf{E} \propto \mathbf{e}_x + \mathbf{e}_y$). Since in the following, we will only consider emitters exhibiting in-plane electric dipole moments, we focus explicitly on the x-y excitation of the gold pentamer in order to obtain the relevant scattering and absorbance spectra.

The scattering spectrum (see Fig. 6.17(a)) of this pentamer structure is dominated by three maxima. One maximum is centered around $700\,\mathrm{nm}$ with the resonance decaying both radiatively and non-radiatively (since the maximum appears in both the scattering and the absorbance spectrum) and a second maximum is located at approximately $900\,\mathrm{nm}$ and mainly radiative since it does not appear in the absorbance spectrum. The third maximum is found close to $400\,\mathrm{nm}$ for which a corresponding, slightly red-shifted maximum also exists in the absorbance spectrum.

Besides from this qualitative considerations, we can also discuss the spectra at a more quantitative level. Due to broad radiative dipolar resonances that typically overlap with a number of other modes, the higher-order resonances in the absorbance spectrum are separated clearer from each other than the resonances in the scattering spectrum. The resonances in the absorbance spectrum can even be approximated by Lorentzian lineshapes describing damped oscillator. We fit the visible part of the absorbance spectrum by the use of four Lorentzians leading to the resonances of eigenfrequency $\omega_{\mathrm{plasm}} = 2\pi c/\lambda_{\mathrm{plasm}}$

and decay rate γ_{plasm} (blue lines at the eigenwavelengths and red dots for the resulting absorbance spectrum in Fig. 6.17(b))

$$
\begin{aligned}
\lambda^1_{\text{plasm}} &= 472.03\,\text{nm}\,, & \gamma^1_{\text{plasm}} &= 3.89 \cdot 10^{-3} \frac{c}{\text{nm}}\,, \\
\lambda^2_{\text{plasm}} &= 604.64\,\text{nm}\,, & \gamma^2_{\text{plasm}} &= 1.37 \cdot 10^{-4} \frac{c}{\text{nm}}\,, \\
\lambda^3_{\text{plasm}} &= 730.05\,\text{nm}\,, & \gamma^3_{\text{plasm}} &= 9.13 \cdot 10^{-5} \frac{c}{\text{nm}}\,, \\
\lambda^4_{\text{plasm}} &= 1165.63\,\text{nm}\,, & \gamma^4_{\text{plasm}} &= 4.34 \cdot 10^{-4} \frac{c}{\text{nm}}\,.
\end{aligned}
\tag{6.36}
$$

Above, the fourth resonance wavelength is rather an auxiliary eigenfrequency that is needed due to the broad tail of the absorbance data between 800 nm and 1000 nm that is due to the mainly radiative resonances appearing at the same wavelengths in the scattering spectrum. From the numbers above, we deduce that the resonances exhibit lifetimes in the femtosecond region which is typical for plasmonic nanostructures.

Since we cannot apply the same fitting routine to the analysis of the scattering spectrum in Fig. 6.17(a), we simply determine the two additional maxima (orange lines) that do not agree with the maxima in the absorbance spectrum

$$
\lambda^0_{\text{plasm}} \approx 447.5\,\text{nm}\,, \quad \lambda^5_{\text{plasm}} \approx 942.5\,\text{nm}\,.
\tag{6.37}
$$

In total, we do thus find five important features in the scattering and absorbance spectrum: three maxima occur in the scattering and three maxima occur in the absorbance spectrum where one of the three maximum (λ^3_{plasm}) agrees in both spectra. Due to the pentamer consisting of five monomers and the D_{4h} symmetry (cf. Ref. [229]), the hybridized plasmonic resonances that exist due to the plasmonic resonances of the single monomers are numerous and overlap in large parts of the spectra. Especially in the mainly radiative region ($\lambda > 800\,\text{nm}$) in which the absorbance spectrum only exhibits the mentioned tail, a combination of different dipolar hybridized modes exist that cannot be easily separated from each other. However, we can assume that all of the plasmonic resonances have lifetimes comparable to the ones determined in the case of the resonances within the absorbance spectrum (see Eq. (6.36)).

6.2.4 A single self-consistent emitter

As an application of the self-consistent emitter, we consider emitters for which the Weisskopf-Wigner approximation (see Eq. (3.31)) breaks down. This specifically happens when the emitter's lifetime in the proximity of the metallic nanostructure becomes comparable to the plasmonic resonance's lifetimes obtained before (see Eq. (6.36)). In this case, we expect a strongly modified and involved temporal dynamics of the emitter's radiation dynamics.

Emitters that are expected to exhibit femtosecond lifetimes (as plasmons usually do) when placed next to a metallic nanostructures, have picosecond lifetimes in vacuum. In the visible, these emitters are hard to come by but nonetheless of great scientific interest. These emitters would allow to image, e.g., biological processes that happen on very short time scales (cf. Refs. [5–7]) with a high degree of spatial resolution. However, some systems indeed exhibit such short lifetimes. These are for example systems exhibiting

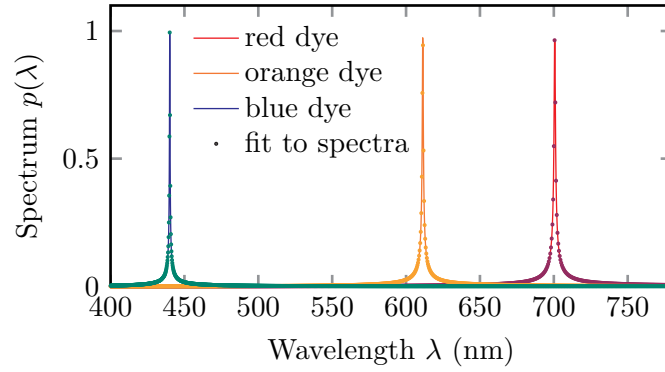# 6 Radiation dynamics of emitters close to metallic nanostructures

Figure 6.18: Vacuum calculations for dipoles radiating with $\omega_{0,\mathrm{r(ed)}}$ and $\gamma_{0,\mathrm{r(ed)}}$, $\omega_{0,\mathrm{o(range)}}$ and $\gamma_{0,\mathrm{o(range)}}$ and $\omega_{0,\mathrm{b(lue)}}$ and $\gamma_{0,\mathrm{b(lue)}}$, respectively (see text). For the vacuum calculations we used the tessellation shown in Fig. 6.16. The spectral information is obtained by use of a discrete Fourier transform. To obtain an error measure, we fit the data (see discussion in text and Eq. (6.39)).

intersystem crossings such as found iridium or copper complexes, see Refs. [24, 25]. The motivation of finding emitters with these short lifetimes has additionally led researchers to the approach of indeed coupling plasmonic nanosphere with longer lifetime emitters (see Ref. [26]). This leads us to the conclusion that even though the search for suited optical picosecond emitters is still on-going, there have been promising experiments that show the interest of scientists into short-time emitters and specifically the coupling of these emitters with metallic nanostructures. Especially, when coupling these emitters to plasmonic nanostructures and then using this coupled system as a probe, the knowledge on the exact radiation dynamics and the consequences of the coupling are of uttermost importance.

When we now couple emitters radiating in the visible, out of all modes discussed in the scattering and absorbance spectra presented in Fig. 6.17, the radiative eigenresonances are of highest importance. To stress this fact and discuss the widest range of emitters possible, we choose in the following three emitters for our discussion, one that radiates with a wavelength very close to the maximum appearing both in the scattering and absorbance spectrum ($\lambda_{\mathrm{plasm}}^3$, red), the second one ($\lambda_{\mathrm{plasm}}^2$, orange) that radiates close to the maximum that only exists in the absorbance spectrum and the third emitter (blue) that radiates at a wavelength close to the smallest wavelength maximum ($\lambda_{\mathrm{plasm}}^0$).
Since we will use the emitters' parameters throughout the remainder of this thesis, we present in Fig. 6.18 the calculation of the dipoles' spectra for a self-consistent emitter placed in vacuum. Here, we post processed the results, fitting the transition frequency $\tilde{\omega}_0$ and decay rate $\tilde{\gamma}_0$ of an oscillator of spectrum

$$p(\omega) = \frac{A_{\mathrm{pump}}(\omega;\omega_0)}{\tilde{\omega}_0^2 - \omega^2 - \mathrm{i}\tilde{\gamma}_0\omega}\,, \tag{6.38}$$

to the discrete Fourier transform of the time evolution of the dipoles. For a perfect computation in vacuum, one expects $\tilde{\omega}_0 = \omega_0$ and $\tilde{\gamma}_0 = \gamma_0 = 10^{-5}c/\mathrm{nm}$ for all emitters.
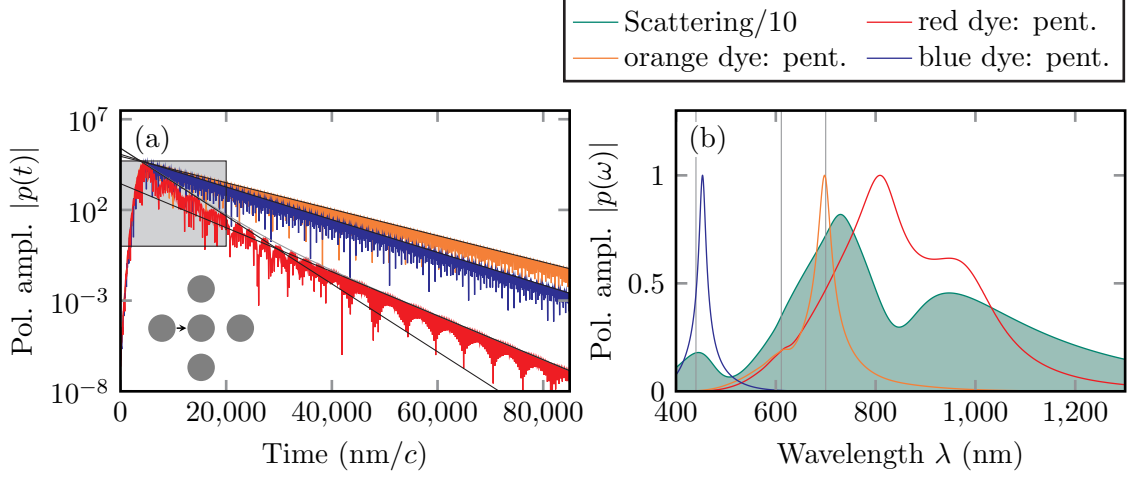
Figure 6.19: Time evolution (a) and corresponding spectra (b) of a self-consistent emitter near a gold pentamer. The emitter is oriented as depicted in the inset of panel (a). We study three emitters with different transition frequency (cf. also Fig. 6.18). The closer the emitter's transition frequency to the dipole resonance of the gold pentamer, the more it is actually influenced by the surface plasmon polaritons leading to a bi-exponential decay in the case of the red emitter. We zoom in Fig. 6.20 into the gray box denoted in panel (a).

From Fig 6.18, we obtain values

$$\frac{\tilde{\omega}_{0,\mathrm{r}} - \omega_{0,\mathrm{r}}}{\omega_{0,\mathrm{r}}} = 0.091\%\,, \quad \frac{\tilde{\gamma}_{0,\mathrm{r}} - \gamma_{0,\mathrm{r}}}{\gamma_{0,\mathrm{r}}} = -0.994\%\,,$$

$$\frac{\tilde{\omega}_{0,\mathrm{o}} - \omega_{0,\mathrm{o}}}{\omega_{0,\mathrm{o}}} = 0.053\%\,, \quad \frac{\tilde{\gamma}_{0,\mathrm{o}} - \gamma_{0,\mathrm{o}}}{\gamma_{0,\mathrm{o}}} = -0.998\%\,, \qquad (6.39)$$

$$\frac{\tilde{\omega}_{0,\mathrm{b}} - \omega_{0,\mathrm{b}}}{\omega_{0,\mathrm{b}}} = 0.014\%\,, \quad \frac{\tilde{\gamma}_{0,\mathrm{b}} - \gamma_{0,\mathrm{b}}}{\gamma_{0,\mathrm{b}}} = -0.834\%\,,$$

with the emitters transition frequencies chosen as $\omega_{0,\mathrm{b}} = 0.014280\,c/\mathrm{nm}$, $\omega_{0,\mathrm{o}} = 0.010283\,c/\mathrm{nm}$ and $\omega_{0,\mathrm{r}} = 0.008976\,c/\mathrm{nm}$ (corresponding to $\lambda_{0,\mathrm{b}} = 440\,\mathrm{nm}$, $\lambda_{0,\mathrm{o}} = 611\,\mathrm{nm}$ and $\lambda_{0,\mathrm{r}} = 700\,\mathrm{nm}$) and the decay rates equal for all three systems and as given above. Thus, we can conclude that this specific computation's error is of below 0.9977% on the decay rate fit but below 0.0998% for the frequency dependent characteristics. This is usually of sufficient accuracy to compare to standard nanophotonic experiments.

When studying those self-consistent emitters in proximity to a gold pentamer (see Fig. 6.16 for parts of the tessellation of the computational domain), we can determine the altered decay rates. In Fig. 6.19, we notice that even in the close proximity to the gold pentamer (gP), the blue and orange emitting emitters still display a mainly mono-exponential decay with

$$\gamma_{\mathrm{o,gP}} = 33.55\gamma_0 \qquad \text{and} \qquad \gamma_{\mathrm{b,gP}} = 41.5\gamma_0\,, \qquad (6.40)$$
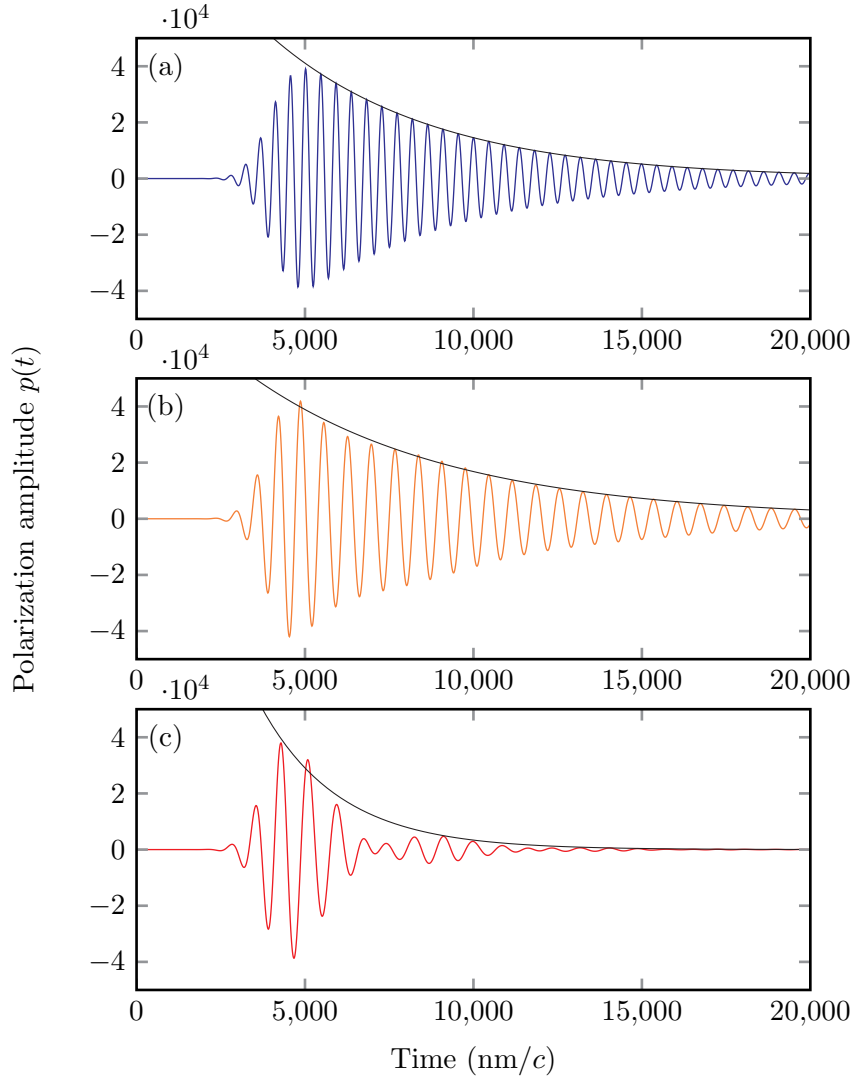
Figure 6.20: Zoom into the time evolution of self-consistent emitters near a gold pentamer (see gray region in Fig. 6.19(a)). It is well visible that exactly as shown in Fig. 6.19(b), the blue emitter behaves almost as a Lorentzian emitter with a well defined decay rate. The orange emitter, however, shows some very small beating at early times while for the red emitter at the times displayed here it is almost not possible to determine a decay rate at all.

while the radiation dynamics of the red shining emitter whose transition frequency is in close proximity of the radiating dipole resonance of the gold pentamer (cf. Fig. 6.17(a)) is far more involved. More specifically, we can find a bi-exponential decay with the short and long time decay rates

$$\gamma_{\text{r,gP,short}} = 86.07\gamma_0 \qquad \text{and} \qquad \gamma_{\text{b,gP,long}} = 55.88\gamma_0 \,. \qquad (6.41)$$

As is well visible in Fig. 6.20, at early times of the emitter's radiation dynamics, both the orange and the red emitter exhibit a beating caused by the coupling to radiative part of
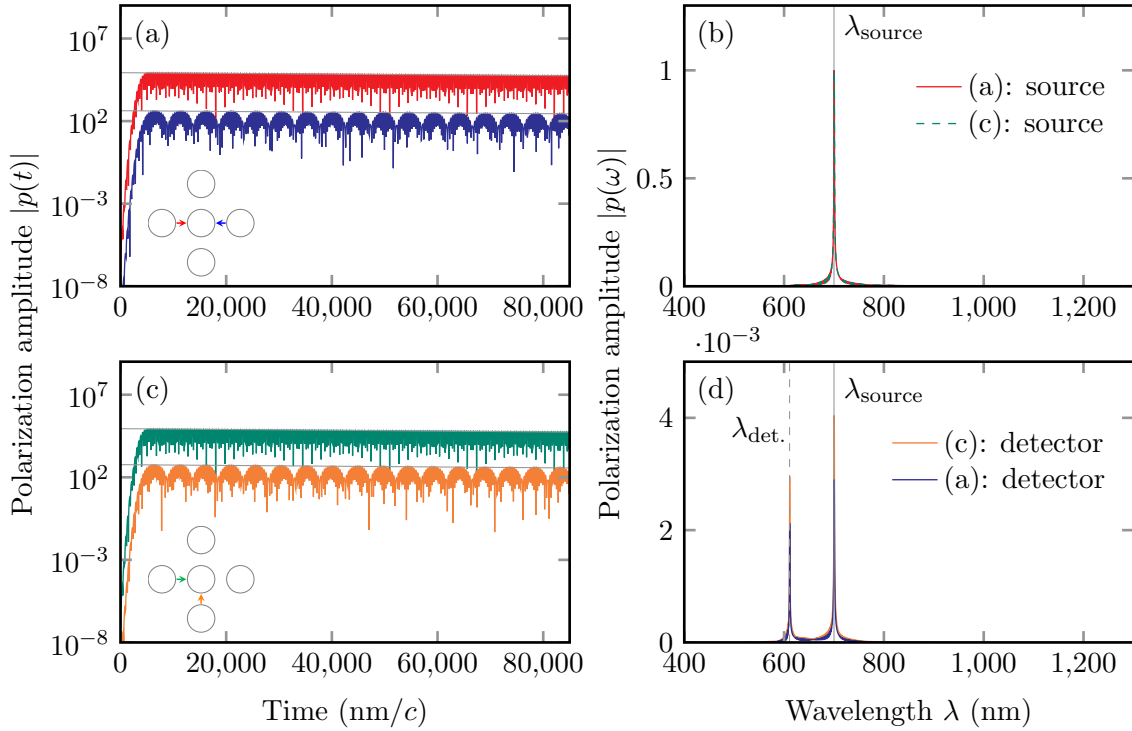
Figure 6.21: Time evolution of two emitters interacting with each other in vacuum. The computation is done in the same tessellation of space as for the simulation of the emitters in proximity to a gold pentamer (cf. Fig. 6.16) despite the pentamers consisting of vacuum (depicted by empty circles in pictogram). In time domain (a,c), the exponential decay (fit: gray lines) with one frequency (source) and two beating frequencies (detector) are clearly visible. This is supported by the frequency resolved polarization amplitudes (panels (b,d)) that are normalized to the maximum value of the source terms. The coupling efficiency of the source emitter to the detecting emitter goes with $\eta = 1.39 \approx \sqrt{2}$ which corresponds to the difference in inter-emitter distance.

the hybrid plasmon resonances. In Fig. 6.19(b), a clear red shift and broadening for all of the three emitters becomes apparent where specifically the broadening is responsible for the breakdown of the Weisskopf-Wigner approximation. By the spectral consideration, we can also understand that the orange emitter is sufficiently broadened and red-shifted such that it couples to the modes positioned at the absolute maximum in the scattering spectrum. For the red emitter this red shift and broadening is even sufficiently strong such that it does not only exhibit a lifetime on the order of the resonance lifetimes but it couples to modes distributed over two scattering maxima ($\lambda > 550\,\mathrm{nm}$). This leads in turn to this very involved time dynamics that we described before when discussing Figs. 6.20(a) and 6.19(a).

6.2.5 Interacting emitters in proximity to a gold pentamer

Due to the self-consistent nature of the classical dipoles, we can additionally study the interaction between two emitters. For this purpose, we choose two of the emitters – the red one that is the fastest decaying as the driver and the orange emitter that is the slowest decaying emitter. First, we start their direct coupling in vacuum at different distances from each other and obtain the results presented in Fig. 6.21. It is important to note that in vacuum both of the emitter decay at the same rate. In this case, we find a lowering of both decay rates to

$$\gamma_{\mathrm{r,coupl.}} = 1.13\gamma_0 \qquad \text{and} \qquad \gamma_{\mathrm{o,coupl.}} = 1.07\gamma_0 \,. \qquad (6.42)$$

It is well visible in the polarization spectra (cf. Fig. 6.21(b,d)), that the detecting emitter exhibits strictly speaking a bi-exponential decay. However, due to the numerical similarity of the two decay rates, this does not show in the time evolution. On the opposite, the time evolution of the polarization of the detecting emitter shows a beating due to the two transition frequencies involved. Additionally, we would like to point the readers attention to the coupling efficiency between the two different geometries. They relate as $\eta = p_{\mathrm{max,(c)}}(\omega)/p_{\mathrm{max,(a)}}(\omega) = 1.39 \approx d_{\mathrm{(a)}}/d_{\mathrm{(c)}}$ with the distance d between the two emitters.

In the next step, we place the two emitters close to the gold nanostructure (with the results given in Fig. 6.22). Here, in the time evolution we can see that the source emitter is in the beginning completely determined by its single emitter dynamics (cf. Fig. 6.19, red line and Eq. (6.41) with $\gamma_{\mathrm{r,gP,short}}$) until the much slower decaying detector emitter has a higher polarization amplitude than the source emitter. After a transition phase, the radiation dynamics of both emitters are completely determined by the radiation dynamics of the single, orange emitter in a gold pentamer structure where the orange emitter emits sufficient radiation such that it can re-excite the original source emitter. Thus detector emitter and source emitter change its functions. In this case, the decay rate of both emitters equals exactly the value of the orange emitter in Eq. (6.40). In Fig. 6.22, the mono-exponential decays are sketched into panels (a,b) with the decay rates exactly equal to the decay rates previously determined.

This coupling behavior can also be detected in the spectrum of the polarization amplitudes where both spectra are normalized to the maximum value of the single source emitter's spectrum (orange line). There, the orange detector emitter, exhibits an additional resonance at the driving frequency of the source emitter. Due to the domination of the detecting emitter at later times, the source emitter's spectrum is slightly influenced at lower wavelengths. However, since the interchange of source and detector function changes sufficiently late in the decay dynamics, the amplitudes of these processes are small compared to the initial driving of the red source emitter.

6.2.6 Conclusions

We have shown in this section that a compete self-consistent modeling even of a classical dipole can deepen the understanding of the light-matter coupling in complex photonic and plasmonic systems significantly. While this knowledge can, in general, in linear systems be derived from a frequency dependent or not self-consistent computation, the modeling
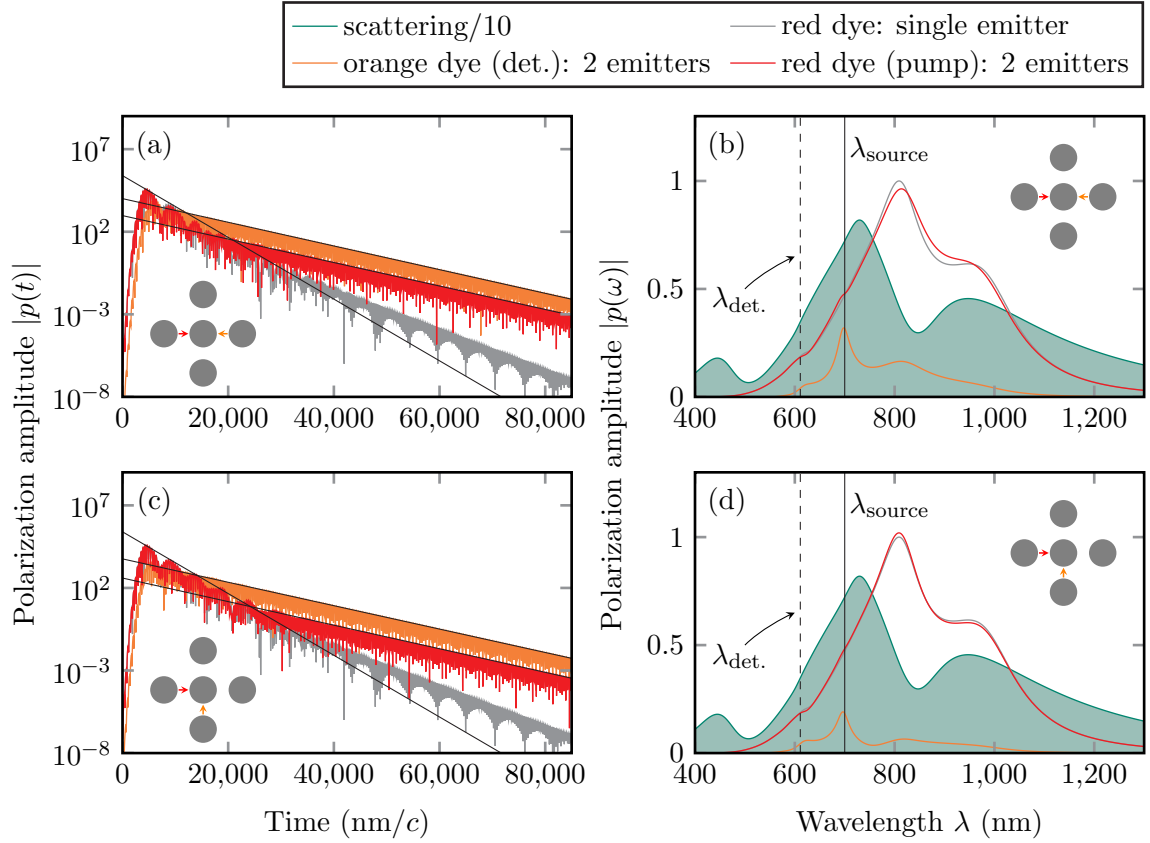
Figure 6.22: The Figure above presents the time evolution and spectrum of two dipoles coupling to each other in proximity of a gold pentamer. The emitter titled source is pumped by a pump pulse while the emitter called detector only responds to the electromagnetic field stemming from the gold pentamer and the first emitter. The source emitter radiates at $\lambda_{\text{source}} = \lambda_{0,\text{r}} = 700\,\text{nm}$ while the second emitter is detuned at $\lambda_{\text{det.}} = \lambda_{0,\text{o}} = 611\,\text{nm}$. In the left panels, we present the time evolution (for color coding see corresponding legends in right panels). In the right panels, we present the spectra obtained via a discrete Fourier transform. Additionally, in green we give the scattering cross section of the pure gold pentamer.

of the time evolution enhances the corresponding intuitively understanding of the setup at hand.

Especially, while we are experimentally approaching the regime where we are able to place emitters with increasingly higher precision as presented in section 6.1, in a variety of fields it is important to enhance the understanding of the dynamics on the picosecond scale. For example, already in 1975, Kaufmann and co-workers (see Ref [230]) developed picosecond spectroscopy in biology. By using single emitters, an increase in the detection of spatially resolved biological processes might be possible. In order to decrease the lifetime of current optical emitters to the picosecond regime, a strong coupling to plasmonic materials for quantum emitters is one possible path (cf. Ref. [26]). The

basis for successful experiments using picosecond emitters is in conclusion the detailed understanding of processes similar to the once discussed in this section.

Furthermore, the convergence studies as provided for the case of a classical self-consistent dipole allow for the future modeling of quantum-mechanically described emitters and will open the possibilities to, e.g., also include non-radiative decay processes and the influence of plasmonic nanostructures onto these decay channels. The resulting equations of motion are often nonlinear such that additionally the mapping between time and frequency domain breaks down and a self-consistent time domain description becomes obligatory. In these cases, even more involved time evolution are to be expected.

CHAPTER **7**

Conclusions, outlook and related work

The last section of this thesis first summarizes and concludes the thesis and then gives a short outlook to future applications of the methods and results presented throughout this thesis. The following discussion of related work shows the embedding of the research presented in this thesis in the research conducted in the group Theoretical Optics & Photonics *at the Humboldt-Universität zu Berlin.*

7.1 Conclusions and Outlook

In this thesis, we presented plasmonic environments in which different types of emitters can be used for the detection of electronic and photonic properties. In the future, the exact knowledge of these properties will help to design more advanced and functionalized hybrid light-matter devices which might be of use in wide areas of quantum technologies. Specifically, in this work we discussed plasmonic environments probed by contrasting mechanisms such as the QE-FLIM where an NV center glued to an AFM cantilever acts as a fluorescence lifetime probe, or the density of an atomic cloud trapped in an atom chip which can be used as a spatially resolved lifetime probe.

In order to arrive at the description of these plasmonic systems and their coupling to electric and magnetic emitters, we applied diverse methods. One of these was the analytical computation of the lifetimes of electric and magnetic emitters above graphene exhibiting a band gap. Here, we showed that the measurement of the lifetimes would indeed allow for an additional path to determine the possible band gap in a graphene monolayer, providing an alternative to ARPES measurements. The specific strength of the setup lies in the spatial resolution allowing, e.g., to study the correlation of spatial band gap and strain fluctuations. This is further enabled by the broad range of transition frequencies exhibited by electric and magnetic emitters. In the case that the emitter is already by construction included in the experimental setup, probing the properties of a graphene monolayer by an emitter instead of other methods, allows for the in-situ determination of the actual state of the graphene monolayer used in the experiment at hand.

Furthermore, we developed more involved numerical tools to describe as exact as necessary the radiation dynamics of the emitters. This includes an analysis of the allowed dipole orientations of an NV center and a method to compute the time evolution of

7 Conclusions, outlook and related work

classical dipole in a self-consistent manner within the DGTD. In the first case, we were able to describe with high qualitative and quantitative agreement the experimental results obtained when conducting the first three-dimensional QE-FLIM. In the second case, we showed the importance of reconsidering the Weisskopf-Wigner approximation that not only in photonic crystal systems but also close to metallic nanostructures can break down. Here, a self-consistent time domain modeling does not only allow for a more intuitive picture but also secures that the involved time evolution and with this the complicated spectrum of the emitter is not overly simplified.

We also introduced the possibility to introduce plane wave pulses under oblique incidence with respect to a periodic structure into the DGTD method in order to increase possible applications of this time-domain Maxwell solver. This is of particular importance in the context of periodically-structured systmes (cf. Ref. [W5]) or for the further analysis of the influences of periodicities on experimental measurements. Also, we discussed in detail the existence of modes in dielectric slab - graphene - dielectric slab setups to deepen the understanding of the processes leading to lifetime modifications of emitters above graphene.

With the development of the numerical methods, we also laid the ground for future work. By including graphene as a sheet conductivity into the DGTD, we will in the future be able to both enhance the description of two-dimensional, structured materials within the DGTD (e.g., by a tight-binding description as discussed in the next section) but also to model further physical properties such as surface roughness of plasmonic nanostructures by use of a surface current (see Ref. [203, 204]) or surface current sources that may be applied, e.g., for the computation of Casimir forces (see Ref. [231, 232]). However, it turns out from numerical studies by Philip Kristensen that a sine-shaped source as the one suggested by the authors of Refs. [231, 232] seems to limit the accuracy of these calculations since it is not divergenceless and thus leads to non-vanishing fields. In this context, it seems more promising to make use of the (self-consistent) dipole as a source of the electromagnetic radiation in a Casimir force calculation.

With respect to the work on emitter dynamics in the proximity of plasmonic and dielectric nanostructures, we will further focus on the effects that graphene and other two-dimensional materials have onto electric and magnetic emitters. In the future, it will be, among others, necessary to include finite temperature effects into the description of the graphene monolayer (see chapter 4) and compute the lifetime modifications when graphene monolayers are placed in a magnetic field that might experimentally be required in order to tune the magnetic transition. By doing so, even further quantitative and qualitative predictions regarding room-temperature experiments are possible allowing for a further discussion of the relevance of graphene's band gap in experiments.

Last, it is of interest to the scientific community to broaden the discussion and research to include the influence of other two-dimensional materials (and their multilayers) on light-matter coupling. Although graphene is already a promising platform, other two-dimensional crystals might allow for an even better performance of hybrid emitter-plasmonic devices such as for instance in an atom chip.

7.2 Related work

In the group *Theoretical Optics & Photonics* at the Humboldt-Universität zu Berlin, a wide range of research is conducted that relates to the work presented in this thesis. Research regarding the radiation dynamics and its modeling in the framework in the DGTD has been conducted within the Bachelor thesis of Franziska Bierbüße (see Ref. [T1]). Her research within the scope of her Bachelor thesis concentrated on the basic numerical framework such as the low storage Runge Kutta (LSRK) solver and the time interpolation needed for the modeling of a self-consistent classical dipole.

In the future, we will move towards the modeling of quantum emitters (two- and three-level-systems) within the DGTD and realize a Maxwell-Schrödinger coupling. Robert Kieschke conducts this research within his Master thesis where he focuses specifically on the radiation dynamics of a quantum emitter close to or embedded in a hyperbolic metamaterial cavity (see Ref. [226]). It has been shown in work from within this group (see Ref. [233]) that in general hyperbolic metamaterials can decrease the lifetime of an emitter close to the material by a factor of up to 1000 for certain transition frequencies. Thus, when assuming, e.g., certain layers of the hyperbolic metamaterial to be doped with a dye, these dyes might exhibit strong modifications to their radiation dynamics.

This directly leads to the point of including a quantum description of such two-dimensional materials into an electromagnetic field time domain solver such as the DGTD. Christian Gryzik within his Master thesis (see Ref. [T2]) focuses on the finite size effects that a graphene nanostructure has on the lifetime modification of electric and magnetic emitters. This is of importance since nanoribbons, e.g., on an atom chip will be finite in size. The influence of finite size effects has previously been discussed elsewhere (cf. Ref. [153, 154]) but is nonetheless different when the graphene nanostructures are excited by magnetic emitters with their much smaller transition energies. Within this project, the long-term goal is the coupling of a time-dependent tight-binding description of graphene to the complete three-dimensional electromagnetic field computation within the algorithm of the DGTD. In turn, he can then compute experimentally relevant structures combining two-dimensional semi-metal with plasmonic and dielectric nanostructures.

APPENDIX A

Bosonic and fermionic states

Although, in the results of this work, we do not explicitly make use of bosonic and fermionic states, in this appendix we present the basic notation, the QFT description of graphene presented in chapter 2 is based on.

The QM description as presented in section 1.2 is in the non-relativistic limit the theory of choice to describe the dynamics of so-called *microscopic objects*[33], such as, e.g., photons and electrons. These objects (or particles) are sorted by their specific properties into two particle classes: bosons and fermions[34]. Bosons (e.g., photons) and fermions (e.g., electrons) are defined by their specific occupation characteristics that follow from the different particle commutator relations applied to a multiparticle wavefunction. While more than one boson can occupy one single state, only one fermion can occupy a given state. This leads to the following statistics at thermodynamic equilibrium

$$f_{\text{Boson}} \equiv \langle n_{\text{Boson}}(E) \rangle = \frac{1}{e^{\beta(E-\mu)} - 1} \qquad \text{and}$$

$$f_{\text{Fermion}} \equiv \langle n_{\text{Fermion}}(E) \rangle = \frac{1}{e^{\beta(E-\mu)} + 1} \,,$$

(A.1)

where $\langle n_i(E) \rangle$ describes the expectation value for the bosonic and fermionic density at a certain energy E. Above, we also introduce the temperature $\beta = (k_{\text{B}}T)^{-1}$ defined via the Boltzmann constant k_B and the chemical potential μ. The bosonic distribution is known as the Bose-Einstein distribution while the fermionic distribution is known as the Fermi-Dirac distribution. For the limit of $T \to 0$, we find

$$\lim_{T \to 0} f_{\text{Boson}}(E) = \delta(E) \,,$$

(A.2)

---

[33] The terminus microscopic objects compares to the concept of macroscopic objects, i.e., a metallic nanostructure that consists of a large amount of these microscopic objects and is thus very well described in the limit of classical physics.

[34] Most general speaking, a third class, the anyons, exist. Anyons are quasiparticles with a very specific occupation probability that is neither fermionic nor bosonic. They are of great importance for the description of the fraction quantum Hall effect (see Ref. [234] for a review) and in the discussion of a possible realization of very fault-tolerant quantum computers (see, e.g., Ref. [235]). They are not the subject of this thesis and are thus not touched further.

where $\delta(E)$ describes a delta function defined by

$$
\delta(x - E) \equiv \frac{1}{2\pi} \int\limits_{-\infty}^{\infty} dq\, e^{iq\,(x-E)} \qquad \text{with} \qquad \int\limits_{-\infty}^{\infty} d\zeta' f(\zeta')\, \delta(\zeta - \zeta') \equiv f(\zeta)\,, \qquad \text{(A.3)}
$$

such that all bosons occupy the zero energy state while

$$
\lim_{T \to 0} f_{\text{Fermion}}(E) = \Theta(\mu - E)\,, \qquad \text{(A.4)}
$$

where $\Theta(\mu - E)$ describes the Heaviside function

$$
\Theta(\mu - E) \equiv \begin{cases} 1\,, & \text{for } E \leq \mu \\ 0\,, & \text{for } E > \mu \end{cases}\,. \qquad \text{(A.5)}
$$

The fermionic particle distribution then leads to the fact that all states with $E \leq \mu$ are occupied while the states with $E > \mu$ are empty.

A.1 Bosonic states

For the example of bosons, we can define an annihilation operator $\hat{a}$ that annihilates a boson and a creation operator $\hat{a}^{\dagger}$ that creates a boson and obey the well-known commutation relations

$$
[\hat{a}, \hat{a}^{\dagger}] = 1 \qquad \text{and} \qquad [\hat{a}^{\dagger}, \hat{a}^{\dagger}] = [\hat{a}, \hat{a}] = 0\,. \qquad \text{(A.6)}
$$

On a so-called Fock or number state $|n\rangle$ which is a state containing n bosons these operators then act as follows:

$$
\hat{a}\,|n\rangle = \sqrt{n}|n - 1\rangle \qquad \text{and} \qquad \hat{a}^{\dagger}|n\rangle = \sqrt{n + 1}\,|n + 1\rangle\,. \qquad \text{(A.7)}
$$

This results in the fact that these states $|n\rangle$ are eigenstates of the number operator

$$
(\hat{a}^{\dagger}\hat{a})|n\rangle = n|n\rangle\,. \qquad \text{(A.8)}
$$

and $|0\rangle$ is the vacuum state without bosons and with $(\hat{a}^{\dagger}\hat{a})|0\rangle \equiv 0$. As a result of these identities, a Fock state can be written as

$$
|n\rangle = \frac{(\hat{a}^{\dagger})^{n}}{\sqrt{n!}}|0\rangle\,. \qquad \text{(A.9)}
$$

These states form an orthogonal

$$
\langle m|n\rangle = \delta_{mn} \equiv \begin{cases} 0 \text{ if } m \neq n\,, \\ 1 \text{ if } m = n \end{cases} \qquad \text{(A.10)}
$$

and complete

$$\sum_{n=0}^{\infty} |n\rangle\langle n| = \mathbb{1} \tag{A.11}$$

set of eigenstates with the Kronecker δ defined in Eq. (A.10) and $\mathbb{1}$ being the identity operator in the Hilbert space of a single-mode system.

A bosonic excitation can experimentally also be prepared in a *coherent state*. These coherent states $|\alpha\rangle$ are most rigorously and general defined as displaced vacuum states

$$|\alpha\rangle = \hat{D}(\alpha)|0\rangle. \tag{A.12}$$

where the displacement operator is given by

$$\hat{D}(\alpha) = e^{\alpha\hat{a}^\dagger - \alpha^*\hat{a}} = e^{-\frac{|\alpha|^2}{2}} e^{\alpha\hat{a}^\dagger} e^{\alpha^*\hat{a}}, \tag{A.13}$$

The last reformulation we perform with the help of Lie's expansion formula (cf. Ref. [236], p. 971)

$$e^{\hat{X}}\hat{Y}e^{-\hat{X}} = \sum_{i=0}^{\infty} \frac{1}{i!}[\hat{X}, \hat{Y}]_i \tag{A.14}$$

with $[\hat{X}, \hat{Y}]_i = [\hat{X}, [\hat{X}, \hat{Y}]_{i-1}]$ and $[\hat{X}, \hat{Y}]_0 = \hat{Y}$ and the Baker-Campbell-Hausdorff Formula (see Ref. [237]) for two non-commuting operators $\hat{X}$ and $\hat{Y}$

$$e^{\hat{X}}e^{\hat{Y}} = e^{\hat{X}+\hat{Y}+\frac{[\hat{X},\hat{Y}]}{2}+\frac{[\hat{X},[\hat{X},\hat{Y}]]-[\hat{Y},[\hat{X},\hat{Y}]]}{12}+\cdots} \tag{A.15}$$

that reads for the bosonic operator relations $[\hat{a}^\dagger, \hat{a}]_n = 0$ for $n \geq 2$ as

$$e^{x\hat{X}+y\hat{Y}} = e^{x\hat{X}}e^{y\hat{Y}}e^{x\cdot y\cdot[\hat{X},\hat{Y}]}. \tag{A.16}$$

In Eq. (A.16), we identify $\hat{X} = \hat{a}^\dagger$, $\hat{Y} = \hat{a}$ and $x = y^* = \alpha$ and arrive at Eq. (A.13).

By applying algebraic reformulations[35], one finds that the coherent state is the right-sided eigenstate of the annihilation operator

$$\hat{a}|\alpha\rangle = \alpha|\alpha\rangle, \tag{A.17}$$

---

[35]The proof goes as follows: For the displacement operator, one finds $\hat{D}^\dagger(\alpha) = \hat{D}^{-1}(\alpha) = \hat{D}(-\alpha)$ and with this and Eq. (A.14), one can write

$$\hat{D}^\dagger(\alpha)\hat{a}\hat{D}(\alpha) = \hat{a} + [\alpha^*\hat{a} - \alpha\hat{a}^\dagger, \hat{a}] = \hat{a} + \alpha,$$

and thus find

$$\hat{a}|\alpha\rangle = \hat{a}\hat{D}(\alpha)|0\rangle = \hat{D}(\alpha)\hat{D}^\dagger(\alpha)\hat{a}\hat{D}(\alpha)|0\rangle.$$

The r.h.s. of the last Equation can be rewritten as

$$\hat{a}|\alpha\rangle = \hat{D}(\alpha)(\hat{a} + \alpha)|0\rangle = \alpha\hat{D}(\alpha)|0\rangle = \alpha|\alpha\rangle$$

with which Eq. (A.18) is proven.

we can expand the coherent states in the complete set of Fock states

$$|\alpha\rangle = \mathrm{e}^{-\frac{|\alpha|^2}{2}} \sum_{n=0}^{\infty} \frac{\alpha^n}{\sqrt{n!}} |n\rangle = \mathrm{e}^{-\frac{|\alpha|^2}{2}} \sum_{n=0}^{\infty} \frac{\alpha^n (\hat{a}^\dagger)^n}{n!} |0\rangle \equiv \mathrm{e}^{-\frac{|\alpha|^2}{2}} \mathrm{e}^{\alpha \hat{a}^\dagger} |0\rangle\,. \tag{A.18}$$

Contrary to the Fock state basis, the coherent states form an over complete set

$$\frac{1}{\pi} \int |\alpha\rangle\langle\alpha| \, \mathrm{d}(\mathrm{Re}\,[\alpha]) \, \mathrm{d}(\mathrm{Im}\,[\alpha]) = \mathbb{1}\,. \tag{A.19}$$

Nonetheless, coherent states are important states since they are considered the most classical states since they simultaneously provide the minimal uncertainty in space and momentum.

A.2 Fermionic states: the Grassman algebra

For the example of fermions, we define an annihilation operator $\hat{c}$ that annihilates a fermion and a creation operator $\hat{c}^\dagger$ that creates a fermion. Contrary to the bosons, these operators obey anti-commutator relation for two operators $\hat{c}_i^{(\dagger)}$ creating and annihilating fermions in different states (such as at different times and positions or with different momentum and energy)

$$\{\hat{c}_i, \hat{c}_j^\dagger\} = \delta_{ij} \qquad \text{and} \qquad \{\hat{c}_i^\dagger, \hat{c}_j^\dagger\} = \{\hat{c}_i, \hat{c}_j\} = 0\,. \tag{A.20}$$

This algebra is known as the *Grassman algebra* (for details see QFT literature, i.e., Ref. [30]). As in the bosonic case, we can define Fock states

$$\hat{c}_i^\dagger \hat{c}_i |n_i\rangle = n_i |n_i\rangle\,, \tag{A.21}$$

and coherent states

$$\hat{c}_i |\eta_i\rangle = \eta_i |\eta_i\rangle\,. \tag{A.22}$$

With the anticommutation relation $\hat{c}_i \hat{c}_j = -\hat{c}_j \hat{c}_i$ and thus with $\eta_i \eta_j = -\eta_j \eta_i$ it is obvious that opposite to the bosonic case the η_i cannot be simple numbers. Instead they have to fulfill the anticommutation relation.

Thus, for the projection of a coherent state onto a Fock state one finds

$$\langle n_i | \eta_i \rangle = \langle -\eta_i | n_i \rangle\,. \tag{A.23}$$

Since the discussion of the Grassman algebra in all depth is far beyond the scope of this work, we do not introduce any additional identities. However, the general concept of fermionic coherent states is analogous to the insight one gathers from the bosonic discussion.

APPENDIX B

The reflection coefficients of a conductive sheet

In this appendix, we present a detailed derivation of the TE and TM reflection coefficients for a conductive sheet for both a classical sheet conductivity $\sigma(\mathbf{q}, \omega)$ as presented in section 2.2.2 and a quantum-field theoretical description via the polarization tensor $\Pi_{\mu\nu}$ as presented in section 2.2.1.

B.1 Calculating the reflection coefficients of a sheet conductivity

TM polarization:

Starting with the divergence equation for the magnetic flux density (1.1b) of Maxwell's equations, we find that $\nabla \cdot \mathbf{B}(\mathbf{r}, t) = 0$ is in the TM mode with $q_y^{(i)} = 0$ and $\underline{\mu}_r = 1$ automatically fulfilled. The second divergence equation (1.1a), leads to the first condition that connects the different components of the electric fields. When taking into account that the system is invariant under displacement in x-direction ($q_x^{(1)} = q_x^{(2)}$), the $\mathrm{e}^{\pm \mathrm{i} q_z^{(i)} z}$ are linear independent of each other for all $\mathbf{q}$, one arrives at

$$\mathcal{E}_z^{(0)}(\mathbf{q}, \omega) = -\frac{q_x^{(1)}}{q_z^{(1)}} \mathcal{E}_x^{(0)}(\mathbf{q}, \omega), \qquad \mathcal{E}_z^{(\mathrm{r})}(\mathbf{q}, \omega) = \frac{q_x^{(1)}}{q_z^{(1)}} \mathcal{E}_x^{(\mathrm{r})}(\mathbf{q}, \omega), \tag{B.1a}$$

$$\mathcal{E}_z^{(\mathrm{t})}(\mathbf{q}, \omega) = -\frac{q_x^{(2)}}{q_z^{(2)}} \mathcal{E}_x^{(\mathrm{t})}(\mathbf{q}, \omega), \qquad \mathcal{E}_z^{(-)}(\mathbf{q}, \omega) = \frac{q_x^{(2)}}{q_z^{(2)}} \mathcal{E}_x^{(-)}(\mathbf{q}, \omega), \tag{B.1b}$$

Next focusing on the curl equation for the electric field (1.1d), using Eqs. (B.1), and $\boldsymbol{\mathcal{B}} = \mu_0 \boldsymbol{\mathcal{H}}$, we find for region (1) as a connecting condition between electric and magnetic field

$$\mathcal{E}_x^{(0)}(\mathbf{q}, \omega) = \frac{q_z^{(1)}}{\varepsilon_1 \omega} \mathcal{H}_y^{(0)}(\mathbf{q}, \omega), \qquad \mathcal{E}_x^{(\mathrm{r})}(\mathbf{q}, \omega) = -\frac{q_z^{(1)}}{\varepsilon_1 \omega} \mathcal{H}_y^{(\mathrm{r})}(\mathbf{q}, \omega). \tag{B.2}$$

For region (2) we replace $(1) \leftrightarrow (2)$, $(0) \leftrightarrow (\mathrm{t})$ and $(\mathrm{r}) \leftrightarrow (-)$ in the equation above. The last curl equation does not yield any additional information.

In order to finally connect the different fields with each other, we need to apply the boundary conditions (2.52). For the TM mode, condition (2.52b) is automatically fulfilled.

B The reflection coefficients of a conductive sheet

Next, from condition (2.52c) with the use of Eq. (B.2) follows

$$\frac{q_z^{(1)}}{\varepsilon_1 \omega} \left(\mathcal{H}_y^{(0)}(\mathbf{q}, \omega) - \mathcal{H}_y^{(\mathrm{r})}(\mathbf{q}, \omega) \right) = \frac{q_z^{(2)}}{\varepsilon_2 \omega} \left(\mathcal{H}_y^{(\mathrm{t})}(\mathbf{q}, \omega) - \mathcal{H}_y^{(-)}(\mathbf{q}, \omega) \right) . \tag{B.3}$$

Condition (2.52d) together with Eq. (B.2) leads to the last condition needed

$$\mathcal{H}_y^{(0)}(\mathbf{q}, \omega) + \mathcal{H}_y^{(\mathrm{r})}(\mathbf{q}, \omega) - \left[\mathcal{H}_y^{(\mathrm{t})}(\mathbf{q}, \omega) + \mathcal{H}_y^{(-)}(\mathbf{q}, \omega) \right]$$

$$= \frac{\sigma^{\mathrm{L}}(\mathbf{k}, \omega) q_z^{(2)}}{\varepsilon_2 \omega} \left[\mathcal{H}_y^{(\mathrm{t})}(\mathbf{q}, \omega) + \mathcal{H}_y^{(-)}(\mathbf{q}, \omega) \right] . \tag{B.4}$$

Both adding and subtracting Eq. (B.3) and (B.4) from each other and assuming $\mathcal{H}_y^{(-)} = 0$, the TM reflection and transmission coefficient for a conductive sheet in between material 1 and 2 (remember, $q_z^{(i)} = \sqrt{\varepsilon_i \omega^2 / c^2 - (q_x^{(i)})^2}$) read

$$r^{\mathrm{TM}} = \frac{\mathcal{H}_y^{(\mathrm{r})}}{\mathcal{H}_y^{(0)}} = \frac{\varepsilon_2 q_z^{(1)} - \varepsilon_1 q_z^{(2)} + q_z^{(1)} q_z^{(2)} \frac{\sigma^{\mathrm{L}}(\mathbf{k}, \omega)}{\omega}}{\varepsilon_2 q_z^{(1)} + \varepsilon_1 q_z^{(2)} + q_z^{(1)} q_z^{(2)} \frac{\sigma^{\mathrm{L}}(\mathbf{k}, \omega)}{\omega}} , \tag{B.5a}$$

$$t^{\mathrm{TM}} = \frac{\mathcal{H}_y^{(\mathrm{t})}}{\mathcal{H}_y^{(0)}} = \frac{2 \varepsilon_2 q_z^{(1)}}{\varepsilon_2 q_z^{(1)} + \varepsilon_1 q_z^{(2)} + q_z^{(1)} q_z^{(2)} \frac{\sigma^{\mathrm{L}}(\mathbf{k}, \omega)}{\omega}} . \tag{B.5b}$$

With these solutions, the remaining of Maxwell's equations and the boundary conditions give the additional information to solve for the electric field.

TE polarization:

In the case of TE polarization, the reflection and transmission coefficients can be derived similar to the ones in Eq. (B.5). In this case, however, of the four Maxwell's equations the divergence condition of the electric field (1.1a) is automatically fulfilled. Exploiting the same properties as for Eqs. (B.1) and (B.2), one arrives at

$$\mathcal{H}_z^{(0)}(\mathbf{q}, \omega) = -\frac{q_x^{(1)}}{q_z^{(1)}} \mathcal{H}_x^{(0)}(\mathbf{q}, \omega) , \qquad \mathcal{H}_z^{(\mathrm{r})}(\mathbf{q}, \omega) = \frac{q_x^{(1)}}{q_z^{(1)}} \mathcal{H}_x^{(\mathrm{r})}(\mathbf{q}, \omega) , \tag{B.6a}$$

$$\mathcal{H}_z^{(\mathrm{t})}(\mathbf{q}, \omega) = -\frac{q_x^{(2)}}{q_z^{(2)}} \mathcal{H}_x^{(\mathrm{t})}(\mathbf{q}, \omega) , \qquad \mathcal{H}_z^{(-)}(\mathbf{q}, \omega) = \frac{q_x^{(2)}}{q_z^{(2)}} \mathcal{H}_x^{(-)}(\mathbf{q}, \omega) , \tag{B.6b}$$

This expression can then (as before) be inserted into the conditions that arise from Eq. (1.1c) which in consequence leads to

$$\mathcal{H}_x^{(0)}(\mathbf{q}, \omega) = \frac{q_z^{(1)}}{\mu_0 \omega} \mathcal{E}_y^{(0)}(\mathbf{q}, \omega) , \qquad \mathcal{H}_x^{(\mathrm{r})}(\mathbf{q}, \omega) = -\frac{q_z^{(1)}}{\mu_0 \omega} \mathcal{E}_y^{(\mathrm{r})}(\mathbf{q}, \omega) . \tag{B.7}$$

Last, as in the case for the TM mode, we will proceed with the boundary conditions finding that this time condition (2.52a) is automatically fulfilled. With condition (2.52b), leading to

$$\mathcal{H}_z^{(2)}(\mathbf{q}, \omega) - \mathcal{H}_z^{(1)}(\mathbf{q}, \omega) = 0 , \tag{B.8}$$

and using condition (B.7), the first condition connecting the electric fields can be obtained from Eq. (2.52c)

$$\mathcal{E}_y^{(0)}(\mathbf{q},\omega) + \mathcal{E}_y^{(\mathrm{r})}(\mathbf{q},\omega) = \mathcal{E}_y^{(\mathrm{t})}(\mathbf{q},\omega) + \mathcal{E}_y^{(-)}(\mathbf{q},\omega)\,, \tag{B.9}$$

and the second condition may be arrived by starting from Eq. (2.52d)

$$\mathcal{E}_y^{(0)}(\mathbf{q},\omega) - \mathcal{E}_y^{(\mathrm{r})}(\mathbf{q},\omega) = \left(-\frac{\mu_0\omega\sigma^{\mathrm{T}}(\mathbf{k},\omega)}{q_z^{(1)}} + \frac{q_z^{(2)}}{q_z^{(1)}}\right)\mathcal{E}_y^{(\mathrm{t})}(\mathbf{q},\omega)$$
$$- \left(\frac{\mu_0\omega\sigma^{\mathrm{T}}(\mathbf{k},\omega)}{q_z^{(1)}} + \frac{q_z^{(2)}}{q_z^{(1)}}\right)\mathcal{E}_y^{(0)}(\mathbf{q},\omega)\,. \tag{B.10}$$

Subtracting and adding Eqs. (B.9) and (B.10) we obtain r^{TE} and t^{TE}, respectively, assuming no incident field from the bottom of the structure ($\mathcal{E}_y^{(0)} = 0$)

$$r^{\mathrm{TE}} = \frac{\mathcal{E}_y^{(\mathrm{r})}}{\mathcal{E}_y^{(0)}} = \frac{q_z^{(1)} - q_z^{(2)} + \mu_0\omega\sigma^{\mathrm{T}}(\mathbf{k},\omega)}{q_z^{(1)} + q_z^{(2)} - \mu_0\omega\sigma^{\mathrm{T}}(\mathbf{k},\omega)}\,, \tag{B.11a}$$

$$t^{\mathrm{TE}} = \frac{\mathcal{E}_y^{(\mathrm{t})}}{\mathcal{E}_y^{(0)}} = \frac{2q_z^{(1)}}{q_z^{(1)} + q_z^{(2)} - \mu_0\omega\sigma^{\mathrm{T}}(\mathbf{k},\omega)}\,. \tag{B.11b}$$

As for the TM mode, the remaining Maxwell's equations and boundary conditions analogously give the missing conditions to calculate the complete solution including all amplitudes of the magnetic fields that were not of interest for the calculation of reflection and transmission coefficients.

B.2 The reflection coefficients from a polarization tensor

In section 2.2.1, we introduce the concept of a polarization tensor within the QED $_{2+1}$ as used to describe the quasi particle propagation in graphene. Since the interaction with the electromagnetic field is confined to a two–dimensional spatial sheet positioned at $z = x^3 = 0$, the polarization tensor is completely described by one temporal and two spatial dimensions. For an easier translation into the generally known boundary conditions for the electromagnetic vector potentials it is customary to generalize the polarization tensor to the 4×4 matrix Π with $\Pi^{3\mu} = \Pi^{\mu 3} = 0$.

For the classical boundary conditions (compare Eq. (2.52)) and when considering to the *Ehrenfest theorem* (see Ref. [101] and Eq. (3.18)), the classical current reads

$$\mathbf{j}(\mathbf{q},\omega) \equiv \langle \hat{\mathbf{j}}(\mathbf{q},\omega) \rangle = \underline{\chi}^j(\mathbf{q},\omega) \cdot \mathbf{A}(\mathbf{q},\omega) \equiv \underline{\underline{\Pi}} \cdot \mathbf{A}(\mathbf{q},\omega)\,. \tag{B.12}$$

Here, we additionally have used Eq. (1.80) and the equivalence between the terminus *current-current response function* $\chi^j_{\alpha\beta}$ and the *polarization operator* $\Pi_{\alpha\beta}$.

With this expression for the current j_μ, Maxwell's equations read (compare Eq. (1.63))

$$\frac{1}{4\mu_0}\partial_\mu F^{\mu\nu} + \delta(x^3)\Pi^{\nu\mu}A_\mu = 0\,. \tag{B.13}$$

B The reflection coefficients of a conductive sheet

Reformulating Eq. (2.52d) in terms of the electromagnetic potentials the resulting boundary condition reads (see Ref. [56, 238, 239])

$$A_\mu|_{x^3=0^+} = A_\mu|_{x^3=0^-}\,,$$
$$(\partial_3 A_\mu)|_{x^3=0^+} = -(\partial_3 A_\mu)|_{x^3=0^-} = \Pi_\mu^\nu A_\nu|_{x^3=0}\,. \tag{B.14}$$

With $\mathbf{x} = (x_1, x_2, x_3)^T$, the Cartesian unit vectors $\mathbf{e}_i$, $i \in \{1, 2, 3\}$, the three-dimensional wavevector $\mathbf{q} = (\mathbf{k}, q_3)^T$ and the 2D projection onto the graphene plane $\mathbf{k} = (k_1, k_2)^T \equiv (k_1, k_2)^T$, we can choose the Ansatz (see Ref. [56, 238]) for the *TE mode*

$$\mathbf{E}^{\mathrm{TE}}(\mathbf{q}, \omega) = (-k_2 \mathbf{e}_1 + k_1 \mathbf{e}_2)\frac{\omega}{c}\Psi(x_3)\,, \tag{B.15a}$$

$$\mathbf{H}^{\mathrm{TE}}(\mathbf{q}, \omega) = \mathrm{i}(k_1 \mathbf{e}_1 + k_2 \mathbf{e}_2)\Psi'(x_3) + \mathbf{e}_3(k_1^2 + k_2^2)\Psi(x_3)\,, \tag{B.15b}$$

and for the *TM mode*

$$\mathbf{E}^{\mathrm{TM}}(\mathbf{q}, \omega) = \mathrm{i}(k_1 \mathbf{e}_1 + k_2 \mathbf{e}_2)\Phi'(x_3) + \mathbf{e}_3(k_1^2 + k_2^2)\Phi(x_3)\,, \tag{B.16a}$$

$$\mathbf{H}^{\mathrm{TM}}(\mathbf{q}, \omega) = (k_2 \mathbf{e}_1 - k_1 \mathbf{e}_2)\frac{\omega}{c}\Phi(x_3)\,, \tag{B.16b}$$

omitting the overall factor $\exp{[\mathrm{i}(x^1 k_1 + x^2 k_2 - \omega t)]}$. Above, we introduced the wave functions

$$\Psi(x_3) = \begin{cases} \mathrm{e}^{\mathrm{i}q_3 x^3} + r_g^{\mathrm{TE}}\mathrm{e}^{-\mathrm{i}q_3 x^3}\,, & x^3 < 0 \\ t_g^{\mathrm{TE}}\mathrm{e}^{\mathrm{i}q_3 x^3}\,, & x^3 > 0 \end{cases}\,, \tag{B.17a}$$

$$\Phi(x_3) = \begin{cases} \mathrm{e}^{\mathrm{i}q_3 x^3} + r_g^{\mathrm{TM}}\mathrm{e}^{-\mathrm{i}q_3 x^3}\,, & x^3 < 0 \\ t_g^{\mathrm{TM}}\mathrm{e}^{\mathrm{i}q_3 x^3}\,, & x^3 > 0 \end{cases}\,, \tag{B.17b}$$

distinguishing between the fields above $(>)$ and below $(<)$ the graphene sheet and forward (prefactor in exponential: $+$) and backwards $(-)$ propagating fields.

With algebra analogously to Appendix B.1, the authors of Ref. [56] arrive at the general expression (as in section 2.2.1, $y^2 = \tilde{\omega}^2 - \tilde{v}_\mathrm{F}^2 \mathbf{k}^2$)

$$r_g^{\mathrm{TE}} = \frac{\mathcal{A}}{2\mathrm{i}q_3 - \mathcal{A}}\,, \qquad t_g^{\mathrm{TE}} = \frac{2\mathrm{i}q_3}{2\mathrm{i}q_3 - \mathcal{A}}\,, \tag{B.18}$$

$$r_g^{\mathrm{TM}} = -\frac{q_3(\mathcal{A} - \tilde{v}_\mathrm{F}^2 \mathbf{k}^2 \mathcal{B})}{2\mathrm{i}y^2 - q_3(\mathcal{A} - \tilde{v}_\mathrm{F}^2 \mathbf{k}^2 \mathcal{B})}\,, \qquad t_g^{\mathrm{TM}} = \frac{2\mathrm{i}y^2}{2\mathrm{i}y^2 - q_3(\mathcal{A} - \tilde{v}_\mathrm{F}^2 \mathbf{k}^2 \mathcal{B})}\,. \tag{B.19}$$

By inserting Eq. (2.36) into Eqs. (B.18) and (B.19), Fialkovsky and co-workers arrive in Ref. [56] at the general Eqs. (2.38) and (2.37).

APPENDIX C

Selection Rules of electric and magnetic dipole transitions

Here, we present a discussion of the selection rules for electric and magnetic dipole transitions. These selection rules determine the existence of a transition and determine the polarization of the electromagnetic fields that can couple to the corresponding dipole moment. Thus, they are important to determine when applying the theoretical results presented in this thesis to experimental setups.

C.1 Selection rules of an electric dipole transition

The selection rules for an electric dipole transition depend on the specific electronic structure of the emitter that we use for the experimental realization.

To understand the basis of the selection rules that apply, we will consider "simple" atoms (e.g., hydrogenic atoms, alkali atoms and singly-ionized alkaline earth elements) that can be described by taking only one electron into account. Additionally, we assume that it is valid to describe the electron's wavefunction by a spherical symmetric function

$$\Psi_{nlm_lm_s}(\mathbf{r}) = \psi_{nlm_l}(\mathbf{r})\,\chi(m_s) = R_{nl}(r)Y_l^{m_l}(\theta,\phi)\,\chi(m_s)\,. \tag{C.1}$$

where these wavefunctions are required to be eigenstates

$$\hat{\mathcal{H}}_0\Psi_{nlm_lm_s} = E_n\Psi_{nlm_lm_s}\,. \tag{C.2}$$

of the system's Hamiltonian

$$\hat{\mathcal{H}}_0 = -\frac{\hbar^2}{2m}\Delta + \hat{V}(\hat{\mathbf{r}})$$

with its kinetic part $\frac{\hbar^2}{2m}\Delta$ and the coulomb potential $\hat{V}(\hat{\mathbf{r}})$ containing the electrostatic interaction between several electrons. Since we are only considering spherically-symmetric potentials $\hat{V}(\hat{\mathbf{r}})$, the eigenfunction of the Hamiltonian is naturally also an eigenfunction of the orbital angular momentum operator $\hat{\mathbf{L}}^2$

$$\hat{\mathbf{L}}^2\Psi_{nlm_lm_s} = l(l+1)\Psi_{nlm_lm_s}\,. \tag{C.3}$$

and to its z-component $\hat{\mathbf{L}}_z$

$$\hat{\mathbf{L}}_z\Psi_{nlm_lm_s} = m_l\Psi_{nlm_lm_s}\,. \tag{C.4}$$

C Selection Rules of electric and magnetic dipole transitions

The latter can be understood as a space quantization and can also be directly derived from the fact that $\Psi_{nlm_lm_s}$ are eigenfunctions of the Hamiltonian. Last, the electronic eigenfunctions are also eigenfunctions of the projected spin operator $\hat{\mathbf{S}}_z$ (with eigenvalues $m_s = \pm 1/2$)

$$\hat{\mathbf{S}}_z \Psi_{nlm_lm_s} = m_s \Psi_{nlm_lm_s}\,. \tag{C.5}$$

These four quantum numbers are sufficient to describe hydrogen-like atoms in the absence of a magnetic field that would lift further degeneracies.

The uncoupled representation introduced by the function $\chi(m_s)$ in Eq. (C.1) is motivated by the fact that the electric dipole operator does not couple to the spin and the selection rule for the spin is given as

$$\Delta m_s = m_s - m_s' = 0\,. \tag{C.6}$$

Additionally, we introduced the normalized spherical harmonics[36]

$$Y_l^{m_l}(\theta, \phi) = (-1)^{m_l} \left[\frac{2l+1}{4\pi}\frac{(l-m_l)!}{(l+m_l)!}\right]^{1/2} P_l^{m_l}(\cos\theta)\mathrm{e}^{\mathrm{i}m_l\phi} \tag{C.8}$$

where $P_l^{m_l}(\cos\theta)$ is the associated Legendre polynomial. Furthermore, $R_{nl}(r)$ is the completely real radial wavefunction. Further information on the electron's wavefunction can be found in any quantum mechanics textbook, i.e., Ref. [119].

Following Ref. [119], we can transform the electric dipole operator from Cartesian coordinates $\hat{\mathbf{d}} = e(x\hat{\mathbf{e}}_x + y\hat{\mathbf{e}}_y + z\hat{\mathbf{e}}z)$ into spherical coordinates

$$\hat{\mathbf{d}} = d\left(-\frac{1}{\sqrt{2}}\sin\theta\mathrm{e}^{-\mathrm{i}\phi}\hat{\boldsymbol{\varepsilon}}_{+1} + \cos\theta\hat{\boldsymbol{\varepsilon}}_0 + \frac{1}{\sqrt{2}}\sin\theta\mathrm{e}^{\mathrm{i}\phi}\hat{\boldsymbol{\varepsilon}}_{-1}\right), \tag{C.9}$$

with $|\langle\hat{\mathbf{d}}\rangle| = d = e\sqrt{x^2 + y^2 + z^2}$ and the spherical basis

$$\hat{\boldsymbol{\varepsilon}}_{\pm 1} = \mp\frac{\hat{\mathbf{e}}_x + \mathrm{i}\hat{\mathbf{e}}_y}{\sqrt{2}} \qquad \text{and} \qquad \hat{\boldsymbol{\varepsilon}}_0 = \hat{\mathbf{e}}_z\,. \tag{C.10}$$

For the ϕ-dependence of the matrix elements, we thus obtain

$$\begin{aligned}
e\int \mathrm{d}^3r\,\psi_{n'l'm_l'}^*\hat{\mathbf{r}}\psi_{nlm_l} = &\; a\hat{\boldsymbol{\varepsilon}}_{+1}\int_0^{2\pi}\mathrm{d}\phi\,\mathrm{e}^{\mathrm{i}(m_l-m_l'-1)\phi} \\
&+ b\hat{\boldsymbol{\varepsilon}}_0\int_0^{2\pi}\mathrm{d}\phi\,\mathrm{e}^{\mathrm{i}(m_l-m_l')\phi} + c\hat{\boldsymbol{\varepsilon}}_{-1}\int_0^{2\pi}\mathrm{d}\phi\,\mathrm{e}^{\mathrm{i}(m_l-m_l'+1)\phi},
\end{aligned} \tag{C.11}$$

---

[36]The normalized spherical harmonics can be written explicitly with the three lowest order ones given by

$$Y_0^0(\theta, \phi) = \sqrt{\frac{1}{4\pi}}, \quad Y_1^0(\theta, \phi) = \sqrt{\frac{3}{4\pi}}\cos\theta, \quad \text{and} \quad Y_1^\pm(\theta, \phi) = \mp\sqrt{\frac{3}{8\pi}}\sin\theta\mathrm{e}^{\pm\mathrm{i}\phi}\,. \tag{C.7}$$

with a, b and c integrals solely over r and θ. In consequence, only transitions between states with

$$\Delta m_l = m_l - m'_l = 0, \pm 1 \,, \tag{C.12}$$

are allowed. Here, there are two interesting facts to denote. First, only one of the three integrals on the r.h.s. of Eq. (C.11) is unequal from zero for a given Δm_l. Since the ε_i are a complete set of basis vector in $\mathbb{R}^3$, the electric field can be expanded into the same basis. Then, only the electric field with a component of ε_j couples two states of given Δm_l. When viewing the electric field polarizations ε_j from the z-axis, one realizes that transitions between two states with $\Delta m_l = +1$ are driven by left circular, with $\Delta m_l = -1$ are driven by right circular and with $\Delta m_l = 0$ are driven by linear polarized light.

Second, since $R_{nl}(r)$ and $P_l^{m_l}(\cos\theta)$ are fully real functions (besides from a global phase factor that can be fixed) the phase of the dipole matrix elements $\mathbf{d}_{\uparrow\downarrow}$ in Eq. (3.7a) is determined purely by Δm_l. Considering a state transition that only couples to linear polarized light ($\Delta m_l = 0$), $\mathbf{d}_{\uparrow\downarrow} = \mathbf{d}_{\uparrow\downarrow}^* \in \mathbb{R}$.

Last, we use the necessary requirement that the integrand of the dipole matrix element is even under parity transformation since it otherwise disappears. The radial wavefunction $R_{nl}(r)$ only depends on radius and is thus even, such that the only functions of importance are the spherical harmonics that transform

$$Y_l^{m_l}(\pi - \theta, \phi + \pi) = (-1)^l Y_l^{m_l}(\theta, \phi) \,,$$

with which under parity transformation, we obtain a prefactor $(-1)^{l+l'+1}$. With the reformulation $(-1)^{l+l'-2l'+1} = (-1)^{l-l'+1}$ we find that Δl is required to be odd. Furthermore recalling Eq. (C.9), one realizes that Eq. (C.11) contains the products $Y_{l'}^{-m'}\cos\theta Y_l^m$ and $Y_{l'}^{-m'}\sin\theta Y_l^m$ with (see Ref. [119])

$$\cos\theta\, Y_l^m = Y_{l+1}^m f(l,m) + Y_{l-1}^m g(l,m) \quad \text{and} \quad \sin\theta\, Y_l^m = Y_{l+1}^{m+1}\tilde{f}(l,m) + Y_{l-1}^{m+1}\tilde{g}(l,m) \,.$$

Here, $f(l,m)$, $g(l,m)$, $\tilde{f}(l,m)$ and $\tilde{g}(l,m)$ are real-valued functions of only l and m. Due to the orthogonality of the spherical harmonics, we can conclude

$$\Delta l = l - l' = \pm 1 \,. \tag{C.13}$$

C.2 Selection rules of a magnetic dipole transition

As for the case of electric dipole transitions, selection rules determine whether or not a magnetic dipole transition between two different states is allowed. However, since the two dipole operators differ, the selection rules are also largely different.

In the previous section, we have assumed a spherical symmetric, one electronic, spinless atom (describing, e.g., the electronic states of the alkali metal Rubidium) with a wavefunction $\psi_{nlm_lm_s}(\mathbf{r}) = \langle\mathbf{r}|n,l,m_l,m_s\rangle$. Due to the coupling of the electronic and nuclear spin and angular momentum to each other and to an external magnetic field (cf. section 3.3),he wavefunction $\psi_{nlm_lm_s}(\mathbf{r})$ is replaced by $\psi_{nlifm_f}(\mathbf{r}) = \langle\mathbf{r}|n,l,i,f,m_f\rangle$ under the assumption of a weak external magnetic field.

C Selection Rules of electric and magnetic dipole transitions

For the total orbital momentum operator $\hat{\mathbf{F}} = (\hat{F}_x, \hat{F}_y, \hat{F}_z)^T$ and $\hat{F}_\pm = (\hat{F}_x \pm \hat{F}_y)/\sqrt{2}$, the eigenvalues of the wavefunctions read

$$\hat{F}_\pm \psi_{nlifm_f}(\mathbf{r}) = (m_f \pm 1)\psi_{nlif(m_f \pm 1)}(\mathbf{r}) \qquad \text{and} \qquad \hat{F}_z \psi_{nlifm_f}(\mathbf{r}) = m_f \psi_{nlifm_f}(\mathbf{r})$$

such that the magnetic dipole matrix element $\langle n', l', i', f', m'_f | \hat{\boldsymbol{\mu}} \cdot \mathbf{B}(\mathbf{r}_0, t) | n, l, i, f, m_f \rangle$ is non-vanishing for

$$\Delta m_f = 0, \pm 1 \tag{C.14}$$

where $\Delta m_f = 0$ is valid for $\mathbf{B} \parallel \mathbf{e}_z$ and $\Delta m_f = \pm 1$ for $\mathbf{B} \perp \mathbf{e}_z$. Due to vectorial addition arguments of $\hat{\mathbf{F}}$ (see Ref. [119]), the selection rules are completed by

$$\Delta f = 0, \pm 1, \qquad \text{with a forbidden transition } |f = 0\rangle \nleftrightarrow |f' = 0\rangle. \tag{C.15}$$

APPENDIX D

Details on the modes of the dielectric-graphene-dielectric slab

---

In this Appendix, we present detailed calculations for the computations of some of the modes in a dielectric-graphene-dielectric slab setup as discussed in chapter 4.2.

D.1 Further expressions for the transverse electric (TE) plasmonic mode of graphene embedded in a bulk dielectric

In Eqs. (4.12), we present the parametrized solution $\hat{k}_{\mathrm{p}}[\hat{\tilde{\omega}}]$ for the dispersion relation of the TE plasmonic resonance. This TE plasmonic resonance can also be expressed in terms of the variable $\hat{y}$ where the low and high frequency case are of interest for the calculation of the plasmonic contribution to the decay rate modification of electric and magnetic emitters over a graphene monolayer. Reintroducing $q = \mathrm{atanh}(\hat{y})$ into Eqs. (4.12) leads to

$$\hat{k}_{\mathrm{p}}[\hat{y}] = \frac{1}{\sqrt{1 - \varepsilon_m \tilde{v}_{\mathrm{F}}^2}} \sqrt{\varepsilon_m \hat{y}^2 + \alpha^2 \left(\mathrm{atanh}(\hat{y}) \frac{\hat{y}^2 + 1}{\hat{y}} - 1 \right)^2},$$

$$\hat{\tilde{\omega}}_{\mathrm{p}}[\hat{y}] = \frac{1}{\sqrt{1 - \varepsilon_m \tilde{v}_{\mathrm{F}}^2}} \sqrt{\hat{y}^2 + \alpha^2 \tilde{v}_{\mathrm{F}}^2 \left(\mathrm{atanh}(\hat{y}) \frac{\hat{y}^2 + 1}{\hat{y}} - 1 \right)^2}.$$

From this expression, we can find the variable $\hat{y}_{\mathrm{p}}$ using $\tilde{v}_{\mathrm{F}}^2 \hat{k}^2 = \hat{\tilde{\omega}}^2 - \hat{y}^2$

$$\hat{y}_{\mathrm{p}}^2 = \frac{\hat{\tilde{\omega}}^2}{\hat{\tilde{\omega}}_{\Delta}^2} - \alpha^2 \tilde{v}_{\mathrm{F}}^2 \left[1 - \frac{\hat{y}_{\mathrm{p}}^2 + 1}{\hat{y}_{\mathrm{p}}^2} \mathrm{atanh}(\hat{y}_{\mathrm{p}}) \right]^2 \tag{D.1}$$

Two different cases are of interest: First, we focus on the case $\hat{\tilde{\omega}} > \hat{\tilde{\omega}}_{\Delta}$ ($\hat{y}_{\mathrm{p}} \to 1^-$) for which the approximation

$$\frac{\hat{y}^2 - 1}{\hat{y}^2} \mathrm{atanh}(\hat{y}) \overset{\hat{y} \to 1^-}{\approx} (1 - \hat{y}) \ln \left(\frac{1 - \hat{y}}{2} \right)$$

eventually leads to

$$\hat{y}_{\mathrm{p}} \approx 1 - 2\exp\left[-\left(\frac{\sqrt{\hat{\tilde{\omega}}^2 - \hat{\tilde{\omega}}_\Delta^2}}{\alpha\tilde{v}_{\mathrm{F}}\hat{\tilde{\omega}}_\Delta} + 1\right)\right].\tag{D.2}$$

Equivalently, for the second case $\hat{\tilde{\omega}} < \hat{\tilde{\omega}}_\Delta$ ($\hat{y} \ll 1$) we can approximate

$$\frac{\hat{y}^2 - 1}{\hat{y}^2}\mathrm{atanh}(\hat{y}) \overset{\hat{y}\ll 1}{\approx} \left(\frac{4\alpha\hat{y}^2}{3}\right)^2,$$

leading to

$$\hat{y}_p^2 = \frac{2(\frac{\hat{\tilde{\omega}}}{\hat{\tilde{\omega}}_\Delta})^2}{1 + \sqrt{1 + 4\left(\frac{4\alpha\tilde{v}_{\mathrm{F}}\hat{\tilde{\omega}}}{3\hat{\tilde{\omega}}_\Delta}\right)^2}} \approx \frac{\hat{\tilde{\omega}}^2}{\hat{\tilde{\omega}}_\Delta^2}\left[1 - \left(\frac{4\alpha\tilde{v}_{\mathrm{F}}\hat{\tilde{\omega}}}{3\hat{\tilde{\omega}}_\Delta}\right)^2\right],\tag{D.3}$$

$$\hat{y}_p \approx \frac{\hat{\tilde{\omega}}}{\hat{\tilde{\omega}}_\Delta}\sqrt{1 - \left(\frac{4\alpha\tilde{v}_{\mathrm{F}}\hat{\tilde{\omega}}}{3\hat{\tilde{\omega}}_\Delta}\right)^2} \approx \frac{\hat{\tilde{\omega}}}{\hat{\tilde{\omega}}_\Delta}\left[1 - 8\left(\frac{\alpha\tilde{v}_{\mathrm{F}}\hat{\tilde{\omega}}}{3\hat{\tilde{\omega}}_\Delta}\right)\right],\tag{D.4}$$

where we approximate $\sqrt{1-x} \approx 1 - x/2$ for $x \ll 1$.

D.2 On the non-existence of the transverse magnetic (TM) plasmonic resonance in graphene with a band gap

In this appendix, we give a detailed derivation of the non-existence of TM plasmonic resonances in gapped but undoped graphene. As we discuss in section 4.2.1, the TM plasmonic resonance condition is given as (see Eq. (4.20))

$$-2\hat{y}^2 + \alpha\hat{\Phi}(\hat{y})\hat{\kappa}_m = 0.$$

Here, we can at first glance exclude certain regions of the (k,ω) space as a possible solution space: For $\hat{\tilde{\omega}} > \tilde{v}_{\mathrm{F}}\hat{k}$, $\hat{y}^2 = \hat{\tilde{\omega}}^2 - \tilde{v}_{\mathrm{F}}^2\hat{k}^2 \in \mathbb{R}_+$ while for $\hat{\tilde{\omega}} < \tilde{v}_{\mathrm{F}}\hat{k}$, $\hat{y}^2 \in \mathbb{R}_-$ (see the distinction between the two red regions in Fig. D.1).

In these two regions, we have to distinguish between two different formulations of $\hat{\Phi}(\hat{y})$. In the light red region ($1 > \hat{y}^2 > 0$), we find

$$\hat{\Phi}(\hat{y}) = 2\left[1 - \left(1 + \frac{1}{\hat{y}^2}\right)\hat{y}\,\mathrm{atanh}(\hat{y})\right] < 2\left[1 - \left(1 + \frac{1}{\hat{y}^2}\right)\hat{y}^2\right] = -2\hat{y}^2 < 0,\tag{D.5}$$

where we make use of the fact that $\mathrm{atanh}(\hat{y}) > \hat{y}$. Thus, with $\hat{\kappa}_m > 0$

$$-2\hat{y}^2 + \alpha\hat{\Phi}(\hat{y})\hat{\kappa}_m > 0, \qquad \text{for} \quad \hat{y}^2 > 1,\tag{D.6}$$

D.3 On the existence of damped modes in the propagating region in the case of graphene embedded between two identical dielectric slab waveguides
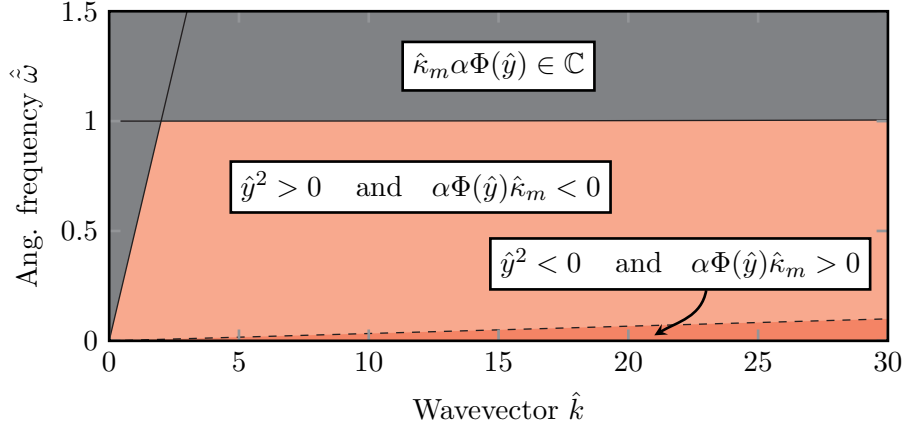

Figure D.1: Above, we display the three different regions that fill the complete $(\hat{k}, \hat{\omega})$ space and due to three different regions forbid the existence of a TM plasmonic resonance due to condition Eq. (4.20). The regions are depicted with the choice $\varepsilon_m = 4.0$.

we find a direct contradiction to Eq. (4.20).

On the other hand, for $\hat{y}^2 = -x^2 < 0$ (dark red region in Fig. D.1), we find

$$\hat{\Phi}(x) = 2\left[1 + \left(1 - \frac{1}{x^2}\right)x\operatorname{atan}(x)\right] > \begin{cases} 2\left[1 + \left(x^2 - 1\right)\left(1 - \frac{x^2}{3}\right)\right] > 2x^2 > 0, \text{ for } x < 1 \\ 2 > 0, \text{ for } x > 1 \end{cases}$$

(D.7)

where we use for $x < 1$ that $\operatorname{atan}(x) > x - x^3/3$. In consequence, in the red regions of Fig. D.1, $\hat{y}^2$ and $\alpha\Phi(\hat{y})\hat{\kappa}_m$ are of opposite sign but for the case of $\hat{y} = 0$.

For the case of $\hat{y} = 0$, we find that r_g^{TM} (see Eq. (2.44)) exhibits a liftable singularity with

$$\lim_{\hat{y}\to 0}\left[r_g^{\text{TM}}\right] = \frac{\hat{\kappa}_0}{2},$$

(D.8)

and thus the solution $\hat{y} = 0$ to Eq. (4.20) does not correspond to a collective excitation of the system.

Last, in the gray region in Fig. D.1, we find that the term $\alpha\Phi(\hat{y})\hat{\kappa}_m \in \mathbb{C}$. Here, in the radiative region $\hat{\kappa}_m \in \mathbb{C}$ while $\alpha\Phi(\hat{y}) \in \mathbb{R}$ and $\hat{y}^2 \in \mathbb{R}$ whereas in the SPE region, $\alpha\Phi(\hat{y}) \in \mathbb{C}$ while $\hat{y}^2 \in \mathbb{R}$ and $\hat{\kappa}_m \in \mathbb{R}$.

Thus, no TM plasmonic mode in the evanescent region (red regions of Fig. D.1) and no real modes in the remaining regions (gray regions of Fig. D.1) exist.

D.3 On the existence of damped modes in the propagating region in the case of graphene embedded between two identical dielectric slab waveguides

In section 4.2.2, we discuss the existence of modes for a layer of graphene embedded between two identical dielectric slab waveguides in the propagating region of the $(\hat{k}, \hat{\tilde{\omega}})$-region $(\hat{\tilde{\omega}} > \hat{k})$. In the following, we show that there exist damped modes which are, however, strongly governed by the properties of the dielectric slab and thus not of particular interest within the scope of this work.

Starting from Eq. (4.25), we find that for any complex logarithm $\log(x) = a + \mathrm{i}b$ and $\hat{q}_{z,m} = \hat{q}'_{z,m} + \mathrm{i}\hat{q}''_{z,m}$ where $\mathrm{Re}\left[\hat{q}_{z,m}\right] = \hat{q}'_{z,m}$ and $\mathrm{Im}\left[\hat{q}_{z,m}\right] = \hat{q}''_{z,m}$

$$\check{d} = \frac{a + \mathrm{i}b}{-2\mathrm{i}\hat{q}_{z,m}} = \frac{a\,\hat{q}''_{z,m} - b\,\hat{q}'_{z,m} + \mathrm{i}(b\,\hat{q}''_{z,m} + a\,\hat{q}'_{z,m})}{2|\hat{q}_{z,m}|^2}\,. \tag{D.9}$$

Assuming that a complex mode $\hat{\tilde{\omega}} = \hat{\tilde{\omega}}' + \mathrm{i}\hat{\tilde{\omega}}''$ (again, $\mathrm{Re}\left[\hat{\tilde{\omega}}\right] = \hat{\tilde{\omega}}'$ and $\mathrm{Im}\left[\hat{\tilde{\omega}}\right] = \hat{\tilde{\omega}}''$) exist for which $\mathrm{Im}\left[\check{d}\right] = 0$, we will show in the following that this necessarily leads to $\check{d} < 0$.

For the definition of the Fourier transform we use in this thesis, Eq. (1.9), a damped mode is comprised of $\hat{\tilde{\omega}}'' < 0$ while $\hat{\tilde{\omega}}' > 0$. With $\hat{k}_{z,m} = \sqrt{\varepsilon_m \hat{\tilde{\omega}}^2 - \hat{k}^2}$ and in the propagating region $\hat{k}'_{z,m} > 0$, we find

$$\hat{q}'_{z,m} = \sqrt{-\frac{\hat{k}^2 - \varepsilon_m(\hat{\tilde{\omega}}')^2 + \varepsilon_m(\hat{\tilde{\omega}}'')^2}{2} + \sqrt{\left[\frac{\hat{k}^2 - \varepsilon_m(\hat{\tilde{\omega}}')^2 + \varepsilon_m(\hat{\tilde{\omega}}'')^2}{2}\right]^2 + (\varepsilon_m \hat{\tilde{\omega}}'\hat{\tilde{\omega}}'')^2}}\,, \tag{D.10}$$

where $\hat{k}^2 - \varepsilon_m(\hat{\tilde{\omega}}')^2 + \varepsilon_m(\hat{\tilde{\omega}}'')^2 < 0$. Thus, always $\hat{q}'_{z,m} > \hat{q}'_{z,0}$.

From $\hat{\tilde{\omega}}'' < 0$, it also automatically follows that $\hat{q}''_{z,m} < 0$.

Then, with these conditions and the demand that Eq. (D.9) be purely real and thus

$$b = \frac{aq'_{z,m}}{q''_{z,m}}\,, \tag{D.11}$$

we find

$$\check{d} = \frac{a}{2q''_{z,m}}\,. \tag{D.12}$$

Thus, we have to determine sign of a to determine the sign (and with this the existence) of the substrate's thickness $\check{d}$. With the relation

$$\mathrm{Re}\left[\log(x)\right] = \frac{1}{2}\log\left(|x|^2\right), \tag{D.13}$$

we have to determine $|x|^2 \gtrless 1$ to find whether $a \gtrless 0$.

With

$$|x| = \frac{|\hat{q}_{z,0} - \hat{q}_{z,m}|}{|\hat{q}_{z,0} + \hat{q}_{z,m}|} \frac{|\alpha\hat{\Phi}(\hat{y}) + 2\mathrm{i}\hat{q}_{z,m}|}{|\alpha\hat{\Phi}(\hat{y}) - 2\mathrm{i}\hat{q}_{z,m}|}, \tag{D.14}$$

and since $\hat{q}'_{z,m} > 0$, $\forall m$ and $\hat{q}''_{z,m} < 0$, $\forall m$ and with this also for $m = 0$, we find that

$$|\hat{q}_{z,0} - \hat{q}_{z,m}| < |\hat{q}_{z,0} + \hat{q}_{z,m}|. \tag{D.15}$$

When first considering dielectric slabs without a graphene monolayer ($\alpha \to 1$), we find

$$|x| = \frac{|\hat{q}_{z,0} - \hat{q}_{z,m}|}{|\hat{q}_{z,0} + \hat{q}_{z,m}|} < 1, \tag{D.16}$$

and with this $a < 0$ and thus indeed a solution

$$\check{d} = \frac{a}{2q''_{z,m}} > 0, \tag{D.17}$$

exists. Thus, for the dielectric slab, damped modes (also known as resonances) always exist.

However, for the case including a graphene monolayer, the situation is more complicated. As shown in Fig. D.2(a,b), we find for all ε_m in the case of $\hat{k} = 0$ (varying $\hat{\tilde{\omega}}$ and thus $\hat{y} = \hat{\tilde{\omega}}$ with $\mathrm{Re}\left[(|\,\hat{y})\right> 0$ and $\mathrm{Im}\left[(|\,\hat{y})\right] < 0)$ that

$$|\alpha\hat{\Phi}(\hat{y}) + 2\mathrm{i}\hat{y}| > |\alpha\hat{\Phi}(\hat{y}) - 2\mathrm{i}\hat{y}|. \tag{D.18}$$

Thus, it is not clear whether $|x| \gtrless 1$. Indeed, when plotting $|x| - 1$ for $\varepsilon_m = 4.0$ and $\varepsilon_m = 10000.0$) in Fig. D.2(d) (for $\alpha = 1$ shown in Fig. D.2(c)), we find that for physically realizable values of ε_m, indeed a damped waveguiding mode exists but for $\hat{y} = 1$ the boundary to the SPE region where $\hat{\Phi}(\hat{y}) \to \infty$.

However, as we show in Fig. D.2(c), the magnitude of α has a strong influence on the existence of a damped waveguide mode. For $\alpha = 1$ almost for now frequency a mode exists. Thus, we conclude that indeed the damped waveguide mode in the propagating region is caused by the dielectric slab and is not due to the graphene monolayer. Its existence would actually even be suppressed if the photon-electron coupling in graphene was be larger.

If the waveguide mode is allowed at $\hat{k} = 0$ for all frequencies at a corresponding thickness, it will definitely also exist for all $\hat{k} < \hat{\tilde{\omega}}$. However, these modes are not of specific interest in this thesis.

D.4 Effective medium model for dielectric-graphene-dielectric slab waveguide

In order to determine the damping of the waveguide modes of a dielectric slab-graphene-dielectric slab waveguide induced in the SPE region, we approximate this waveguide by a slab of effective complex permittivity

$$\varepsilon_{\mathrm{eff}} = \varepsilon_m + \mathrm{i}\varepsilon^{(1)}, \tag{D.19}$$

D Details on the modes of the dielectric-graphene-dielectric slab

with $\varepsilon_m \in \mathbb{R}$. Furthermore, we assume that $\varepsilon^{(1)} \ll \varepsilon$ which seems appropriate considering that the losses in the waveguide are induced via the coupling of the mode to the graphene monolayer that is controlled via the fine structure constant $\alpha \ll 1$.

For such a waveguide, in TE polarization and within the waveguiding region given by $\hat{\tilde{\omega}} < \hat{k} < \sqrt{\varepsilon_{\text{eff}}}\hat{\tilde{\omega}}$ the mode condition reads

$$\sin\left(d\sqrt{\varepsilon_{\text{eff}}\hat{\tilde{\omega}}^2 - \hat{k}^2}\right)(\varepsilon_{\text{eff}}\hat{\tilde{\omega}}^2 - \hat{k}^2) = \sqrt{\varepsilon_{\text{eff}}\hat{\tilde{\omega}}^2 - \hat{k}^2}\sqrt{\hat{k}^2 - \hat{\tilde{\omega}}^2}\cos\left(d\varepsilon_{\text{eff}}\hat{\tilde{\omega}}^2 - \hat{k}^2\right). \quad (\text{D.20})$$

Next, considering the two sides of the equation apart with $\varepsilon_{\text{eff}}\hat{\tilde{\omega}}^2 - \hat{k}^2 = a + \mathrm{i}b$ and $b \ll a$, we find

$$(a + \mathrm{i}b)\sin\left(\sqrt{a + \mathrm{i}b}d\right) = a\sin\left(d\sqrt{a}\right) + \frac{\mathrm{i}}{2}\left[d\sqrt{a}\cos\left(d\sqrt{a}\right) + 2\sin\left(d\sqrt{a}\right)\right]b + \mathcal{O}(b^2),$$

$$\sqrt{a + \mathrm{i}b}\cos\left(\sqrt{a + \mathrm{i}b}d\right) = a\cos\left(d\sqrt{a}\right) + \frac{\mathrm{i}}{2}\left[\frac{\cos\left(d\sqrt{a}\right)}{\sqrt{a}} - d\sin\left(d\sqrt{a}\right)\right]b + \mathcal{O}(b^2).$$

$$(\text{D.21})$$

In order to be able to compare Eq. (D.20) to the respective equation in the case of a dielectric slab-graphene-dielectric slab waveguide

$$\left(\varepsilon_m\hat{\tilde{\omega}}^2 - \hat{k}^2\right)\sin(d\sqrt{\varepsilon_m\hat{\tilde{\omega}}^2 - \hat{k}^2}) - \sqrt{\varepsilon_m\hat{\tilde{\omega}}^2 - \hat{k}^2}\sqrt{\hat{k}^2 - \hat{\tilde{\omega}}^2}\cos\left(d\sqrt{\varepsilon_m\hat{\tilde{\omega}}^2 - \hat{k}^2}\right)$$

$$= \alpha\Phi(\hat{y})\left[\sin\left(d\sqrt{\varepsilon_m\hat{\tilde{\omega}}^2 - \hat{k}^2}\right)\sqrt{\hat{k}^2 - \hat{\tilde{\omega}}^2} + \cos\left(d\sqrt{\varepsilon_m\hat{\tilde{\omega}}^2 - \hat{k}^2}\right)\sqrt{\varepsilon_m\hat{\tilde{\omega}}^2 - \hat{k}^2}\right],$$

$$(\text{D.22})$$

we assume a very tiny damping $\text{Im}\left[\hat{\tilde{\omega}}\right] \ll 1$ and thus neglect $\text{Im}\left[\hat{\tilde{\omega}}\right] \approx 0$. Then by writing $a = \varepsilon_m\hat{\tilde{\omega}}^2 - \hat{k}^2$ and $b = \varepsilon^{(1)}\hat{\tilde{\omega}}^2$, we find for Eq. (D.20)

$$\left(\varepsilon_m\hat{\tilde{\omega}}^2 - \hat{k}^2\right)\sin\left(d\sqrt{\varepsilon_m\hat{\tilde{\omega}}^2 - \hat{k}^2}\right) - \sqrt{\varepsilon_m\hat{\tilde{\omega}}^2 - \hat{k}^2}\sqrt{\hat{k}^2 - \hat{\tilde{\omega}}^2}\cos\left(d\sqrt{\varepsilon_m\hat{\tilde{\omega}}^2 - \hat{k}^2}\right)$$

$$= \frac{\mathrm{i}}{2}\varepsilon^{(1)}\hat{\tilde{\omega}}^2\left[\frac{\cos\left(d\sqrt{\varepsilon_m\hat{\tilde{\omega}}^2 - \hat{k}^2}\right)}{\sqrt{\varepsilon_m\hat{\tilde{\omega}}^2 - \hat{k}^2}}\left(-d(\varepsilon_m\hat{\tilde{\omega}}^2 - \hat{k}^2) + \sqrt{\hat{k}^2 - \hat{\tilde{\omega}}^2}\right)\right.$$

$$\left. - \sin\left(d\sqrt{\varepsilon_m\hat{\tilde{\omega}}^2 - \hat{k}^2}\right)\left(2 + d\sqrt{\hat{k}^2 - \hat{\tilde{\omega}}^2}\right)\right].$$

$$(\text{D.23})$$

Under these assumptions, we can compare the right hand side of Eqs. (D.22) and (D.23) since the left hand side of both equations agree. Then, we find

$$\varepsilon^{(1)} \propto \alpha, \quad (\text{D.24})$$

186

where the damping of the mode is thus proportional to the fine structure constant as stated in the main part of this thesis and in Ref. [W3].
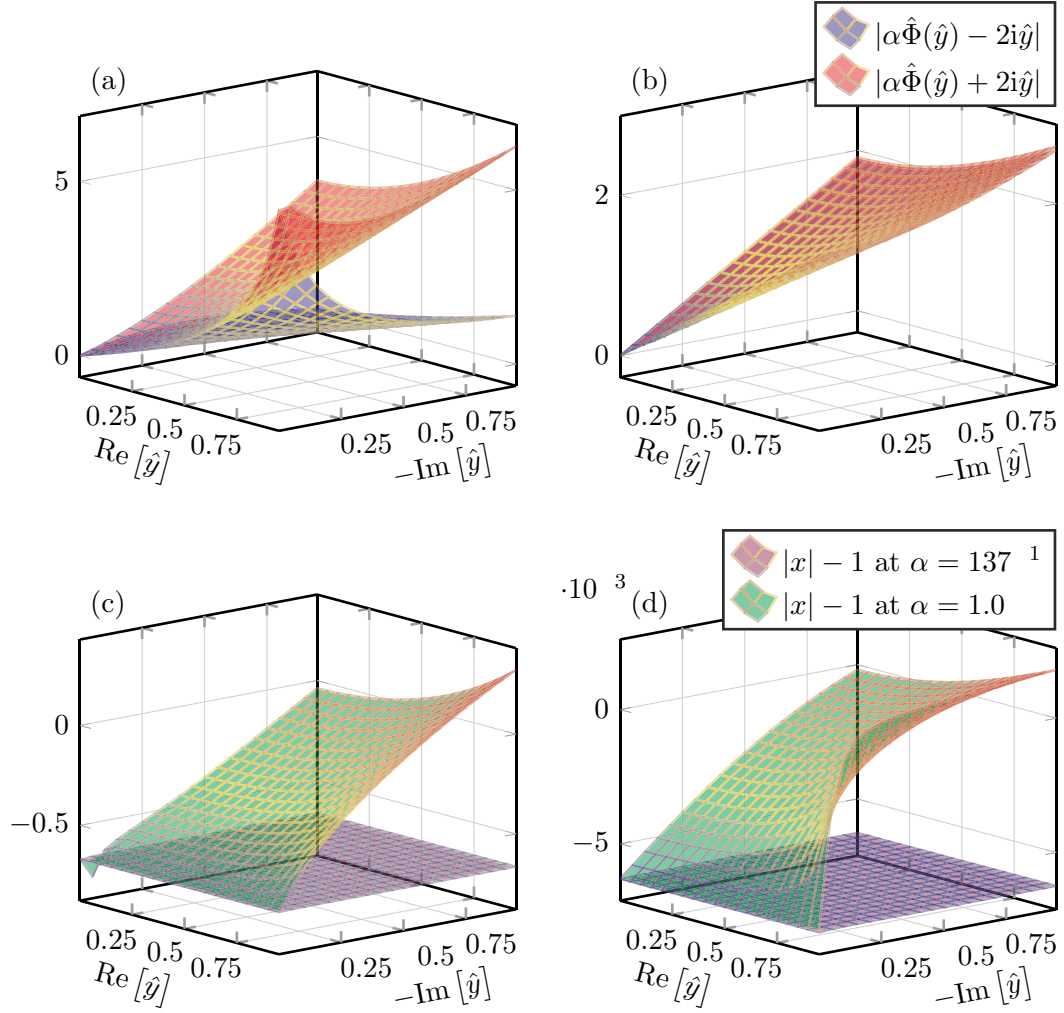
Figure D.2: Comparison of $|\alpha\hat{\Phi}(\hat{y}) \pm 2\mathrm{i}\hat{y}|$ for different complex values $\hat{y}$ and at normal incidence $\hat{k} = 0$. In panel (a), we show the solutions for $\alpha = 1$, while in panel (b), we show the solutions for $\alpha = 137^{-1}$. For all complex $\hat{y}$, we find that $|\alpha\hat{\Phi}(\hat{y}) + 2\mathrm{i}\hat{y}| > |\alpha\hat{\Phi}(\hat{y}) - 2\mathrm{i}\hat{y}|$ where this relation is important for the comparison in Eq. (D.14). In panel (c,d), we show $|x| - 1$ from Eq. (D.14) for different values of α and $\varepsilon_m = 4.0$ (c) and $\varepsilon_m = 10000$ (d), respectively.

APPENDIX E

Fitting the conductivity of graphene

The following appendix describes the fitting procedure of the frequency dependent conductivity of graphene at finite temperature and with finite chemical potential. We make use of the fitted functions in order to transform the frequency dependent conductivity into a time dependent ADE. This appendix is adapted from the appendix of Ref. [W7].

As discussed in Sec. 5.5, the real part of the interband conductivity of graphene Eq. (2.65) can be described analytically when assuming $\Gamma \to 0$. Since we fit the interband conductivity of graphene with two critical point conductivities (cf. Eq. (5.39)), we present the real part of this critical point conductivity

$$
\mathrm{Re}\left[\sigma_{\mathrm{CP}}(\omega)\right] = 2A_m\Omega_m\omega^2 \frac{-\sin(\phi_m)\omega^2 + \sin(\phi_m)\left(\Omega_m^2 - \Gamma_m^2\right) + 2\cos(\phi_m)\Gamma_m\Omega_m}{\omega^4 + 2\left(\Gamma_m^2 - \Omega_m^2\right)\omega^2 + \left(\Omega_m^2 + \Gamma_m^2\right)^2} \,.
\tag{E.1}
$$

In analogy to Ref. [192], we introduce the variable $\sqrt{x} = \frac{\omega}{2k_{\mathrm{B}}T}$ and rewrite

$$
\mathrm{Re}\left[\sigma_{\mathrm{CP}}(x)\right] = \frac{A + Bx}{C + Dx + x^2}x \,.
$$

With this we find

$$
\begin{aligned}
\Omega_m &= 2k_{\mathrm{B}}T\sqrt{\frac{\sqrt{C}}{2} - \frac{D}{4}} \,, \\
\Gamma_m &= 2k_{\mathrm{B}}T\sqrt{\frac{\sqrt{C}}{2} + \frac{D}{4}} \,, \\
\phi_m &= -\arctan\left(B\sqrt{\frac{4C - D^2}{2A - BD}}\right) \,, \\
A_m &= \frac{e^2}{8k_{\mathrm{B}}T\hbar}\frac{-B}{\sin(\phi_m)\sqrt{2\sqrt{C} - D}} \,.
\end{aligned}
\tag{E.2}
$$

Additionally, the intraband conductivity $\sigma_{\mathrm{intra}}(\omega)$, Eq. (2.64), is modeled by a Drude

E Fitting the conductivity of graphene

pole, relating

$$\omega_{\text{Drude}} = \sqrt{\frac{2k_{\text{B}}Te^2}{\hbar\pi} \ln\left(2\cosh\left(\frac{\mu}{2k_{\text{B}}T}\right)\right)}. \qquad (\text{E.3})$$

Oblique incidence: error on test computations

In section 5.6, we introduce the concept of oblique incidence calculations within our time-domain Maxwell solver, the DGTD. This method is tested against analytical solutions in section 5.6.3 where we only present absolute values. The errors on the computation we present in this appendix.
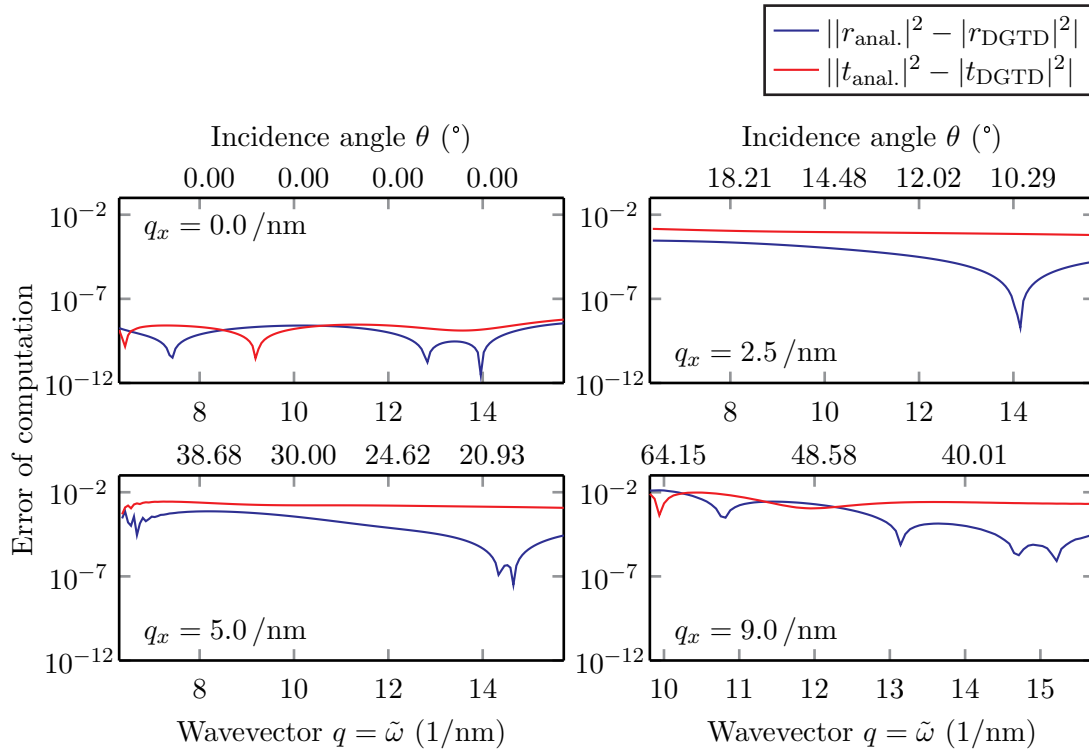

Figure F.1: Error for three-dimensional TM transmittance and reflectance for a dielectric slab ($\varepsilon = 2.25$ and thickness $d = 0.15\,\mathrm{nm}$) under different Bloch boundary conditions. The errors correspond to the absolute difference between analytical and DGTD computed results as presented in Fig. 5.12.
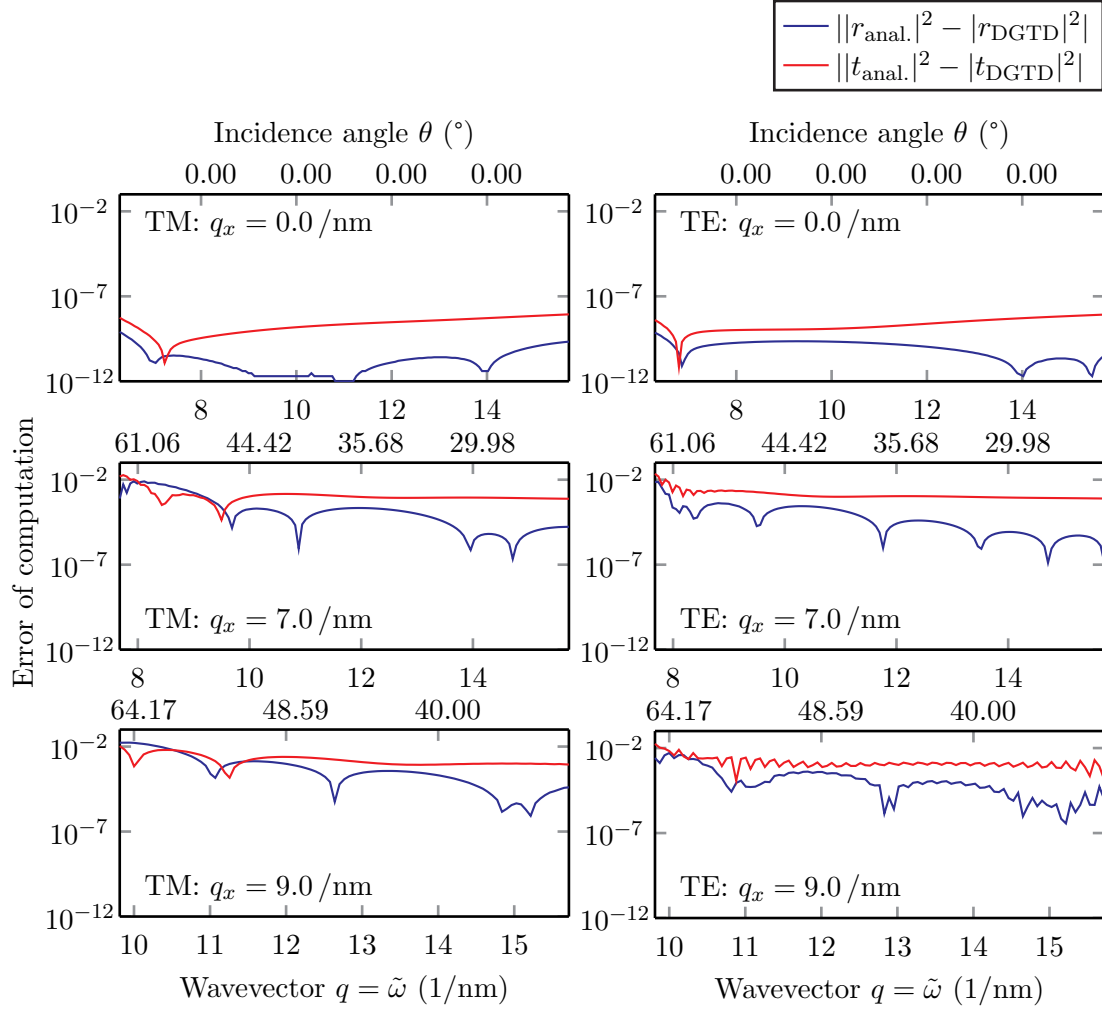
Figure F.2: Error for two-dimensional TE and TM transmittance and reflectance for a dielectric slab ($\varepsilon = 2.25$ and thickness $d = 0.15\,\text{nm}$) under different Bloch boundary conditions. The errors correspond to the absolute difference between analytical and DGTD computed results as presented in Fig. 5.13.

Publications in peer-reviewed journals

W1. J. F. M. Werra, P. Longo and K. Busch, "Spectra of coherent on–resonant light pulses interacting with a two–level atom in a waveguide", Phys. Rev. A **87,** 063821 (2013).

W2. A. W. Schell, P. Engel, J. F. M. Werra, C. Wolff, K. Busch and O. Benson, "Scanning single quantum emitter fluorescence lifetime imaging: quantitative analysis of the local density of photonic states", Nano Lett. **14,** 2623 (2014).

W3. J. F. M. Werra, F. Intravaia and K. Busch, "TE resonances in graphene-dielectric structures", J. Opt. **18,** 034001 (2016).

W4. J. F. M. Werra, P. Krüger, K. Busch and F. Intravaia, "Determining graphene's induced band gap with magnetic and electric emitters", Phys. Rev. B **93,** 081404(R) (2016).

W5. T. Pfadler, T. Kiel, M. Stärk, J. F. M. Werra, C. Matyssek, D. Sommer, J. Boneberg, K. Busch, J. Weickert and L. Schmidt-Mende, "Structure-induced Resonant Tail-State Regime Absorption in Polymer:Fullerene Bulk-Heterojunction Solar Cells", Phys. Rev. B **93,** 205305 (2016).

W6. J. F. M. Werra and K. Busch, "The self-consistent emitter in the discontinuous Galerkin time-domain method", (to be submitted).

Conference proceedings

W7. J. F. M. Werra, C. Wolff, C. Matyssek and K. Busch, "Current sheets in the Discontinuous Galerkin Time-Domain method: an application to graphene", Proc. SPIE Optics+Optoelectronics **95020,** 95020E (2015).

Oral presentations

W8. J. F. M. Werra, C. Wolff and K. Busch, "Computing the projected Local Density of States in anisotropic systems", SFB HIOS Young Researcher Workshop (2013).

W9. J. F. M. Werra, A. W. Schell, P. Engel, C. Wolff, O. Benson and K. Busch, "Probing the local density of states in nano-photonic systems: a numerical discussion", DPG Spring Meeting, Dresden (2014).

W10. J. F. M. Werra, "Detecting the properties of strained graphene utilizing magnetic and electric emitters", University of Nottingham (2015).

W11. J. F. M. Werra, F. Intravaia and K. Busch, "Detecting TE plasmons and bandgaps in strained graphene: atoms as a universal probe", COST MP1403 ESR Workshop (2015).

W12. J. F. M. Werra, F. Intravaia and K. Busch, "On the existence of TE resonances in graphene-dielectric structures", DPG Spring Meeting, Hannover (2016).

Poster presentations

W13. J. F. M. Werra, P. Longo and K. Busch, "Wavepacket dynamics of coherent states in waveguiding structures coupled to a quantum emitter", DPG Spring Meeting, Berlin (2012).

W14. J. F. M. Werra, P. Longo and K. Busch, "Wavepacket dynamics of coherent states in waveguiding structures coupled to a quantum emitter", 500. Wilhelm-Else-Heraeus-Seminar: Frontiers of Quantum Optics (2012).

W15. J. F. M. Werra, F. Intravaia and K. Busch, "Probing strained graphene through the dynamics of electric and magnetic emitters", 600. Wilhelm-Else-Heraeus-Seminar: Frontiers of Quantum Optics (2015).

W16. J. F. M. Werra, F. Intravaia and K. Busch, "Probing strained graphene through the dynamics of electric and magnetic emitters", Graphene Study (2016).

Supervised theses

T1. F. L. Bierbüße, *Der selbstkonsistente Dipol: Zerfalls- und Abstrahlcharakteristika im Rahmen des unstetigen Galerkin-Verfahrens*, Bachelor thesis (Humboldt-Universität zu Berlin, 2014).

T2. C. Gryzik, *(working title) Finite size effects of graphene on emitters closeby*, Master thesis (Humboldt-Universität zu Berlin, hand-in date: March 2017).

Bibliography

1. S. W. Hell and J. Wichmann, "Breaking the diffraction resolution limit by stimulated emission: stimulated-emission-depletion fluorescence microscopy", Opt. Lett. **19,** 780 (1994).

2. S. W. Hell and M. Kroug, "Ground-state-depletion fluorscence microscopy: A concept for breaking the diffraction resolution limit", Appl. Phys. B **60,** 495 (1995).

3. S. W. Hell, M. Dyba and S. Jakobs, "Concepts for nanoscale resolution in fluorescence microscopy", Current opinion in neurobiology **14,** 599 (2004).

4. H. Knobloch, H. Brunner, A. Leitner, F. Aussenegg and W. Knoll, "Probing the evanescent field of propagating plasmon surface polaritons by fluorescence and Raman spectroscopies", The Journal of chemical physics **98,** 10093 (1993).

5. D. J. Arndt-Jovin, M. Robert-Nicoud, S. J. Kaufman and T. M. Jovin, "Fluorescence digital imaging microscopy in cell biology", Science **230,** 247 (1985).

6. G. Marriott, R. M. Clegg, D. J. Arndt-Jovin and T. M. Jovin, "Time resolved imaging microscopy. Phosphorescence and delayed fluorescence imaging.", Biophys. J. **60,** 1374 (1991).

7. M. Bruchez, M. Moronne, P. Gin, S. Weiss and A. P. Alivisatos, "Semiconductor nanocrystals as fluorescent biological labels", Science **281,** 2013 (1998).

8. M. Gierling, P. Schneeweiss, G. Visanescu, P. Federsel, M. Häffner, D. P. Kern, T. E. Judd, A. Günther and J. Fortágh, "Cold-atom scanning probe microscopy", Nature Nanotech. **6,** 446 (2011).

9. K. Suenaga and M. Koshino, "Atom-by-atom spectroscopy at graphene edge", Nature **468,** 1088 (2010).

10. J. Chen, M. Badioli, P. Alonso-González, S. Thongrattanasiri, F. Huth, J. Osmond, M. Spasenović, A. Centeno, A. Pesquera, P. Godignon, *et al.,* "Optical nano-imaging of gate-tunable graphene plasmons", Nature **487,** 77 (2012).

11. W. Kort-Kamp, B. Amorim, G. Bastos, *et al.,* "Active magneto-optical control of spontaneous emission in graphene", Phys. Rev. B **92,** 205415 (2015).

12. K. Tielrooij, L. Orona, A. Ferrier, M. Badioli, G. Navickaite, S. Coop, S. Nanot, B. Kalinic, T. Cesca, L. Gaudreau, *et al.,* "Electrical control of optical emitter relaxation pathways enabled by graphene", Nature Phys. **11,** 281 (2015).

13. A. Huck and U. L. Andersen, "Coupling single emitters to quantum plasmonic circuits", Nanophotonics **5,** 483 (2016).

Bibliography

14. D. E. Chang, A. S. Sørensen, P. R. Hemmer and M. D. Lukin, "Quantum Optics with Surface Plasmons", Phys. Rev. Lett. **97,** 053002 (2006).

15. S. Sengupta, V. N. Kotov and D. P. Clougherty, "Infrared dynamics of cold atoms on hot graphene membranes", Phys. Rev. B **93,** 235437 (2016).

16. G. A. Sinuco-León, K. A. Burrows, A. S. Arnold and B. M. Garraway, "Inductively guided circuits for ultracold dressed atoms", Nature Commun. **5,** 5289 (2014).

17. J. L. O'Brien, A. Furusawa and J. Vučković, "Photonic quantum technologies", Nature Photon. **3,** 687 (2009).

18. A. Politi, J. C. Matthews and J. L. O'Brien, "Shor's quantum factoring algorithm on a photonic chip", Science **325,** 1221 (2009).

19. J. L. O'Brien, "Optical quantum computing", Science **318,** 1567 (2007).

20. J. B. Spring, B. J. Metcalf, P. C. Humphreys, W. S. Kolthammer, X.-M. Jin, M. Barbieri, A. Datta, N. Thomas-Peter, N. K. Langford, D. Kundys, *et al.,* "Boson sampling on a photonic chip", Science **339,** 798 (2013).

21. P. Longo, P. Schmitteckert and K. Busch, "Few-Photon Transport in Low-Dimensional Systems: Interaction-Induced Radiation Trapping", Phys. Rev. Lett. **104,** 023602 (2010).

22. "Birth of the programmable optical chip", Nature Photon. **10,** 1 (2016).

23. F. H. Koppens, D. E. Chang and F. J. G. de Abajo, "Graphene plasmonics: a platform for strong light–matter interactions", Nano Lett. **11,** 3370 (2011).

24. L. Bergmann, *New Emitters for OLEDs: The Coordination-and Photo-Chemistry of Mononuclear Neutral Copper (I) Complexes* (Logos Verlag Berlin GmbH, 2016).

25. G. J. Hedley, A. Ruseckas and I. D. Samuel, "Ultrafast intersystem crossing in a red phosphorescent iridium complex", J. Phys. Chem. A **113,** 2 (2008).

26. M. P. Busson, B. Rolly, B. Stout, N. Bonod and S. Bidault, "Accelerated single photon emission from dye molecule-driven nanoantennas assembled on DNA", Nature Commun. **3,** 962 (2012).

27. J. D. Jackson, *Classical Electrodynamics* (Wiley, New York, 1999).

28. L. Novotny and B. Hecht, *Principles of Nano-Optics* , 2nd ed. (Cambridge University Press, 2012).

29. A. I. Akhiezer and V. B. Berestetskii, *Quantum Electrodynamics* (Interscience Publishers, 1965).

30. A. Altland and B. Simons, *Condensed Matter Field Theory* (Cambridge Univ. Press, 2007).

31. G. D. Mahan, *Many-Particle Physics* (Plenum Press, 1990).

32. L. D. Landau and E. M. Lifshitz, *Lehrbuch der theoretischen Physik 1: Mechanik* (Akademie Verlag, 2011).

33. W. Greiner and J. Reinhardt, *Field quantization : with 52 worked examples and problems* (Springer, Berlin, 1996).

34. P. Nozières and D. Pines, *The theory of quantum liquids* (Perseus Books, Cambridge, Mass., 1999).

35. G. Giuliani and G. Vignale, *Quantum theory of the electron liquid*, 1. publ. (Cambridge Univ. Press, Cambridge, 2005).

36. S. A. Maier, *Plasmonics: fundamentals and applications* (Springer Science & Business Media, 2007).

37. S. A. Maier and H. A. Atwater, "Plasmonics: Localization and guiding of electromagnetic energy in metal/dielectric structures", J. Appl. Phys. **98,** 011101 (2005).

38. P. J. Feibelman, "Surface electromagnetic fields", Progress in Surface Science **12,** 287 (1982).

39. A. V. Zayats and I. I. Smolyaninov, "Near-field photonics: surface plasmon polaritons and localized surface plasmons", J. Opt. A: Pure Appl Opt **5,** S16 (2003).

40. W. Li, M. Zhao, X. Zhao, Y. Xia and Y. Mu, "Hydrogen saturation stabilizes vacancy-induced ferromagnetic ordering in graphene", Phys. Chem. Chem. Phys. **12,** 13699 (2010).

41. P. Wallace, "The band theory of graphite", Phys. Rev. **71,** 622 (1947).

42. A. C. Neto, F. Guinea, N. Peres, K. Novoselov and A. Geim, "The electronic properties of graphene", Rev. Mod. Phys. **81,** 109 (2009).

43. N. D. Mermin, "Crystalline Order in Two Dimensions", Phys. Rev. **176,** 250 (1968).

44. K. Novoselov, A. K. Geim, S. Morozov, D. Jiang, Y. Zhang, S. Dubonos, I. Grigorieva and A. Firsov, "Electric field effect in atomically thin carbon films", Science **306,** 666 (2004).

45. J. C. Meyer, A. K. Geim, M. Katsnelson, K. Novoselov, T. Booth and S. Roth, "The structure of suspended graphene sheets", Nature **446,** 60 (2007).

46. A. Fasolino, J. Los and M. Katsnelson, "Intrinsic ripples in graphene", Nature Mater. **6,** 858 (2007).

47. R. S. Deacon, K.-C. Chuang, R. J. Nicholas, K. S. Novoselov and A. K. Geim, "Cyclotron resonance study of the electron and hole velocity in graphene monolayers", Phys. Rev. B **76,** 081406(R) (2007).

48. V. Gusynin, S. Sharapov and J. Carbotte, "AC conductivity of graphene: from tight-binding model to 2+ 1-dimensional quantum electrodynamics", Int. J. Mod. Phys. B **21,** 4611 (2007).

49. I. F. Herbut, "Interactions and Phase Transitions on Graphene's Honeycomb Lattice", Phys. Rev. Lett. **97,** 146401 (2006).

50. Y. Zhang, T.-T. Tang, C. Girit, Z. Hao, M. C. Martin, A. Zettl, M. F. Crommie, Y. R. Shen and F. Wang, "Direct observation of a widely tunable bandgap in bilayer graphene", Nature **459,** 820 (2009).

Bibliography

51. K. F. Mak, C. H. Lui, J. Shan and T. F. Heinz, "Observation of an Electric-Field-Induced Band Gap in Bilayer Graphene by Infrared Spectroscopy", Phys. Rev. Lett. **102,** 256405 (2009).

52. M. C. S. Escaño, T. Q. Nguyen and H. Kasai, "Analysis of band gap formation in graphene by Si impurities: Local bonding interaction rules", Chem. Phys. Lett. **515,** 85 (2011).

53. G. Giovannetti, P. A. Khomyakov, G. Brocks, P. J. Kelly and J. van den Brink, "Substrate-induced band gap in graphene on hexagonal boron nitride: Ab initio density functional calculations", Phys. Rev. B **76,** 073103 (2007).

54. J. Jung, A. M. DaSilva, A. H. MacDonald and S. Adam, "Origin of band gaps in graphene on hexagonal boron nitride", Nature Commun. **6,** 6308 (2015).

55. F. Schwabl, *Quantenmechanik für Fortgeschrittene* (Springer, Berlin, 1997).

56. I. V. Fialkovsky, V. N. Marachevsky and D. V. Vassilevich, "Finite-temperature Casimir effect for graphene", Phys. Rev. B **84,** 035446 (2011).

57. M. Bordag, G. L. Klimchitskaya, V. M. Mostepanenko and V. M. Petrov, "Quantum field theoretical description for the reflectivity of graphene", Phys. Rev. D **91,** 045037 (2015).

58. J. Schwinger, "On gauge invariance and vacuum polarization", Phys. Rev. **82,** 664 (1951).

59. A. Dobado, A. Gómez-Nicola, A. L. Maroto and J. R. Peláez, *Effective Lagrangians for the Standard Model* (Springer, 1997).

60. C. S. Withers and S. Nadarajah, "log det A= tr log A", International Journal of Mathematical Education in Science and Technology **41,** 1121 (2010).

61. R. Dashen, "Chiral SU(3)$\bigotimes$SU(3) as a Symmetry of the Strong Interactions", Phys. Rev. **183,** 1245 (1969).

62. F. Mandl and G. Shaw, *Quantum field theory* (John Wiley & Sons, 2010).

63. M. Bordag and I. G. Pirozhenko, "Surface plasmons for doped graphene", Phys. Rev. D **91,** 085038 (2015).

64. V. P. Gusynin and S. G. Sharapov, "Transport of Dirac quasiparticles in graphene: Hall and optical conductivities", Phys. Rev. B **73,** 245411 (2006).

65. V. Zeitlin, "QED$_{2+1}$ with nonzero fermion density and the quantum Hall effect", Phys. Lett. B **352,** 422 (1995).

66. G. Klimchitskaya, U. Mohideen and V. Mostepanenko, "Theory of the Casimir interaction from graphene-coated substrates using the polarization tensor and comparison with experiment", Phys. Rev. B **89,** 115419 (2014).

67. T. Stauber, N. M. R. Peres and A. K. Geim, "Optical conductivity of graphene in the visible region of the spectrum", Phys. Rev. B **78,** 085432 (2008).

68. T. W. Appelquist, M. Bowick, D. Karabali and L. C. R. Wijewardhana, "Spontaneous chiral-symmetry breaking in three-dimensional QED", Phys. Rev. D **33,** 3704 (1986).

69. M. Chaichian, G. L. Klimchitskaya, V. M. Mostepanenko and A. Tureanu, "Thermal Casimir-Polder interaction of different atoms with graphene", Phys. Rev. A **86,** 012515 (2012).

70. M. Bordag, I. V. Fialkovsky, D. M. Gitman and D. V. Vassilevich, "Casimir interaction between a perfect conductor and graphene described by the Dirac model", Phys. Rev. B **80,** 245406 (2009).

71. M. Bordag and I. G. Pirozhenko, "Transverse-electric surface plasmon for graphene in the Dirac equation model", Phys. Rev. B **89,** 035421 (2014).

72. I. Fialkovsky and D. Vassilevich, "Quantum Field Theory in Graphene", Int. J. Mod. Phys. A **27,** 1260007 (2012).

73. E. Gorbar, V. Gusynin, V. Miransky and I. Shovkovy, "Magnetic field driven metal-insulator phase transition in planar systems", Phys. Rev. B **66,** 045108 (2002).

74. J. González, F. Guinea and M. Vozmediano, "Non-Fermi liquid behavior of electrons in the half-filled honeycomb lattice (A renormalization group approach)", Nucl. Phys. B **424,** 595 (1994).

75. R. Nair, P. Blake, A. Grigorenko, K. Novoselov, T. Booth, T. Stauber, N. Peres and A. Geim, "Fine structure constant defines visual transparency of graphene", Science **320,** 1308 (2008).

76. T. Ando, Y. Zheng and H. Suzuura, "Dynamical conductivity and zero-mode anomaly in honeycomb lattices", J. Phys. Soc. Jpn. **71,** 1318 (2002).

77. V. P. Gusynin, S. G. Sharapov and J. P. Carbotte, "Unusual Microwave Response of Dirac Quasiparticles in Graphene", Phys. Rev. Lett. **96,** 256802 (2006).

78. M. Jablan, H. Buljan and M. Soljačić, "Plasmonics in graphene at infrared frequencies", Phys. Rev. B **80,** 245435 (2009).

79. G. Klimchitskaya, V. Mostepanenko and B. E. Sernelius, "Two approaches for describing the Casimir interaction in graphene: Density-density correlation function versus polarization tensor", Phys. Rev. B **89,** 125407 (2014).

80. B. E. Sernelius, "Retarded interactions in graphene systems", Phys. Rev. B **85,** 195427 (2012).

81. I. Meric, M. Y. Han, A. F. Young, B. Ozyilmaz, P. Kim and K. L. Shepard, "Current saturation in zero-bandgap, top-gated graphene field-effect transistors", Nature Nanotech. **3,** 654 (2008).

82. A. Lherbier, X. Blase, Y.-M. Niquet, F. Triozon and S. Roche, "Charge Transport in Chemically Doped 2D Graphene", Phys. Rev. Lett. **101,** 036808 (2008).

83. X. Wang, X. Li, L. Zhang, Y. Yoon, P. K. Weber, H. Wang, J. Guo and H. Dai, "N-doping of graphene through electrothermal reactions with ammonia", Science **324,** 768 (2009).

84. Y. Shao, S. Zhang, M. H. Engelhard, G. Li, G. Shao, Y. Wang, J. Liu, I. A. Aksay and Y. Lin, "Nitrogen-doped graphene and its electrochemical applications", J. Mater. Chem. **20,** 7491 (2010).

Bibliography

85. L. S. Panchakarla, K. S. Subrahmanyam, S. K. Saha, A. Govindaraj, H. R. Krishnamurthy, U. V. Waghmare and C. N. R. Rao, "Synthesis, structure, and properties of boron-and nitrogen-doped graphene", Adv. Mater. **21,** 4726 (2009).

86. H. Liu, Y. Liu and D. Zhu, "Chemical doping of graphene", J. Mater. Chem. **21,** 3335 (2011).

87. L. Falkovsky and A. Varlamov, "Space-time dispersion of graphene conductivity", Eur. Phys. J. B **56,** 281 (2007).

88. I. V. Iorsh, I. S. Mukhin, I. V. Shadrivov, P. A. Belov and Y. S. Kivshar, "Hyperbolic metamaterials based on multilayer graphene structures", Phys. Rev. B **87,** 075416 (2013).

89. F. J. García de Abajo, "Graphene plasmonics: Challenges and opportunities", ACS Photon. **1,** 135 (2014).

90. T. Winzer, A. Knorr and E. Malic, "Carrier multiplication in graphene", Nano Lett. **10,** 4839 (2010).

91. D. Brida, A. Tomadin, C. Manzoni, *et al.,* "Ultrafast collinear scattering and carrier multiplication in graphene", Nature Commun. **4,** 1987 (2013).

92. T. Plötzing, T. Winzer, E. Malic, D. Neumaier, A. Knorr and H. Kurz, "Experimental Verification of Carrier Multiplication in Graphene", Nano Lett. **14,** 5371 (2014).

93. L. Allen and J. H. Eberly, *Optical Resonance and Two-Level Atoms* (Dover Publ., New York, 1987).

94. R. Folman, P. Krüger, J. Schmiedmayer, J. Denschlag and C. Henkel, "Microscopic atom optics: from wires to an atom chip", Adv. At. Mol. Opt. Phys. **48,** 263 (2002).

95. T. S. Stein, J. P. Carrico, E. Lipworth and M. C. Weisskopf, "Permanent Electric Dipole Moment of the Cesium Atom. An Upper Limit to the Electric Dipole Moment of the Electron", Phys. Rev. **186,** 39 (1969).

96. B. Graner, Y. Chen, E. G. Lindahl and B. R. Heckel, "Reduced Limit on the Permanent Electric Dipole Moment of ^{199}Hg", Phys. Rev. Lett. **116,** 161601 (2016).

97. J. Wolters, *Integrated Quantum Hybrid Systems* (Pan Stanford, 2015).

98. F. Jelezko and J. Wrachtrup, "Single defect centres in diamond: A review", phys. stat. sol. (a) **203,** 3207 (2006).

99. C. Kurtsiefer, S. Mayer, P. Zarda and H. Weinfurter, "Stable solid-state source of single photons", Phys. Rev. Lett. **85,** 290 (2000).

100. M. W. Doherty, N. B. Manson, P. Delaney, F. Jelezko, J. Wrachtrup and L. C. Hollenberg, "The nitrogen-vacancy colour centre in diamond", Phys. Rep. **528,** 1 (2013).

101. P. Ehrenfest, "Bemerkung über die angenäherte Gültigkeit der klassischen Mechanik innerhalb der Quantenmechanik", Z. Phys. **45,** 455 (1927).

102. M. Moeferdt, P. Schmitteckert and K. Busch, "Correlated photons in one-dimensional waveguides", Opt. Lett. **38,** 3693 (2013).

103. M. P. Schneider, T. Sproll, C. Stawiarski, P. Schmitteckert and K. Busch, "Green's-function formalism for waveguide QED applications", Phys. Rev. A **93,** 013828 (2016).

104. N. Vats, S. John and K. Busch, "Theory of fluorescence in photonic crystals", Phys. Rev. A **65,** 043808 (2002).

105. J. F. M. Werra, *Analysis of Spectral Properties of Coherent Light Pulses in a Waveguide with Side–Coupled Two–Level System*, Diplomarbeit (Karlsruhe Institut für Technologie, 2012).

106. V. Weisskopf and E. Wigner, "Berechnung der natürlichen Linienbreite auf Grund der Diracschen Lichttheorie", Z. Phys. **63,** 54 (1930).

107. V. S. Vladimirov, *Equations of mathematical physics* (New York, 1971).

108. S. Scheel, L. Knöll and D.-G. Welsch, "Spontaneous decay of an excited atom in an absorbing dielectric", Phys. Rev. A **60,** 4094 (1999).

109. J. Knoester and S. Mukamel, "Intermolecular forces, spontaneous emission, and superradiance in a dielectric medium: Polariton-mediated interactions", Phys. Rev. A **40,** 7065 (1989).

110. R. J. Glauber and M. Lewenstein, "Quantum optics of dielectric media", Phys. Rev. A **43,** 467 (1991).

111. S. Scheel, L. Knöll, D.-G. Welsch and S. M. Barnett, "Quantum local-field corrections and spontaneous decay", Phys. Rev. A **60,** 1590 (1999).

112. P. de Vries and A. Lagendijk, "Resonant Scattering and Spontaneous Emission in Dielectrics: Microscopic Derivation of Local-Field Effects", Phys. Rev. Lett. **81,** 1381 (1998).

113. C.-K. Duan, M. F. Reid and Z. Wang, "Local field effects on the radiative lifetime of emitters in surrounding media: Virtual-or real-cavity model?", Phys. Lett. A **343,** 474 (2005).

114. D. Steck, *URL: http://steck.us/alkalidata/rubidium87numbers.pdf* (retrieved on: 2016/04/21).

115. H. Haakh, F. Intravaia, C. Henkel, S. Spagnolo, R. Passante, B. Power and F. Sols, "Temperature dependence of the magnetic Casimir-Polder interaction", Phys. Rev. A **80,** 062905 (2009).

116. H. R. Haakh, *Fluctuation-Mediated Interactions of Atoms and Surfaces on a Mesoscopic Scale*, PhD thesis (Universität Potsdam, 2012).

117. J. Reichel, W. Hänsel and T. W. Hänsch, "Atomic Micromanipulation with Magnetic Surface Traps", Phys. Rev. Lett. **83,** 3398 (1999).

118. S. Wildermuth, P. Krüger, C. Becker, M. Brajdic, S. Haupt, A. Kasper, R. Folman and J. Schmiedmayer, "Optimized magneto-optical trap for experiments with ultracold atoms near surfaces", Phys. Rev. A **69,** 030901 (2004).

119. A. Corney, *Atomic and Laser Spectroscopy* (Oxford Science Pub, 1977).

120. T. Esslinger, I. Bloch and T. W. Hänsch, "Bose-Einstein condensation in a quadrupole-Ioffe-configuration trap", Phys. Rev. A **58,** R2664 (1998).

Bibliography

121. J. Fortágh and C. Zimmermann, "Magnetic microtraps for ultracold atoms", Rev. Mod. Phys. **79,** 235 (2007).

122. S. Earnshaw, "On the nature of the molecular forces which regulate the constitution of the luminiferous ether", Trans. Camb. Phil. Soc **7,** 97 (1842).

123. M. S. Yoon, *Experiments on magnetic transport, magnetic trapping and Bose-Einstein condensation*, PhD thesis (University of Oxford, 2009).

124. C. Henkel, S. Pötting and M. Wilkens, "Loss and heating of particles in small and noisy traps", Appl. Phys. B **69,** 379 (1999).

125. B. Zhang, C. Henkel, E. Haller, S. Wildermuth, S. Hofferberth, P. Krüger and J. Schmiedmayer, "Relevance of sub-surface chip layers for the lifetime of magnetically trapped atoms", EPJ D **35,** 97 (2005).

126. S. Wildermuth, S. Hofferberth, I. Lesanovsky, E. Haller, L. M. Andersson, S. Groth, I. Bar-Joseph, P. Krüger and J. Schmiedmayer, "Bose–Einstein condensates: microscopic magnetic-field imaging", Nature **435,** 440 (2005).

127. H. Casimir and D. Polder, "The influence of retardation on the London-van der Waals forces", Phys. Rev. **73,** 360 (1948).

128. F. Intravaia, C. Henkel and A. Lambrecht, "Role of surface plasmons in the Casimir effect", Phys. Rev. A **76,** 033820 (2007).

129. F. Intravaia, C. Henkel and M. Antezza. *Casimir Physics* 345 (Springer, 2011).

130. Y.-j. Lin, I. Teper, C. Chin and V. Vuletić, "Impact of the Casimir-Polder potential and Johnson noise on Bose-Einstein condensate stability near surfaces", Phys. Rev. Lett. **92,** 050404 (2004).

131. G. Gómez-Santos and T. Stauber, "Fluorescence quenching in graphene: A fundamental ruler and evidence for transverse plasmons", Phys. Rev. B **84,** 165438 (2011).

132. A. Y. Nikitin, F. Guinea, F. J. García-Vidal and L. Martín-Moreno, "Edge and waveguide terahertz surface plasmon modes in graphene microribbons", Phys. Rev. B **84,** 161407 (2011).

133. S. Scheel, P.-K. Rekdal, P. L. Knight and E. A. Hinds, "Atomic spin decoherence near conducting and superconducting films", Phys. Rev. A **72,** 042901 (2005).

134. S. Y. Zhou, G.-H. Gweon, A. V. Fedorov, P. N. First, W. A. De Heer, D.-H. Lee, F. Guinea, A. H. Castro Neto and A. Lanzara, "Substrate-induced bandgap opening in epitaxial graphene", Nature Mater. **6,** 770 (2007).

135. K. S. Novoselov, "Mind the gap", Nature Mater. **6,** 720 (2007).

136. A. Damascelli, "Probing the electronic structure of complex systems by ARPES", Phys. Scripta **2004,** 61 (2004).

137. K. A. Ritter and J. W. Lyding, "The influence of edge structure on the electronic properties of graphene quantum dots and nanoribbons", Nature Mater. **8,** 235 (2009).

138. C. Neumann, S. Reichardt, P. Venezuela, M. Drögeler, L. Banszerus, M. Schmitz, K. Watanabe, T. Taniguchi, F. Mauri, B. Beschoten, *et al.,* "Raman spectroscopy as probe of nanometre-scale strain variations in graphene", Nature Commun. **6,** 8429 (2015).

139. Z. H. Ni, T. Yu, Y. H. Lu, Y. Y. Wang, Y. P. Feng and Z. X. Shen, "Uniaxial strain on graphene: Raman spectroscopy study and band-gap opening", ACS Nano **2,** 2301 (2008).

140. S.-M. Choi, S.-H. Jhi and Y.-W. Son, "Effects of strain on electronic properties of graphene", Phys. Rev. B **81,** 081407R (2010).

141. T. Low, F. Guinea and M. I. Katsnelson, "Gaps tunable by electrostatic gates in strained graphene", Phys. Rev. B **83,** 195436 (2011).

142. G. J. Verbiest, C. Stampfer, S. E. Huber, M. Andersen and K. Reuter, "Interplay between nanometer-scale strain variations and externally applied strain in graphene", Phys. Rev. B **93,** 195438 (2016).

143. S.-J. Han, A. V. Garcia, S. Oida, K. A. Jenkins and W. Haensch, "Graphene radio frequency receiver integrated circuit", Nature Commun. **5,** 3086 (2014).

144. S. Anthony, *URL: http://www.extremetech.com/extreme/175727-ibm-builds-graphene-chip-thats-10000-times-faster-using-standard-cmos-processes* (retrieved on: 2016/04/29).

145. IBM press release, *URL: http://www-03.ibm.com/press/us/en/pressrelease/4435 7.wss* (retrieved on: 2016/04/29).

146. T. Stauber, "Plasmonics in Dirac systems: from graphene to topological insulators", J. Phys. - Condens. Mat. **26,** 123201 (2014).

147. B. Wunsch, T. Stauber, F. Sols and F. Guinea, "Dynamical polarization of graphene at finite doping", New J. Phys. **8,** 318 (2006).

148. E. H. Hwang and S. Das Sarma, "Dielectric function, screening, and plasmons in two-dimensional graphene", Phys. Rev. B **75,** 205418 (2007).

149. J. Christensen, A. Manjavacas, S. Thongrattanasiri, F. H. Koppens and F. J. García de Abajo, "Graphene plasmon waveguiding and hybridization in individual and paired nanoribbons", ACS Nano **6,** 431 (2011).

150. S. Thongrattanasiri, A. Manjavacas and F. J. G. de Abajo, "Quantum finite-size effects in graphene plasmons", ACS Nano **6,** 1766 (2012).

151. S. Thongrattanasiri and F. J. García de Abajo, "Optical field enhancement by strong plasmon interaction in graphene nanostructures", Phys. Rev. Lett. **110,** 187401 (2013).

152. L. Zhang, J. Yang, X. Fu and M. Zhang, "Graphene disk as an ultra compact ring resonator based on edge propagating plasmons", Appl. Phys. Lett. **103,** 163114 (2013).

153. T. Christensen, W. Wang, A.-P. Jauho, M. Wubs and N. A. Mortensen, "Classical and quantum plasmonics in graphene nanodisks: Role of edge states", Phys. Rev. B **90,** 241414R (2014).

Bibliography

154. W. Wang, T. Christensen, A.-P. Jauho, K. S. Thygesen, M. Wubs and N. A. Mortensen, "Plasmonic eigenmodes in individual and bow-tie graphene nanotriangles", Sci. Rep. **5,** 9535 (2015).

155. S. A. Mikhailov and K. Ziegler, "New electromagnetic mode in graphene", Phys. Rev. Lett. **99,** 016803 (2007).

156. O. Kotov, M. Kol'chenko and Y. E. Lozovik, "Ultrahigh refractive index sensitivity of TE-polarized electromagnetic waves in graphene at the interface between two dielectric media", Opt. Express **21,** 13533 (2013).

157. H. Alkorre, G. Shkerdin, J. Stiens and R. Vounckx, "Coupled TM surface plasmon features of graphene-metal layered structure in the sub-THz frequency range", J. Opt. **17,** 045003 (2015).

158. B. E. Saleh and M. C. Teich, *Grundlagen der Photonik* (Wiley-VCH, Weinheim, 2008).

159. G. Klimchitskaya, C. Korikov and V. Petrov, "Theory of reflectivity properties of graphene-coated material plates", Phys. Rev. B **92,** 125419 (2015).

160. P. T. Kristensen, J. R. de Lasson and N. Gregersen, "Calculation, normalization, and perturbation of quasinormal modes in coupled cavity-waveguide systems", Opt. Lett. **39,** 6359 (2014).

161. G. F. A. Marquis de L'Hospital, *Analyse des infiniment petits* (Paris, 1768).

162. M.-H. Bae, Z. Li, Z. Aksamija, P. N. Martin, F. Xiong, Z.-Y. Ong, I. Knezevic and E. Pop, "Ballistic to diffusive crossover of heat flow in graphene ribbons", Nature Commun. **4,** 1734 (2013).

163. A. K. Geim and K. S. Novoselov, "The rise of graphene", Nature Mater. **6,** 183 (2007).

164. K. S. Novoselov, Z. Jiang, Y. Zhang, S. Morozov, H. Stormer, U. Zeitler, J. Maan, G. Boebinger, P. Kim and A. Geim, "Room-temperature quantum Hall effect in graphene", Science **315,** 1379 (2007).

165. A. A. Balandin, "Thermal properties of graphene and nanostructured carbon materials", Nature Mater. **10,** 569 (2011).

166. B. Guo, L. Fang, B. Zhang and J. R. Gong, "Graphene doping: a review", Insciences J. **1,** 80 (2011).

167. R. Ruppin, "Decay of an excited molecule near a small metal sphere", The Journal of Chemical Physics **76,** 1681 (1982).

168. Wolfram Research, Inc., *Mathematica* , Version 10.4 (Wolfram Research, Inc., Champaign, Illinois, 2016).

169. J. Tisler, T. Oeckinghaus, S. R. J, R. Kolesov, R. Reuter, F. Reinhard and J. Wrachtrup, "Single defect center scanning near-field optical microscopy on graphene", Nano Lett. **13,** 3152 (2013).

170. L. Gaudreau, K. Tielrooij, G. Prawiroatmodjo, J. Osmond, F. G. de Abajo and F. Koppens, "Universal distance-scaling of nonradiative energy transfer to graphene", Nano Lett. **13,** 2030 (2013).

171. C. Henkel and S. Pötting, "Coherent transport of matter waves", Appl. Phys. B **72,** 73 (2001).

172. G. Sinuco-León, B. Kaczmarek, P. Krüger and T. M. Fromhold, "Atom chips with two-dimensional electron gases: Theory of near-surface trapping and ultracold-atom microscopy of quantum electronic systems", Phys. Rev. A **83,** 021401R (2011).

173. J. S. Hesthaven and T. Warburton, "Nodal high-order methods on unstructured grids: I. Time-domain solution of Maxwell's equations", J. Comp. Phys. **181,** 186 (2002).

174. J. Niegemann, W. Pernice and K. Busch, "Simulation of optical resonators using DGTD and FDTD", J. Opt. A: Pure Appl. Opt. **11,** 114015 (2009).

175. N. Feth, M. König, M. Husnik, K. Stannigel, J. Niegemann, K. Busch, M. Wegener and S. Linden, "Electromagnetic interaction of split-ring resonators: The role of separation and relative orientation", Opt. Express **18,** 6545 (2010).

176. C. Matyssek, J. Niegemann, W. Hergert and K. Busch, "Computing electron energy loss spectra with the Discontinuous Galerkin Time-Domain method", Photonic. Nanostruct. **9,** 367 (2011).

177. F. von Cube, S. Irsen, R. Diehl, J. Niegemann, K. Busch and S. Linden, "From isolated metaatoms to photonic metamaterials: evolution of the plasmonic near-field", Nano Lett. **13,** 703 (2013).

178. B. Schröder, T. Weber, S. V. Yalunin, *et al.,* "Real-space imaging of nanotip plasmons using electron energy loss spectroscopy", Phys. Rev. B **92,** 085411 (2015).

179. A. Taflove and S. C. Hagness, *Computational electrodynamics : the finite-difference time-domain method* (Artech House, Boston, 2005).

180. K. Busch, M. König and J. Niegemann, "Discontinuous Galerkin methods in nanophotonics", Laser Photon. Rev. **5,** 773 (2011).

181. M. König, *Discontinuous Galerkin Methods in Nanophotonics*, PhD thesis (Karlsruhe Institute of Technology, 2011).

182. J. S. Hesthaven and T. Warburton, *Nodal discontinuous Galerkin methods: algorithms, analysis, and applications* (Springer, 2008).

183. J. Niegemann, *Higher-Order Methods for Solving Maxwell's Equations in the Time-Domain*, PhD thesis (Universität Karlsruhe, 2009).

184. A. Hille, M. Moeferdt, C. Wolff, C. Matyssek, R. Rodriguez-Oliveros, C. Prohm, J. Niegemann, S. Grafström, L. M. Eng and K. Busch, "Second Harmonic Generation from Metal Nano-Particle Resonators: Numerical Analysis Based on the Hydrodynamic Drude Model", J. Phys. Chem. C **120,** 1163 (2015).

185. J. Niegemann, R. Diehl and K. Busch, "Efficient low-storage Runge–Kutta schemes with optimized stability regions", J. Comput. Phys. **231,** 364 (2012).

186. E. Hairer, *Solving Ordinary Differential Equations I: Nonstiff Problems* (Springer-Verlag Berlin Heidelberg, 2010).

Bibliography

187. J.-P. Berenger, "A perfectly matched layer for the absorption of electromagnetic waves", J. Comput. Phys. **114,** 185 (1994).

188. M. König, C. Prohm, K. Busch and J. Niegemann, "Stretched-coordinate PMLs for Maxwell's equations in the discontinuous Galerkin time-domain method", Opt. Express **19,** 4618 (2011).

189. Z. S. Sacks, D. M. Kingsland, R. Lee and J.-F. Lee, "A perfectly matched anisotropic absorber for use as an absorbing boundary condition", IEEE Trans. Antennas Propag. **43,** 1460 (1995).

190. D.-N. Huynh, M. Moeferdt, C. Matyssek, C. Wolff and K. Busch, "Ultrafast three-wave-mixing in plasmonic nanostructures", Appl. Phys. B **122,** 139 (2016).

191. N. D. Ashcroft Neil W. ; Mermin, *Solid State Physics* (Brooks/Coole Thomson Learning, Singapore, 2005).

192. L. J. Prokopeva and A. V. Kildishev, "Efficient time-domain model of the graphene dielectric function", SPIE NanoScience+Engineering, 88060H (2013).

193. A. Andryieuski and A. Lavrinenko, "Graphene metamaterials based tunable terahertz absorber: effective surface conductivity approach", Opt. Express **21,** 9144 (2013).

194. A. H. Mohammadian, V. Shankar and W. F. Hall, "Computation of electromagnetic scattering and radiation using a time-domain finite-volume discretization procedure", Comput. Phys. Commun. **68,** 175 (1991).

195. A. Vial, "Implementation of the critical points model in the recursive convolution method for modelling dispersive media with the finite-difference time domain method", J. Opt. A: Pure Appl Opt **9,** 745 (2007).

196. L. J. Prokopeva, J. D. Borneman and A. V. Kildishev, "Optical dispersion models for time-domain modeling of metal-dielectric nanostructures", IEEE Trans. Magn. **47,** 1150 (2011).

197. A. Kuzmenko, E. Van Heumen, F. Carbone and D. Van Der Marel, "Universal optical conductance of graphite", Phys. Rev. Lett. **100,** 117401 (2008).

198. G. D. Bouzianas, N. V. Kantartzis, C. S. Antonopoulos and T. D. Tsiboukis, "Optimal modeling of infinite graphene sheets via a class of generalized FDTD schemes", IEEE Trans. Magn. **48,** 379 (2012).

199. A. Poddubny, I. Iorsh, P. Belov and Y. Kivshar, "Hyperbolic metamaterials", Nature Photon. **7,** 948 (2013).

200. F. Yang, J. Chen, R. Qiang and A. Elsherbeni, "A simple and efficient FDTD/PBC algorithm for scattering analysis of periodic structures", Radio Science **42** (2007).

201. J. A. Roden, S. D. Gedney, M. P. Kesler, J. G. Maloney and P. H. Harms, "Time-domain analysis of periodic structures at oblique incidence: orthogonal and nonorthogonal FDTD implementations", IEEE Trans. Microw. Theory Techn. **46,** 420 (1998).

202. N. C. Miller, A. D. Baczewski, J. D. Albrecht and B. Shanker, "A Discontinuous Galerkin Time Domain Framework for Periodic Structures Subject to Oblique Excitation", IEEE Trans. Antennas Propag. **62,** 4386 (2014).

203. J. Sipe, "Bulk-selvedge coupling theory for the optical properties of surfaces", Phys. Rev. B **22,** 1589 (1980).

204. J. Sipe, J. F. Young, J. Preston and H. Van Driel, "Laser-induced periodic surface structure. I. Theory", Phys. Rev. B **27,** 1141 (1983).

205. J. Michaelis, C. Hettich, J. Mlynek and V. Sandoghdar, "Optical microscopy using a single-molecule light source", Nature **405,** 325 (2000).

206. J. P. Hoogenboom, G. Sanchez-Mosteiro, G. Colas des Francs, D. Heinis, G. Legay, A. Dereux and N. F. van Hulst, "The single molecule probe: nanoscale vectorial mapping of photonic mode density in a metal nanocavity", Nano Lett. **9,** 1189 (2009).

207. K. Imura, T. Nagahara and H. Okamoto, "Near-field optical imaging of plasmon modes in gold nanorods", J. Chem. Phys. **122,** 154701 (2005).

208. Y. De Wilde, F. Formanek, R. Carminati, B. Gralak, P.-A. Lemoine, K. Joulain, J.-P. Mulet, Y. Chen and J.-J. Greffet, "Thermal radiation scanning tunnelling microscopy", Nature **444,** 740 (2006).

209. R. Beams, D. Smith, T. W. Johnson, S.-H. Oh, L. Novotny and A. N. Vamivakas, "Nanoscale fluorescence lifetime imaging of an optical antenna with a single diamond NV center", Nano Lett. **13,** 3807 (2013).

210. A. W. Schell, G. Kewes, T. Hanke, A. Leitenstorfer, R. Bratschitsch, O. Benson and T. Aichele, "Single defect centers in diamond nanocrystals as quantum probes for plasmonic nanostructures", Opt. Express **19,** 7914 (2011).

211. C. Ropp, Z. Cummins, S. Nah, J. T. Fourkas, B. Shapiro and E. Waks, "Nanoscale imaging and spontaneous emission control with a single nano-positioned quantum dot", Nature Commun. **4,** 1447 (2013).

212. X. Zhu, S. Saito, A. Kemp, K. Kakuyanagi, S.-i. Karimoto, H. Nakano, W. J. Munro, Y. Tokura, M. S. Everitt, K. Nemoto, *et al.,* "Coherent coupling of a superconducting flux qubit to an electron spin ensemble in diamond", Nature **478,** 221 (2011).

213. F. Jelezko, C. Tietz, A. Gruber, I. Popa, A. Nizovtsev, S. Kilin and J. Wrachtrup, "Spectroscopy of single NV centers in diamond", Single Molecules **2,** 255 (2001).

214. M. Huxter, T. A. A. Oliver, D. Budker and G. R. Fleming, *Vibrational and electronic ultrafast relaxation of the nitrogen-vacancy centers in diamond EPJ Web Conf.* **41** (2013), 04009.

215. H. Mamin, M. Kim, M. Sherwood, C. Rettner, K. Ohno, D. Awschalom and D. Rugar, "Nanoscale nuclear magnetic resonance with a nitrogen-vacancy spin sensor", Science **339,** 557 (2013).

216. J. Wolters, J. Kabuss, A. Knorr and O. Benson, "Deterministic and robust entanglement of nitrogen-vacancy centers using low-Q photonic-crystal cavities", Phys. Rev. A **89,** 060303R (2014).

217. J. Weber, W. Koehl, J. Varley, A. Janotti, B. Buckley, C. Van de Walle and D. D. Awschalom, "Quantum computing with defects", Proc. Natl. Acad. Sci. USA **107,** 8513 (2010).

Bibliography

218. R. J. Glauber, "The quantum theory of optical coherence", Phys. Rev. **130,** 2529 (1963).

219. MATLAB, *Version 8.1 (R2013a)* (The MathWorks Inc., Natick, Massachusetts, 2013).

220. P. B. Johnson and R. W. Christy, "Optical Constants of the Noble Metals", Phys. Rev. B **6,** 4370 (1972).

221. A. Delga, J. Feist, J. Bravo-Abad and F. Garcia-Vidal, "Quantum emitters near a metal nanoparticle: strong coupling and quenching", Phys. Rev. Lett. **112,** 253601 (2014).

222. C. Van Vlack, P. T. Kristensen and S. Hughes, "Spontaneous emission spectra and quantum light-matter interactions from a strongly coupled quantum dot metal-nanoparticle system", Phys. Rev. B **85,** 075303 (2012).

223. H. Takeda and S. John, "Self-consistent Maxwell-Bloch theory of quantum-dot-population switching in photonic crystals", Phys. Rev. A **83,** 053811 (2011).

224. U. Hoeppe, C. Wolff, J. Küchenmeister, J. Niegemann, M. Drescher, H. Benner and K. Busch, "Direct observation of non-Markovian radiation dynamics in 3D bulk photonic crystals", Phys. Rev. Lett. **108,** 043603 (2012).

225. A. Deinega and T. Seideman, "Self-interaction-free approaches for self-consistent solution of the Maxwell-Liouville equations", Phys. Rev. A **89,** 022501 (2014).

226. R. Kieschke, *(working title) Quantum emitters near to hyperbolic metamaterial cavities*, Master thesis (Humboldt-Universität zu Berlin, hand-in date: October 2017).

227. P. W. Milonni, *The quantum vacuum : an introduction to quantum electrodynamics* (Academic Press, Boston [u.a.], 1994).

228. K. Drexhage, "Influence of a dielectric interface on fluorescence decay time", JOL **1,** 693 (1970).

229. S. J. Barrow, X. Wei, J. S. Baldauf, A. M. Funston and P. Mulvaney, "The surface plasmon modes of self-assembled gold nanocrystals", Nature Commun. **3,** 1275 (2012).

230. K. J. Kaufmann and P. M. Rentzepis, "Picosecond spectroscopy in chemistry and biology", Acc. Chem. Res. **8,** 407 (1975).

231. A. W. Rodriguez, A. P. McCauley, J. D. Joannopoulos and S. G. Johnson, "Casimir forces in the time domain: Theory", Phys. Rev. A **80,** 012115 (2009).

232. A. P. McCauley, A. W. Rodriguez, J. D. Joannopoulos and S. G. Johnson, "Casimir forces in the time domain: Applications", Phys. Rev. A **81,** 012119 (2010).

233. F. Intravaia and K. Busch, "Fluorescence in nonlocal dissipative periodic structures", Phys. Rev. A **91,** 053836 (2015).

234. A. Stern, "Anyons and the quantum Hall effect – a pedagogical review", Ann. Phys. **323,** 204 (2008).

235. A. Y. Kitaev, "Fault-tolerant quantum computation by anyons", Ann. Phys. **303,** 2 (2003).

236. H. Kleinert, *Path integrals in quantum mechanics, statistics, polymer physics, and financial markets* (World Scientific, 2009).

237. J. E. Campbell, "On a law of combination of operators (second paper)", Proc. London Math. Soc. **1,** 14 (1897).

238. I. Fialkovsky and D. Vassilevich, "Parity-odd effects and polarization rotation in graphene", J. Phys. A **42,** 442001 (2009).

239. I. Fialkovsky and D. Vassilevich, "Faraday rotation in graphene", EPJ B **85,** 384 (2012).

Acknowledgments

"Never trust a computer you can't throw out a window" [37]

Steve Wozniak

First and foremost, I would like to acknowledge my gratitude to Prof. Kurt Busch who has put his trust in me and supported me first during my Diploma thesis and then of course during the last three and a half years. Second, I would like to extend this gratitude to the two referees of my thesis, Prof. N. Asger Mortensen and Prof. Stefan Scheel, who agreed to invest their time to read and grade this thesis.

My research during the last three years was financed by the Studienstiftung des deutschen Volkes. I would like to express my appreciation to this independent source of finances that allowed me to steer the research the way it was appropriate and with the huge number of seminars offered helped me to broaden my horizon beyond my research.

Furthermore, I would like to thank all collaborators that I had the pleasure working and exchanging ideas with over the last three years. This includes Prof. Oliver Benson, Dr. Andreas Schell and Philip Engel from the Humboldt-Universität zu Berlin as well as Prof. Peter Krüger from the University of Nottingham, Dr. Thomas Pfadler from the Universität Konstanz and Manuel Peter from the Universität Bonn.

Then, it is very important to me to thank all my colleagues in this group that have walked on this path together with me. It has been some marvelous almost five years in the group. Relating to the quote at the beginning of the chapter, I would like to stress that even though somebody installed bars in front of our windows in the physics building such that we never managed to actually throw a computer out of any of the institute's window, these people have nonetheless helped me through a lot of frustration (especially when we were all fighting with frozen computers) but also shared the joy of doing this research. Especially, I would like to name Dr. Francesco Intravaia who has worked on all the graphene related topics with me and has been a great source of experience[38] and Dr. Christian Matyssek who has been a very invested administrator of our codebase called *Spreewaldgurke*. With him and also Dr. Christian Wolff I had the pleasure to work on a number of software development issues. Additionally, I would like to thank all the co-doctoral students who have been longer or shorter walking alongside with me and the students I was favored to work with (Franziska Bierbüße, Marcel Gawek, Christian Gryzik

---

[37] *URL: http://lifehacker.com/5222989/how-apple-co-funder-steve-wozniak-gets-tings-done* (retrieved on: 2016/05/23).

[38] One of his wisdom, in which a lot of truth lies, is: *"The life of a scientist is a life in misery with delta like momenta of joy"*.

Acknowledgments

and Robert Kieschke). In this context, I would like to especially thank Torsten Wendav, my office mate throughout all this time, Dr. Christoph Martens and Matthias Moeferdt, my Diploma thesis colleagues that carried on with me in the group and Dan-Nha Huynh and Kathrin Herrmann with whom I had two awesome female colleagues.

In the last step of writing this thesis, I would also like to express my sincerest appreciation for all the comments of colleagues proof-reading my thesis.

Last but not less importantly, I would like to thank my friends and family. The friends from the Taizé circle that sometimes helped me without knowing with fundamental physical problems in my thesis (thanks, Theresas, Steph, Anna, Veronika, Elisabeth and Clara) and the friends from old Karlsruhe times that are now scattered all over Germany (thanks, Yvonne, Elisabeth, Jochen, Benedikt and Moritz). My family, including my four siblings Ursula, Nicola, Markus and Clara and over all my mom have all been corner stones throughout this period of my life. I could not have done it without the five of you!

Thanks to everybody I have not mentioned explicitly. I know that I owe all of you!